U.S. Department of Energy
FreedomCAR and Vehicle Technologies
1000 Independence Avenue, S.W.
Washington, D.C. 20585-0121

FY 2002

Progress Report for Energy Storage Research and Development

Energy Efficiency and Renewable Energy
FreedomCAR and Vehicle Technologies

Tien Q. Duong
Manager, Energy Storage R&D

May 2003

TABLE OF CONTENTS

I. INTRODUCTION

The number of vehicles on American roads and the number of miles driven by those vehicles continue to grow, resulting in increased air pollution, increased petroleum consumption, and, indirectly, increased reliance on foreign sources of that petroleum. To counter these trends, new vehicles and fuels must be introduced that can achieve better fuel economy while producing fewer harmful emissions.

In addition, two successful hybrid vehicles have been introduced into the American automotive market over the past two years, the Toyota Prius and the Honda Insight. The challenge is for the United States to work towards energy independence, market leadership, while maintaining consumer choice and mobility. The Energy Storage Research and Development Effort is working to help ensure that these challenges are met and surpassed.

I.A. FreedomCAR and Vehicle Technologies Program Overview

On January 9, 2003, the Department of Energy (DOE) and the leadership of General Motors Corporation, Ford Motor Company, and DaimlerChrysler Corporation announced the creation of the FreedomCAR Partnership[1]. This partnership is focused on funding high-risk research that promises improvements in critical components needed for more fuel efficient, clean vehicles. The overarching goal of the program is to develop the component technologies needed for affordable cars and light trucks that will reduce our dependence on foreign petroleum, reduce emissions, yet do not impact American's historic mobility and freedom of vehicle choice.

The long-term goal of the FreedomCAR Partnership is the achievement of vehicles that lead to a clean vehicle fleet that provides enhanced fuel economy and therefore leads to a sustainable energy future. Transportation consumes 2/3 of all petroleum consumed in the United States, and is therefore a natural place to focus efforts on increased efficiencies.

The Department of Energy has reorganized its Office of Energy Efficiency and Renewable Energy (EERE) in response to a recent program performance review. This new structure will strengthen DOE's programs and their ability to meet industry's needs efficiently.

Key aspects of the Office of Transportation Technologies have been incorporated into the FreedomCAR & Vehicle Technologies Program. This new program works with industry to develop and deploy advanced transportation technologies that reduce the nation's use of imported oil and improve air quality. Some of the technologies being supported by this office are Hybrid Systems R&D, Advanced Combustion Engine R&D, Electric Vehicle R&D, Materials Technologies R&D, Heavy Vehicle Systems R&D, Fuels Utilization R&D, and the R&D-related or private sector related elements of Technology Utilization. As shown, the program maintains a balanced set of R&D activities in light and heavy vehicle technologies, including combustion/emission control, alternative

[1] For more information, please see http://www.uscar.org/Media/2002issue1/p1_freedomcar.htm, or www.ott.doe.gov/pdfs/freedomcar_plan.pdf.

fuels, and hybrid technologies and maintains extensive industry relations such as the Government/Industry Truck Partnership

I.B. Energy Storage Research & Development Overview

Energy storage technologies, especially batteries, have been identified as critical enabling technologies for the successful development of advanced, fuel-efficient, light and heavy duty vehicles. The Energy Storage Research and Development Effort within the FreedomCAR and Vehicle Technologies (FCVT) Program is responsible for advancing and facilitating the commercialization of innovative batteries for a wide range of vehicle applications, including hybrid electric vehicles (HEVs), battery electric vehicles (EVs), the emerging range of 42 volt vehicle systems (42V), as well as fuel cell vehicles (FCVs). The office is working in close partnership with the automotive industry, represented by the United States Advanced Battery Consortium (USABC)[2].

Advanced battery technologies are needed to support both the full range of hybrid electric vehicles, from those that require high-energy batteries to those that require high power batteries. The new Energy Storage R&D Effort has been created in response to the converging needs and plans of both high energy (electric vehicle) and high-power (hybrid electric vehicle) battery research. As part of this streamlining, the former program structure that consisted of two programs, one each for the hybrid and electric vehicle battery work, has been combined into a single electric energy storage R&D effort. The benefits of this are primarily to focus all of DOE's researchers' efforts onto the critical technical barriers, and to minimize the administrative and management overhead associated with this work.

The new effort is comprised of three major activities, Battery Technology Development, Applied Research, and Long-term, Exploratory Research. The work done in each of these is described below:

Battery Technology Development is one of the primary activities of the energy storage effort. It is subdivided into three closely related sets of activities: full system development, technology assessment, and benchmark testing.

Full System Development - In cooperation with the USABC, efforts are focused on developing and evaluating a cost-optimized liquid cooled NiMH monoblock module for HEVs, on addressing the issues that reduce the useful life of lithium ion batteries in EVs, on reducing the cost of lithium ion HEV modules, and on the development of an advanced lithium sulfur (Li/S) battery system that has the potential of meeting all EV targets, including cost.

Technology Assessment - Technology assessments are often conducted on newly emerging technologies before entering into the development of full systems. These limited, 12-month projects assess a developer's overall capabilities and validate technical claims by independent testing. Current assessment projects include cells based on Li-ion gel technology, a spinel based chemistry, and a new $LiFePO_4$ cathode active material.

Benchmark Testing - Benchmark testing of emerging technologies is important for remaining abreast of the latest industry developments. Working with the national laboratories, FCVT

[2] The USABC is a partnership, formed in 1991, between DaimlerChrysler, Ford, and General Motors to initiate a domestic advanced battery industry based on new technology.

purchases and independently tests hardware against the manufacturer's specifications and the most applicable technical targets. Recently completed benchmark testing included Li-ion/manganese spinel chemistries against HEV and EV targets.

Applied Research is focused on addressing the cross-cutting barriers that face Li-ion systems, the technologies that are closest to meeting all of the technical energy and power requirements for vehicle applications. Five national laboratories participate in this activity, each bringing its own expertise, as summarized below:

- Argonne National Laboratory (ANL): battery system development and electrochemical diagnostics;
- Brookhaven National Laboratory (BNL): x-ray diagnostics;
- Idaho National Engineering and Environmental Laboratory (INEEL): battery testing and electrolyte development;
- Lawrence Berkeley National Laboratory (LBNL): spectroscopy and microscopy diagnostics; and,
- Sandia National Laboratory (SNL): abuse evaluation, accelerated life test protocol development, and statistical analysis.

Long-term Research addresses fundamental problems of chemical instabilities that impede the development of advanced batteries. This research provides a better understanding of why systems fail, develops models that predict system failure and permit system optimization, and investigates new and promising materials. The work presently concentrates on six research areas:

- In *Cell Development,* experimental cells incorporating novel materials are prepared and evaluated.
- Investigators working on *Anodes* are searching for a material that do not suffer from capacity loss on cycling due to structural changes.
- Work on *Electrolytes* has mostly focused on solid polymer electrolytes, including composite polymer electrolytes, to overcome the problems of dendrite formation.
- Work on *Cathodes* has concentrated on two materials: low cost, stable, abuse resistant $LiFePO_4$ and high voltage, high capacity $LiNi_xM'_yMn_{1-x-y}O_2$. .
- Work in *Diagnostics* has resulted in enhanced tools to assist researchers in better understanding the processes occurring in actual cells.
- *Modeling* efforts have led to a better understanding of ion transport in organic solvents, and to a better understanding of cathode structure and the sources of capacity fade. .

This report highlights the activities and progress achieved in the Energy Storage Research and Development Effort during FY 2002. We are pleased with the progress made during the year and look forward to continuing working with our industrial, government, and scientific partners to overcome the challenges that remain to delivering advanced energy storage systems for vehicle applications.

Tien Q. Duong
Manager, Energy Storage Research and Development
FreedomCAR and Vehicle Technologies Program

II. BATTERY TECHNOLOGY DEVELOPMENT

II.A. Vehicle High-Power Energy Storage

II.A.1. Introduction

The number of vehicles on American roads and the number of miles driven by those vehicles continue to grow, resulting in increased air pollution, increased petroleum consumption, and, indirectly, increased reliance on foreign sources of that petroleum. To counter these trends, new vehicles are being introduced that achieve better fuel economy while producing fewer harmful emissions.

Under the leadership of the Department of Energy's (DOE) Office of Advanced Automotive Technologies (OAAT), the Vehicle High-Power Battery Program is part of a multifaceted effort to further develop and perfect the technologies needed to encourage the adoption of cleaner, more fuel-efficient hybrid-electric (hybrid) vehicles in the commercial marketplace. Among other programs, the Vehicle High-Power Battery Program supports the FreedomCAR Program and contributed to the success of the Partnership for a New Generation of Vehicles (PNGV). These government-industry partnerships have made considerable progress towards developing a mid-sized passenger vehicle capable of surpassing current emissions and vehicle mileage standards while maintaining performance, safety, and comfort.

Hybrid vehicles have fuel economy and emissions advantages over ICEs, and have already enjoyed some commercial acceptance (e.g., see the successful Toyota Prius and Honda Insight, and the recent announcement by US automakers of their intent to release hybrid sport utility vehicles in the U.S. market). Lightweight, affordable, high-power batteries are one of the critical technologies and improvements in this technology are essential for the continuing development of hybrids.

Hybrid vehicles generally need much less energy storage capacity than pure electric vehicles because they have a small ICE that supplies most of the vehicle's energy needs, but they still require significant power levels. This means that at the cell level, hybrid vehicle batteries must have a higher ratio of peak power capability to energy storage capability. The Vehicle High-Power Battery Program is focused on overcoming the main technical barriers associated with improved commercialization of hybrid vehicles by concentrating on four major areas, namely:

Cost

The current cost of nickel-metal hydride and lithium-based batteries (the most promising high-power battery chemistries) is prohibitively high on a kW or kWh basis. The main cost drivers being addressed are:

- High cost of raw materials and materials processing, and
- Cell and module packaging cost.

Battery Life

The life of lithium-based batteries is estimated to be approximately 10 years (quickly approaching 12). Nickel-metal hydride batteries have a calendar life of 6+ years. However, a 15-year calendar life is required to reduce overall system costs and to make the technology more attractive to consumers.

Battery Performance

The barriers related to battery performance are the reduced discharge pulse power that is available at low temperatures, and the loss of available power over time due to use and aging.

Abuse Tolerance

High power batteries are not intrinsically tolerant of abuse such as short circuits, overcharge, over-discharge, mechanical shock, vibration, crush, or fire exposure. Multiple strings of cells pose a problem for lithium-based technologies, because they require overcharge and over-discharge protection at the cell level. Low-cost, failsafe electric and mechanical safety devices need to be developed. In addition, challenging thermal management requirements need to be addressed.

II.A.2. Overview[3]

The Vehicle High-Power Battery Program was created to develop solutions to the technical challenges outlined above by developing low-cost, high-power batteries that meet or exceed the energy storage requirements shown in Table 1 (set by the PNGV), by 2008. The specific objectives of the Vehicle High-Power Battery Program include:

By 2004, demonstrate fabrication and assembly of thin electrode components at high throughput rates, along with high-speed assembly of electrodes and components, into compact, lightweight, high-power batteries, and

By 2008, develop low-cost, high-power battery technology that meets or exceeds the energy storage requirements for the power-assist and dual-mode hybrid vehicles.

[3] Note that this report reflects what appears in the public domain and does not include any "Protected Battery Information."

Table 1: Energy Storage Requirements

Goals		**Power Assist**	**Dual Mode**
	Units	**Minimum**	**Minimum**
Pulse discharge power (18s)	kW	25	45 for 12-sec
Max regen pulse (10s)	kW	30 (50Wh pulse)	35 (97Wh pulse)
Total available energy	kWh	0.3	1.5 (at 6kW rate)
Round trip efficiency	%	>90, 25Wh PA cycle	>88, 100Wh DM Eff cycle
Cycle life for specified SOC increments	Cycles	200k for 25Wh PA cycles	2500 DM cycles
Cold cranking power at –30°C [4]	kW	5	5
Calendar life	Yrs	10	10
Max weight	kg	40	100
Max volume	Liters	32	75
Production cost @ 100k units/year	$	300	500
Maximum operating voltage	Vdc	<= 440	<= 440
Minimum operating voltage	Vdc	>= 0.55 Vmax	>= 0.50 Vmax
Maximum dc link current	A	<= 217	<= 217
Maximum self discharge	Wh/d	50	50
Operating temperature	°C	-40 to +52	-40 to +52
Survival temperature	°C	-46 to +66	-46 to +66

Two candidate battery chemistries have been identified as the most likely to meet performance and cost targets: nickel-metal hydride (Ni-MH) and lithium-based technology, including Li-sulfur couples. Ni-MH batteries offer relatively good power capability as a result of the good ionic conductivity of the potassium hydroxide electrolyte. Lithium-based batteries offer excellent energy density that can be traded for higher power.

Four USABC subcontracts to establish baseline cell chemistries and electrode designs were awarded at the program's inception in 1997. During 1997, two of the four subcontractors – SAFT America and VARTA – were awarded follow-on subcontracts to develop and demonstrate their high-power battery technologies at the nominal 50-V module level with electronic and thermal management. The SAFT technology is based on 6 and 12-Ah lithium-ion cells; the VARTA technology uses 10-Ah Ni-MH cells.

Responding to new developments in lithium-polymer technology and the potential for lower cost Ni-MH, the USABC awarded two lithium-polymer and two Ni-MH development subcontracts in 2000. The contracts were awarded to Delphi (lithium-polymer), AVESTOR (lithium-polymer), Texaco-Ovonic (Ni-MH), and Electro Energy, Inc. (bipolar Ni-MH) to benchmark and demonstrate that their respective technologies can meet the technical requirements for this application.

The separator used in high power, lithium/ion cells of the type being developed for hybrid electric vehicles (HEV's) is a thin, microporous film of one or more polymeric materials. It represents one of the single most costly materials in the cell. In some cell designs, the cost of the separator will be over 30% of the total materials' cost. The current market price for separators is in excess of two dollars per square meter and can exceed three dollars. This cost reflects the complex manufacturing processes necessary to transform bulk plastics into a microporous thin film. In order to reduce the cost of separators, the DOE, in conjunction with the USABC, is supporting research

[4] Three 2 sec pulses, 10 sec rests between.

and development efforts in industry to create novel low cost materials and to improve processing techniques so that currently available materials may be produced in a less costly manner.

As a result of the recognition that separator cost is a significant barrier to commercialization of lithium batteries, two new contracts to research and develop lower-cost separators were awarded in 2002, one each to Celgard and ENTEK. The early results of this work has been extremely encouraging, with both ENTEK and Celgard reporting that they will meet the new cost target well ahead of schedule. In addition, advanced supercapacitor technology is being reviewed and evaluated for applicability to HEVs.

The main participants currently involved in the Vehicle High-Power Battery Program, and their primary responsibilities, are described below and summarized in Table 2.

- Under DOE sponsorship, Texaco Ovonic (TOBS) has developed liquid-cooled plastic monoblock nickel-metal hydride (NiMH) batteries for power-assist applications. In Phase 1, development of an improved electrode stack resulted in a two-fold increase in power and reduced the projected $/kW battery cost by half. In Phase 2, the plastic monoblock module evolved from a labor-intensive battery proof-of-concept to one more amendable to mass production. The new Battery X20 design, which also evolved from Phase 2 work, provided a lower cost approach even better adapted to mass production with the added benefit of significant improvements in packaging efficiency.

  The objective of the Phase 3 program is to complete technology development needed for a total battery system that attains viable commercial products for the FreedomCAR partners. First, the program will target additional cost reduction to achieve a projected selling price of about $750 for full battery pack systems at a mature volume of 100K packs per year. Second, additional hardware development for Battery X20, not anticipated in Phase 2, will be completed. Third, qualification of the battery cycle life and calendar life is planned.

- SAFT was awarded a follow-on 18-month contract starting June 1, 2001 to reduce the cost of a hybrid-electric power-assist lithium-ion battery by 50 percent of the Phase II final price based on 100,000 batteries per year and to fabricate nominal 50-volt modules for performance and life validation. To achieve the targeted cost reduction SAFT will focus on material cost reduction, and process and assembly optimization. To validate the performance and life SAFT will validate the improved low-cost cell, validate the performance and life of nominal 50-volt modules, refurbish the 276-volt DOE mini battery packs at INEEL, and perform a system abuse tolerance assessment study.

- Celgard, Inc., headquartered in Charlotte, NC, is engaged in a two-phase, 24-month effort to develop an improved process for the manufacture of low-cost separators for Li-ion cells. The target is to meet or exceed FreedomCAR goals and achieve $1/m^2 price.

- ENTEK Membranes LLC's work is focused on the evaluation and improvements of Teklon separators. ENTEK Membranes will use its proprietary process to develop separator samples. The samples are targeted to meet or exceed FreedomCAR goals and achieve $1/m^2 price.

Contracts have an industry cost-share of at least 50%.

Table 2: Vehicle High-Power Program Participants

Participant	Responsibility
SAFT America, Inc.	Develop and demonstrate high-power technologies based on nominal 6 and 12-Ah lithium-ion cells at the 50-V module level with electronic and thermal management. See Exhibit 1.
Texaco-Ovonic (TOBS, formerly GMO)	Benchmark and demonstrate that Texaco-Ovonic, Inc.'s NiMH technology can meet all technical targets.
ENTEK	Research and deliver lower cost separators.
Celgard	Research and deliver lower cost separators.

II.A.3. FY 2002 Highlights

The major accomplishments in the Vehicle High-Power Battery Program in the first half of FY 2002 were:

- During FY 2002, FCVT sought proposals through the SBIR/STTR Program for the development of lower cost separators. Two Phase I SBIR contracts were awarded for the development of novel materials. These contracts, with the Lithion Division of Yardney Technical Products and with Optodot Corporation, will conclude in the second quarter of FY '03; at that time, the possibility of Phase II contract awards will be investigated.

- The USABC sought similar proposals from industry, with an emphasis on improved production technology associated with low cost separators. Several proposals were received, from which two USABC contracts were let with ENTEK and Celgard during FY '02. Other contracts may be awarded in FY '03. Both Celgard and ENTEK, in preliminary and draft communications, report that they have met the cost target of $\$1/m^2$ for their separator and that the new material performs as well as Celgard's current commercially available separator.

- Texaco-Ovonic Battery Systems (TOBS) has demonstrated a new bi-polar Ni-MH battery design provides a lower cost approach better adapted to mass production with the added benefit of significant improvements in packaging efficiency.

- Saft has demonstrated a greater than 10 year life using accelerated life testing

- Saft delivered 2 full packs to DOE, one of which has completed 300,000 HEV test cycles suffering less than 2% power fade.

The National Laboratories' accomplishments in high-power batteries (focused on lithium technology) are detailed in a comparison report on the ATD Program.

Future Directions

Looking ahead, the Vehicle High-Power Battery Program will continue to research lower cost separators, will define energy storage requirements for heavy hybrids, will ensure that new materials are made available to manufacturers, and promote information exchange among the various participants in the program.

II.B. Electric Vehicle Battery Research and Development

II.B.1. Introduction

The Electric Vehicle Battery Research and Development Program has been a part of the Office of FreedomCAR and Vehicle Technologies since its inception in the late 1970s. Advanced batteries have been an integral part of the high-risk/high-payoff activities sponsored by the Department on electric vehicles R&D. The program supports the development of battery technologies that would enable commercially competitive electric vehicles (EV). The technical requirements of the program are defined in Table 1.

The advantage of fully EV vehicles (over other vehicles, including HEVs) is the fact that they emit zero emissions, that is, they do not pollute the air at all. Of course, the energy needed to power these vehicles, or to charge their batteries, must be produced at power plants. However, it is widely recognized that it is easier to control and mitigate emissions from a small number of power plants than it is to reduce emissions from millions of automobiles.

The Electric Vehicle Battery Research and Development Program has had several major successes, including the development and introduction of the nickel metal hydride (NiMH) battery for EV use. Over 1000 NiMH battery EVs have been put into service in the past several years. The program conducts extensive benchmarking studies of advanced batteries from the U.S. and abroad. Work is currently proceeding to benchmark both NiMH and lithium-ion systems (at the cell level).

II.B.2. FY 2002 Highlights

SAFT will continue development of the lithium-ion electric vehicle battery with emphasis on meeting interim commercialization goals. SAFT will engineer and build lithium-ion cells to evaluate alternative battery system materials and will provide more detailed testing and analysis against USABC and Society of Automotive Engineers (SAE) criteria for evaluation of abuse to these batteries. This will enable acceptance of these batteries by the auto industry. The program focus will be on materials research and selection. SAFT will conduct

comprehensive safety analysis including testing and failure modes and effects analysis. In 2002, work in this area resulted in:

- Cell performance generally exceeding initial goals
- Cells attaining a large power margin
- Cells having attained over 1400 cycles

Table 1: U.S. Advanced Battery Consortium Goals for Electric Vehicle Batteries

Primary Criterion	**Long-term goals[5] (2005-2008)**
Power Density, W/l	460
Specific Power, W/kg (80% DOD/30 sec)	300
Energy Density (Wh/l) (C/3 discharge rate)	230
Specific Energy, Wh/kg (C/3 discharge rate)	150
Life (years)	10
Cycle life (cycles)	1000 (80% DOD) 1,600 (50% DOD) 2670 (30% DOD)
Power and capacity degradation[6] (% of rated spec)	20%
Ultimate price[7] ($/kWh) (10,000 units @ 40 kWh)	<$150 (desired to 75)
Operating environment	-30C to 65 C
Recharge time[2]	< 6 hours
Continuous discharge in 1 hour (no failure)	75% (of rated energy capacity)
Secondary Criteria	**Long-term goals (2005-2008)**
Efficiency[2] (C/3 discharge and C/6 charge[8])	80%
Self-discharge[2]	<20% in 12 days
Maintenance	No maintenance. Service by qualified personnel only.
Thermal loss[2]	Covered by self-discharge
Abuse resistance[2]	Tolerant. Minimized by on-board controls.
Specified by contractor Packaging constraints Environmental impact Safety Recyclability Reliability Overcharge/over-discharge tolerance	

Lithium/sulfur, rechargeable batteries offer the possibility of several advantages over the current state-of-the-art in lithium/ion rechargeable cells. Because sulfur is inexpensive relative to the lithiated metal oxides used for the cathodes in lithium/ion systems, the lithium/sulfur system has the promise of significantly lower cost per kilowatt-hour of stored energy. The use of a metallic lithium anode in lithium/sulfur cells may allow for improved specific energy and energy density relative to the lithium/ion system which must use a non-reactive matrix material, such as carbon, for the anode.

[5] For interim commercialization (reflects USABC revisions of September 1996).
[6] Specifics on criteria can be found in *USABC Electric Vehicle Battery Test Procedures Manual, Rev. 2*, DOE/ID 10479, January 1996,
[7] Cost to the original equipment manufacturers.
[8] Roundtrip charge/discharge efficiency.

The complex chemistry of the lithium/sulfur cell may also provide a "shuttle mechanism" that would allow the cell to be overcharged without significant safety problems or other adverse effects. Unfortunately, the lithium/sulfur system is not mature enough for these potential advantages to be demonstrated in commercial cells. Therefore, the DOE, in conjunction with the USABC, intends to support research and development on this systems through one or more contracts with industry.

Two long-term research and development contracts have been considered to investigate the lithium sulfur system. Early phases of these programs will focus on finding a means to improve the anode-electrolyte interface against parasitic reactions and to improve the cells' cycling efficiency.

During FY 2002, FCVT sought proposals through the SBIR/STTR Program and as subcontracts to the contract with USABC to further investigate and develop the lithium-sulfur system. Several proposals were received in response to both solicitations during FY '02. Negotiations were conducted towards the goal of letting contracts in FY '03.

Also, two major technology assessments were undertaken in 2002, one on the Zebra battery ($Na/NiCl_2$), and a second set on Li-ion batteries from multiple domestic and foreign suppliers.

All contracts have industry cost-share of at least 50%.

Future activities

Over the next year, the Electric Vehicle Battery Research and Development Program will focus on testing and demonstrating the performance of the lithium sulfur cells against the USABC requirements.

III. APPLIED RESEARCH

III.A. Introduction to the Applied Research Activity

The Energy Storage R&D Effort funds high-risk research and development to provide enabling technologies for fuel efficient and environmentally friendly vehicles. The Applied Research Activity focuses on high-power battery development in support of the FreedomCAR Partnership's goal of affordable cars and light trucks that will reduce our dependence on foreign petroleum, reduce emissions, yet do not impact American's historic mobility and freedom of vehicle choice.

Started in late 1998 as the ATD program, the Applied Research Activity focuses on finding solutions to barriers that are impeding U.S. battery manufacturers in their efforts to produce and market high-power batteries for use in hybrid electric vehicles (HEVs).
The major challenges facing the commercialization of high-power battery technology can be characterized under one of three headings: life, abuse tolerance, and cost. Of these, cost is the overriding factor and the other three must be pursued with a continual consideration of their impact on battery cost.

C*alendar Life* of 15years is required to meet the California emissions standards. Calendar life of the current generation of lithium-based batteries is estimated to be approximately 6–10 years, although there are encouraging estimates approaching 12 years. Mechanisms that lead to poor calendar life are intensified as the temperature of the system increases. This requires additional effort in advanced thermal management and the development of more robust chemistries. To address issues associated with the calendar life of high-power batteries, the Applied Research Activity is:

- developing and validating accelerated life test methods,
- identifying life-limiting mechanisms, and
- finding advanced cell components that address these life-limiting mechanisms and extend cell life.

Abuse Tolerance is a primary requirement for a high power device in an automotive application. High power batteries are not intrinsically tolerant of abuse such as short circuits, overcharge, overdischarge, mechanical shock, vibration, crush, or fire exposure. Chemical additives that circumvent smoke and/or fire generation are being designed and evaluated to operate in conjunction with mechanical safeguards. In addition, challenging thermal management requirements faced during stressful periods in a driving cycle need to be addressed. The general approach to safety issues includes:

- Specify relevant abuse conditions and desired responses to those conditions, along with standards for abuse testing.
- Test, evaluate, and redesign cell and chemistry (developer proprietary information) to ensure abuse tolerance.

- Develop detection and management controls for battery state-of-charge, battery temperatures, and electrical faults. Controls at the cell level will include devices for relief of internal pressure buildup and for internal circuit interruption.

- Develop *in situ* overcharge protection.

The thermal failure modes are being investigated through comprehensive cell testing and diagnostic efforts. It is anticipated that the detailed thermal runaway mechanisms will be understood and addressed with more optimal materials. This information will be shared with the developers and used to develop cells, modules, and full systems that are more inherently safe.

The current *cost* of high-power lithium-based cells is prohibitively high on a kW or kWh basis. Multiple strings of cells pose a problem for lithium-based technologies because they require overcharge and overdischarge protection at the cell level. The main cost drivers being addressed in the Applied Research Activity are the high cost of raw materials and materials processing, cell and module packaging cost, and low-cost, failsafe electric and mechanical safety devices. Specific activities include:

- Evaluating lower cost cell components: electrolytes, anodes, and cathodes.

- Developing low-cost processing methods for producing advanced cell materials.

- Working with potential US suppliers to implement low-cost material production.

- Developing low-cost cell packaging alternatives.

The Applied Research Activity requires the close coordination of research and diagnostic efforts of five national laboratories: Argonne National Laboratory (ANL), Brookhaven National Laboratory (BNL), Idaho National Engineering and Environmental Laboratory (INEEL), Lawrence Berkeley National Laboratory (LBNL), and Sandia National Laboratory (SNL). Close communication is maintained with battery developers, automobile manufacturers, and related corporations to ensure that the issues being investigated will be of direct benefit to the U.S. battery manufacturing community. To make an impact on the cost barriers, relationships with over a dozen present and potential battery component vendors have been established. In addition, close ties are maintained with other governmental organizations involved in advanced battery research through the Interagency Power Working Group. This ensures that relevant technical issues being addressed and timely solutions being developed are disseminated amongst all interested government agencies

The following section highlights the activities and progress achieved in the Applied Research Effort during FY 2002. The report is comprised of nine technical project summaries submitted by the national laboratories, universities, and industrial firms that participated in this exciting work.

III.B. Life Testing And Power Fade

III.B.1. Life Testing and Power Fade

Jon Christophersen, Chet Motloch, Randy Wright, Chinh Ho, David Glenn, Tim Murphy
Idaho National Engineering and Environmental Laboratory, Idaho Falls, ID 83415-3830
(208) 526-4280; fax: (208) 526-0969; e-mail: chrijp@inel.gov

Ira Bloom, Scott Jones, Vince Battaglia, Gary Henriksen
Argonne National Laboratory, Argonne, IL 60439-4837
(630) 252-4516; fax: (630) 252-4176; e-mail: bloom@cmt.anl.gov

Pete Roth, Herb Case, Ganesan Nagasubramanian, Dan Doughty
Sandia National Laboratories, Albuquerque, NM 87185-0613
(505) 844-3949; fax: (505) 844-6972; e-mail: eproth@sandia.gov

---

Objectives

- Help identify and quantify the factors responsible for power fade through data analysis of aged cells
- Provide aged cells to diagnostics laboratories
- Provide analyzed performance data to enable correlations against diagnostic results and facilitate selection of most useful tools
- Develop aging protocols and explore new tests, analyses, and modeling methodologies related to calendar and cycle life and provide results to battery developers and other laboratories

Approach

- Perform independent, but coordinated, performance testing at INEEL, ANL, and SNL using the cell-specific test plans:
  - INEEL has been tasked with cycle-life testing and life modeling
  - ANL has been tasked with calendar-life testing and life modeling
  - SNL has been tasked with accelerated-life testing and life modeling
- Utilize the end-of-test criteria designed to provide diagnostics laboratories aged cells at specified intervals based upon power fade
- Analyze performance data based upon the *PNGV Battery Test Manual*, Revision 3, to help identify factors that limit cell life
- Measure the Gen 2 baseline performance and evaluate subsequent electrochemistry improvements of the variant chemistry cells
- Correlate capacity fade, resistance and AC impedance growth, power fade, and changes in differential capacity against calendar and cycle life

Accomplishments

- Continued refining ATD test procedures and coordinating methodologies between participating laboratories
- Continued testing the Gen 2 Baseline and Variant C cells under various test conditions
- Collated test results from all three test laboratories and identified state-of-charge (SOC), temperature and time-dependent trends:
- Fade increases with temperature
- Fade increases with SOC
- Fade is generally lowest for the calendar-life cells, in the middle for the cycle-life cells, and highest for the accelerated-life cells at a given test temperature and SOC
- Fade begins as a parabolic function of time (possibly attributable to the cathode) and changes to a linear time dependence (possibly attributable to the anode)
- Continued to ship aged Gen 2 cells to diagnostic laboratories at specified intervals
- Completed performance analysis of all available Gen 2 characterization and life-testing data

Future Studies

- Complete life testing and data analyses for the Gen 2 Baseline and Variant C cells
- Continue to coordinate testing at INEEL, ANL, and SNL and resolve testing related issues
- Continue to supply aged cells to diagnostics labs at specified intervals
- Develop phenomenological hypotheses to explain performance degradation and power fade
- Correlate testing results with diagnostic results
- Continue to develop predictive models for calendar life and cycle life

---

Introduction

The U.S. Department of Energy initiated the Advanced Technology Development (ATD) Program in 1998 to address the outstanding barriers that limit the commercialization of high-power Lithium-ion batteries, specifically for hybrid electric vehicle applications. As part of the program, 18650-size cells are aged using calendar- and cycle-life tests developed under the Partnership for a New Generation of Vehicles (PNGV) Power Assist goals. [In January 2002 PNGV was be superseded by the formation of a new program between the U.S. Government and the U.S. Council for Automotive Research, dubbed FreedomCAR (Freedom Cooperative Automotive Research).]

ATD testing of the second generation of cells (referred to as Gen 2 cells) is now underway at the Idaho National Engineering and Environmental Laboratory (INEEL), Argonne National Laboratory (ANL), and Sandia National Laboratories (SNL). The Gen 2 cells consist of a baseline cell chemistry and one variant chemistry (referred to as Variant C). The Baseline cells were manufactured by Quallion, LLC, to the following specifications, as developed by ANL:

- **Positive Electrode**
  - 84 wt% $LiNi_{0.8}Co_{0.15}Al_{0.05}O_2$
  - 4 wt% carbon black
  - 4 wt% SFG-6
  - 8 wt% PVDF binder
- **Negative Electrode**
  - 92 wt% MAG-10
  - 8 wt% PVDF binder
- **Electrolyte**
  - 1.2 M $LiPF_6$ in EC/EMC (3:7 wt%)
- **Separator**
  - 25 μm thick PE Celgard

The Variant C cell chemistry differs from the baseline chemistry by an increase to the aluminum dopant from 5% to 10% and a decrease to the cobalt from 15% to 10% in the cathode (i.e., $LiNi_{0.8}Co_{0.1}Al_{0.1}O_2$). This change resulted in a 20% drop in the $C_1/1$ rated capacity (0.8 Ah) at beginning of life (BOL) compared to the Baseline cell rated capacity of 1.0 Ah.

Accomplishments: Testing

Testing considerations, cell ratings and limitations, and early test results are available in

	Baseline Cells					Variant C Cells	
	Calendar-Life	Cycle-Life	Accelerated-Life			Calendar-Life	Cycle-Life
	60% SOC	60% SOC	60% SOC	80% SOC	100% SOC	60% SOC	60% SOC
25°C	-	15	3	3	3	-	-
35°C	-	-	3	3	3	-	-
45°C	2	15	3	3	5	15	15
55°C	15	-	3	5	5	-	-

Table 1. Cell Matrix and Distribution

References 1 and 2. The Gen 2 Baseline and Variant C cells have been distributed over a matrix consisting of three states-of-charge (SOC) (60, 80, and 100% SOC), four temperatures (25, 35, 45, and 55°C) and three life tests (calendar-, cycle-, and accelerated-life). The matrix and cell distribution is summarized in Table 1. Testing is performed in accordance with the *PNGV Battery Test Manual*, Revision 3 (Reference 3), and the cell specific test plans (References 4 and 5).

All ATD Gen 2 calendar-life testing is performed at ANL. The cells are tested at the clamped voltage corresponding to 60% SOC. Additionally, a once-per-day standard calendar-life test pulse profile is executed, as defined in Reference 3. Its purpose is to calculate daily pulse resistances and powers during the time at the target SOC. All cycle-life testing is performed at INEEL. The cells are tested using the standard PNGV 25-Wh Power Assist cycle-life profile, as defined in Reference 3. This profile is repeated continuously during life testing and, for the Gen 2 cells, is centered around 60% SOC. All accelerated-life testing is performed at SNL. These cells undergo a special calendar-life test. The cells are clamped at a voltage corresponding to the appropriate SOC and undergo the standard PNGV 25-Wh Power Assist cycle-life profile once every 24 hours.

Life testing for the calendar-, cycle-, and accelerated-life cells is interrupted every 4 weeks (i.e., every 28 days for the calendar-life tests and 33,600 cycles for the cycle-life test) for reference performance tests (RPTs), which are used to quantify changes in capacity, resistance, and power. RPTs generally consist of a $C_1/1$ static capacity test, a $C_1/25$ static capacity test, a low current hybrid pulse power characterization (L-HPPC) test, and electrochemical impedance spectroscopy (EIS) at 60% SOC. These tests are defined in References 2 and 3. All RPT's are performed at 25°C. *Capacity fade* is the percentage loss in the discharge capacity during the $C_1/1$ or $C_1/25$ test. *Power fade* is the percentage loss in the power at 300 Wh (Reference 2). The fades are normalized to the characterization RPT (i.e., at characterization, the capacity and power fades are both 0%).

The Gen 2 end-of-test (EOT) criteria are specified in References 4 and 5. As shown in Table 1, the Gen 2 calendar- and cycle-life cells are organized in groups of fifteen (the two 45°C calendar-life cells were added to the matrix after testing had begun). One cell from each group was sent to a diagnostic lab for evaluation after the BOL RPT was completed. Following the 4-week RPT, another two cells were removed from test and sent to diagnostic laboratories. The EOT criteria for the remaining 12 cells are based on equal power fade increments such that the penultimate pair of cells are sent for diagnostic evaluation when the power fade reaches 30%. Some of the remaining cells are aged to as much as 50% fade. The accelerated-life cells are removed from test either when the power fade

reaches 50% or the L-HPPC data is no longer able to yield useful data.

Accomplishments: Results

Table 2 shows the number of cells remaining and the number of weeks completed for the calendar-, cycle-, and accelerated-life cells. Six cycle-life cells remain after 52 weeks of testing at 25°C. Seven accelerated-life cells are continuing at 25°C after 40 weeks of testing and eight accelerated-life cells are continuing testing at 35°C after 36 weeks of testing. Only two cells each remain for the calendar- and cycle-life cells testing at 45°C after 52 weeks of testing and only three cells remain for the accelerated life test at 45°C and 60% SOC after 36 weeks of testing. Nine Variant C cells remain after 32 weeks of calendar- and cycle-life testing at 45°C. All 55°C cells have already been removed from test.

	Baseline Cells										Variant C Cells			
	Calendar-Life		Cycle-Life		Accelerated-Life						Calendar-Life		Cycle-Life	
	60% SOC		60% SOC		60% SOC		80% SOC		100% SOC		60% SOC		60% SOC	
	Cells	Wks	Cells	Wks	Cells	Wks	Cells	Wks	Cells	Wks	Cells	Wks	Cells	Wks
25°C	-	-	6	52	2	40	2	40	3	40	-	-	-	-
35°C	-	-	-	-	3	36	3	36	2	36	-	-	-	-
45°C	2	52	2	52	3	36	0	36	0	36	5	32	4	32
55°C	0	40	-	-	0	32	0	20	0	20	-	-	-	-

Table 2. ATD Gen 2 Testing Status

Temperature (color)	Test (symbol)	Chemistry (symbol background)
25°C (blue)	calendar-life (circle)	Baseline cells (filled symbol)
35°C (red)	cycle-life (square)	Variant C cells (empty symbol)
45°C (purple)	accelerated-life (triangle)	
55°C (green)		

Table 3. Standardized Graphical Representation

Since testing is performed at multiple temperatures and SOCs, as shown in Table 1, a standardized method of presenting the data in this report has been established. Unless otherwise stated on the figure legends, the data is presented using the format summarized in Table 3.

The Gen 2 data can be modeled in numerous ways. For this report, the fits to the data were selected based upon an attempt to correlate against physical processes, rather than arbitrary mathematical functions. A square root of time dependence can be related to a thermal diffusion process for the formation of a solid electrolyte interface (SEI) layer. Linear time dependence can be related to a steady-state formation of the SEI layer where the electrolyte / salt decomposition reaction at the surface of the SEI layer determines the rate of SEI growth. The natural log of time dependence may be related to the transport of ions due to the electric fields present at the SEI layer (Reference 6). It has been postulated that a parabolic behavior is related to changes on the cathode whereas a linear fade is related to changes on the anode. This hypothesis is currently under investigation using half-cell experiments and through diagnostics at ANL, Lawrence Berkeley National Laboratory and Brookhaven National Laboratory.

Capacity Fade

Figure 1 shows the average $C_1/1$ static capacity fade as a function of test time at 60% SOC for the Baseline calendar-, cycle- and accelerated-life cells. The 25°C cycle-life Baseline cells show a square root of time dependence through 52 weeks of testing. All other cell groups show a mechanistic change with an initial square root of time dependence, followed by a linear dependence. When the second mechanism dominates, the $C_1/1$ capacity fade rate increases. The fade rate also increases with increasing temperature. The accelerated-life cells show the largest increase in the fade rate, and the calendar-life cells show the least increase in the fade rate. Within each life-test group (i.e., cycle-, calendar-, and accelerate-life), the breakpoints between mechanisms occur earlier at higher temperatures. The 80 and 100% SOC accelerated-life cells show comparable results (Reference 2). The capacity fade rate generally increases with increasing SOC.

Figure 2 shows the $C_1/1$ static capacity fade as a function of test time at 60% SOC and 45°C for the Variant C calendar- and cycle-life cells. As seen with the Baseline cells, the cycle-life cells show more fade than the calendar-life cells. These cells also show mechanistic changes with the initial

mechanism being square root of time dependent and the second mechanism being linearly dependent on test time. When the second mechanism dominates,

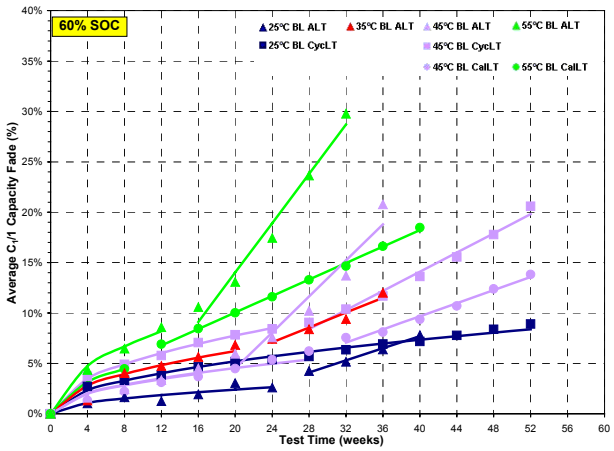

Figure 1. Average $C_1/1$ static capacity fade as a function of test time for the 60% SOC Baseline cells.

the Variant C cells show little or no capacity fade as a function of test time. Since the capacity fade rate significantly slows down as a function of test time, the Variant C cells may be following a different time dependence. The Variant C $C_1/1$ static capacity fade can also be modeled with a natural log of time dependence, as shown in Figure 3. The logarithmic rate is typically seen in the low-temperature oxidation of metals (Reference 6). The calendar-life cells still show a mechanistic change with a linear time dependence after 20 weeks of aging.

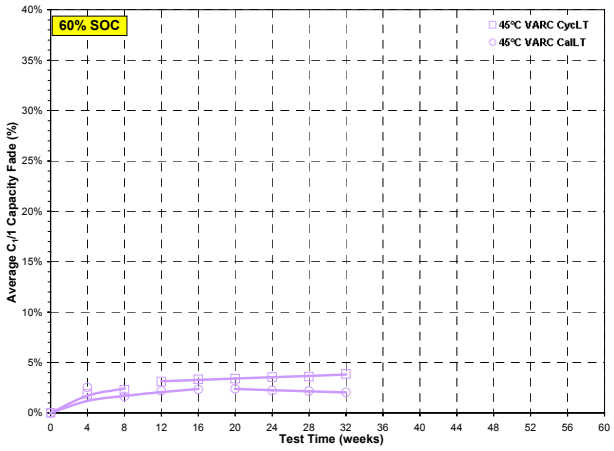

Figure 2. Average $C_1/1$ static capacity fade as a function of test time for the 60% SOC Variant C cells.

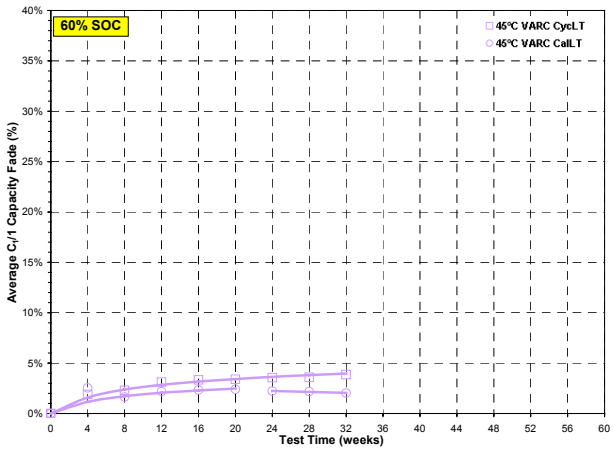

Figure 3. Average $C_1/1$ static capacity fade as a function of the natural log of time for the 60% SOC Variant C cells.

Figure 4 shows the average $C_1/25$ capacity fade as a function of test time at 60% SOC for the Baseline calendar-, cycle- and accelerated-life cells. The fade rates within each temperature group are similar, and increase as a function of increasing test temperature. All cells show a square root of time dependence with no apparent mechanistic changes. This is primarily due to the slower diffusion rates during the $C_1/25$ test. However, mechanistic changes do appear for the 80 and 100% SOC accelerated-life cell groups (Reference 2).

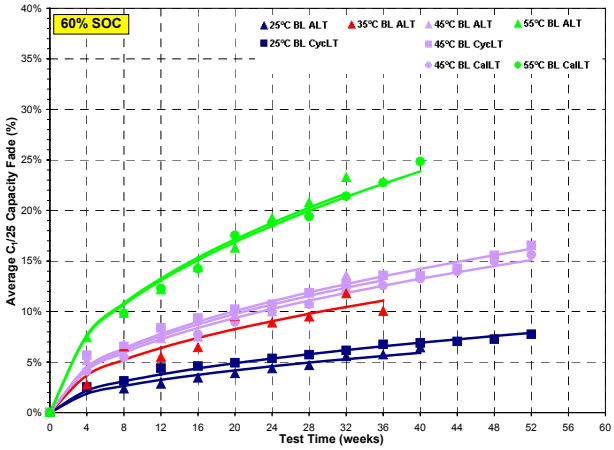

Figure 4. Average $C_1/25$ static capacity fade as a function of test time for the 60% SOC Baseline cells.

Figures 5 and 6 show the average $C_1/25$ static capacity fade for the 45°C Variant C cells aged at 60% SOC as a function of the square root of time and the natural log of time, respectively. As shown, the Variant C cells do not show any obvious mechanistic changes with either time dependence fits. Like the Baseline cells, the Variant C cells show similar fade rates through 32 weeks of testing.

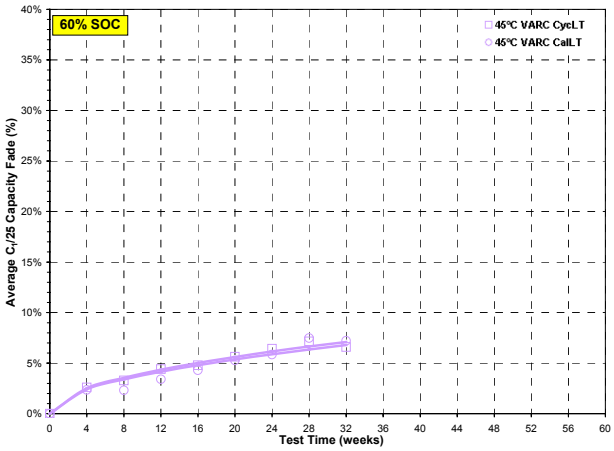

Figure 5. Average $C_1/25$ static capacity fade as a function of test time for the 60% SOC Variant C cells.

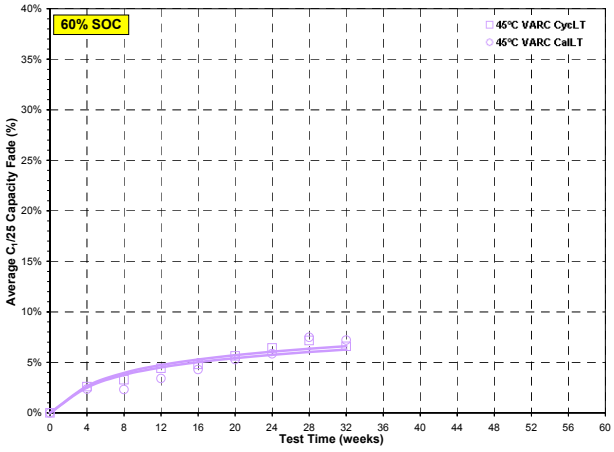

Figure 6. Average $C_1/25$ static capacity fade as a function of the natural log of time for the 60% SOC Variant C cells.

Differential Capacity

The $C_1/25$ static capacity data are used to calculate the relative change in capacity as a function of the voltage, normalized to the average BOL $C_1/25$ capacity. Its purpose is to gain further insights into the mechanisms operating during the degradation of cell performance. The $C_1/25$ data are first smoothed, then the differential capacity is calculated using $1/Q_{BOL} * d(Ah)/dV$.

Figure 7 shows the differential capacity for a representative Baseline cell cycle-life tested at 45°C for 52 weeks. Differential capacity decreases as a function of cycle time. The locations of the SOC peaks increase slightly in SOC as a function of aging, as shown by shifts to higher voltages. The point at which cycle-life testing is performed (60% SOC) is outside of a peak region and shows no significant capacity loss as a function of time.

Figure 8 shows the differential capacity for a representative Baseline cell calendar-life tested at 45°C for 52 weeks. The BOL locations of the peaks occur at similar SOCs as the cycle-life cells. Whereas the cycle-life cells show a small shift in the peak locations and a large drop in differential capacity (Figure 7), the calendar-life cells show a large shift in the peak locations and a small drop in differential capacity. The 40 and 80% SOC peaks appear to be shifting towards each other for both the cycle- and calendar-life cells. As a result, the middle peak appears to broaden. This could be attributable to the alteration of the crystalline lattice in the electrodes.

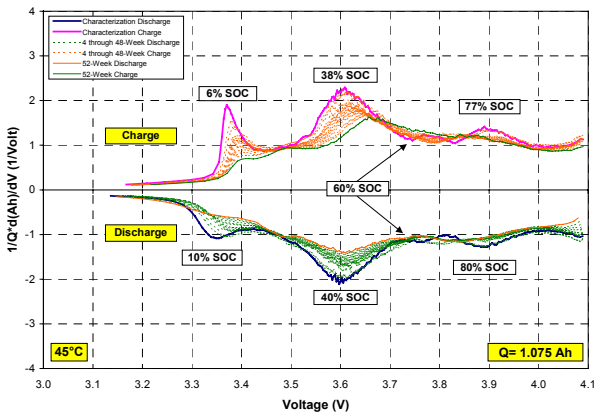

Figure 7. $C_1/25$ differential capacity for a representative 45°C cycle-life Baseline cell.

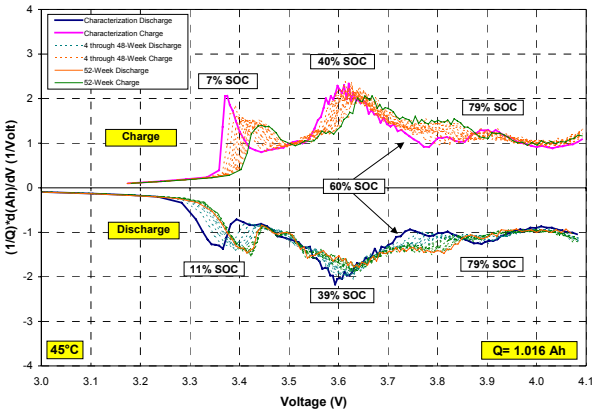

Figure 8. $C_1/25$ differential capacity for a representative 45°C calendar-life Baseline cell.

Power

Figure 9 shows the average power fade as a function of test time at 60% SOC for the Baseline calendar-, cycle- and accelerated-life cells. The 25°C cycle-life Baseline cells show a linear time dependence through 52 weeks of testing with no apparent mechanistic change. This is consistent with the 25°C $C_1/1$ and $C_1/25$ capacity fades (Figures 1 and 4). All other cell groups show mechanistic changes with an initial square root of time dependence, followed by a linear dependence. For all cell groups, the power fade rate increases when the second mechanism takes effect. Within each life-test group, the fade rate also increases with increasing temperature. Within each life-test group, the breakpoints between mechanisms generally occur earlier at higher temperatures. All of these trends are consistent with the $C_1/1$ capacity fade results shown in Figure 1. The 80 and 100% SOC accelerated-life cells show the same general trends as the 60% SOC cells (Reference 2).

Figures 10 and 11 show the average power fade for the 45°C Variant C cells aged at 60% SOC as a function of the square root of time and the natural log of time, respectively, for the calendar- and cycle-life cells. As shown, the Variant C cells show an initial square root of time dependence followed by linear time dependence. However, the natural log of time fit shows no obvious breakpoints.

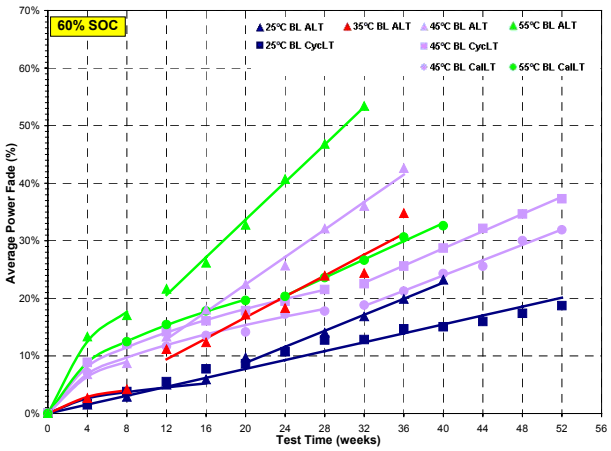

Figure 9. Average power fade as a function of test time for the 60% SOC Baseline cells.

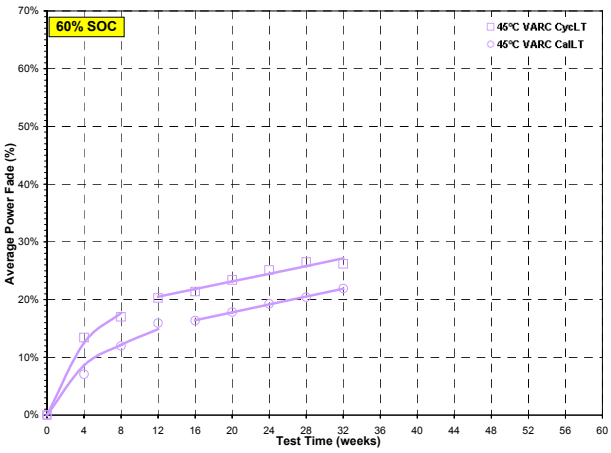

Figure 10. Average power fade as a function of test time for the 60% SOC Variant C cells.

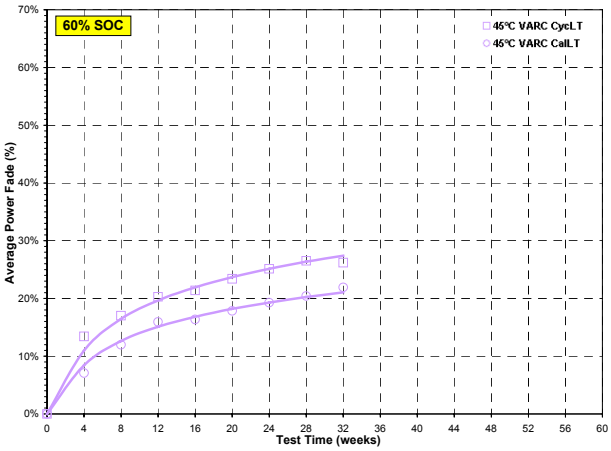

Figure 11. Average power fade as a function of the natural log of time for the 60% SOC Variant C cells.

Electrochemical Impedance Spectroscopy

Figure 12 shows the EIS Nyquist curve for a representative Baseline cell cycle-life tested at 45°C for 52 weeks. The impedance grows monotonically as a function of test time. The majority of the growth occurs in the mid-frequency region (Reference 2).

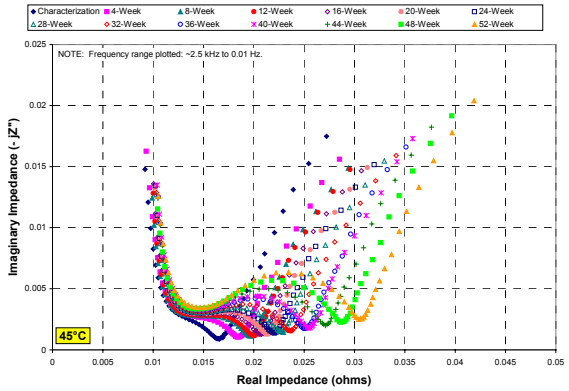

Figure 12. EIS Nyquist curve for a representative 45°C cycle-life Baseline cell.

Figure 13 shows the average EIS magnitude growth at the semicircle trough as a function of test time at 60% SOC for the Baseline calendar- and cycle-life cells. As seen with the power fade (Figure 9), the 25°C cycle-life Baseline cells show a linear time dependence with no apparent mechanistic change. The 45 and 55°C cell groups show mechanistic changes with an initial square root of time dependence followed by a linear time dependence. The growth rates also increase once the second mechanism takes effect, and the breakpoints occur earlier with increasing temperature.

Figure 14 shows the average EIS magnitude growth at the semicircle trough as a function of the square root of test time at 60% SOC for the 45°C calendar- and cycle-life Variant C cells. These cell groups show a mechanistic change with a linear time dependence after the breakpoint. The Variant C cell groups show a higher average growth than the Baseline cell groups at 45°C, but the growth rates are smaller in the linear region. Unlike the power fade results (Figure 10), the calendar-life Variant C cells show a slightly higher growth than the cycle-life cells. Figure 15 shows the average Variant C EIS magnitude growth at the semicircle trough as a function of the natural log of time. The logarithmic fit does not show any mechanistic changes.

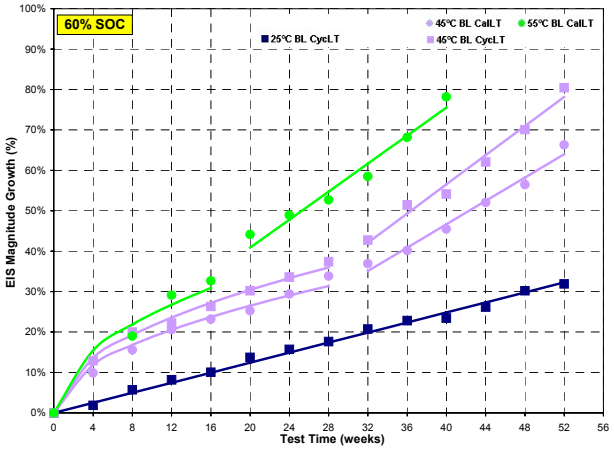

Figure 13. Average EIS growth as a function of test time for the calendar- and cycle-life Baseline cells.

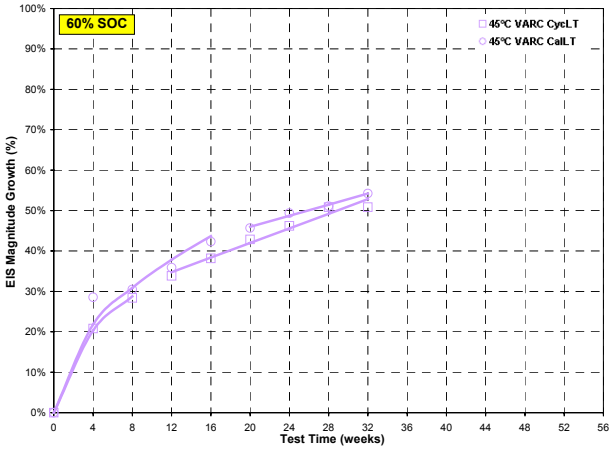

Figure 14. Average EIS growth as a function of test time for the calendar- and cycle-life Variant C cells.

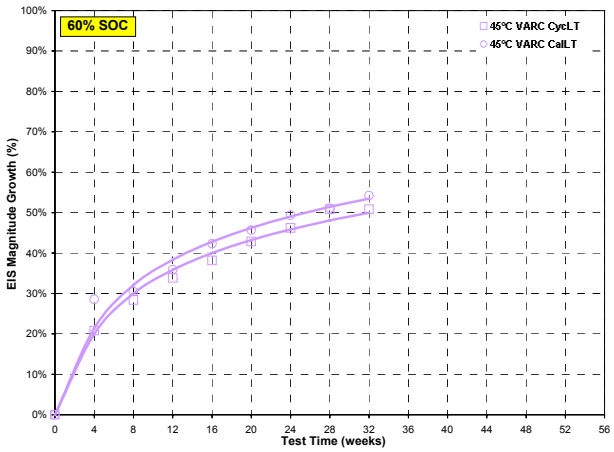

Figure 15. Average EIS growth as a function of the natural log of time for the calendar- and cycle-life Variant C cells.

Conclusions

From the RPTs conducted every 4 weeks during life testing, the C_1/1 capacity fade, C_1/25 capacity fade, power fade at 300 Wh, and EIS growth at the semicircle trough are calculated and used as measures of cell degradation. In general, the Baseline cell degradation increases with increasing temperature and SOC. The degradation is generally lowest for the calendar-life cells, in the middle for the cycle-life cells, and highest for the accelerated-life cells at a given test temperature and SOC. The Baseline cell degradation generally shows an initial square root of time dependence followed by a linear time dependence. A square root of time dependence may be attributable to a thermal diffusion process for the formation of an SEI layer. A linear-time dependence may be attributable to the steady-sate formation of the SEI layer. Once the second mechanism dominates, the Baseline cell rate of degradation generally increases. The ATD Program is investigating the possibility that the initial parabolic fade is related to changes in the cathode and the subsequent linear time dependence is attributable to changes in the anode.

The 45°C Variant C calendar- and cycle-life cells follow the same general trends as the Baseline cells. These cell groups show an initial square root of time dependence followed by a linear time dependence and the calendar-life cell degradation is generally lower than the cycle-life cells. Unlike the Baseline cells, cell degradation generally decreases once the second mechanism dominates, which may suggest an alternate time dependency. Consequently, the Variant C cells were also modeled with a natural log of time dependency, which may be related to the transport of ions due to electric fields present at the SEI layer. This fit did not generally show any mechanistic changes through 32 weeks of testing. More data are required to determine the time dependency that best supports the behavior of the Variant C cell degradation.

Future Studies

All ATD Gen 2 testing will continue until the specified EOT criteria have been met. Six cycle-life and seven accelerated-life Baseline cells remain on test at 25°C. The cycle-life cells will reach EOT when the power fade is 30% plus one fade increment (i.e., approximately 36%). The accelerated-life cells will continue until the power fade reaches 50%. Eight accelerated-life Baseline cells remain on test at 35°C and two calendar-life, two cycle-life, and three accelerated-life Baseline cells remain on test at 45°C. These cells will also continue until the power fade reaches 50%. Also at 45°C, five calendar-life and four cycle-life Variant C cells remain and will continue until 50% power fade. All 55°C cell groups have already been removed from test.

References

1. Raymond A. Sutula et al., "FY 2001 Progress Report for the Advanced Technology Development Program," U.S. Department of Energy, Office of Advanced Automotive Technologies, February 2001.
2. Jon P. Christophersen et al., "Advanced Technology Development Program for Lithium-Ion Batteries: Gen 2 Performance Evaluation Interim Report," INEEL/EXT-03-00095, February 2003.
3. "PNGV Battery Test Manual, Revision 3," Idaho National Engineering and Environmental Laboratory, DOE/ID-10597, February 2001.
4. "PNGV Test Plan for Advanced Technology Development Gen 2 Lithium-Ion Cells," Idaho National Engineering and Environmental Laboratory, EHV-TP-121, Rev. 6, October 5, 2001.
5. "SNL ATD Gen 2 Test Plan," Sandia National Laboratories, SNL-ATD G2-TP, Rev. 3, April 26, 2001.
6. Per Kofstad, *High-Temperature Oxidation of Metals*, John Wiley & Sons, New York, 1966.

III.B.2. Cell Diagnostics

III.B.2.a. Diagnostic Study of Gen 2 Cells and Cell Components

Daniel Abraham, Dennis Dees, Yoo-Eup Hyung, Jun Liu, Khalil Amine, and Gary Henriksen
Building 205, Argonne National Laboratory, Argonne, IL 60439
(630) 252-4332; fax: (630) 972-4406; e-mail: abraham@cmt.anl.gov

Ivan Petrov, Rick Haasch, Scott Maclaren, Ernie Sammann, and Ray Twesten
Center for Microanalysis of Materials, University of Illinois at Urbana-Champaign
(217) 333-8396; fax: (217) 244-2278; e-mail: petrov@uiuc.edu

Objectives

- Develop advanced diagnostic techniques to identify cell components that are responsible for capacity and power fade during the aging and cycling of lithium-ion cells.
- Develop electrochemical models to link the information from analytical diagnostic studies to cell impedance rise observed in EIS and HPPC tests on Gen 2 cells.
- Apply these analytical and modeling techniques to determine power fade mechanisms in Gen 2 cells.

Approach

- Use reference-electrode cell studies to determine relative contributions of the positive and negative electrodes to full cell impedance.
- Use x-ray photoelectron spectroscopy (XPS), and secondary ion mass spectroscopy (SIMS) to determine aging-induced changes on the electrode surfaces.
- Use solvent extraction and nuclear magnetic resonance (NMR) techniques to identify species present on the electrode surfaces.
- Use electron microscopy imaging and spectroscopy techniques and x-ray characterization techniques to determine aging-induced changes in the electrode and separator materials.
- Use gas chromatography to identify and quantify the gases generated during formation, cycling, and aging of Gen 2 cells.
- Use high-performance liquid chromatography to identify electrolyte reactions during formation, cycling, and aging of Gen 2 cells.
- Use results from experimental diagnostic studies as a basis for the development of an electrochemical model of Gen 2 cells.
- Use the electrochemical model to conduct parametric studies and follow the evolution of Gen 2 cell EIS and HPPC tests to determine power fade mechanisms.

Accomplishments

- Identified the positive electrode as the main contributor to cell impedance rise during the early stages of aging; the negative electrode contribution becomes significant as cell aging progresses.
- Identified polyethylene oxide and several phosphorous-oxygen species in the positive electrode surface films.
- Correlated positive electrode impedance rise with composition changes in the electrode surface films for cells that showed less than 35% power fade.
- Identified oxide particle bulk damage in cells that showed greater than 50% power fade.
- Determined that the positive electrode carbons are not significant contributors to Gen 2 cell impedance rise.
- Correlated negative electrode impedance rise with thickness changes of the solid electrolyte interface (SEI) layer.
- Determined that the cell separator and current collector materials are not significant contributors to the impedance rise observed in Gen 2 cells.
- Developed an EIS electrochemical model for Gen 2 cells and used the model to identify the probable mechanism of the positive electrode impedance rise, as well as methods of mitigating its effect on the overall cell performance.

Future Studies

- Continue systematic studies of electrode surfaces to identify surface film constituents and determine their relative importance in cell power fade.
- Develop diagnostic tools to determine components and parameters that limit cell performance during thermal abuse testing.
- Develop diagnostic techniques into predictive tools that will assist in the design and selection of materials for future generations of lithium-ion cells.
- Extend modeling studies to simulate the HPPC tests, and thereby strengthen the link between analytical diagnostic studies and electrochemical characterization tests.

Reference-Electrode Measurements

Reference-electrode measurements were conducted to determine relative contributions of the positive and negative electrodes to Gen 2 cell impedance rise. The electrochemical cells were assembled with flat, single-sided, 32 cm^2 electrodes punched from fresh laminates. A 25 μm tin-plated copper wire was placed between two separator membranes; the wire tip region was charged with lithium to form a Li-Sn reference electrode. The newly assembled cells were characterized at room temperature by AC impedance measurements (100 kHz to 10 mHz), capacity measurements, and hybrid pulse power characterization (HPPC) testing to obtain baseline values. The cells were then held at 55°C, 60% state-of-charge (SOC), and periodically tested (at room temperature) to determine the effect of aging on cell capacity and pulse power properties. Representative HPPC test data from a cell with Gen 2 electrolyte and electrode materials are shown in Figs 1 and 2. The measurements showed that in Gen 2 cells both positive and negative electrodes contribute to impedance rise (and hence cell power fade), with the positive electrode contributing the larger fraction especially during the early stages of aging. The AC impedance data showed that the most prominent change during cell aging occurred at

the mid-frequency arc, which is usually attributed to the charge transfer resistance at the electrode surface-electrolyte interface.

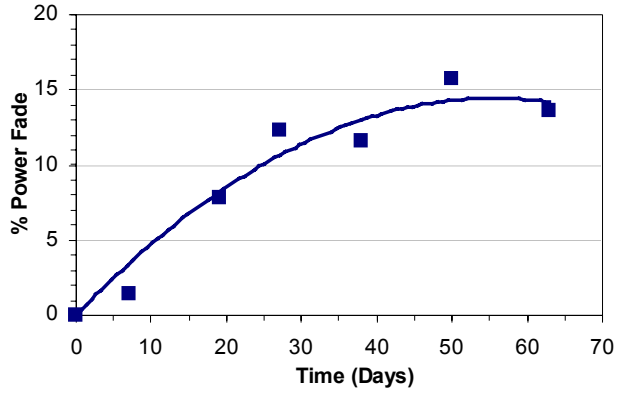

Figure 1. Power fade, calculated at 60%SOC, from 18-s pulse discharge data.

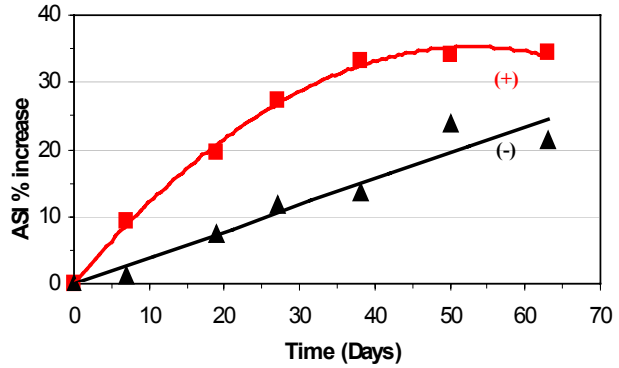

Figure 2. ASI increase, calculated at 60%SOC, for the positive and negative electrodes.

Electrode Materials Characterization

The charge transfer resistance is influenced by a surface film at the positive electrode-electrolyte interface. NMR data have shown that, in addition to electrolyte residue, this surface film contains polyethylene oxide (PEO), which could have resulted from the ring-opening polymerization of ethylene carbonate (EC). Small amounts of electrolyte transesterification products such as DEC, DEDOHC, EMDOHC and DMDOHC were also observed. XPS data suggested that the surface film contained both organic and inorganic species that include lithium alkyl carbonate, LiF, Li_xPO_y and $Li_xPO_yF_z$ species. XPS and SIMS sputtering data indicated that the thickness of this surface film does not correlate with aging. However, changes in the surface film composition (see Figs. 3 and 4) may affect lithium ion motion to and from the oxide particles, producing the measured impedance rise.

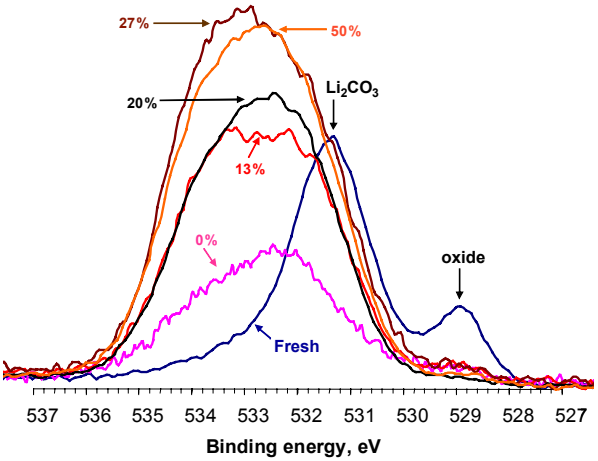

Figure 3. O1s XPS positive electrode data for fresh and aged cells; power fade values (%) are shown in the figure. The fresh laminate had no electrolyte exposure.

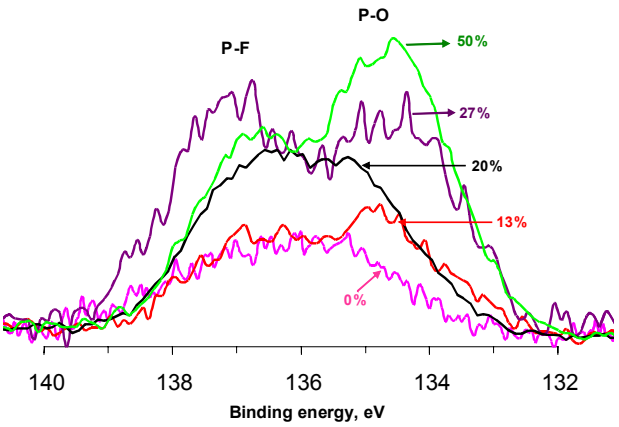

Figure 4. P2p XPS positive electrode data for tested cells; power fade values (%) are shown.

The charge transfer resistance could also be influenced by the modified surface layer present on oxide particles used to prepare the Gen 2 positive electrode laminates. Surface-sensitive x-ray absorption spectroscopy and high-resolution electron microscopy showed the presence of a ~5 nm thick surface layer on the oxide particles (see Fig. 5). Fast Fourier transform patterns showed that the (003) reflection that is characteristic of a layered oxide was absent in the near-surface patterns. Electron energy loss spectroscopy (EELS) composition and edge analysis data revealed that the surface had a

$Li_xNi_{1-x}O$-type (NaCl) structure, which is different from the ordered rock salt (α-$NaFeO_2$) structure of the oxide bulk. The surface layer would impede lithium motion because lithium diffusion in and out of a NaCl-structure is slower than diffusion through the layered structure. For Gen 1 cells, the positive electrode impedance increase upon accelerated aging could be correlated to an increase in thickness of the oxide surface layer. In Gen 2 cells, however, aging did not change the oxide surface layer thickness, indicating that the Al-bearing Gen 2 oxide ($LiNi_{0.8}Co_{0.15}Al_{0.05}O_2$) is more stable than the Gen 1 oxide ($LiNi_{0.8}Co_{0.2}O_2$).

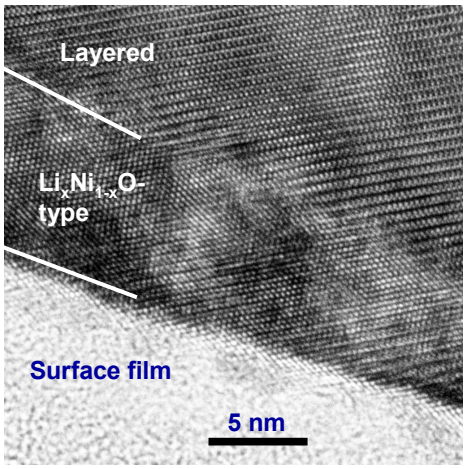

Figure 5. HREM image showing $Li_xNi_{1-x}O$ –type layer on the bulk layered oxide.

The $LiNi_{0.8}Co_{0.15}Al_{0.05}O_2$ particles from several cells that showed varying levels of power fade were examined by transmission electron microscopy (TEM) for crystal structure disorder and damage that can lead to property degradation during electrochemical cycling and long-term storage. The particles appeared to be free of obvious defects, such as particle fractures, dislocations, and stacking faults in cells that displayed up to 35% power fade. However, crystal structure disorder and damage were observed in cells that showed >50% power fade. Such oxide particle damage may have induced rapid impedance increases for the positive electrodes in cells with high power fade.

The negative electrodes (see Fig. 6) from cells that showed varying levels of power fade were examined to determine the sources of impedance rise. XPS data showed that the SEI layer contains a mosaic of micro-phases that includes both organic and inorganic constituents. The organic products resulted from solvent reduction and include polymeric species, ether compounds, and lithium alkyl carbonates; the inorganic products result from salt reduction and include LiF, Li_xPO_y and $Li_xPO_yF_z$ compounds. The surface analysis data were similar for samples from various aged cells, which indicated that aging-induced changes in SEI layer composition were small. However, dynamic SIMS sputtering data showed that the SEI layer thickness increases upon aging. A thicker SEI could provide a barrier to lithium-ion motion and hence increase electrode impedance.

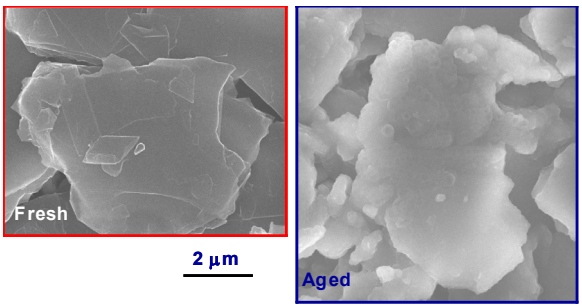

Figure 6. SEM images of negative electrode graphite particles from fresh and aged laminates. The SEI layer produces a rounded appearance on the edges of the aged graphite.

The bulk structure of graphite in the negative electrodes was studied by electron microscopy and x-ray diffraction. TEM data showed the presence of twins in the starting graphite material; obvious defects such as particle fractures were not observed for the aged samples. For XRD measurements, the anode samples were loaded into a hermetically sealed holder (designed at ANL) to prevent air exposure; the incident and diffracted X-ray beams entered and exited the holder through beryllium windows. Graphite peak positions and peak widths were similar for anode samples subjected to various aging conditions. These diffraction and microscopy data indicate that graphite damage is not a major consequence of cell aging. Consequently, the impedance rise that may be attributed to graphite damage is likely to be small.

Electrochemical Cell Modeling

The general methodology for the electrochemical model follows the work of Professor

J. Newman at Berkeley. Concentrated solution theory was used to describe the transport of salt in the electrolyte. Volume-averaged transport equations accounted for the composite electrode geometry. Electrode kinetics, thermodynamics, and diffusion of lithium in the active particles were also included.

Based on the post-test diagnostic analysis, interfacial effects on both electrodes were described with a multi-layer active particle/electrolyte interface. Along with the model development, a complete parameter set for the Gen 2 cells was established using a wide range of experimental electrochemical studies that included EIS measurements on reference-electrode cells. The EIS positive electrode electrochemical model was used to conduct a series of parametric studies to examine possible aging mechanisms that could cause the positive electrode impedance to rise, as well as methods of mitigating its effect on the overall cell performance. These studies served to eliminate a number of proposed mechanisms, and they further identified that changes in the lithium transport characteristics across the interfacial area had the greatest impact on the electrode interfacial impedance. The theoretical studies also suggest that the standard Gen 2 positive electrode has a limited reserve electrochemically active area for the current to spread into as the interfacial impedance rises with time. One can infer from this work that either increasing the electrode thickness or decreasing the active particle size should reduce the power fade associated with the Gen 2 positive electrode.

III.B.2.b. The Development of Diagnostic Techniques for Examining Cathode Structural Degradation

James McBreen, M. Balasubramanian, X. Q. Yang, and X. Sun
MSD Bldg. 555, Brookhaven National Laboratory, P.O. Box 5000, Upton, NY 11973-5000
Phone: (631)344-4513, fax. (631)344-5815; email jmcbreen@bnl.gov

---

Objective

- Determine the nature of the degradation processes that cause increase in impedance in high-power lithium-ion cells and the reactions that lead to thermal runaway in charged cells at elevated temperature.

Approach

- Apply techniques that can identify and characterize changes in the bulk and surface of electrodes from cycled and abused cells. A combination of high-resolution *in situ* x-ray diffraction (XRD) and x-ray absorption spectroscopy (XAS) is used to characterize the bulk. Soft x-ray XAS is used to characterize the surface. High-resolution XRD with fast data acquisition times is used to study cathode decomposition at high temperature.

Accomplishments

- Soft x-ray XAS at F and P K edges detected several electrolyte salt decomposition products on the surface of electrodes from cycled and abused cells.

- XAS at the O K edge indicated that, unlike $LiCoO_2$, the composition of the surface of Ni-based cathodes is different than the bulk. This is true for $LiNiO_2$ and the cathode materials for both Gen 1 and Gen 2 cells.

- Demonstrated the use of high-resolution XRD with fast data collection times to follow the decomposition of charged cathodes at elevated temperature in the presence of electrolyte.

Future Studies

- Soft x-ray XAS at O and F K-edges and at the L-edges of Mn, Ni and Co.
- Soft x-ray XAS studies at the B K-edge to identify B-containing decomposition products from LiBoB-based electrolytes on the surface of electrodes.
- Identify the contribution of these decomposition products to cell impedance increase and power fade.
- Identify the overall reactions of charged cathodes at elevated temperatures in the presence of electrolyte.

Publications

- M. Balasubramanian, H. S. Lee, X. Sun, X. Q. Yang, A. R. Moodenbaugh, J. McBreen, D. A. Fischer, and Z. Fu, "Formation of Solid Electrolyte Interface on Cycled Lithium-Ion Battery Cathodes: Soft X-ray Absorption Study," E*lectrochem. Solid State Lett.* **5**, A22 (2002).
- D.P. Abraham, R.D. Twesten, M. Balasubramanian, I. Petrov, J. McBreen, K. Amine, "Surface Changes on $LiNi_{0.8}Co_{0.2}O_2$ Particles During Testing of High-Power Lithium-Ion Cells," *Electrochem. Commun.* **8**, 620 (2002).

Introduction

The diagnostic effort focuses on the application of advanced techniques to identify electrode surface and bulk processes that occur in cycled and abused cells. In this work it has become apparent that, in the case of both Gen 1 and Gen 2 cells, power fade was mostly due to surface processes on the cathode. Another goal is to identify the overall cathode reactions that contribute to thermal runaway in charged cells at elevated temperature. The soft x-ray (500-1000 eV) XAS technique takes advantage of the fact that the x-ray probe simultaneously generates two signals from which the x-ray absorption can be determined. One is due to Auger electrons and the other to fluorescence x-rays. In soft x-ray XAS the Auger electrons have an escape depth of ~50 Å and the fluorescence x-rays have an escape depth of ~3000 Å. By carrying out simultaneous measurements in both the total electron yield (TEY) and the fluorescence yield (FY) mode it is possible to obtain element-specific surface and bulk information. High-resolution XRD, with fast data collection times, is used to follow the decomposition of charged cathodes at elevated temperature in the presence of electrolyte. In this work, charged cathode samples that are still wet with electrolyte are removed from cells and sealed in thin quartz capillaries. The capillaries are mounted in the thermal stage of diffractometer and XRD patterns are quickly recorded with either a position sensitive or an image plate detector. Measurements can be performed up to 300˚C.

Accomplishments

F K edge XAS: F K edge XAS indicates the precipitation of LiF on all examined cathodes and anodes from cycled and abused Gen 2 cells. More extensive work was carried out on the cathodes. There was considerable distortion of the FY spectra due to self-absorption effects. This is indicative of the precipitation of considerable quantities of LiF on the cathode surface. Removal of the LiF revealed the presence of the poly(vinylidenedifluoride) (PVdF) binder, indicating that the LiF most likely arises from decomposition of $LiPF_6$ in the electrolyte.

P K edge XAS: Figure 7 shows XAS spectra at the P K edge for an anode and cathode taken from calendar-life cell G2.50C55, A212.24.28.24.G. L. Also shown are spectra for Li_3PO_4 and 0.05 M $LiPF_6$. All cathodes contain pentavalent P species (e.g. PO_4^{3-} or PF_6^-). In all cathodes ~10-15% of the P is in PF_6^-. The PF_6^- is most likely intercalated in the graphite conductive diluent and is not extracted by the solvent. Intercalation of PF_6^- in the carbon

conductive diluent could affect the stability of the carbon and its conductivity. In the anode there is a shift in the P K edge to lower energies, indicating the presence of some trivalent P species (PO_3^{3-}) on the anode. These results, together with the F K edge data, confirm that the $LiPF_6$ is not stable under cell operating conditions. The precipitation LiF and various phosphate products can contribute to power fade.

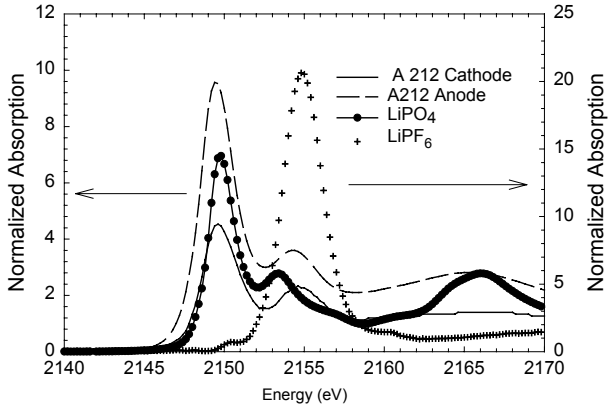

Figure 7. XAS spectra at the P K edge for an anode and cathode taken from calendar-life cell G2.50C55.A212.24.28.24.G. L. Also shown are spectra for Li_3PO_4 and 0.05 M $LiPF_6$. Note different scale for $LiPF_6$ data.

O K edge XAS: The soft x-ray region includes the L_3 and L_2 edges of the first-row transition metals. However, studies at the O K edge proved to be a far superior tool for studying the surface cathode material particles. O K edge XAS in the electron-yield and fluorescence modes indicate that the surface composition of Ni-based cathode materials is different than the bulk. This is true for as-received material, fresh electrodes, and cycled and abused electrodes from both Gen 1 and Gen 2 cells. Fluorescence O XAS data on fresh and cycled electrodes indicate that beyond a depth of a few hundred Å the bulk of the material in fresh and cycled electrodes is intact. The outer layer is either NiO or Li_xNiO. O K edge XAS on tested Gen 2 cathodes have signals for $LiNi_{0.8}Co_{0.15}Al_{0.05}O_2$. This indicates that either the SEI layer or the NiO layer is thinner in tested Gen 2 cells. The NiO is due to the tendency of the higher-valent nickel oxides to lose oxygen. This phenomenon is not seen in $LiCoO_2$. The NiO layer can contribute to interparticle contact resistance and cause power fade. The results indicate that we need a more-stable electrolyte salt and cathode material.

Future Studies

Future work will include (1) soft x-ray XAS on cathodes at O and F K-edges and at the L-edges of Mn, Ni and Co; (2) soft x-ray XAS studies at the B K-edge to identify B-containing decomposition products from LiBoB-based electrolytes on the surface of electrodes; (3) studies to identify the contribution of these decomposition products to the impedance increase and power fade; and (4) identification of the overall reactions of charged cathodes at elevated temperatures in the presence of electrolyte.

III.B.2.c. Advanced Diagnostic Techniques for Characterizing Electrode Surfaces and Processes

Frank McLarnon, Robert Kostecki, Laura Norin, Kathryn McCarthy, Philip Ross, Sherry Zhang, Vera Zhuang, Thomas Richardson, Xiangyun Song, Kim Kinoshita, and John Kerr
Building 70R0108B, Lawrence Berkeley National Laboratory, Berkeley CA 94720-8168
(510) 486-4636; fax: (510) 486-4260; e-mail: frmclarnon@lbl.gov

---

Objectives

- Use advanced diagnostic techniques to determine cell component structural, morphological, and surface chemical changes that lead to cell performance degradation as it is cycled or aged.
- Study solid electrolyte interphase (SEI) formation and dissolution as cells are cycled or aged, and determine its effect on cell power and capacity loss.
- Identify electrolyte reactivity trends in lithium-ion cells with respect to cell history.

Approach

- Use atomic force microscopy, Raman microscopy, and other microprobe techniques to detect and characterize surface processes which occur on a local scale and contribute to cell deterioration.
- Use infrared spectroscopy and x-ray photoelectron spectroscopy to provide detailed chemical analyses of electrode surfaces.
- Use high-resolution transmission electron microscopy and energy dispersive x-ray analysis to determine changes of electrode crystallographic structure, particle morphology, surface layers, and elemental composition which accompany cell cycling and aging.
- Use solvent extraction, gas and liquid chromatography, and thermal analysis to characterize cell components, and carry out control experiments to facilitate data interpretation.

Accomplishments

- Confirmed that carbon black recedes from the surface and bulk of cathodes in aged/cycled Gen 2 cells.
- Determined that $LiPF_6$ salt decomposition contributes to separator degradation and is responsible for about 10% of total cell power loss.
- Demonstrated that the MAG-10 graphite anode undergoes gradual structural degradation upon cycling at elevated temperatures, leading to increased anode surface reactivity *vs*. the electrolyte.
- Found that the most likely correlation of ATR-FTIR analysis of cell components with cell power fade is the change in composition and possibly the structure of the SEI layer on the anode. This change in composition appears to be the result of thermal hydrolysis (by water in the cell) of Li^+-ion-conducting organo-lithium salts into non-conducting lithium oxide.
- Observed micro-defects, including dislocations, micro-twinning, and lattice disorder, in cathode samples from cells with high power fade. These defects appear to be associated with an increased spread of Ni/Co elemental ratios.

- Identified small particles (~ 100 nm) in cathodes as carbon, and confirmed the reduction in the number of these particles in electrodes from cells with high power fade.

- Found impurities (Mg, Fe, Si) in cycled cathodes. The source of Mg and Fe appears to be the Al current collector.

- Discovered a tentative correlation between the molecular weight and amount of water-soluble polymeric material extracted from cell components with increasing cell power fade.

- Noted that extractable products from cell components change during glove-box storage in a manner consistent with the volatility and reactivity of PF_5 (from $LiPF_6$). It is important to specify the date of the diagnostic test relative to the date of cell opening.

Future Directions

- Continue systematic spectroscopic and microscopic studies of aged and cycled cells to correlate changes of electrode surface and structural characteristics with cell performance degradation.

- Carry out a series of model experiments to determine the mechanism of detrimental processes, which are determined in the course of diagnostic work.

- Correlate SEI composition with cell performance.

- Use quantitative techniques to determine reaction product distributions as a function of cell history, and use this data to develop models of cell performance and to predict cycle and calendar life

- Continue studies to identify cell reaction products and carry out control experiments to further enhance mechanistic understanding.

Publications

- R. Kostecki and F. McLarnon, "Degradation of $LiNi_{0.8}Co_{0.2}O_2$ Cathode Surfaces in High-Power Lithium-Ion Batteries", *Electrochemical and Solid State Letters,* **5***,* A164 (2002).

- L. Norin, R. Kostecki, and F. McLarnon, "Study of Membrane Degradation in High-Power Lithium-ion Cells", *Electrochemical and Solid State Letters,* **5**, A67 (2002).

- R. Kostecki and F. McLarnon, "MicroProbe Study of the Effect of Li Intercalation on the Structure of Graphite", 11th International Meeting on Lithium Batteries, June 2002, Monterey, California, Meeting Abstract no. 223

- L. Norin, R. Kostecki, and F. McLarnon, "Study of Polypropylene Separator Degradation in High-Power Lithium-Ion Cells", 201st Meeting of the Electrochemical Society, Philadelphia, PA, May 2002.

- F. F. McLarnon and R. Kostecki, "Effects of Interfacial Processes on the Performance and Life of Lithium-Ion Batteries," paper no. 1I03 presented by F. McLarnon at the 43rd Battery Symposium in Japan, Fukuoka, Japan (October 2002).

- G. Nadeau, XY. Song, M. Masse, A. Guerfi, G. Brisard, K. Kinoshita, K. Zaghib, "Effect of heat-treatment and additives on the particles and carbon fibers as anodes for lithium-ion batteries," *J. Power Sources*, **108**, 86 (2002).

Microprobe Characterization

High-resolution Raman microscopy measurements at various locations on the surfaces of cathodes taken from tested Gen 1 cells revealed strong intensity variation of the sub-peaks which contribute to the overall "oxide" peak at 520 cm^{-1}. These results not only provided clear evidence for significant spatial variations of the chemical composition and structure of $LiNi_{0.8}Co_{0.2}O_2$ on the cathode surface but also confirmed our earlier AFM and Raman observations of surface phase segregation. A series of Raman measurements on reference nickel and cobalt oxides was carried out to determine the origins of sub-peaks in the micro Raman spectra. We determined that tested Gen 1 cathode surfaces exhibited increased concentrations of Ni_2O_3 or NiO_2, which are decomposition products of the original $LiNi_{0.8}Co_{0.2}O_2$. However, the exact stoichiometries of these new nickel oxide phases could not be determined because all higher-valent ($n \geq 3$) nickel oxides are isostructural and display identical vibrational spectra. Raman microscopy spectra of tested Gen 2 cathodes displayed features typical for a partially charged electrode, *i.e.*, the cathode surface state of charge (SOC) is non-uniform and generally higher than expected for a cathode nominally poised to 0% SOC. AFM images of cathodes from tested cells showed no evidence of new oxide phase formation, suggesting improved surface stability of $LiNi_{0.8}Co_{0.15}Al_{0.05}O_2$ compared to $LiNi_{0.8}Co_{0.2}O_2$. Thousands of micro-Raman spectra of Gen 2 cathodes recorded at 0.7 μm lateral resolution were converted to color-coded Raman image maps to illustrate how the surface composition [relative amounts of $LiNi_{0.8}Co_{0.15}Al_{0.05}O_2$, graphite, and acetylene black] varies over a 40 x 60 μm area of a typical electrode (Fig. 8). The Raman image map for the aged cathode exhibits several sites of bare active material with no carbon deposit, in marked contrast to the Raman image maps of a single-sided cathode (not shown) and a fresh cathode, both of which are almost completely covered with carbon black and graphite. The apparent disappearance of carbon from the cathode surface during testing therefore correlates with cell power loss.

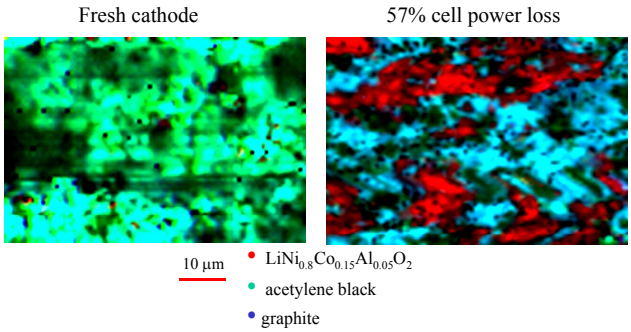

Figure 8. Raman microscopic images of 60x40 μm regions of two Gen 2 cathodes. $LiNi_{0.8}Co_{0.15}Al_{0.05}O_2$, carbon black, and graphite are represented by red, blue, and green, respectively

The color-coded Raman microscopic maps of Gen 2 cathodes clearly indicated that significant changes in the $LiNi_{0.8}Co_{0.015}Al_{0.05}O_2$/elemental carbon surface concentration ratio accompanied cell storage and cycling at elevated temperatures. In order to quantify these changes, we have carried out semi-quantitative analyses of these Raman maps. The results are presented in Fig. 9 as a function of cell power loss. The oxide/carbon ratios for a fresh Gen 2 composite cathode and a cathode taken from a fresh cell are both about 0.05, indicating almost complete carbon coverage of the cathode surface. The oxide surface concentration appears to increase monotonically with increasing cell power loss, up to an apparent break point at about 20% cell power loss. Interestingly, this break point coincides with the break point in the cell power loss *vs*. test time data shown elsewhere in this report. Above 20% cell power loss, there is no clear correlation between oxide surface concentration and cell power loss. It should be recognized that the changes in $LiNi_{0.8}Co_{0.015}Al_{0.05}O_2$/elemental carbon concentration ratio observed with the Raman microscope may arise from at least three distinct phenomena: (*i*) recession of carbon from the cathode surface, (*ii*) modification of the distribution of carbon in the cathode, and (iii) alteration of the Raman scattering cross-section of the carbon by, for example, anion intercalation described above. How the carbon additive "retreat" or "rearrangement" or "modification" influences cathode performance remains an open question.

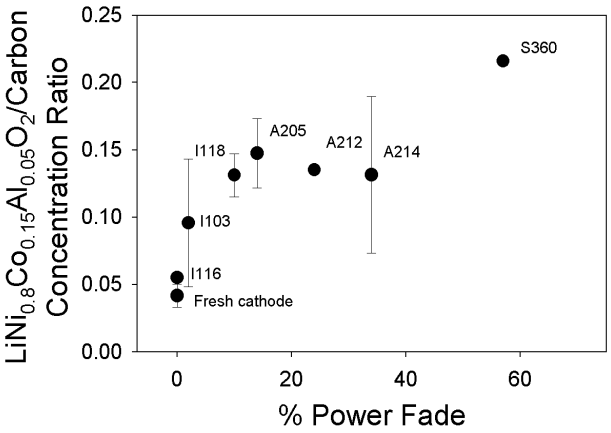

Figure 9. Plot of Raman-derived oxide/carbon surface concentration ratio vs. Gen 2 cell power loss. The error bars reflect the variation in measured oxide/carbon surface concentration ratio for Raman maps recorded at more than one location on the cathode surface of a given Gen 2 cell. Shorthand notation is used to label the data points.

We have completed our study of the source and nature of Gen 2 cell separator degradation. Our results indicate that observed porosity loss could be attributed to an adherent non-uniform, strongly fluorescent deposit on the separator surface that gives the fibers a swollen appearance and covers pores. We have determined that this deposit results from a $LiPF_6$-EC-EMC electrolyte decomposition process. We found that the deposit most likely consists of halophosphates LiPOx:MeF, where Me is a co-crystallized impurity such as transition metal ions. These compounds precipitate from the electrolyte, affecting both the separator porosity and the chemistries on both electrodes, *e.g.*, SEI (re)formation. Although membrane degradation does not appear to be a primary cause of power loss in Gen 2 cells (<10%) it can be a good indicator of detrimental processes in Li-ion cells.

Infrared Studies

We examined the surfaces of anodes, cathodes, and the separators extracted from cells G2.60C55.A211.34.40.34.G.L (A211) and G2.60C55.A214.34.40.34.G.L (A214) with Fourier Transform Infrared Spectroscopy (FTIR) using the Attenuated Total Reflection (ATR) geometry. The cells were subjected to calendar aging at 60% SOC and 55°C and had nominally identical power fade (34 %). The high quality of the IR spectra enabled us to identify the chemical composition of the passive films on these electrodes. Both the cathode and the separator have a surface layer composed of an EC/$LiPF_6$ solvate formed by distillation of the more volatile co-solvents EMC, DEC and DMC. When the solvate layer is washed from the cathode with DMC, only IR features characteristic of the binder are observed. A pre-existing layer of lithium carbonate that is on the oxide in fresh cathode powder is not present in a cathode taken from a fresh cell nor in either of the two aged cathodes. Presumably the pre-existing layer of lithium carbonate decomposes during the cell formation cycles to form CO_2 and lithium oxide. This reaction may be the principal source of CO_2 seen in the gas of the control cells. By ATR-FTIR analysis (Fig. 10), the cathodes and separators of the calendar-aged cells are essentially identical to those from a fresh cell. The composition of the film on an anode from a fresh cell is composed of lithium oxalate ($Li_2C_2O_4$), lithium carboxylate (*e.g.*, lithium succinate $LiO_2CCH_2CH_2CO_2Li$) and lithium methoxide ($LiOCH_3$). After aging, in addition to these compounds, there is also lithium hydroxide (LiOH) and methanol (CH_3OH), and in some cases lithium hydrogen carbonate ($LiHCO_3$). The latter three compounds are probably associated with the reaction of water (thermal hydrolysis) in the cell with the methoxide and oxalate, respectively, upon calendar aging. Washing a calendar-aged electrode with DMC produced substantially different spectra. Typically, washing eliminated the features from methanol and bicarbonate, enhanced the intensity of the lithium hydroxide peak, and produced new features attributed to lithium carbonate (Li_2CO_3). Washing an anode with DMC appears to not only remove residual electrolyte, but also change the composition of the passive film; this procedure will require further study to be useful for in-depth anode characterization. At present, the most likely correlation of our ATR-FTIR analysis of cell components with cell power fade is the change in composition and possibly the structure of the SEI layer on the anode. This change in composition appears to be the result of thermal hydrolysis (by water in the cell) of Li^+-ion conducting organo-lithium salts into non-conducting lithium oxide.

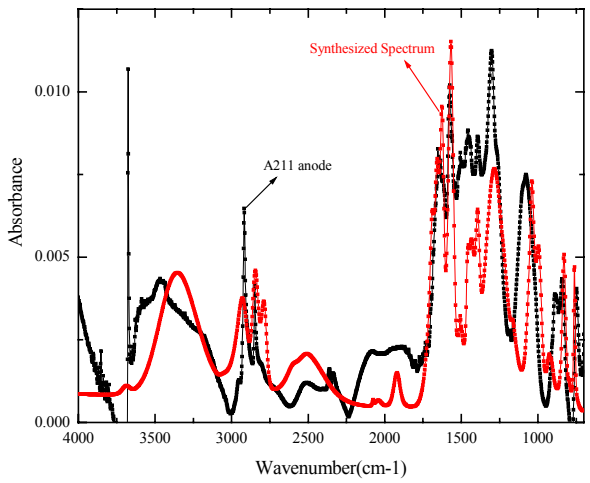

Figure 10. ATR-IR spectrum of an anode harvested from cell A211 compared to a synthesized spectrum composed of individual spectra from pure compounds using the given weighting factors: lithium succinate (0.70); lithium bicarbonate (0.23); lithium methoxide (0.06); methanol (0.01). The strong, sharp peak near 3700 cm^{-1} is characteristic of LiOH, but it was not included in the synthetic spectrum.

TEM, SEM and EDX Characterization

TEM, SEM, and EDX studies of cathodes from cells with higher power fade revealed changes in both microstructure and composition. As expected, SEM/EDX confirmed the identity of the smaller particles in the cathodes as carbon. Comparison of images from various cells showed a trend to fewer of these particles visible in the cells with highest power fade. TEM micrographs of the cathode from cell G2.80C55.S446.XX.20.54.G.L show direct evidence of structural damage as shown in Fig. 11. From the lattice image, we find that the LiNi0.8Co0.15Al0.05O2 grain has been separated into several individual nano-domains with different orientations. The fast Fourier transform (FFT) of the lattice image demonstrates the polycrystalline pattern produced as a result of the damage. The lattice parameters in the degraded grain are expanded from those in uncycled grains. EDX analyses of this and similar samples show much wider variations in the Ni/Co atomic ratios in high-power-fade cathodes than in fresh cathodes. Furthermore, iron, magnesium, silicon, and possibly germanium impurities were found widely, but inhomogeneously, deposited in these cathodes. In FY 2003 we will continue to look at surface and compositional features and to work with the other ATD groups to arrive at a comprehensive mechanism for power fading in Gen2 cells.

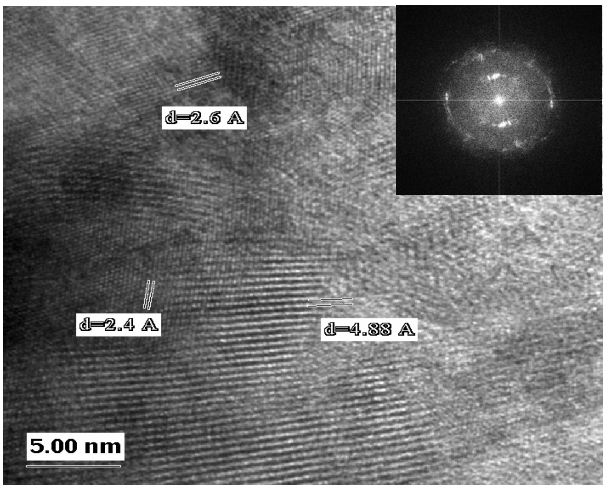

Figure 11. TEM lattice image and FFT electron diffraction pattern showing structural degradation and lattice expansion in $Li(Ni_{0.8}Co_{0.15}Al_{0.05})O_2$ grain.

Quantitative Chemical Analyses

Analyses were developed for transesterification and polymer products using gas chromatography and gel permeation chromatography (GPC) respectively. High molecular weight (M.Wt.) material of up to 100,000 was found in water extracts of cell components from cells G2.60C55.A214.34.40.34.G.L (A214) and G2.60C55.A212.24. 28.24.G.L (A212), which had 34% and 24% power fade, respectively. The maximum M. Wt. of material extracted from cells such as G2.60L45.I118.04.04.10.G.L (10% P.F.) was much lower (~ 20,000 max.) and was even lower for cells with lower P.F. Quantification of the amount extracted was achieved by an external standard method using PEO standards to calibrate for both polymer M.Wt. and quantity. The amounts of water-extractable material were found to be considerably greater on the separator material than from the electrodes. The actual separator polymer material was lower in M.Wt. These results are consistent with the separator experiments reported by Robert Kostecki (see Microprobe Characterization).

GPC analyses were repeated on cell components from A212 and A214 after six months of storage in a glove box at ambient temperature. The same extraction procedure was used but dramatically smaller amounts of extractable polymer material were found. The M.Wt. distribution was also altered in a seemingly random fashion. These results indicate that chemical reactivity continues even after the cells are opened and the components are apparently dry. This result may give some clues to the apparently conflicting results found by different diagnostic laboratories, as diagnostic examination of samples may be influenced by the time delay after cell opening as well as sample preparation. The importance of standardization of sample preparation seems to be evident.

III.B.3. Accelerated Life Test Protocol Development

Ed Thomas, Dan Doughty, Peter Roth
Mail Stop 0613, Sandia National Laboratory, Albuquerque, NM 87185
Contact: Ed Thomas phone: 505-844-6247 fax: 505-844-9037 ; e-mail: EVTHOMA@Sandia.gov

Objectives

- Develop accelerated aging test and analysis protocols to rapidly evaluate new cell designs with respect to expected lifetime.
- Apply protocols to make life assessment of GEN2 cells.

Approach

- Use statistical experimental design philosophy to develop testing protocols.
- Use statistical linear model theory and methodology to develop protocols for analyzing accelerated degradation data and for estimating cell lifetime.

Accomplishments

- Developed three-phase experimental strategy for testing cells: 1. Screening experiments (if needed) used to identify accelerating factors, 2. Primary aging experiments used to obtain a basic assessment of cell lifetime, and 3. Secondary aging experiments (if needed) used to improve the estimate of cell life and for validation.
- Developed analysis strategy for estimating cell life that involves fitting a single-mechanism, first-order kinetics model (in terms of accelerating factors) to performance data (e.g., relative power). The fitted degradation model is then evaluated at use conditions to estimate cell life.

Future Directions

- Explore diagnostic procedures that would allow an analyst to detect the presence of multiple mechanisms. Develop protocols (experimental design and modeling) that facilitate modeling the degradation associated with multiple mechanisms.
- Develop experimental and data analysis strategies for assessing the adequacy of static models (developed using test data from cells that experience a constant accelerating environment) to predict the performance degradation of cells that are experiencing variable environments.

Introduction

The objective is the development of a protocol for rapidly obtaining a *useful* assessment of the *average lifetime* (at some specified use conditions) that might be expected from cells of a particular new design. Emphasis is placed on understanding typical cell behavior rather than quantifying the variation in performance from cell to cell. An understanding of cell-to-cell (or battery-to-battery) variation would be critical with regard to the development of warranty policies. However, one would need to test actual production cells to effectively develop such warranty policies. Thus, the focus here is on the capability of the cell design rather than the ability to produce homogeneous cells in large quantities.

Due to the expected relatively long cell life and the need to rapidly assess cell lifetime, it is necessary to use accelerated aging experiments as the means to estimate the average cell lifetime at normal operating conditions. Through the acquisition of appropriate degradation data over time, an unambiguous assessment of the effects of accelerating factors (e.g., temperature and state of charge [SOC]) on various measures of the health of a cell (e.g., power and capacity) will result. In order to make a useful assessment of the average cell lifetime, it is necessary to construct an accurate model that relates the rate of performance degradation to the levels of the accelerating factors.

It is important to have an effective and efficient experimental strategy for assessment of aging effects and developing accelerated aging models. The experimental strategy recommended here involves a number of sequential stages. Initially, experiments might be performed to select viable accelerating factors. Follow-on experiments involving the selected factors would be used to obtain an accurate assessment of cell lifetime.

In order to make an accurate assessment of average cell lifetime it is necessary to couple the experimental protocol with effective data analysis and modeling. The model form needs to provide a good representation of the experimental data. If the degradation phenomenon is related to a chemical reaction with first-order kinetics, it is possible to prescribe a general data analysis protocol that is useful for making a prediction of cell lifetime with an associated estimate of uncertainty.

Experimental Strategy

The recommended experimental strategy involves up to three sequential stages: screening experiments, primary aging experiments, and secondary aging experiments. The purpose of the screening experiments (which may or may not be required) is to select viable accelerating factors. One might opt to use screening experiments in cases when the cell design/chemistry is a radical departure from existing designs such that accelerating factors are unknown. The primary aging experiments represent the kernel of the experimental strategy. These experiments involve known accelerating factors and provide the means to obtain a basic assessment of cell lifetime. The secondary aging experiments (which may or may not be needed) are used to improve the basic assessment of cell lifetime as well as validate accelerated aging models that were developed from the primary aging experiments. If necessary, the precision associated with estimates of average cell lifetime may be improved by augmenting the primary experimental design with additional testing involving more cells and/or continued aging/testing of cells associated with the primary experimental design.

Design and analysis of the screening experiment involves a number of specific considerations. Given that suitable response variables have been selected, the first goal is to select a candidate pool of accelerating factors. A good way to accomplish this is via a brainstorming session with a group of subject-matter experts. Criteria for selecting a factor for the candidate pool include the factor's perceived ability to accelerate performance degradation as well as the experimenter's ability to control the factor. It may not be necessary to include certain factors (such as aging temperature) in the candidate pool if it is known that they will be involved in the primary aging experiments. Once the candidate pool of factors has been fixed, it is necessary to select two

level settings for each factor (denoted least and most accelerating). For the *least* accelerating level, one should choose a benign use condition. For the *most* accelerating level it is important to choose a level far enough away from the benign level such that there is a reasonable chance for observing accelerated performance degradation in a relatively short period of time. The analysis of the data from the screening experiment is very simple. An outcome of the analysis is a list of the top ranked statistically significant factors for each response variable. Assuming that the lists are consistent across response variables, then the top ranked factors should be considered for use in the primary aging experiments.

The primary aging experiment involves a number of specific considerations. Accelerating factors are selected based on the results of screening experiments or basic subject-matter knowledge. In general, it is recommended that 3 levels be selected for each accelerating factor. It is also assumed that the degradation mechanism is consistent across the range of factor levels and the use conditions of the cell. The *least accelerating level* of each factor should be as chosen as close as possible to the target-use condition of the cell such that some measurable degradation is expected to occur over the course of the experiment at that condition. The *most accelerating level* of each factor should be chosen to provide the maximum acceleration without changing the mechanism for degradation. Once the accelerating factors and associated factor levels have been determined it is necessary to specify the set of experimental conditions to be examined. With fewer than 4 accelerating factors, full factorial designs are recommended. Full factorial designs involve every possible combination of factor levels. For example, suppose that there are 2 factors each involving 3 levels. Then there are 3^2 or 9 possible experimental conditions. In cases where there are 4 or more factors, other more complex designs are recommended (see e.g., Chapter 15 in Box and Draper (1987)). It is recommended that at least two (and preferably three) cells be allocated to each experimental condition. If available, additional cells should be allocated to the least-accelerating experimental conditions (perhaps representing use conditions) in order to help resolve small changes in performance over time. Such cells could be kept on test indefinitely to serve to validate predictions of cell life. Another important design issue is to select the times at which cells are removed from storage and tested. In order to minimize resource expenditures associated with testing, we recommend testing at intervals that are uniformly spaced in log time. All cells should be measured prior to aging.

Analysis Strategy

There are a number of analysis strategies that might be used to model accelerated degradation data. One model formulation that is general enough that it could be useful in number of battery applications assumes a chemical reaction, $A \rightarrow$ Reaction Products, where the reaction is first-order with respect to A. Thus, the rate law is $\frac{-d[A]}{dt} = k \cdot [A]$, where $[A]$ is the concentration of A, k is the rate constant, and t is time. If $\log(k) = \beta_0 + \beta_1 \cdot \frac{1}{T}$, where T is the absolute temperature and β_0 and β_1 are parameters, then the Arrhenius model follows. That is,

$$[A(t)] = [A(0)] \cdot \exp\left\{-\exp\left(\beta_0 + \beta_1 \cdot \frac{1}{T}\right) \cdot t\right\}.$$

β_0 is often referred to as the *pre-exponential factor* while the activation energy (E_A) is given in terms of β_1 (i.e., $E_A = -R \cdot \beta_1$). In accelerated aging experiments we might observe some measure of performance (such as power) over various storage temperatures and time. Let $P(X;t)$ denote a generic performance metric at $X = T^{-1}$ and time, t. Following the Arrhenius model, we have $P(X;t) = P(X;0) \cdot \exp\{-\exp(\beta_0 + \beta_1 \cdot X) \cdot t\}$. There are a number of ways that this basic equation could be generalized with respect to the effects of time and additional accelerating factors. If we assume that there are "q" accelerating factors $(X_1, X_2, \ldots, X_q)$, we might consider models of the form

$$P(X_1, X_2, \ldots, X_q; t) = P(X_1, X_2, \ldots, X_q; 0) \cdot \exp\left\{-\exp\left(f\left(X_1, X_2, \ldots, X_q\right)\right) \cdot t^{\rho}\right\},$$

where, for example, $f\left(X_1, X_2, \ldots, X_q\right) = \beta_0 + \sum_{j=1}^{q} \beta_j \cdot X_j + \sum_{j \neq k} \beta_{jk} \cdot X_j \cdot X_k + \sum_{j=1}^{q} \beta_{jj} \cdot X_j^2$.

The general form of the model can be re-expressed as

$$Z(X_1, X_2, \ldots, X_q; t) = \frac{P(X_1, X_2, \ldots, X_q; t)}{P(X_1, X_2, \ldots, X_q; 0)} = \exp\left\{-\exp\left(f\left(X_1, X_2, \ldots, X_q\right)\right) \cdot t^{\rho}\right\},$$

where $Z(\cdot)$ is the value of the performance metric relative to its value at $t = 0$. Further re-expression leads to

$$\log\left\{\frac{-\log\left(Z(X_1, X_2, \ldots, X_q; t)\right)}{t^{\rho}}\right\} = f\left(X_1, X_2, \ldots, X_q\right).$$

In terms of the simple Arrhenius model, $Y = \log\left\{\frac{-\log\left(Z(X; t)\right)}{t^{\rho}}\right\} = \beta_0 + \beta_1 \cdot X$, where $X = T^{-1}$.

The *joint estimation* of ρ and the β's is complicated, since the model is not linear in ρ. However, a simple two-step process can be used to resolve this complication. First, it is assumed that a valid metric for "fit quality" exists across values of ρ. For a fixed value of ρ, the β's can be estimated directly by linear regression. For each case of ρ (and the implied estimates of the β's), the "fit quality" can be obtained. Thus, one can compare model fits across values of ρ and select a value for ρ based on that metric. With ρ selected, the estimated β's are determined by linear regression.

Accomplishments

Estimation of Cell Lifetime - GEN2 Cells

The methodology described in earlier sections was applied to the high-power 18650-size Gen2 Li-ion cells that were built specifically for the ATD program. For this discussion we are concerned only with the response generated by the HPPC test at 25°C. The PNGV minimum power goal for HEV batteries is 25 kW discharge power at 300 Wh available energy. This equates to about a 23% cell power fade when the appropriate power margins and scaling are applied. Thus, a cell's lifetime is defined to be the point at which 77% of the cell's original power remains.

The primary aging experiment involved two accelerating factors (storage temperature and SOC). The experiment involved four levels for storage temperature and three levels for state of charge. Four levels of storage temperature were selected, as it was not clear (before the experiment was performed) at what point the degradation mechanism changes. A full factorial design involving all possible twelve experimental conditions was selected (see Table 1).

	25 degrees C	**35 degrees C**	**45 degrees C**	**55 degrees C**
60% State of Charge	3	3	3	3
80% State of Charge	3	3	3	5
100% State of Charge	3	3	5	5

Table 1. Replication at Each Experimental Condition

Local models of relative power (specific to each SOC) were developed using degradation data acquired through 32 weeks of aging. These models are of the form $Y = \log\left\{\frac{-\log\left(Z(X; t)\right)}{t}\right\} = \beta_0 + \beta_1 \cdot X$ (the experimental data were well represented using $\rho = 1$), where $X = T^{-1}$. Table 2 provides summary statistics regarding the model fit for each state of charge.

	$\hat{\beta}_0$ $(\hat{\sigma}_{\hat{\beta}_0})$	$\hat{\beta}_1$ $(\hat{\sigma}_{\hat{\beta}_1})$	**Estimated Activation Energy:** $\hat{E}_A = -R \cdot \hat{\beta}_1$
60% SOC	10.85 (.21)	-4.83×10^3 (1.5×10^2)	9.7 kcal per mole
80% SOC	15.72 (.56)	-6.26×10^3 (1.8×10^2)	12.5 kcal per mole
100% SOC	12.13 (.40)	-4.99×10^3 (1.3×10^2)	10.0 kcal per mole

Table 2. Estimates of Model Parameters (with standard errors)

Figure 1 indicates the quality of the fit for the case with 60% state of charge.

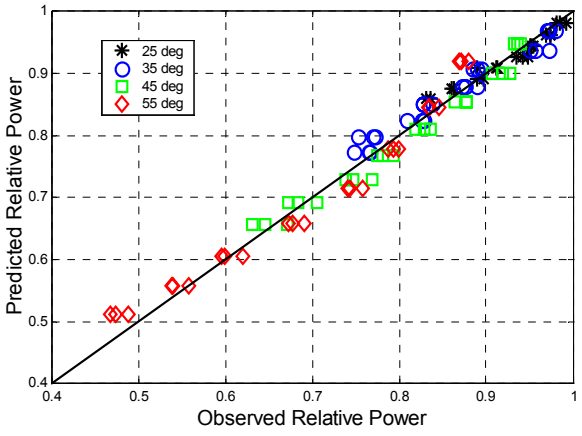

Figure 1. Predicted versus Observed Relative Power for 60% State of Charge

Given static aging at 25^{o} C and 60% SOC, the estimated mean lifetime of GEN2 cells derived from the 60% state of charge model is 55.1 ± 3.7 weeks.

Future Directions

Despite providing a reasonable representation of the experimental data, the model could benefit from some additional refinement. For example, in Figure 1, the predicted relative power for each storage temperature seems to exhibit a parabolic pattern about the line of identity. That is, power predictions associated with early time (e.g., week 4) and later time (e.g., week 32) generally exceed the actual power that is observed. On the other hand, the power predictions associated with mid time (e.g., 20 weeks) are generally less than the measured relative powers. This effect is consistent for cells stored at each of the four storage temperatures (particularly in the case of the 55 degree C data).

Thus, in the next fiscal year we plan to investigate other model forms, some of which involve multiple mechanisms. On a related note, we plan to explore diagnostic procedures that would allow an analyst to detect the presence of multiple mechanisms as well as develop protocols (experimental design and modeling) that facilitate modeling the degradation associated with multiple mechanisms.

Finally, we plan to develop experimental and data analysis strategies for assessing the adequacy of static models (developed using test data from cells that experience a constant accelerating environment) to predict the performance degradation of cells that age in a dynamic environment.

References

Box G. E. P. and Draper N. E., Empirical Model-Building and Response Surfaces, 1997, Wiley.

Acknowledgements

Thanks to Herb Case and Bryan Sanchez for conducting the electrical testing and data processing for this study.

We acknowledge the support of DOE Office of Advanced Automotive Technology through the FreedomCar Advanced Technology Development (ATD) High Power Battery Development Program. Sandia National Laboratories is a multiprogram laboratory operated by Sandia Corporation, a Lockheed Martin Company, for the United States Department of Energy under contract DE-AC04-94AL85000.

III.C. Abuse Tolerance

III.C.1. Cell And Component Response To Thermal Ramp

Peter Roth, Chris Crafts, Dan Doughty
Mail Stop 0613, Sandia National Laboratory, Albuquerque, NM 87185
Contact: E. P. Roth phone: 505-844-3949 fax: 505-844-6972; e-mail: eproth@sandia.gov

---

Objectives

- Develop abuse methods which can establish cause and effect relationships between variations in abuse tolerance, thermal instabilities, or reduced lifetimes to changes in cell design or materials
- Identify mechanisms and chemical constituents leading to reduced thermal tolerance, reduced thermal stability, or reduced operational lifetime in Li-ion cells.
- Identify chemical mechanisms resulting in gas generation that leads to cell venting.
- Determine factors affecting flammability of cell vent products under abusive conditions.
- Characterize the thermal response and gas generation products of cells under various overcharge conditions.
- Develop a knowledge base of cell thermal properties leading to improved cell designs.

Approach

- Test full size cells by the method of Accelerating Rate Calorimetry (ARC) to determine cell properties leading to cell thermal runaway.
- Measure gas generation in full cells as a function of temperature and cell properties such as state of charge and aging/cycling history.
- Measure the thermal inter-reactivity of fresh cell solvents, conductive salts, and fresh/aged cell electrodes recovered from disassembled test cells by using Differential Scanning Calorimetry (DSC) and ARC.
- Measure gas-generating reactions and evolved gas species in ARC bomb capsules of electrode materials in electrolyte.
- Determine thermal response of whole cells from measurements of the thermal reactivity and interactions between the cell components leading to improved cell designs.
- Video document the flammability behavior of vented cells in air and in inert gas with/without an external ignition source.
- Perform and video document overcharge and thermal heating tests on cells to benchmark the unsafe or thermal runaway behaviors seen in Li-Ion hardware.

- Develop real time gas sampling and identification techniques to track rapid gas generation events during thermal abuse

Accomplishments

- Demonstrated that cell thermal runaway profiles can be characterized in three major temperature stages:
    - Stage 1: Room Temperature to 125°C – Onset of thermal runaway
    - Stage 2: 125°C - 180°C – Venting and accelerated heating (smoke)
    - Stage 3: 180°C and above – Explosive decomposition (flame)
- Identified the electrolyte salt ($LiPF_6$) as having significant impact on the thermal exothermic decomposition of the electrolyte
- Demonstrated that the addition of the salt to the solvent resulted in greatly increased gas generation
- Shown that EMC is the source of gas generation (venting) and that EC is the source of exothermic electrolyte decomposition.
- Shown that the composition of the decomposition gases did not change with increasing salt molarity
- Showed that there is reduced gas evolution at the anode from entrapped electrolyte
- Showed that gas evolution leading to venting and ejection of cell material can be attributed initially to cathode and electrolyte decomposition gases
- Developed the capability to continuously demonstrate the flammability or non-flammability of evolved gases during overcharge and thermal heating tests
- Showed that the generated cell gases did not ignite in inert gas even in the presence of an ignition source
- Determined cell thermal response and runaway behavior during overcharge

Future Directions

- Develop and characterize improved thermal response of Li-ion cells with more stable anode and cathode active materials
- Determine effect of less reactive salts on stability of electrolyte and electrolyte/electrode reactions in order to reduce explosive decomposition reactions
- Determine the effects of additives on mitigation of thermal runaway and gas generation in Li-ion cells
- Determine effect of additives on flammability of vented gases
- Identify source of overcharge explosive reactions in cells
- Measure and identify “real time” gas species from venting cells during thermal ramp and overcharge abuse profiles
- Identify materials combinations for high abuse tolerant Li-ion cell

Introduction

The use of high-power Li-ion cells in hybrid electric vehicles is determined not only by the electrical performance of the cells but by the inherent safety and stability of the cells under normal and abusive conditions. The thermal response of the cells is determined by the intrinsic thermal reactivity of the cell components and the thermal interactions in the full cell configuration. The purpose of this study is to identify the thermal response of these constituent cell materials and their contribution to the overall cell thermal performance. Calorimetric techniques such as Accelerating Rate Calorimetry (ARC) and Differential Scanning Rate Calorimetry (DSC) were used as a sensitive measure of these thermophysical properties.

Accomplishments

Thermal Component Analysis

Much of this year's work has centered on identifying and quantifying the reactions that are the source of this rapidly accelerating heat and gas generation. ARC and DSC measurements were performed on the cell materials removed from end of life cells to characterize the individual cell component reactions. A study was also performed on the electrolyte decomposition reaction and the role of the $LiPF_6$ salt in determining the stability of the electrolyte.

ARC allows determination of adiabatic cell response to increasing temperature and thus measures the onset and development of thermal runaway under controlled conditions. Previously we have reported ARC runs performed on Sony, GEN1 and GEN2 chemistries as shown in Figure 1. The thermal runaway profiles can be characterized in three major temperature regimes:

- Room Temperature to 125°C – Onset of thermal runaway
- 125°C - 180°C – Venting and accelerated heating (smoke)
- 180°C and above – Explosive decomposition (flame)

Figure 1 shows that the GEN2 cell at 100% state of charge (SOC) had greater thermal activity than seen for the GEN1 cells. The onset of self-generated heating was around 50°C as was seen for GEN1 cells but the heating rate accelerated with increasing temperature very similar to that seen for the SONY cells. However, the GEN2 cells did not show the SEI breakdown reaction at 100°C as was seen for the SONY cells. These results suggest that the GEN2 cells were not experiencing an effective anode SEI passivation film growth which was very effective in the GEN1 cells. Figure 2 illustrates that this is the case where we can see that the GEN1 MCMB carbon particles were smooth and round while the GEN2 particles were flaky with exposed edges (micrographs provided by ANL). This difference in particle morphology largely determines the thermal response of the cell up to 140°C. Above this temperature, the cell heat and gas generation rate increase sharply.

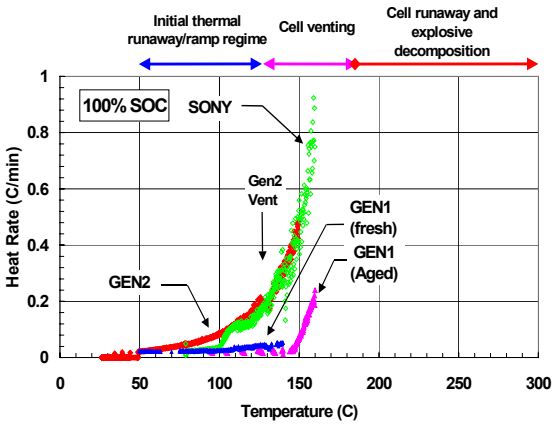

Figure 1. ARC runs of Li-ion cells (SONY, GEN1,GEN2) showing 3 major temperature regimes.

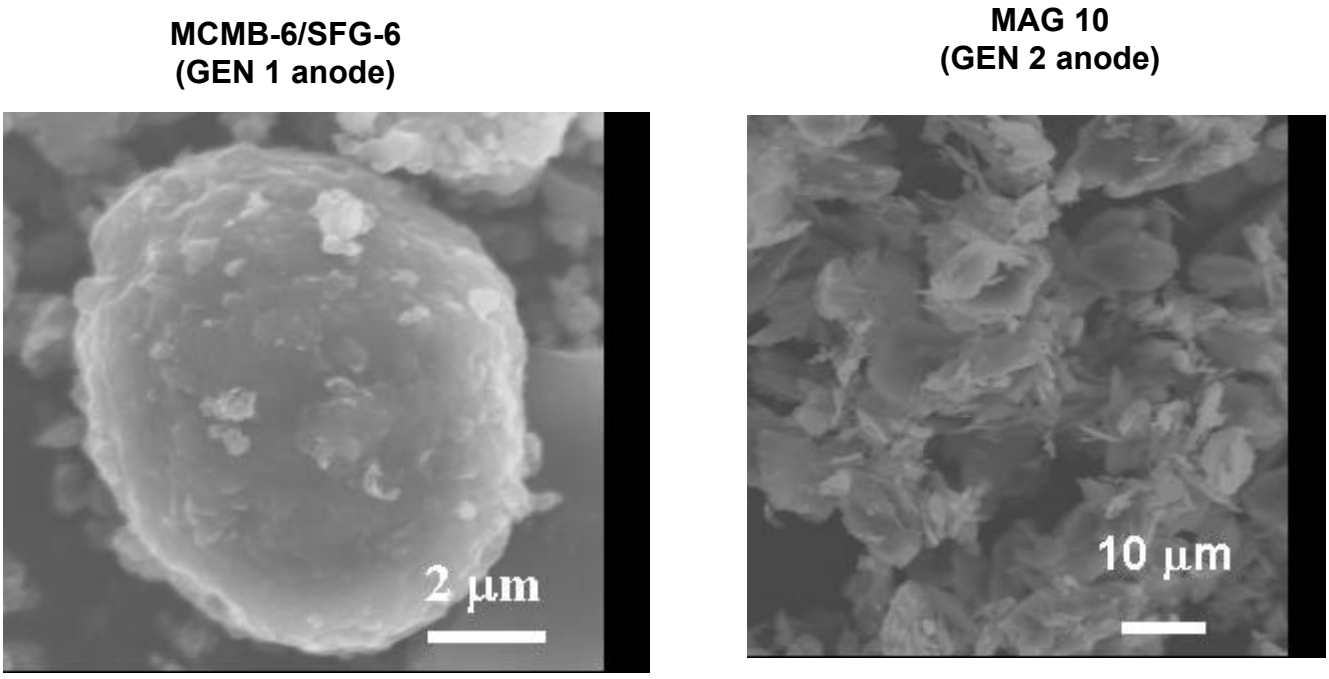

Figure 2. SEM micrographs of GEN1 and GEN2 carbon anode particles.

Cathode/Anode Reactions

ARC bomb runs were performed on cathode materials removed from end of life cells from the ALT cell group. The ARC data more closely matches the thermal runaway temperature profile seen for the full cells and have reaction peaks at lower temperatures than obtained with the fast scan DSC. Figure 3 shows the ARC results for cathode material from an ALT cell with no added electrolyte (estimated residual electrolyte 5% of dry film wt.). The heating rates were all calculated based on the dry film weight. The highest peak corresponds to the temperature at which the cells undergo explosive decomposition during thermal heat block tests. Pressure and heat generation began about 140ºC and reached a maximum around 175ºC which closely matches the observed cell response during the ARC runs. This gas results primarily from cathode decomposition since so little electrolyte was present.

Comparisons of the anode and cathode materials in electrolyte for this end of life cell are shown in Figure 4. The heating rates have been normalized by the electrical charge state capacity of each material to allow a more direct comparison of the total cell material balance. Electrolyte has been added so that the film/electrolyte ratio is about 1:1. The addition of electrolyte has not moved the main cathode peak or significantly changed the magnitude of the heating rate. The lower temperature reactions are not seen due to the addition of the electrolyte which can mask these reactions by endothermic gas generation. The anode material was observed to peak at a higher temperature than for the cathode but showed a comparable normalized heating rate. The anode material still undergoes low temperature reactions well before the cathode material but they are below the threshold of sensitivity for the ARC bomb runs. During rapid thermal runaway, there may be little observable difference in behavior from the offset in thermal peaks due to the very high heating rate at these temperatures in a full cell. The cell would ramp through this temperature range in only a few seconds.

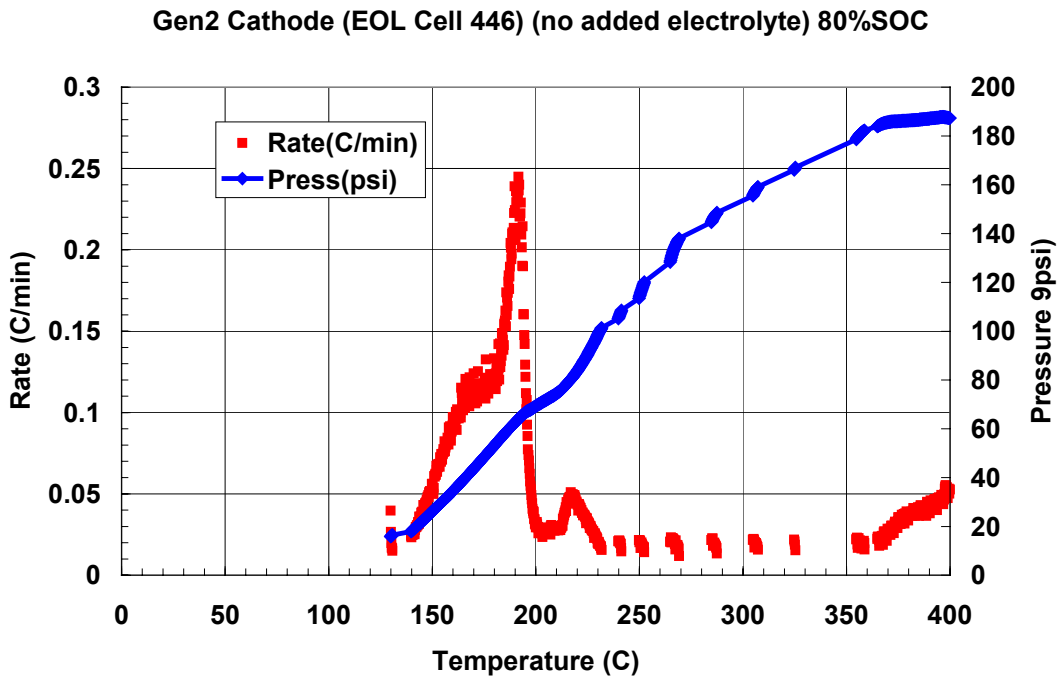

Figure 3. ARC bomb runs of end-of-life cathode with no added electrolyte.

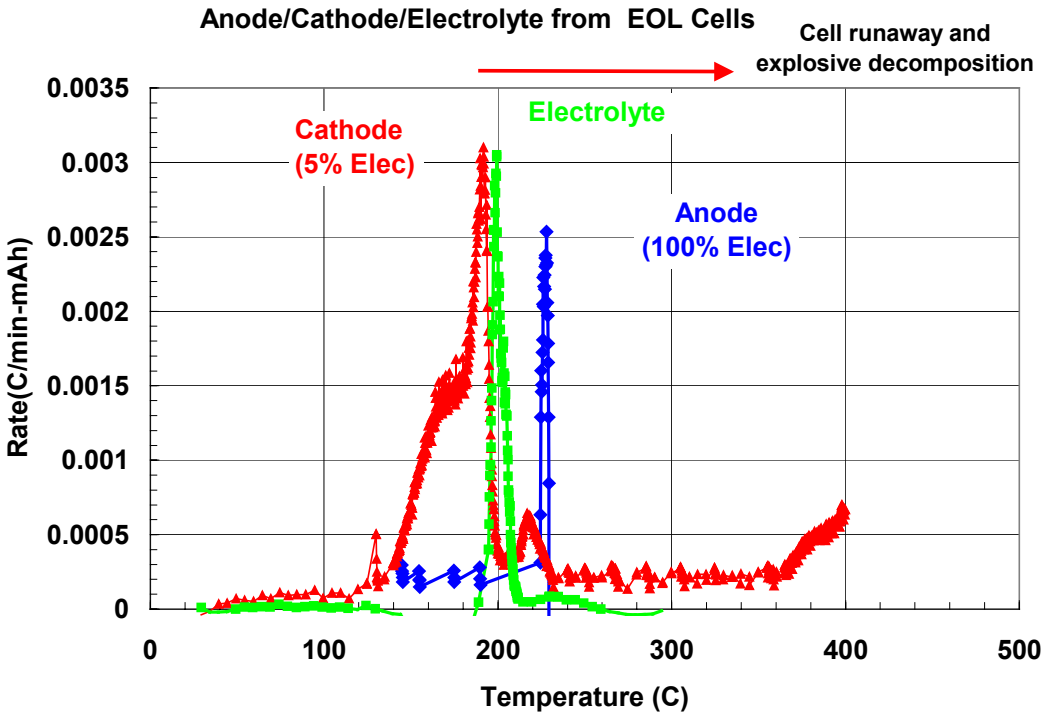

Figure 4. ARC bomb runs of anode and cathode material with added electrolyte. Normalized to total SOC capacity (mAh).

Electrolyte Decomposition

Gas evolution results from reactions of the cell electrodes and the cell electrolyte. A quantitative approach has been taken to identify the chemical mechanisms leading to thermal runaway and venting. The gas evolution attributable to electrolyte breakdown was determined by performing ARC bomb capsule runs of the GEN2 solvent and electrolytes. The ARC system was modified to allow not only measurement of the total pressure increase during the ARC run but also to allow gas collection during or after the run.

The solvent (EC:EMC) and electrolyte (EC:EMC/$LiPF_6$) were each measured under identical conditions. Figure 5 shows the ARC bomb exothermic heat rate data while Figure 6 shows the associated pressure data. The solvent showed little exothermic behavior or gas generation up to 300°C. ***The addition of the salt to the solvent resulted in greatly increased gas generation and exothermic reaction***. Additional gas evolution was seen starting at 140°C followed by a sharp exotherm at 185°C. GC analysis of these evolved gases showed that the solvent gases were largely CO_2 with small amounts of methane and ethylene. The addition of the $LiPF_6$ salt resulted in new generation of smaller amounts of H_2 and ethylene.

The role of the ***$LiPF_6$ was identified as having significant impact on the thermal exothermic decomposition of the electrolyte***. A study was undertaken to identify and quantify the effect of different $LiPF_6$ molarities on the decomposition rate and gas evolution rate of GEN2 EC:EMC (3:7) solvents. ARC bomb runs were performed on prepared solutions (~500mg) from RT up to 300°C. The ratio of the number of moles of evolved gas to number of moles of solvent was calculated and plotted as a function of temperature during the ARC run. Figure 7 shows this data for solutions of 0.0M (pure EC:EMC), 0.2M, 0.6M, 1.2M, and 1.8M $LiPF_6$. The gas decomposition for 0.0M and 0.2M were very similar and only showed evidence of decomposition above 225°C. For the 0.6M solution, gas generation increased sharply at 200°C. Increasing the molarity to 1.2M, equal to the value used in the GEN2 cells, caused the onset of gas generation to decrease to around 160°C and subsequently reached a plateau in the gas generation/solvent at 210°C. Further increasing the molarity to 1.8M did not significantly affect the solvent decomposition.

The relative contributions of the EC and EMC components to the total gas generation were investigated by running a separate set of measurements of electrolytes containing only EMC with increasing molarities of $LiPF_6$. The same salt molarities were chosen and the bombs run over the same temperature range as for the EC:EMC. The moles of evolved gas were calculated and ratioed to the number of moles of EMC. Figure 8 shows the resultant data for these runs. The moles of evolved gas were much reduced at each salt molarity up to 1.2M but continued to increase with increasing molarity. However, the 1.8M sample showed an evolved gas ratio of about 1.8 as was seen for the EC:EMC solvent. Figure 9 shows a comparison of the EMC and EC:EMC data for the 1.8M LiPF6 solution using EMC as the basis for comparison. As can be seen, the calculated evolved gas ratios are in very good agreement. This shows that ***EMC is the source of gas evolution during thermal decomposition of the electrolyte*** and that EC plays a secondary role in increasing the rate of decomposition but does not undergo any significant gas generating reactions of its own. The combination of temperature, LiPF6 concentration and the presence of EC give full decomposition for salt molarities of 1.2M or greater.

The heat generation rate for the EC:EMC also showed significant dependence on salt molarity. Figure 10 shows that there was no heat generation until a salt level of 0.6M was reached and even at 0.6M only a small, non-sustaining exotherm at 210°C was observed. A strong exotherm was observed at 190°C for the 1.2M concentration which we have seen many times for the standard GEN2 electrolyte measurements. Increasing the concentration to 1.8M lowered the onset of the exotherm peak to 185°C and gave a

much narrower and higher rate reaction. The EMC/$LiPF_6$ samples showed no sustainable exothermic data up to 300°C. These results are consistent with our earlier observations that ***EMC is the source of gas generation (venting) and that EC is the source of exothermic electrolyte decomposition***.

The evolved gas composition for each salt molarity is shown in Figure 11. The evolved gas species are the same as we have reported previously for electrolyte and cell ARC runs, consisting primarily of CO_2. Most interestingly, ***the composition of the decomposition gases did not change with increasing salt molarity***.

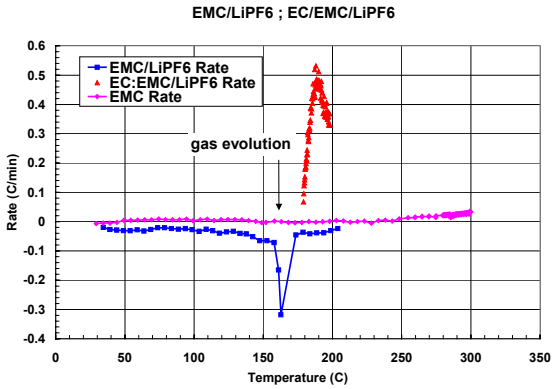

Figure 5. ARC bomb heating rates of electrolyte and electrolyte components**.**

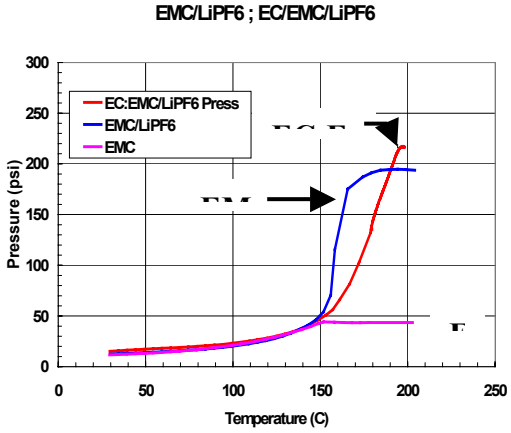

Figure 6. ARC bomb pressure of electrolyte and electrolyte components.

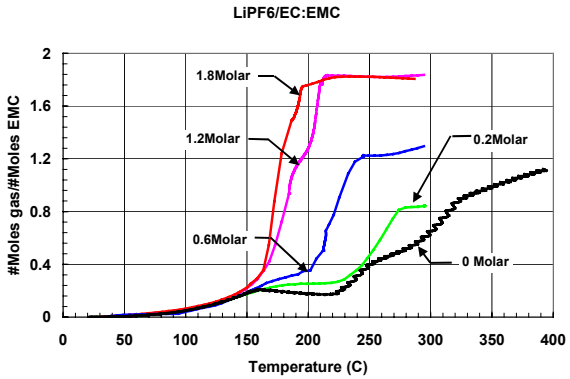

Figure 7. Moles of evolved gas per mole of EMC during ARC bomb runs of EC:EMC/LiPF6 at increasing salt molarity

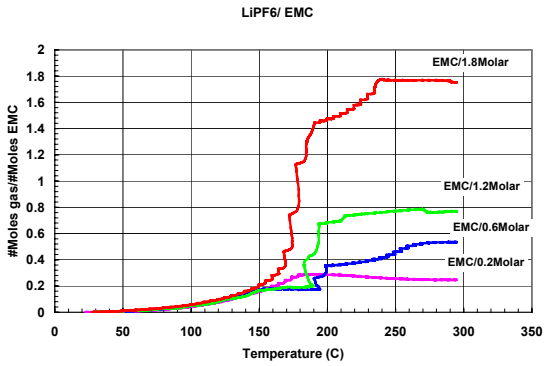

Figure 8. Moles of evolved gas per Mole of EMC for ARC bomb run of EMC/$LiPF_6$ at increasing salt molarity.

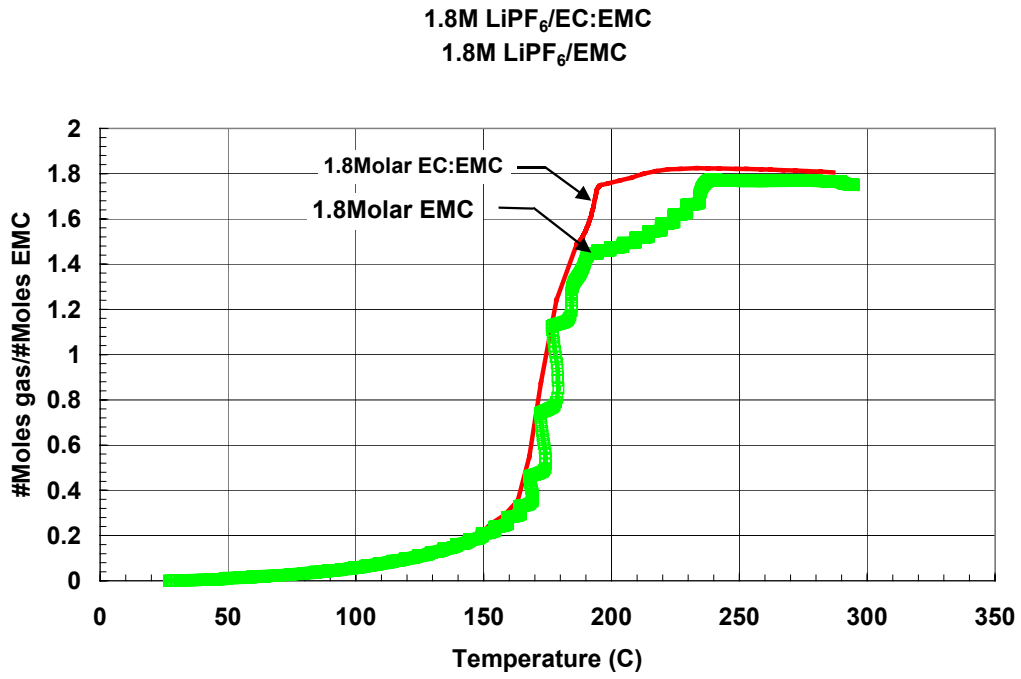

Figure 9. Comparison of evolved gas molar ratios for solutions of EMC and EC:EMC at 1.8M $LiPF_6$ concentration.

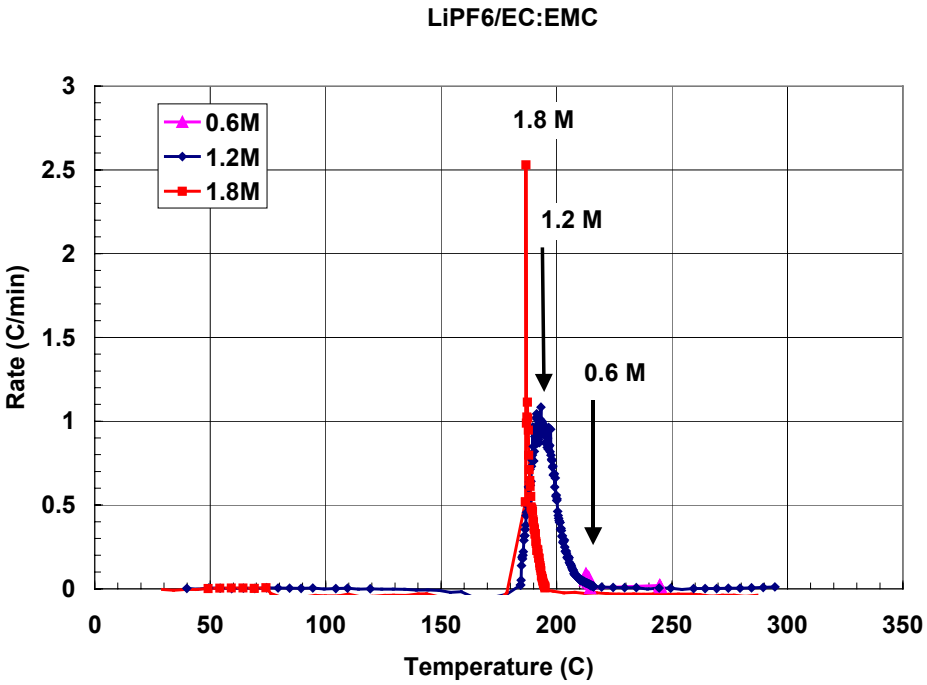

Figure 10. ARC bomb heating rates of GEN2 electrolytes (EC:EMC) with increasing $LiPF_6$ molarity.

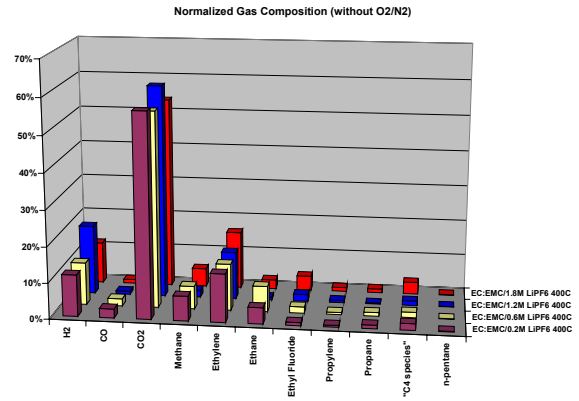

Figure 11. Normalized gas composition of decomposition gases as a function of $LiPF_6$ molarity in EC:EMC.

Cathode/Anode/Electrolyte Decompositions

The gas and heat generating decomposition reactions of the cell electrode materials were measured using the calibrated ARC system to quantify the reactions and compare to the electrolyte reactions just measured. Anode and cathode materials were obtained from an end-of-life cell (Cell 446: aged 55°C, 80%SOC, 21wks) and measured in the ARC using the same quantity of GEN2 electrolyte (1.2M LiPF6/EC:EMC) as in the salt molarity study. Figure 12 shows that the evolved gas from the anode/electrolyte run was slightly higher than for the comparable 1.2M electrolyte run at low temperatures but did not show the sharp increase in gas generation until above 215°C. The gas generation was more similar to that seen for the 0.6M electrolyte run. The anode film is known to absorb electrolyte on a 1:1 mass basis. The electrolyte/anode film ratio for this run was such that the great majority of the electrolyte would have been contained in the film pores. Thus, ***electrolyte interactions with the lithiated anode surfaces could affect the evolved gas products***. ***Reduced gas evolution at the anode could result from reaction of the gas products (CO_2) with the anode carbon material or could result from reduction in the salt molarity due to salt reactions with the carbon***. This behavior has been seen for anode materials from post mortem cells as well as from lab cell cycled material.

Cathode/electrolyte reactions were also measured using this post mortem cell material. Cathode material was run with equal amounts of electrolyte as was done for the anode material. However, the cathode material has been observed to only absorb about 5%-10% by weight of electrolyte. Thus, this run had a high level of free electrolyte. Figure 13 shows that the cathode/1.2M electrolyte reaction was similar to the 1.2M electrolyte reactions but that the amount of evolved gas did not plateau as seen for the pure electrolyte. Gas generation continued to increase with temperature up to the maximum run temperature of 350°C. This indicates that the ***cathode decomposition was a source of additional gas generation***. A second run was performed on cathode material from the post mortem cell without added electrolyte. Figure 9 shows that the cathode went into an exothermic regime starting around 130°C. The reaction rate increased with temperature, reaching a peak near 190°C, close to what we see for cathode material with excess electrolyte. The gas generation started at the same temperature and continued to increase up to 400°C. Thus, ***gas evolution leading to venting and ejection of cell material can be attributed initially to cathode and electrolyte decomposition gases followed by anode/electrolyte gases***.

We have thus shown that cell thermal runaway initiates at the anode due to breakdown of the protective SEI layer followed by exothermic reduction of the electrolyte by the lithiated carbon. During the second stage of thermal runaway (125°C - 180°C) the cathode begins to contribute to the exothermic decomposition accompanied by gas generation from both the cathode itself and the reacting electrolyte. Cell venting usually occurs in this region.. In the third and final stage of thermal runaway (180°C and above) the exothermic reactions accelerate rapidly with a series of peak reactions first involving the cathode/electrolyte followed closely by excess electrolyte decomposition and then anode/electrolyte

reactions. This region is characterized by explosive decomposition of the cell with high rate venting of the electrolyte. Ignition of the electrolyte vapors can occur in the presence of air and an ignition source.

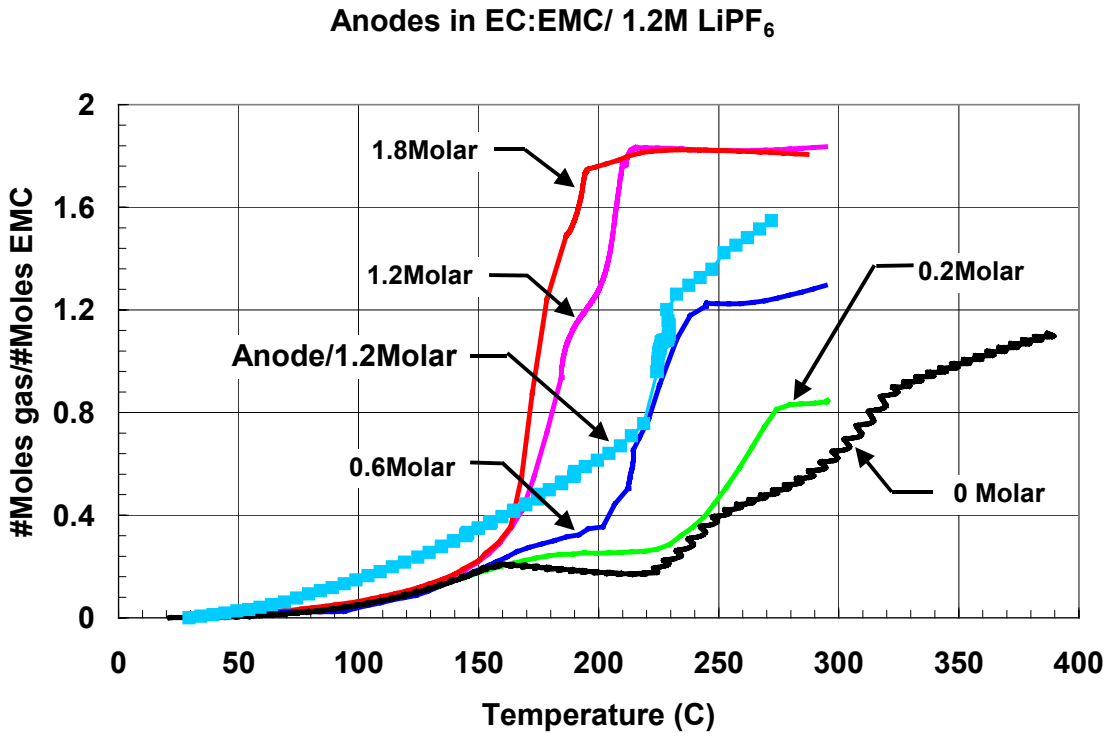

Figure 12. Anode material from GEN2 cell in 1.2M electrolyte compared with electrolytes of increasing molarity.

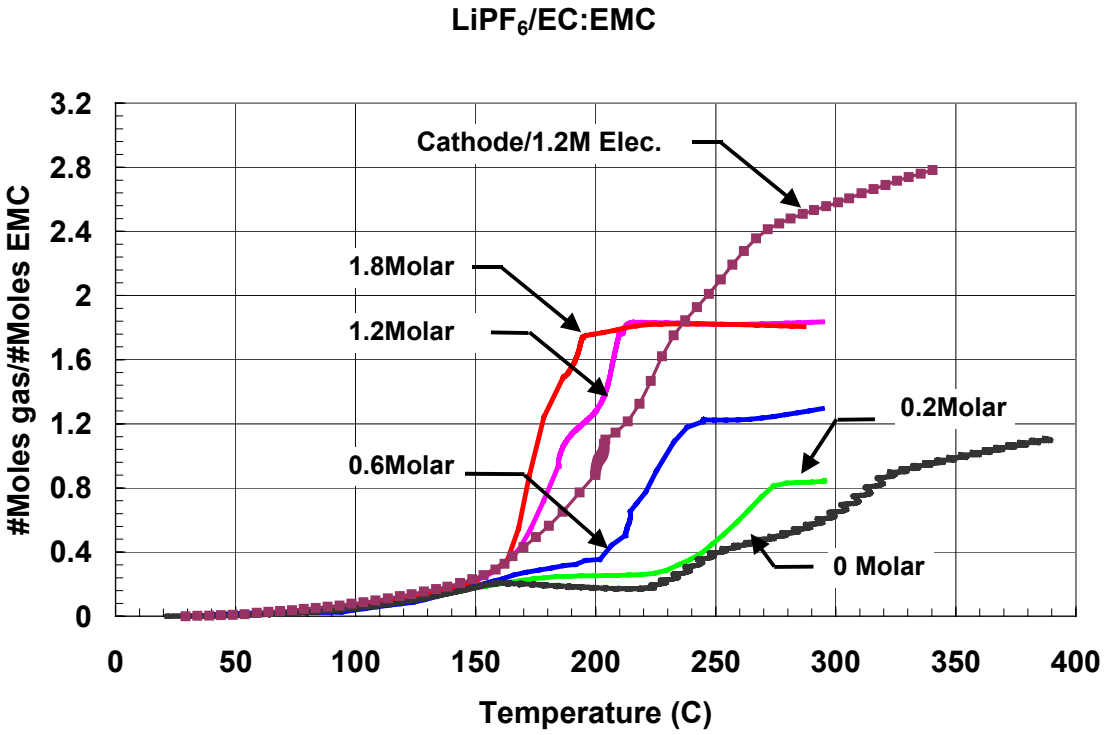

Figure 13. Cathode material from GEN2 cell in 1.2M electrolyte compared with electrolytes of increasing molarity.

Cell Flammability Study

A study was conducted to test the inherent flammability of vented cell gases and electrolyte under controlled conditions. Thermal block ramps were performed on GEN1 and GEN2 cells in air and in a newly developed inert gas (N_2) container in the presence of a spark source. Previously, we have shown that both GEN1 and GEN2 cell vent products can ignite if an ignition source is present. A new containment system has been developed, shown in Figure 14, which consists of a Lucite enclosure (3'x2'x2') through which N_2 gas flows. Spark ignition sources were present near the top of the cell fixture. The cell was placed in a heated copper block that was ramped from 3-4°C/min to the point of cell venting and thermal runaway. GEN1 cells vented around 160°C followed by thermal runaway near 200°C. Large quantities of smoke were observed venting at high rates from the cell. However, ***the generated gases did not ignite in the inert gas enclosure even in the presence of the spark ignition source***. Similar behavior was seen for the GEN2 cell which also went into thermal runaway around 200°C with large quantities of vented gas. Figure 15 shows the temperature and cell voltage profiles for this run.

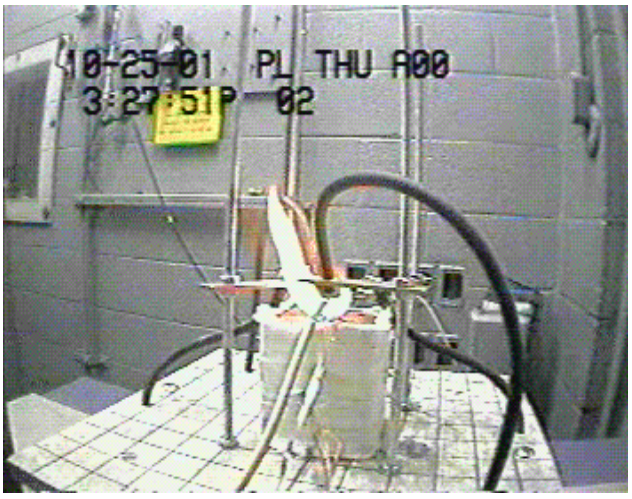

Figure 14. GEN2 cell spark ignition test in air.

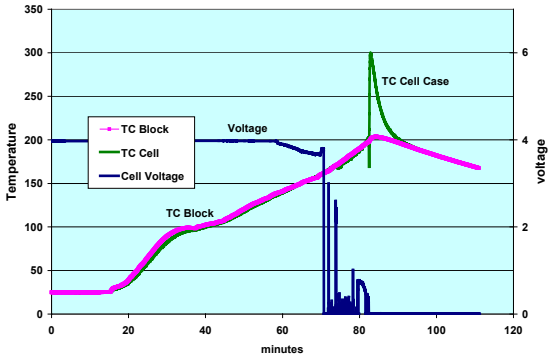

Figure 15. Temperature and cell voltage profile during thermal block ramp.

A separate run was performed using a GEN2 cell (80%SOC) in a steel bomb enclosure to allow grab sampling of the evolved gases and an estimation of the evolved gas volume. The bomb enclosure had been flooded with He prior to starting the thermal ramp. A total of six samples were taken during the ramp to 200°C and were taken at the temperatures indicated in Figure 16. An initial sample was taken around 130°C prior to any indication of major venting. Venting occurred around 150°C at which point two more gas samples were taken. Two more samples were taken around 170°C immediately prior to thermal runaway (200°C) and one sample was taken after thermal runaway. Figure 17 shows the evolved gas analysis taken by Gas Chromatography (GC). The vent gases measured below thermal runaway were primarily CO_2 and CO as seen for all of the previous cells measured. These gas volumes increased with increasing temperature. After thermal runaway and at cell temperatures above 250°C larger portions of CO_2 were generated along with new gas species of H_2 and O_2. The quantities of these gases apparently do not reach the explosive limit during the spark source runs. A rough value of one liter of evolved gas was obtained from pressure measurements.

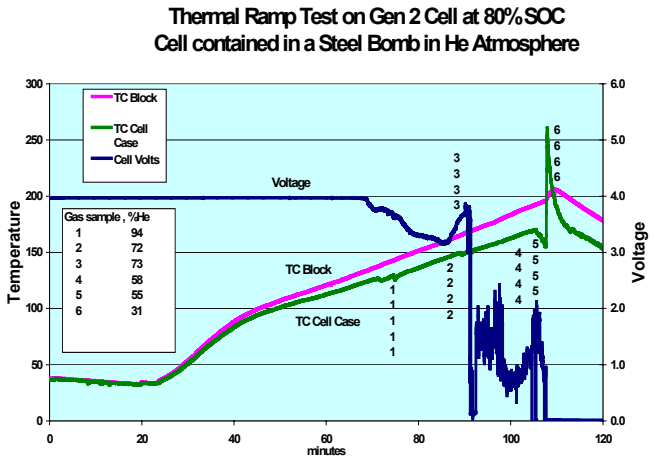

Figure 16. Temperature and voltage data for GEN2 cell in steel bomb.

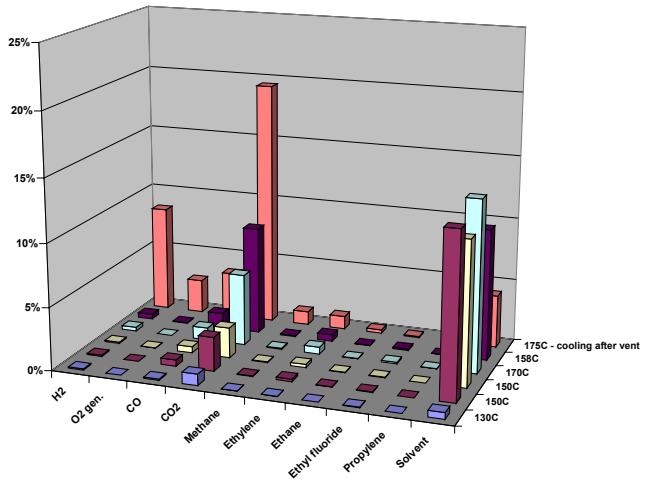

Figure 17. GC gas analysis of bomb grab samples.

Overcharge Study

Initial measurements have been performed on the overcharge thermal response of 18650 Li-ion cells using a new system designed to allow determination of cell heat generation as well as gas evolution. Initial measurements were performed on a GEN2 cell which had been removed from ALT testing after cycling at 45°C/100%SOC until 57% power fade. The cell was wrapped in a layer of insulating tape and placed in a brass thermal block. An access hole was drilled into the cell header which allowed insertion of a thermocouple directly into the cell mandrel hole and thus allowed monitoring of internal cell temperature during overcharge. The cell was resealed to prevent loss of electrolyte and generated gases. The thermal block containing the cell was instrumented with thermocouples and placed in an insulating can which was then placed in a pressure tight Lexan container. Figure 18 shows a sketch of the assembly and Figure 19 shows a photograph of the full system. The Lexan enclosure was purged with Helium and the temperature and pressure of the enclosure gas was monitored during the run. Initial calibrations were performed using an inserted heater in place of the cell to scale the temperature response of the system. These initial measurements were intended only as a scaling experiment and were not used to perform quantitative heat flow measurements. These results will be used to design the following system which will allow accurate measurement of heat flow during the cell overcharge profiles.

Figure 20 shows the cell voltage response during a series of stepped overcharges. Four charging profiles of currents from 1-5 amps were applied in one amp steps to achieve a total of 1 Ah overcharge. The temperature response for the four charging profiles is shown in Figure 21. The cell block temperature increased 15°C while the cell inner temperature increased by 25°C. The temperature difference will be calibrated in the future to allow accurate measurement of the total cell heat generation.

Overcharging continued at a 1 amp rate until an additional amp hour of capacity had been added, achieving a 100% overcharge level, during which time the cell vented at about 90°C. Overcharging then continued at a 2 amp rate until the cell underwent an explosive reaction. Figure 22 shows that above 200% overcharge the cell underwent an explosive reaction resulting in a cell temperature over 500°C. The onset temperature of this explosive reaction was about 190°C, the temperature at which we have previously seen strong thermal reactions of the cell components leading to cell disassembly. Thus, ***the initial overcharge response of the cell is very similar to that of a thermally ramped cell at 100%SOC or lower***. Future experiments will investigate the heat evolution at high states of overcharge while maintaining the cell at lower temperatures to determine if an electrochemical decomposition reaction may occur at some higher SOC.

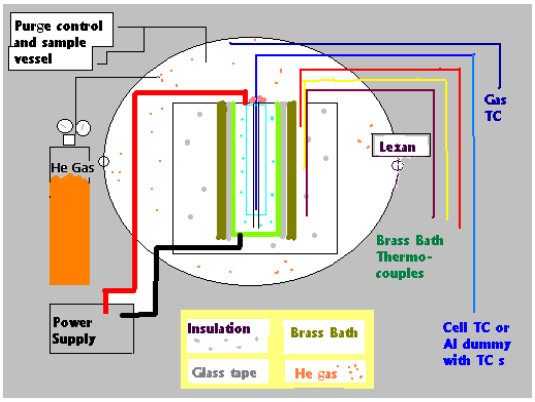

Figure 18. Sketch of cell overcharge test assembly.

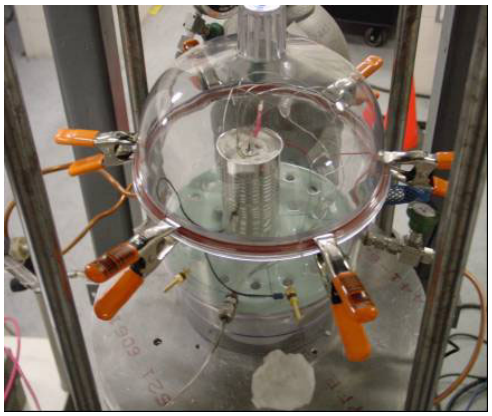

Figure 19. Photograph of Lexan enclosure with cell assembly.

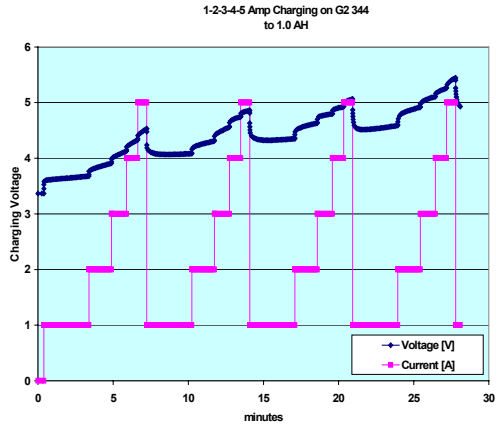

Figure 20. Charging voltage profiles during four overcharging steps.

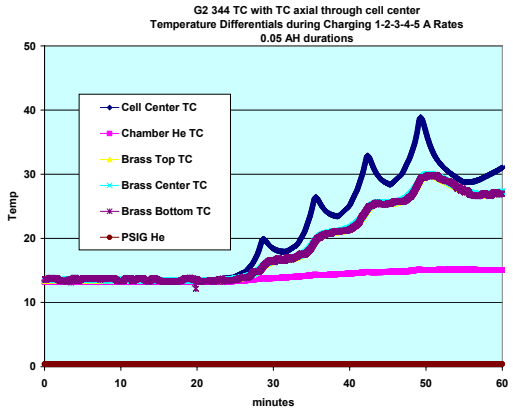

Figure 21. Temperature profile during the four overcharge steps.

Figure 22. Explosive cell reaction above 200%

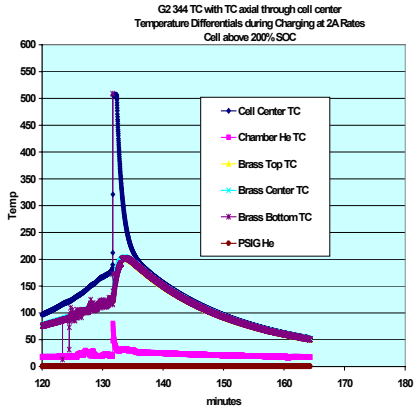

overcharge level.

Thermal Runaway Overview

Three temperature regimes during thermal runaway:

Stage 1: Onset of Thermal Runaway
Room Temperature to 125°C

- Exotherms begin at anode due to SEI decomposition
- Low level heat output starting at 50°C
- Highly influenced by morphology of anode carbon particles
- SEI decomposition leads to exothermic reduction of electrolyte
  at exposed lithiated carbon surface
- Gas generation slowly increasing (primarily from EMC)

Stage 2: Venting and Accelerated Heating (smoke)
125°C - 180°C

- Gas generation increase at 125°C
- Cathode contributes to early gas generation
- CO_2 main decomposition gas followed by CO, C_2H_4, H_2
- Increase in heating rate above 150°C:
- Both anode and cathode participate
- Complex reactions
- Electrolyte amount is critical and determines full cell response
- EMC/$LiPF_6$ source of main gas generation
- EC/$LiPF_6$ reaction source of heat generation

Stage 3: Explosive Decomposition (flame) 180°C and Above

- In full cell, rapid increase in heat and gas generation rate with explosive decomposition around 200°C
- Confluence of reactions over narrow temperature range
- High-rate reactions from cathode in 150°C -200°C range with peak in heating rate at 180°C
- High-rate reactions from anode in 200°C - 225°C range with peak in heating rate at 225°C
- Peak in electrolyte decomposition rate in 180°C -200°C range
- Sudden increase in gas evolution from anode above 200°C in addition to continued gas evolution from cathode
- Gases serve as propellant to eject any remaining electrolyte
- Ignition by external source in the presence of air
- Vent gases are non-flammable in inert atmosphere

Future Studies

The thermal abuse program in the future will build on the detailed knowledge that we have obtained from our extensive characterization of the ATD GEN1 and GEN2 cell chemistries. We will conduct focused studies of the effects of improved anode and cathode active materials on the critical regions of heat and gas generation that we have identified from our studies. In particular we will look at new anode materials that should develop more stable SEI layers that will increase the stability temperature for the onset of Stage1 thermal runaway. We will characterize cathode materials with higher stability temperatures that should minimize gas generation and increase the temperature for the onset of Stage 2 thermal runaway. New electrolyte salts will be investigated that will develop stable anode SEI layers but with reduced exothermic decomposition reactions. All new materials will be characterized with the goal of identifying material combinations that will increase the temperature of the explosive Stage 3 decomposition reactions.

The role of additives on thermal mitigation of decomposition reactions will be investigated using special 100 mAh cells built by Quallion using materials specified by Argonne National Lab. We will compare the thermal response of the cells with our baseline data and use diagnostic techniques developed during the ATD program to identify the reaction mechanisms that have been affected by the new additives. In particular, the gas species generated in these test cells will be quantitatively measured and used to help identify the reaction mechanisms. The effect of flame retardant additives will also be investigated using test cells in our thermal ramp test fixture with spark ignition sources.

The study of cell response during overcharge conditions will continue to be studied this year. Cell thermal output will be quantitatively measured during overcharge to determine the regime responsible for the onset of explosive decomposition. We will study the effects of overcharge using high and low charge rates to separate the effects due to high temperature thermal reactions from electrochemical decomposition reactions.

Gas analysis techniques will be used that have been developed to measure “real time” gas species from venting cells during thermal ramp or overcharge conditions. Multiple measurement techniques are used to identify the wide range of gas species. These techniques include Gas Chromatography (GC), Mass Spectrometry (MS), and Fourier Transform Infrared (FTIR) spectrometry. These techniques allow determination of gases from the range of small inorganic species up to large organic molecules.

Collaborative efforts will be expanded to include the diagnostic laboratories and the testing/development laboratories to build a Thermal Abuse Study team that will more precisely identify the critical reaction mechanisms responsible for poor thermal abuse tolerance. This collaboration will direct the development and identification of new materials leading to Li-ion cells which not only meet the requirements of performance and lifetime but also meet the requirements for safety and use in the FreedomCar program.

Acknowledgements

This study has been made possible by the efforts of many individuals including: Bob Patton and Carla Tatum for DSC measurements, and Paul Carpenter and Dave Johnson for ARC measurements.

We acknowledge the support of DOE Office of Advanced Automotive Technology through the FreedomCar Advanced Technology Development (ATD) High Power Battery Development Program. Sandia National Laboratories is a multiprogram laboratory operated by Sandia Corporation, a Lockheed Martin Company, for the United States Department of Energy under contract DE-AC04-94AL8500

III.C.2. Additives to Mitigate Thermal Events

Khalil Amine, Yoo-Eup Hyung, Don Vissers and Gary Henriksen
Argonne National Laboratory, Argonne, IL 60439
(630) 252-3838; fax: (630) 252-4176; e-mail: amine@cmt.anl.gov

Jai Prakash
Illinois Institute of Technology, Chicago, IL 60616
(312) 567-3639; fax (312) 567-8874; email: prakash@charlie.cns.iit.edu

---

Objectives

- Develop a mechanistic understanding of the thermal abuse characteristics of our Gen 2 baseline cell components
- Quantify mechanistic changes associated with the use of different electrolyte additives, different electrolyte salts and solvents, different types of graphite anode material, different electrode binder materials, and flame retardant additives
- Overall goal is to understand the factors that control thermal abuse in our high-power Gen 2 baseline cells and to recommend changes to the cell chemistry that will significantly enhance the inherent safety of high-power lithium-ion cells

Approach

- Utilize differential scanning calorimetery (DSC) to thoroughly characterize the thermal behavior of our Gen 2 baseline cell components

  - Determine the activation energy for each exothermic and endothermic reaction that occurs at the delithiated Gen 2 positive electrode and the lithiated Gen 2 negative electrode in the presence of Gen 2 electrolyte during a controlled thermal ramp

  - Determine the enthalpy for each exothermic and endothermic reaction that occurs at the delithiated Gen 2 positive electrode and the lithiated Gen 2 negative electrode in the presence of Gen 2 electrolyte during a controlled thermal ramp

- Utilize DSC to quantify changes in the thermal characteristics (onset and/or peak temperature, activation energy, and enthalpy of each reaction) at the delithiated positive electrode and lithiated negative electrode via the use of electrolyte additives, alternative electrolyte salts and solvents, a more optimal round-edge graphite anode material, different electrode binder materials, and flame retardant additives

- Fabricate sealed prismatic cells with modified cell chemistries to obtain preliminary validation of enhanced thermal abuse tolerance via ARC tests (at ANL and SNL).

- Fabricate sealed high-power 18650 cells with the most optimal cell chemistries for more thorough validation and quantification of enhanced thermal abuse tolerance via ARC tests at SNL

Accomplishments

- Completed thorough characterization of the thermal behavior of the Gen 2 baseline anodes and cathodes with the Gen 2 electrolyte, using DSC, and confirmed general agreement of our results with those of SNL. Our results include the onset temperatures, activation energies and enthalpies of the reactions that occur during a thermal ramp in the presence of the Gen 2 electrolyte.

- Quantified the changes in the onset temperatures, activation energies and enthalpies of these reactions when electrolyte additives (VEC and TPP) are added to the Gen 2 cell chemistry.

- Quantified the changes in the thermal properties of the anode when the graphite is switched from the MAG-10 flake graphite to the GDR round-edge carbon-coated graphite. Results were obtained using the Gen 2 electrolyte, with and without the VEC additive.

- Demonstrated preliminary validation of the thermal mitigation benefits associated with the use of the VEC electrolyte additive and the GDR graphite, via ARC tests on small sealed prismatic cells

Future Studies:

- Continue detailed DSC & ARC studies to quantify thermal mitigation benefits associated with:

  - Other electrolyte additives

  - Alternative electrolyte salts (relative to $LiPF_6$)

  - Soft rubber binders and other PVDF binders

  - Different flame retardant additives

Introduction

One of the key barriers to the use of high-power lithium-ion batteries for the hybrid electric vehicle application is its lack of inherent abuse tolerance. This application requires scaling-up the lithium-ion cell, lowering the internal impedance for improved high-power performance, and improving the cell's thermal stability to reduce safety risks. The two former items tend to heighten the severity of the cell component reactivity. With respect to thermal safety, it has been well documented in the literature that the exothermic reactions of electrodes with the electrolyte can cause the Li-ion cells to undergo thermal runaway at relatively low temperatures, especially at increasing states of charge. Use of calorimetric methods such as differential scanning calorimetry (DSC) and accelerated rate calorimetry (ARC) can provide valuable information regarding the thermal behavior of Li-ion cells**.** The ARC provides the thermal behavior and thermal runaway conditions of the full cell under adiabatic conditions at various states of charge. The adiabatic condition created in the ARC is similar to a thermal reaction occurring in the cell in which no heat is lost. This creates the thermal runaway situation. DSC, on the other hand, is a powerful method to investigate thermal behavior of the individual electrodes in presence of electrolyte and under various states of charge. Different peaks observed in the DSC scan can be associated with the decomposition of the solid electrolyte interface (SEI) layer, reactions among electrode components, and between these electrode components and the electrolyte. This is a complimentary technique to the ARC with its small sample size (~ 1 mg) and relatively short experimental time (~ 1 hour) and is a convenient means of evaluating the reactivity of anode and cathode active materials with the electrode binders and with the electrolyte salt and/or solvents.

There are three properties to quantify the degree of reactivity: heat, rate, and decomposition temperature. The derivative DSC trace provides information on the enthalpy, activation energy, and temperature of the decomposition reactions of the cell components. This temperature defines the upper temperature limit for the safe operation of the cell. Some information can be extracted by running the ARC with cell components, i.e. anode, cathode, electrolyte, and binder, but its sensitivity is less. The ARC measures only the onset of the thermal runaway reaction, while the DSC provides information on multiple reactions that can elucidate the sources of the cell's reactivity. By running experiments at different heating rates, the activation energy for each of these reactions can be determined, while by the ARC, only the overall activation energy can be determined. The activation energies and enthalpies are extracted from DSC traces for the specific exothermic reactions occurring at various temperatures for the lithiated anode and delithiated cathode materials in the presence of electrolytes that consist of lithium salts and organic carbonate solvent blends. These findings provide insight into which components of the lithium-ion cell are most responsible for the thermal runaway condition. Both of these techniques were used to thoroughly study the reactions that occur between our Gen 2 baseline electrolyte and our lithiated anode materials and delithiated cathode materials. We then studied changes in these reactions associated with modifications to our Gen 2 baseline cell chemisty.

A Perkin-Elmer DSC 7 differential scanning calorimeter was used in these studies. The Gen 2 baseline electrodes were assembled into 2032 coin cells, using metallic lithium counter electrodes to more accurately control the levels of lithiation and delithiation for the anode and cathode, respectively. The cells were formed and cycled several times using Arbin cycle testers. Prior to disassembly, the cells were charged to 4.3 volts. The charged cells were opened in a glove box under argon atmosphere and the charged electrode materials were harvested and sealed in stainless steel capsules with a gold coated copper seal and a threaded top. This high pressure capsule, filled with the electrode material and electrolyte, was heated from 25^{o}C to 400^{o}C. DSC runs are performed at several heating rates over the range of 0.5^{o}C/min. to 50^{o}C/min to calculate the activation energy, which is defined as:

$$\ln\frac{a}{T_m^2} = \ln\frac{AR}{E_a} - \frac{E_a}{T_m}$$

Where a = heating rate, T_m = Peak temperature, A = Frequency factor, E_a = Activation energy, and R = gas constant. An increase in the activation energy decreases the rate of reaction. The $-E_a/R$ term was extracted from the above equation by taking the slope of the Arrhenius plot of the ln (a/T_m^2) versus the reciprocal absolute DSC peak temperature. The enthalpy of each reaction was also obtained by integrating the area under each peak of interest in the DSC trace.

Effect of Additives on Thermal Behavior of Gen 2 Anode

Figure 1 shows DSC traces for the charged Gen 2 anode/electrolyte at three heating rates. Multiple peaks are visible in Fig. 1. The increase in the heating rate was found to shift the peaks to higher temperatures. In addition, the heat rate associated with these peaks was observed to increase with the increasing heating rate. An increase in the heating rate creates a larger thermal gradient relative to the sample pan and therefore a larger signal, and a delay of the onset temperature for the decomposition reactions. A small peak at about 100-130°C (Peak A) has been attributed to the rearrangement and decomposition of the SEI film formed on Gen 2 anode, followed by multiple peaks (B, C, and D), due to the charged anode reacting with electrolyte. The sharp peak at 300-350°C has been tentatively assigned to the reaction between the charged anode and binder. More experiments are needed for the quantitative assignment of these peaks.

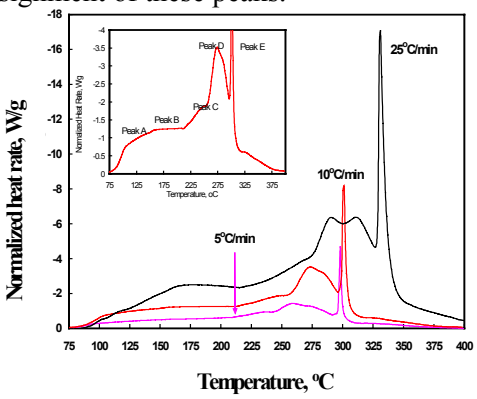

Fig. 1. DSC behavior of Gen 2 anode at different scan rates.

The DSC's sensitivity indicates that the initial reaction, corresponding to peak A, is related to the breakdown of the SEI layer and the heat from this reaction can raise the temperature and initiate the more elevated temperature reactions that involve the electrolyte, the lithiated graphite and the binder. Heat generated after the decomposition of the SEI layer could catalyze further reactions within the cell chemistry. By using materials that have a higher activation energy associated with their decomposition, more energy will be required to activate their decomposition and the cell will be inherently safer. We have attempted to increase the activation energy of the SEI film by using additives such as VEC and TPP. These additives are expected to modify the SEI film and hence increase the activation energy associated with the SEI decomposition.

The DSC traces for a fully charged Gen 2 anode with 2-wt% VEC additive are shown in Fig. 2. It can be seen by comparing Figures 1 and 2 that addition of the VEC additive changes the peak height and the peak temperatures for various exothermic reactions. A plot showing only the SEI decomposition temperature range (provided in Figure 3) clearly shows that the addition of VEC significantly reduces the heat associated with the SEI decomposition.

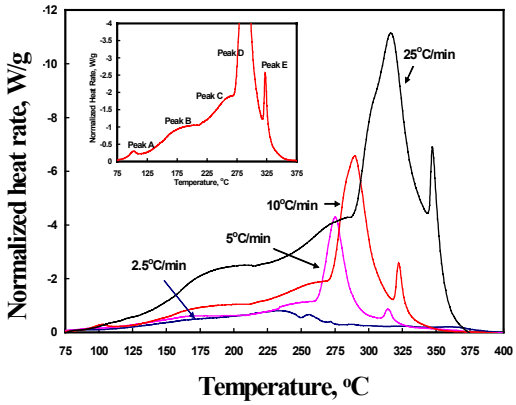

Fig. 2. Effect of 2-wt% VEC on the heat generation rate of the Gen 2 anode.

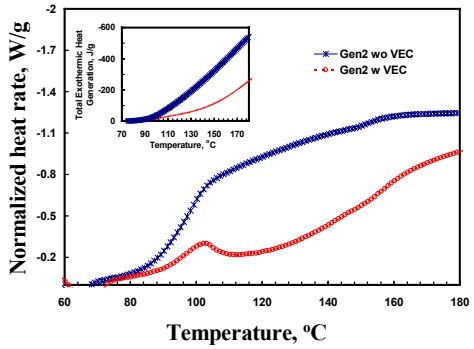

Fig. 3. Effect of 2-wt% VEC on the heat produced during SEI layer decomposition.

Figure 4 shows the typical Arrhenius plots of Gen 2 anode containing 2-wt% VEC. The slope of the line is the activation energy divided by the gas constant. The activation energies for various exothermic peaks are also provided in Figure 4.

The peak attributed to the SEI layer decomposition (peak A) has a low peak temperature and low activation energy, both of which contribute to its increased reactivity. In addition to the activation energy, the enthalpy also needs to be considered because these exothermic reactions will provide heat for more material to decompose, leading to the thermal runaway condition.

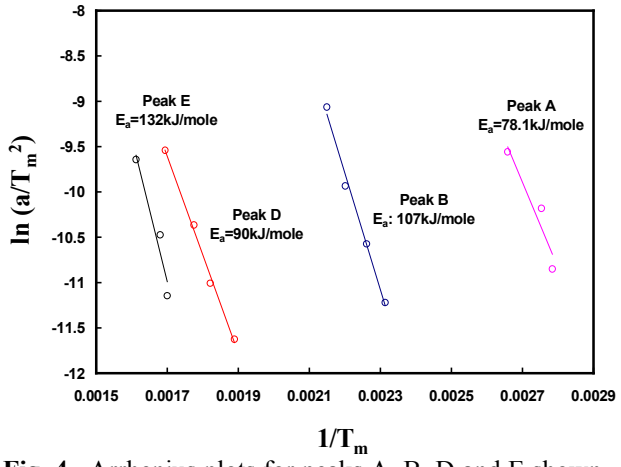

Fig. 4. Arrhenius plots for peaks A, B, D and E shown in Fig. 2.

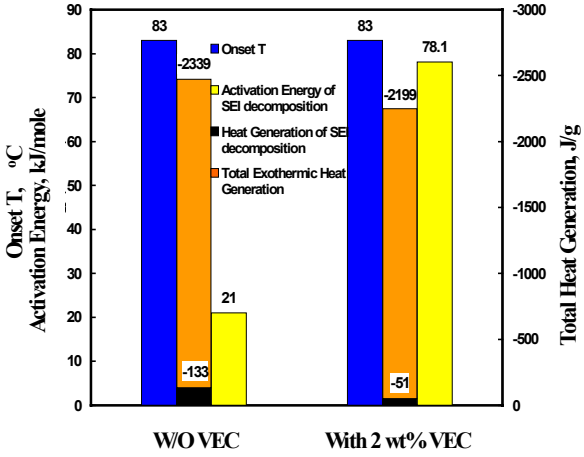

Fig. 5. Summary of the thermal parameters for the Gen 2 anode.

The activation energy, the enthalpy, and the other thermal parameters of the Gen 2 anode, with and without the VEC additive, are summarized in Figure 5. It can be seen that the addition of 2-wt% VEC increases the activation energy of the SEI decomposition reaction, reduces the heat generation associated with the SEI decomposition, and the total heat generation thereby significantly improving the inherent thermal safety of the cell chemistry.

ARC studies carried out on Gen 2 anodes containing VEC and/or TPP additives (provided in Figure 6) show that with all additives, the overall activation energy of the reaction increases. One needs to keep in mind that unlike DSC, ARC provides only the overall activation energy.

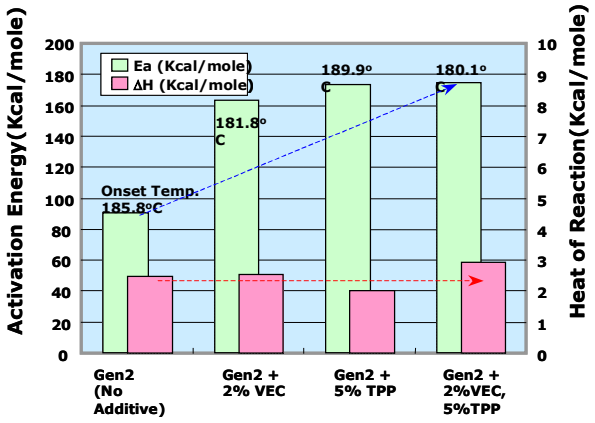

Fig. 6. Results of ARC studies carried out on Gen 2 anodes with and without electrolyte additives.

Effect of Additives on Thermal Behavior of Gen 2 Cathode

DSC traces for the 100% state-of-charge (SOC) Gen 2 cathode + electrolyte samples, at three different heating rates, are provided in Figure 7. It can be seen that the traces follow the same trend as the Gen 2 anode + electrolyte samples. Four peaks (A, B, C, and D) are clearly visible in the DSC traces of Figure 7. Increasing the heating rate again shifts the peaks to higher temperatures with a larger signal at the higher heating rates. Based on the onset temperatures and the enthalpy values for various peaks in Figure 6, and the onset temperatures for the exothermic reactions observed for the Gen 2 cell components (provided in Table 1), we have assigned following exothermic reactions to various peaks seen in Figure 7:

Peak A: Catalytic reaction of delithiated cathode and the electrolyte.
Peak B: Decomposition of the electrolyte and salt.
Peak C: Reaction of the PVDF, remaining cathode, oxygen, and electrolyte.
Peak D: Reaction of conductive carbon and oxygen.

Cell Component	Temp. (^{o}C)
Cathode + Electrolyte	180-200
EC	205-250
EMC	195-235
EC-EMC	205-250
$LiPF_6$/EC-EMC	240-300
PVDF	263, 313
PVDF/Electrolyte	263, 313
PVDF/Electrolyte/Cathode	313-360

Table 1. Gen 2 lithium-ion cell components and their DSC exotherm temperatures.

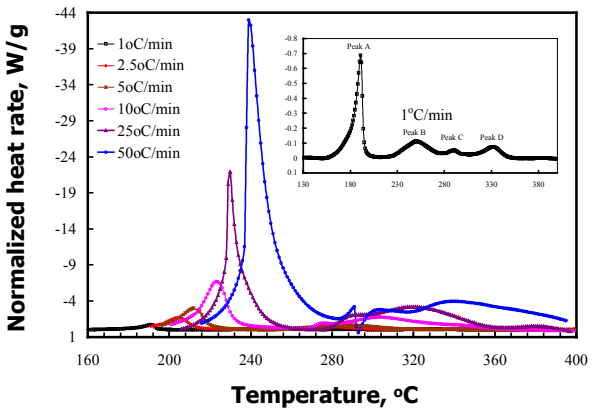

Fig. 7. DSC behavior of Gen 2 cathode at different scan rates.

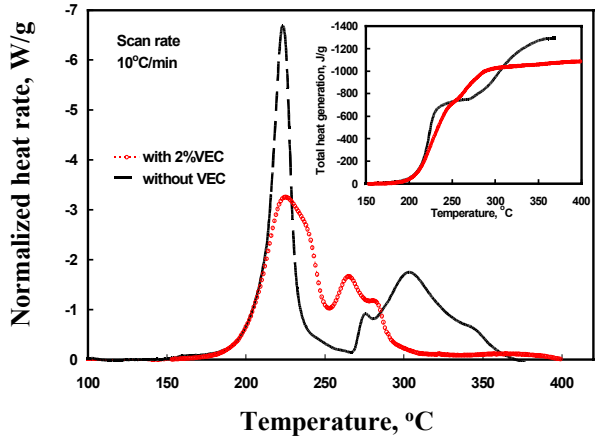

Fig. 8. Effect of 2-wt% VEC on the heat generation rate of the Gen 2 cathode.

From a structural point of view, under a fully charged condition, the Li single layers in the Gen 2 cathode material are suspected to disappear and the strong electronegative force caused by the electronegative oxygen layers irreversibly coverts the layered structure into a $CdCl_2$ type structure. Furthermore, the Co^{4+} and Ni^{4+} are thermally unstable and hence will react with the electrolyte thus producing peak A followed by peaks B, C, and D. The addition of the VEC additive, however, had a slight effect on the thermal behavior of the Gen 2 cathode as is shown in Figures 8 and 9. The VEC additive was observed to depress the first exothermic peak (180-250^{o}C) and reduce the overall exothermic heat generation by 16%. However, it did not change the activation

energy, nor the onset temperature for the major exothermic reaction.

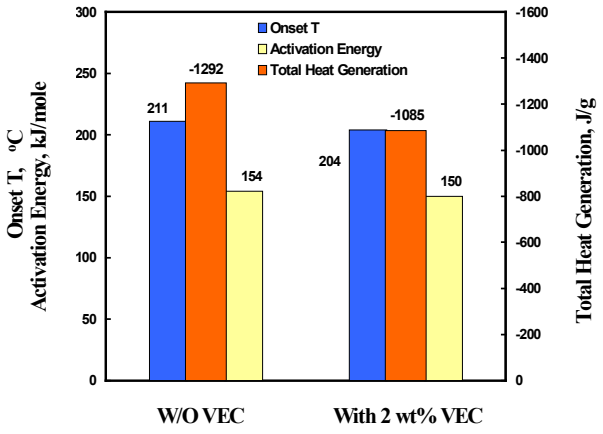

Fig. 9. Summary of the thermal parameters for the Gen 2 cathode.

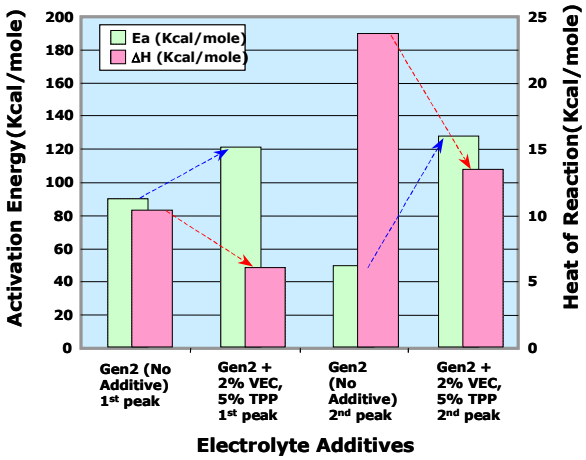

Fig. 10. Results of the ARC studies carried out on Gen 2 cathodes with and without electrolyte additives.

ARC studies carried out on the Gen 2 cathode with and without TPP and VEC additives (see Figure 10) show that these additives reduce the overall enthalpy of reaction and increase the activation energy of the Gen 2 cathode reactions. It was also found that these additives not only improve the thermal safety but may also reduce the cell pressure. For example, ARC studies (see Figure 11) clearly indicate that the addition of 2% VEC + 5% TPP additives significantly reduce the gassing from both Gen 2 positive and negative electrodes.

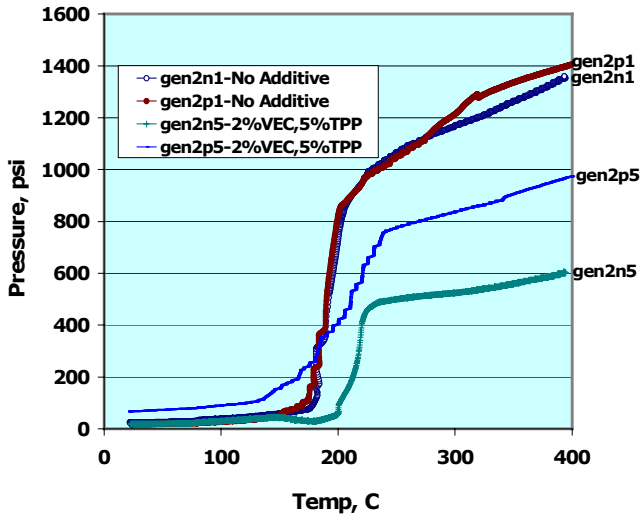

Fig. 11. Pressure generated in reactions between Gen 2 electrodes, at 100%SOC, and Gen 2 electrolyte, with and without additives.

Effect of using a Round-Edge Graphite on the Thermal Behavior of the Anode

Our Gen 2 anode used a MAG-10 flake type synthetic graphite, which was considerably less expensive than the MCMB-6 synthetic graphite that was used in our Gen 1 anode (~$15/kg vs. ~$50/kg). Since the flake type graphites are non-optimal from a safety perspective, we examined a new round-edge natural graphite material to establish the safety advantages of this material relative to our Gen 2 anode material. The material studied was a soft carbon-coated round-edge natural graphite from Mitsui Mining. ANL has been evaluating this material over the last two years and providing feedback and recommendations to Mitsui Mining in an effort to make a more optimal version of this material for high-power applications. The latest version of their material for high-power applications is their grade GDR-AA-3. It has an average particle size of ~16μm and a 6% by weight soft carbon coating. SEM photomicrographs of the GDR-AA-3 and MAG-10 (Gen 2) graphites are provided in Fig. 12, while Fig. 13 provides a comparison of the DSC behavior of fully charged anodes that employ the same weight percent of these two graphite materials.

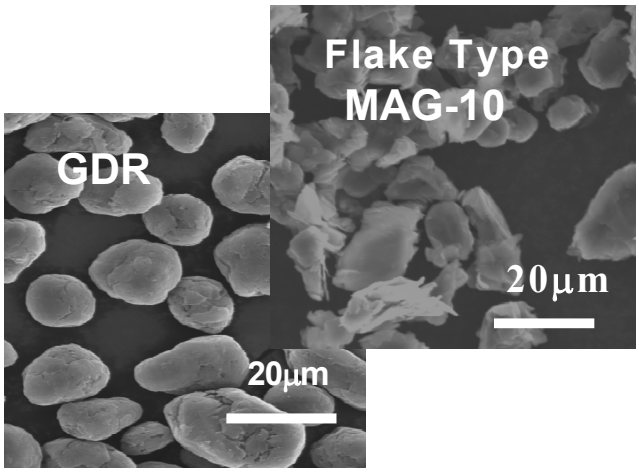

Fig. 12. SEM photomicrograph of GDR-AA-3 soft carbon-coated round-edge natural graphite.

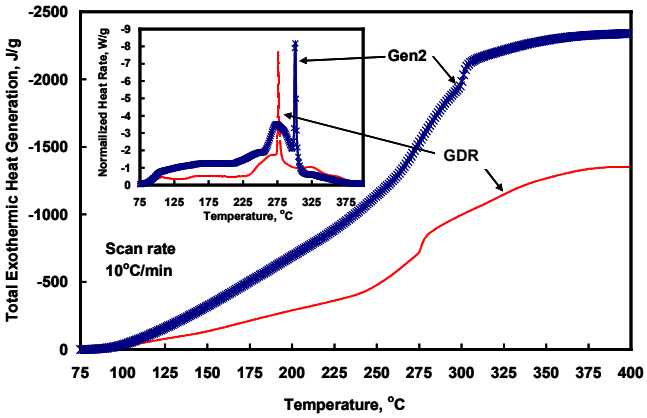

Fig. 13. Comparative thermal data on lithiated anodes made with MAG-10 flake graphite (Gen 2) and GDR soft carbon-coated round-edge graphite, via DSC studies.

It is apparent from the SEM photographs in Fig. 12, that the MAG-10 flake graphite has a lot of active edge sites on which the SEI layers seem to be relatively unstable. The round-edge GDR graphite is absent of these active edge sites and should exhibit better thermal characteristics. The DSC results, shown in Fig. 13, indicate that the GDR anode produces only 58% of the exothermic heat produced by the Gen 2 anode. Some of the improvements in the thermal properties of the anode, resulting from the use of GDR graphite, are summarized in Table 2.

Thermal Parameter	Gen 2	GDR
Onset T of SEI decomoposition (°C), based on 10°C/min	83	84
ΔH of SEI decomposition reaction (J/g)	-133	-85
E_a of SEI decomposition (kJ/mole)	21	72.7
Total heat generation (J/g)	-2339	-1350

Table 2. Effect of using round-edge GDR graphite on thermal properties of the anode.

Additional improvements in the thermal properties of the GDR anode are obtained when VEC is used as an electrolyte additive. The use of 2 wt% VEC with the GDR anode shifts the onset temperature of SEI decomposition from 84°C to 115°C and reduces the heat associated with the SEI decomposition, as shown in Fig. 14. Also, the activation energy for the SEI decomposition reaction is increased from 73 kJ/mole to 124 kJ/mole through the use of the VEC additive.

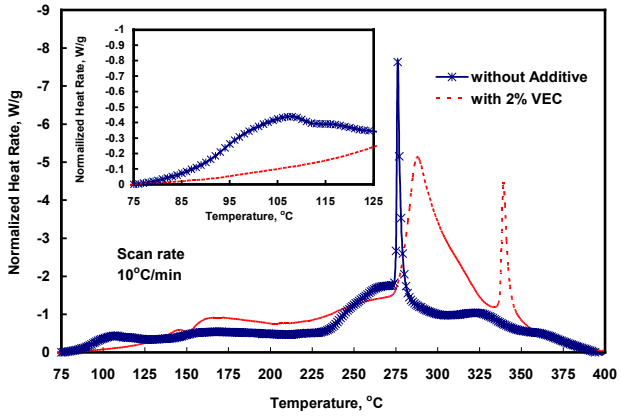

Fig. 14. Comparative thermal data on lithiated GDR anodes, with and without 2 wt% VEC additive in the electrolyte, via DSC studies.

Conclusions & Future Studies

The results reported here indicate the following major conclusions:

- Lithiated soft carbon-coated round-edge GDR graphite is thermally more benign than lithiated MAG-10 (Gen 2) flake graphite.

- The VEC electrolyte additive appears to effectively modify the SEI layer on both types of graphite and mitigates the thermally-induced reactivity of lithiated anodes.

- The VEC electrolyte additive appears to reduce the overall heat generation of our delithiated Gen 2 cathode.

Small sealed 100 mAh prismatic cells were built, with these and other modifications to the Gen 2 cell chemistry, to verify that improvements observed in our DSC studies transfer to improved thermal characteristics in sealed cells. Cells of this type were provide to SNL for use in ARC studies. ANL conducted a few preliminary ARC tests and some of the results are shown in Fig. 15. It can be seen from these preliminary studies that the soft carbon-coated round-edge graphite and VEC electrolyte additive are effective in suppressing thermal runaway in these small sealed cells.

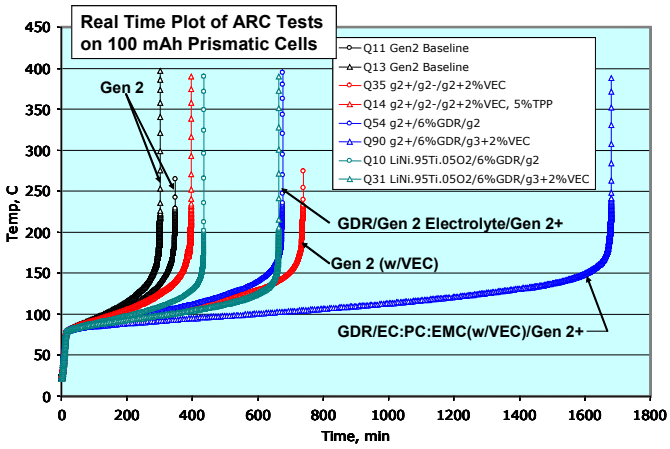

Fig. 15. Comparative ARC data showing the suppression of thermal runaway in small cells associated with the use of GDR graphite and VEC additive.

In the future, we plan to continue detailed DSC studies to establish and quantify the thermal mitigation benefits of other electrolyte additives. Also, the roles of other components of the Gen 2 cell chemistry are being elucidated in our studies and those of SNL. Therefore, we plan to establish and quantify the thermal benefits of alternative electrolyte salts (relative to $LiPF_6$) and alternative electrode binders (relative to the PVDF binders used in the Gen 2 electrodes). Additionally, we have been screening flame retardant additives, via flame propagation tests, to identify additives that are effective in suppressing the flammability of our organic carbonate electrolyte systems. We plan to conduct detailed DSC studies on the most promising of these flame retardant additives to establish and quantify the changes in thermal properties that result from the use of these additives.

III.D. Materials Evaluation And Cost Reduction

III.D.1. Novel Materials: Advanced Cathode Materials

Khalil Amine, Yoo-Eup Hyung, Don Vissers and Gary Henriksen
Argonne National Laboratory, Argonne, IL 60439
(630) 252-3838; fax: (630) 252-4176; e-mail: amine@cmt.anl.gov

Jai Prakash
Illinois Institute of Technology, Chicago, IL 60616
(312) 567-3639; fax (312) 567-8874; email: prakash@charlie.cns.iit.edu

---

Objectives

- Develop a mechanistic understanding of the thermal abuse characteristics of our Gen 2 baseline cell components.
- Quantify mechanistic changes associated with the use of different electrolyte additives, different electrolyte salts and solvents, different types of graphite anode material, different electrode binder materials, and flame retardant additives.
- Overall goal is to understand the factors that control thermal abuse in our high-power Gen 2 baseline cells and to recommend changes to the cell chemistry that will significantly enhance the inherent safety of high-power lithium-ion cells.

Approach

- Utilize differential scanning calorimetery (DSC) to thoroughly characterize the thermal behavior of our Gen 2 baseline cell components.
    - Determine the activation energy for each exothermic and endothermic reaction that occurs at the delithiated Gen 2 positive electrode and the lithiated Gen 2 negative electrode in the presence of Gen 2 electrolyte during a controlled thermal ramp.
    - Determine the enthalpy for each exothermic and endothermic reaction that occurs at the delithiated Gen 2 positive electrode and the lithiated Gen 2 negative electrode in the presence of Gen 2 electrolyte during a controlled thermal ramp.
- Utilize DSC to quantify changes in the thermal characteristics (onset and/or peak temperature, activation energy, and enthalpy of each reaction) at the delithiated positive electrode and lithiated negative electrode via the use of electrolyte additives, alternative electrolyte salts and solvents, a more optimal round-edge graphite anode material, different electrode binder materials, and flame retardant additives.
- Fabricate sealed prismatic cells with modified cell chemistries to obtain preliminary validation of enhanced thermal abuse tolerance via ARC tests (at ANL and SNL).
- Fabricate sealed high-power 18650 cells with the most optimal cell chemistries for more thorough validation and quantification of enhanced thermal abuse tolerance via ARC tests at SNL.

Accomplishments

- Completed thorough characterization of the thermal behavior of the Gen 2 baseline anodes and cathodes with the Gen 2 electrolyte, using DSC, and confirmed general agreement of our results with those of SNL. Our results include the onset temperatures, activation energies and enthalpies of the reactions that occur during a thermal ramp in the presence of the Gen 2 electrolyte.

- Quantified the changes in the onset temperatures, activation energies and enthalpies of these reactions when electrolyte additives (VEC and TPP) are added to the Gen 2 cell chemistry.

- Quantified the changes in the thermal properties of the anode when the graphite is switched from the MAG-10 flake graphite to the GDR round-edge carbon-coated graphite. Results were obtained using the Gen 2 electrolyte, with and without the VEC additive.

- Demonstrated preliminary validation of the thermal mitigation benefits associated with the use of the VEC electrolyte additive and the GDR graphite, via ARC tests on small sealed prismatic cells

Future Studies

- Continue detailed DSC & ARC studies to quantify thermal mitigation benefits associated with:
  - Other electrolyte additives
  - Alternative electrolyte salts (relative to $LiPF_6$)
  - Soft rubber binders and other PVDF binders
- Different flame retardant additives

Introduction

One of the key barriers to the use of high-power lithium-ion batteries for the hybrid electric vehicle application is its lack of inherent abuse tolerance. This application requires scaling-up the lithium-ion cell, lowering the internal impedance for improved high-power performance, and improving the cell's thermal stability to reduce safety risks. The two former items tend to heighten the severity of the cell component reactivity. With respect to thermal safety, it has been well documented in the literature that the exothermic reactions of electrodes with the electrolyte can cause the Li-ion cells to undergo thermal runaway at relatively low temperatures, especially at increasing states of charge. Use of calorimetric methods such as differential scanning calorimetry (DSC) and accelerated rate calorimetry (ARC) can provide valuable information regarding the thermal behavior of Li-ion cells**.** The ARC provides the thermal behavior and thermal runaway conditions of the full cell under adiabatic conditions at various states of charge. The adiabatic condition created in the ARC is similar to a thermal reaction occurring in the cell in which no heat is lost. This creates the thermal runaway situation. DSC, on the other hand, is a powerful method to investigate thermal behavior of the individual electrodes in presence of electrolyte and under various states of charge. Different peaks observed in the DSC scan can be associated with the decomposition of the solid electrolyte interface (SEI) layer, reactions among electrode components, and between these electrode components and the electrolyte. This is a complimentary technique to the ARC with its small sample size (~ 1 mg) and relatively short experimental time (~ 1 hour) and is a convenient means of evaluating the reactivity of anode and cathode active materials with the electrode binders and with the electrolyte salt and/or solvents.

There are three properties to quantify the degree of reactivity: heat, rate, and decomposition temperature. The derivative DSC trace provides information on the enthalpy, activation energy, and temperature of

the decomposition reactions of the cell components. This temperature defines the upper temperature limit for the safe operation of the cell. Some information can be extracted by running the ARC with cell components, i.e. anode, cathode, electrolyte, and binder, but its sensitivity is less. The ARC measures only the onset of the thermal runaway reaction, while the DSC provides information on multiple reactions that can elucidate the sources of the cell's reactivity. By running experiments at different heating rates, the activation energy for each of these reactions can be determined, while by the ARC, only the overall activation energy can be determined. The activation energies and enthalpies are extracted from DSC traces for the specific exothermic reactions occurring at various temperatures for the lithiated anode and delithiated cathode materials in the presence of electrolytes that consist of lithium salts and organic carbonate solvent blends. These findings provide insight into which components of the lithium-ion cell are most responsible for the thermal runaway condition. Both of these techniques were used to thoroughly study the reactions that occur between our Gen 2 baseline electrolyte and our lithiated anode materials and delithiated cathode materials. We then studied changes in these reactions associated with modifications to our Gen 2 baseline cell chemisty.

A Perkin-Elmer DSC 7 differential scanning calorimeter was used in these studies. The Gen 2 baseline electrodes were assembled into 2032 coin cells, using metallic lithium counter electrodes to more accurately control the levels of lithiation and delithiation for the anode and cathode, respectively. The cells were formed and cycled several times using Arbin cycle testers. Prior to disassembly, the cells were charged to 4.3 volts. The charged cells were opened in a glove box under argon atmosphere and the charged electrode materials were harvested and sealed in stainless steel capsules with a gold coated copper seal and a threaded top. This high pressure capsule, filled with the electrode material and electrolyte, was heated from 25°C to 400°C. DSC runs are performed at several heating rates over the range of 0.5°C/min. to 50°C/min to calculate the activation energy, which is defined as:

$$\ln\frac{a}{T_m^2} = \ln\frac{AR}{E_a} - \frac{E_a}{T_m}$$

Where a = heating rate, T_m = Peak temperature, A = Frequency factor, E_a = Activation energy, and R = gas constant. An increase in the activation energy decreases the rate of reaction. The $-E_a/R$ term was extracted from the above equation by taking the slope of the Arrhenius plot of the ln (a/T_m^2) versus the reciprocal absolute DSC peak temperature. The enthalpy of each reaction was also obtained by integrating the area under each peak of interest in the DSC trace.

Effect of Additives on Thermal Behavior of Gen 2 Anode

Figure 1 shows DSC traces for the charged Gen 2 anode/electrolyte at three heating rates. Multiple peaks are visible in Fig. 1. The increase in the heating rate was found to shift the peaks to higher temperatures. In addition, the heat rate associated with these peaks was observed to increase with the increasing heating rate. An increase in the heating rate creates a larger thermal gradient relative to the sample pan and therefore a larger signal, and a delay of the onset temperature for the decomposition reactions. A small peak at about 100-130°C (Peak A) has been attributed to the rearrangement and decomposition of the SEI film formed on Gen 2 anode, followed by multiple peaks (B, C, and D), due to the charged anode reacting with electrolyte. The sharp peak at 300-350°C has been tentatively assigned to the reaction between the charged anode and binder. More experiments are needed for the quantitative assignment of these peaks.

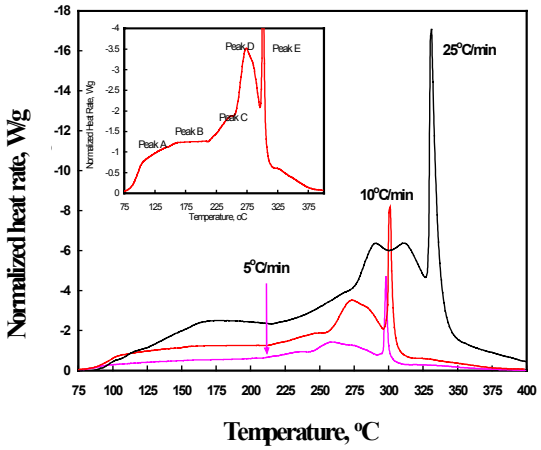

Fig. 1. DSC behavior of Gen 2 anode at different scan rates

The DSC's sensitivity indicates that the initial reaction, corresponding to peak A, is related to the breakdown of the SEI layer and the heat from this reaction can raise the temperature and initiate the more elevated temperature reactions that involve the electrolyte, the lithiated graphite and the binder. Heat generated after the decomposition of the SEI layer could catalyze further reactions within the cell chemistry. By using materials that have a higher activation energy associated with their decomposition, more energy will be required to activate their decomposition and the cell will be inherently safer. We have attempted to increase the activation energy of the SEI film by using additives such as VEC and TPP. These additives are expected to modify the SEI film and hence increase the activation energy associated with the SEI decomposition.

The DSC traces for a fully charged Gen 2 anode with 2-wt% VEC additive are shown in Fig. 2. It can be seen by comparing Figures 1 and 2 that addition of the VEC additive changes the peak height and the peak temperatures for various exothermic reactions. A plot showing only the SEI decomposition temperature range (provided in Figure 3) clearly shows that the addition of VEC significantly reduces the heat associated with the SEI decomposition.

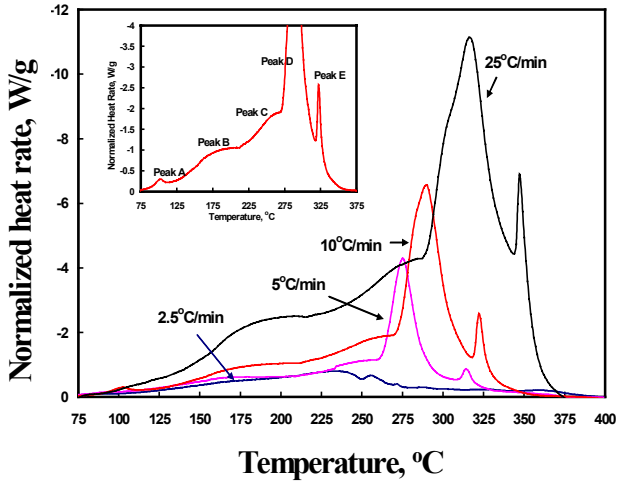

Fig. 2. Effect of 2-wt% VEC on the heat generation rate of the Gen 2 anode.

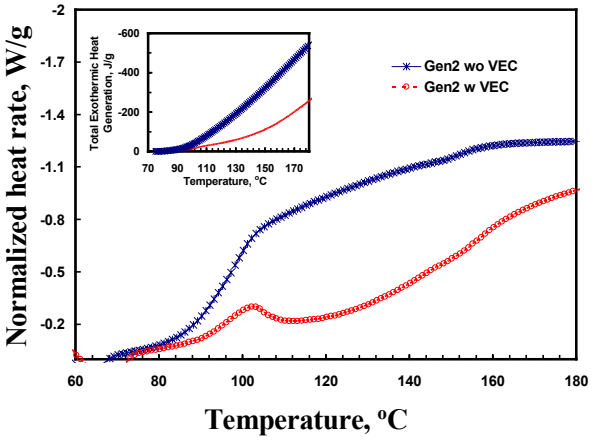

Fig. 3. Effect of 2-wt% VEC on the heat produced during SEI layer decomposition.

Figure 4 shows the typical Arrhenius plots of Gen 2 anode containing 2-wt% VEC. The slope of the line is the activation energy divided by the gas constant. The activation energies for various exothermic peaks are also provided in Figure 4.

The peak attributed to the SEI layer decomposition (peak A) has a low peak temperature and low activation energy, both of which contribute to its increased reactivity. In addition to the activation energy, the enthalpy also needs to be considered because these exothermic reactions will provide heat for more material to decompose, leading to the thermal runaway condition.

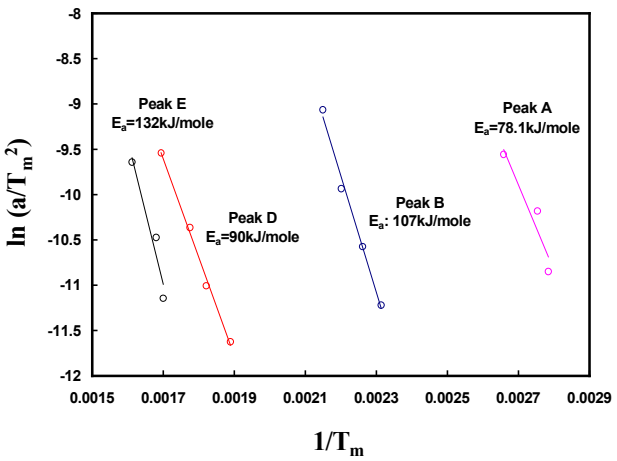

Fig. 4. Arrhenius plots for peaks A, B, D and E shown in Fig. 2.

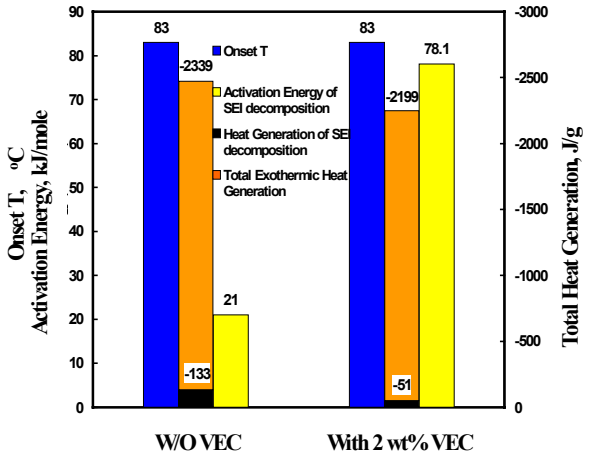

Fig. 5. Summary of the thermal parameters for the Gen 2 anode.

The activation energy, the enthalpy, and the other thermal parameters of the Gen 2 anode, with and without the VEC additive, are summarized in Figure 5. It can be seen that the addition of 2-wt% VEC increases the activation energy of the SEI decomposition reaction, reduces the heat generation associated with the SEI decomposition, and the total heat generation thereby significantly improving the inherent thermal safety of the cell chemistry.

ARC studies carried out on Gen 2 anodes containing VEC and/or TPP additives (provided in Figure 6) show that with all additives, the overall activation energy of the reaction increases. One needs to keep in mind that unlike DSC, ARC provides only the overall activation energy.

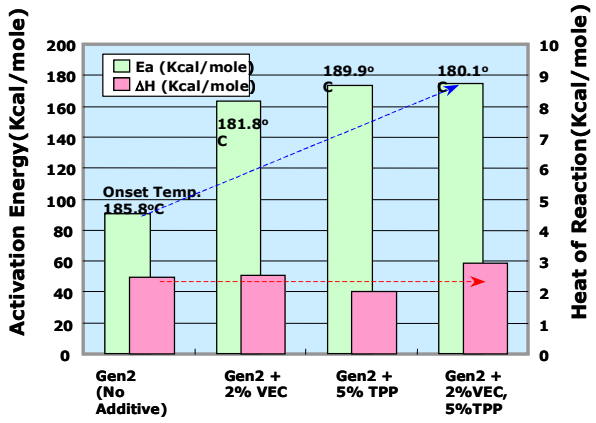

Fig. 6. Results of ARC studies carried out on Gen 2 anodes with and without electrolyte additives.

Effect of Additives on Thermal Behavior of Gen 2 Cathode

DSC traces for the 100% state-of-charge (SOC) Gen 2 cathode + electrolyte samples, at three different heating rates, are provided in Figure 7. It can be seen that the traces follow the same trend as the Gen 2 anode + electrolyte samples. Four peaks (A, B, C, and D) are clearly visible in the DSC traces of Figure 7. Increasing the heating rate again shifts the peaks to higher temperatures with a larger signal at the higher heating rates. Based on the onset temperatures and the enthalpy values for various peaks in Figure 6, and the onset temperatures for the exothermic reactions observed for the Gen 2 cell components (provided in Table 1), we have assigned following exothermic reactions to various peaks seen in Figure 7:

Peak A: Catalytic reaction of delithiated cathode and the electrolyte.
Peak B: Decomposition of the electrolyte and salt.
Peak C: Reaction of the PVDF, remaining cathode, oxygen, and electrolyte.
Peak D: Reaction of conductive carbon and oxygen.

Cell Component	Temp. (°C)
Cathode + Electrolyte	180-200
EC	205-250
EMC	195-235
EC-EMC	205-250
$LiPF_6$/EC-EMC	240-300
PVDF	263, 313
PVDF/Electrolyte	263, 313
PVDF/Electrolyte/Cathode	313-360

Table 1. Gen 2 lithium-ion cell components and their DSC exotherm temperatures.

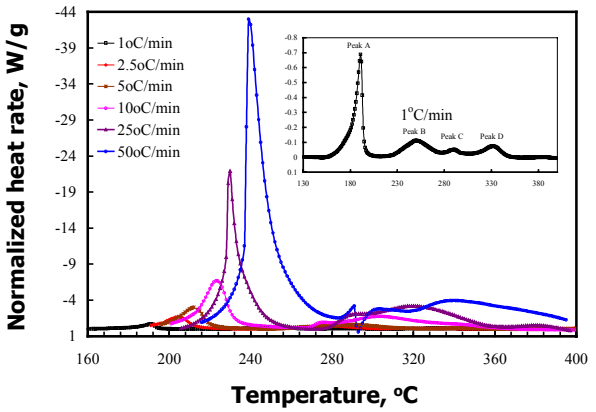

Fig. 7. DSC behavior of Gen 2 cathode at different scan rates.

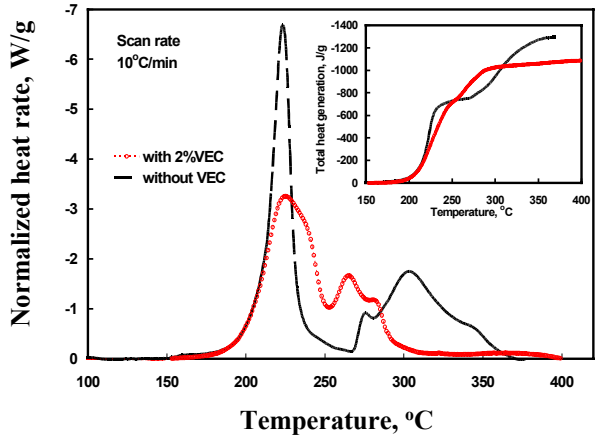

Fig. 8. Effect of 2-wt% VEC on the heat generation rate of the Gen 2 cathode.

From a structural point of view, under a fully charged condition, the Li single layers in the Gen 2 cathode material are suspected to disappear and the strong electronegative force caused by the electronegative oxygen layers irreversibly coverts the layered structure into a $CdCl_2$ type structure. Furthermore, the Co^{4+} and Ni^{4+} are thermally unstable and hence will react with the electrolyte thus producing peak A followed by peaks B, C, and D. The addition of the VEC additive, however, had a slight effect on the thermal behavior of the Gen 2 cathode as is shown in Figures 8 and 9. The VEC additive was observed to depress the first exothermic peak (180-250°C) and reduce the overall exothermic heat generation by 16%. However, it did not change the activation energy, nor the onset temperature for the major exothermic reaction.

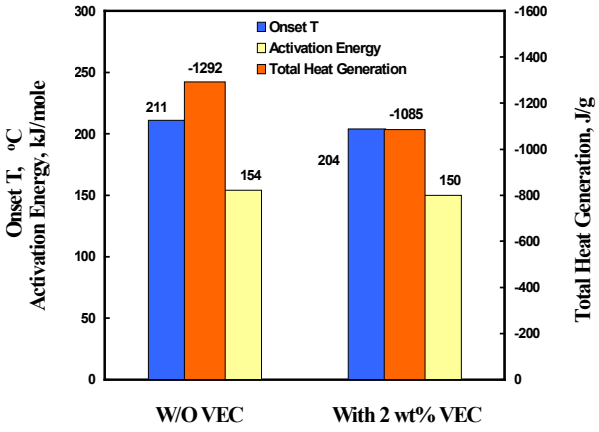

Fig. 9. Summary of the thermal parameters for the Gen 2 cathode.

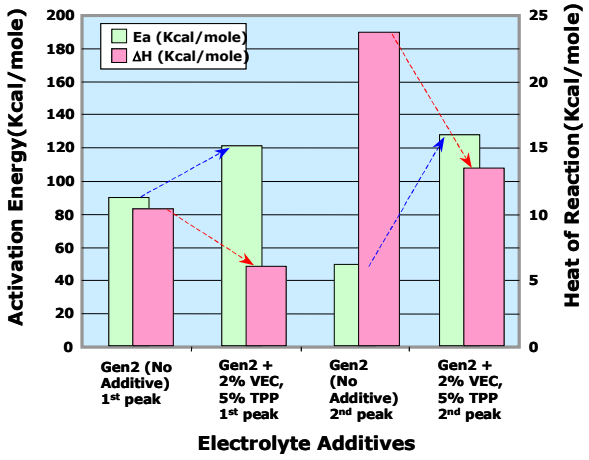

Fig. 10. Results of the ARC studies carried out on Gen 2 cathodes with and without electrolyte additives.

ARC studies carried out on the Gen 2 cathode with and without TPP and VEC additives (see Figure 10) show that these additives reduce the overall enthalpy of reaction and increase the activation energy of the Gen 2 cathode reactions. It was also found that these additives not only improve the thermal safety but may also reduce the cell pressure. For example, ARC studies (see Figure 11) clearly indicate that the addition of 2% VEC + 5% TPP additives significantly reduce the gassing from both Gen 2 positive and negative electrodes.

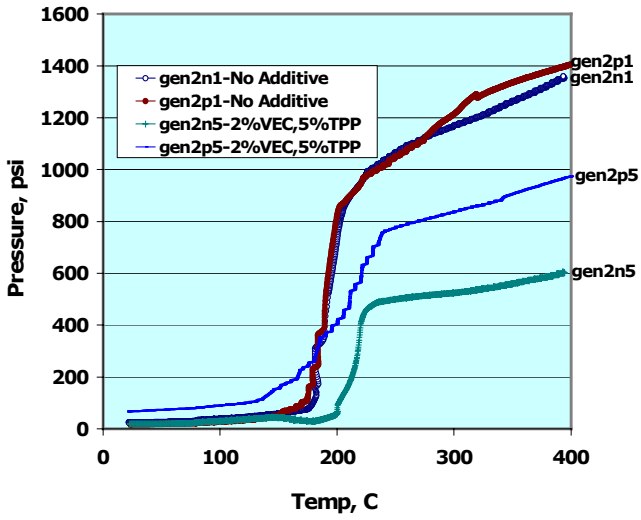

Fig. 11. Pressure generated in reactions between Gen 2 electrodes, at 100%SOC, and Gen 2 electrolyte, with and without additives.

Effect of using a Round-Edge Graphite on the Thermal Behavior of the Anode

Our Gen 2 anode used a MAG-10 flake type synthetic graphite, which was considerably less expensive than the MCMB-6 synthetic graphite that was used in our Gen 1 anode (~$15/kg vs. ~$50/kg). Since the flake type graphites are non-optimal from a safety perspective, we examined a new round-edge natural graphite material to establish the safety advantages of this material relative to our Gen 2 anode material. The material studied was a soft carbon-coated round-edge natural graphite from Mitsui Mining. ANL has been evaluating this material over the last two years and providing feedback and recommendations to Mitsui Mining in an effort to make a more optimal version of this material for high-power applications. The latest version of their material for high-power applications is their grade GDR-AA-3. It has an average particle size of ~16μm and a 6% by weight soft carbon coating. SEM photomicrographs of the GDR-AA-3 and MAG-10 (Gen 2) graphites are provided in Fig. 12, while Fig. 13 provides a comparison of the DSC behavior of fully charged anodes that employ the same weight percent of these two graphite materials.

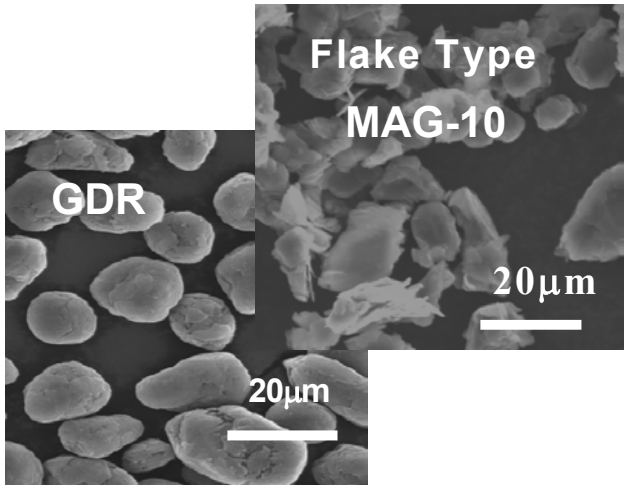

Fig. 12. SEM photomicrograph of GDR-AA-3 soft carbon-coated round-edge natural graphite.

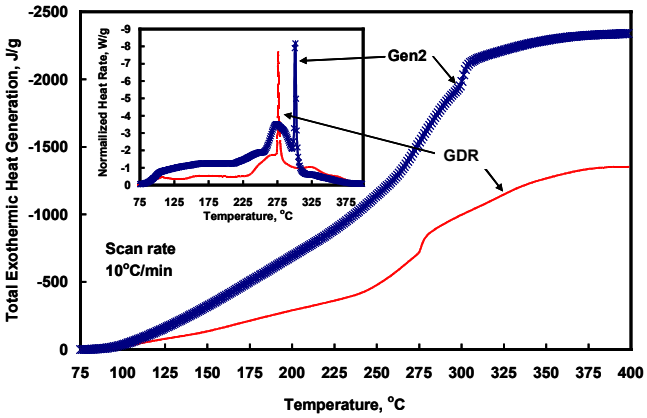

Fig. 13. Comparative thermal data on lithiated anodes made with MAG-10 flake graphite (Gen 2) and GDR soft carbon-coated round-edge graphite, via DSC studies.

It is apparent from the SEM photographs in Fig. 12, that the MAG-10 flake graphite has a lot of active edge sites on which the SEI layers seem to be relatively unstable. The round-edge GDR graphite is absent of these active edge sites and should exhibit better thermal characteristics. The DSC results, shown in Fig. 13, indicate that the GDR anode produces only 58% of the exothermic heat produced by the Gen 2 anode. Some of the improvements in the thermal properties of the anode, resulting from the use of GDR graphite, are summarized in Table 2.

Thermal Parameter	Gen 2	GDR
Onset T of SEI decomoposition (^{o}C), based on 10^{o}C/min	83	84
ΔH of SEI decomposition reaction (J/g)	-133	-85
E_a of SEI decomposition (kJ/mole)	21	72.7
Total heat generation (J/g)	-2339	-1350

Table 2. Effect of using round-edge GDR graphite on thermal properties of the anode.

Additional improvements in the thermal properties of the GDR anode are obtained when VEC is used as an electrolyte additive. The use of 2 wt% VEC with the GDR anode shifts the onset temperature of SEI decomposition from 84^{o}C to 115^{o}C and reduces the heat associated with the SEI decomposition, as shown in Fig. 14. Also, the activation energy for the SEI decomposition reaction is increased from 73 kJ/mole to 124 kJ/mole through the use of the VEC additive.

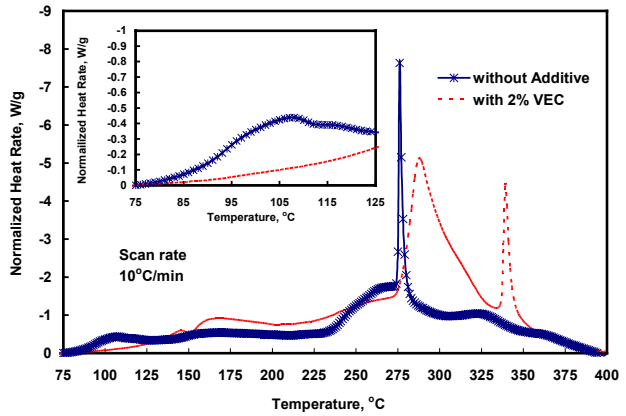

Fig. 14. Comparative thermal data on lithiated GDR anodes, with and without 2 wt% VEC additive in the electrolyte, via DSC studies.

Conclusions & Future Studies

The results reported here indicate the following major conclusions:

- Lithiated soft carbon-coated round-edge GDR graphite is thermally more benign than lithiated MAG-10 (Gen 2) flake graphite.
- The VEC electrolyte additive appears to effectively modify the SEI layer on both types of graphite and mitigates the thermally-induced reactivity of lithiated anodes.
- The VEC electrolyte additive appears to reduce the overall heat generation of our delithiated Gen 2 cathode.

Small sealed 100 mAh prismatic cells were built, with these and other modifications to the Gen 2 cell chemistry, to verify that improvements observed in our DSC studies transfer to improved thermal characteristics in sealed cells. Cells of this type were provide to SNL for use in ARC studies. ANL conducted a few preliminary ARC tests and some of the results are shown in Fig. 15. It can be seen from these preliminary studies that the soft carbon-coated round-edge graphite and VEC electrolyte additive are effective in suppressing thermal runaway in these small sealed cells.

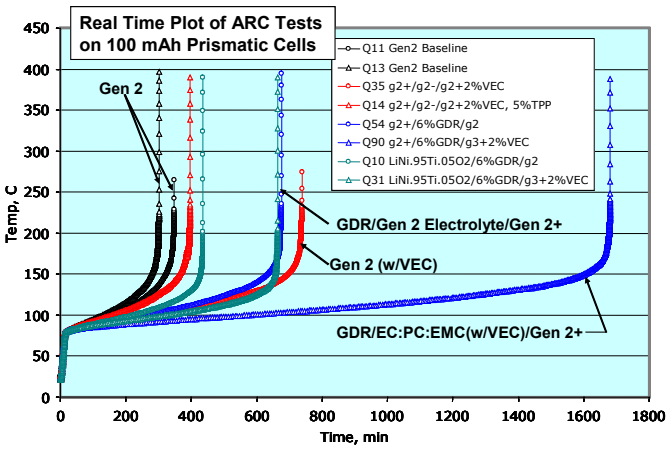

Fig. 15. Comparative ARC data showing the suppression of thermal runaway in small cells associated with the use of GDR graphite and VEC additive.

In the future, we plan to continue detailed DSC studies to establish and quantify the thermal mitigation benefits of other electrolyte additives. Also, the roles of other components of the Gen 2 cell chemistry are being elucidated in our studies and those of SNL. Therefore, we plan to establish and quantify the thermal benefits of alternative electrolyte salts (relative to $LiPF_6$) and alternative electrode binders (relative to the PVDF binders used in the Gen 2 electrodes). Additionally, we have been screening flame retardant additives, via flame propagation tests, to identify additives that are effective in suppressing the flammability of our organic carbonate electrolyte systems. We plan to conduct detailed DSC studies on the most promising of these flame retardant additives to establish and quantify the changes in thermal properties that result from the use of these additives.

III.D.2. Materials from Suppliers

Gary Henriksen, Khalil Amine, Jun Liu, Arthur Kahaian, and Shelley Oliver
Argonne National Laboratory, Argonne, IL 60439
(630) 252-44591; fax: (630) 252-4176; e-mail: henriksen@cmt.anl.gov

Objectives

- Identify and secure advanced low-cost cell materials from international material suppliers and evaluate samples for their suitability in high-power HEV applications.
- Provide feedback to material suppliers on the capabilities and limitations of their materials for HEV applications and recommend methods to improve their materials. Also, provide input to battery design and battery-level material cost models.
- Develop lower-cost high-power cell chemistries--using the most promising materials--and conduct preliminary performance, life, and safety evaluations to establish their viability.
- Transfer results, conclusions, and recommendations to the FreedomCAR industrial battery developers, with the goal of helping the industrial developers to simultaneously achieve the FreedomCAR performance, life, abuse tolerance, and cost goals. Assist in obtaining samples of materials for evaluation by the industrial developers upon request.

Approach

- Establish and maintain contact with the major international industrial material suppliers and educate them about the FreedomCAR Program.
- Provide annual production volume information to industrial material suppliers and solicit production-scale material cost projections from the material suppliers.
- Secure samples of the most advanced materials from these material suppliers.
- Develop and refine rapid screening test protocols for use in assessing the suitability of these materials for the high-power HEV application.
- Employ the appropriate rapid screening test protocols to evaluate the capabilities and limitations of each advanced material. Provide feedback to the industrial material suppliers, including recommendations for improving their materials for use in high-power HEV batteries. Also, provide input data to ANL's battery design and battery-level material cost models.
- Combine the most promising low-cost materials to develop advanced high-power cell chemistries and conduct preliminary evaluations on their performance, life, and safety characteristics, using sealed prismatic cells.
- Transfer results, conclusions, and recommendations to the FreedomCAR industrial battery developers via project review meetings, report deliverables, and DOE annual reports.

- Assist in securing samples of advanced materials for evaluation by the FreedomCAR industrial battery developers, when requested to do so.

Accomplishments

- Established and/or maintained contacts with major international material suppliers. This involved trips to Japan, Korea, and Europe.

- Obtained samples of advanced natural and synthetic graphite materials, advanced layered and 3D spinel cathode materials, advanced electrolyte salts, advanced separators, and advanced binder materials for evaluation.

- Conducted comprehensive screening tests on these advanced materials and provided feedback to the industrial material suppliers, including recommendations for improving their materials for the high-power application. One notable accomplishment was the development of a more optimal form of GDR carbon-coated round-edge natural graphite for high-power applications by Mitsui Mining, via the feedback and recommendations from ANL.

- Identified promising advanced materials for use in high-power lithium-ion cells and batteries. A few of the most promising materials are:
  - Mitsui Mining GDR soft carbon coated round-edge natural graphite
  - Seimi $LiNi_{1/3}Mn_{1/3}Co_{1/3}O_2$ layered cathode material
  - Tosoh $LiMn_2O_4$ spinel cathode material
  - Kureha ultra high adhesion PVDF binder materials for anode and cathode
  - Chemetal LiBOB salt for use with $LiMn_2O_4$ spinel cathode material

- Transferred results, conclusions, and recommendations to the FreedomCAR industrial battery developers via project review meetings, report deliverables, and DOE annual reports.

Future Studies

- Maintain contacts and/or establish new contacts with major international material suppliers and continue to solicit samples of the most advanced low-cost cell materials for evaluation at ANL.

- Solicit samples of separator materials from the industrial firms that are developing low-cost separators under the FreedomCAR Partnership.

- Continue conducting comprehensive screening tests of these new materials and providing feedback/ recommendations to the industrial material suppliers.

- Continue to transfer results, conclusions, and recommendations to the FreedomCAR industrial battery developers via project review meetings, report deliverables, and DOE annual reports.

Introduction

There are three major barriers to the use of high-power lithium-ion batteries as the energy storage device for HEVs and FCEVs under the FreedomCAR Partnership: calendar life, abuse tolerance, and cost. Our efforts to evaluate advanced cell materials from international material suppliers address all three of these barriers, but the overall emphasis is on low-cost advanced materials. The cost target for a FreedomCAR HEV energy storage device is $20/kW. DOE's ATD Program is addressing this cost target via several parallel approaches: (a) identifying and developing advanced low-cost cell materials, (b) evaluating advanced gel-polymer electrolyte systems, and (c) developing low-cost flexible cell packaging technology. This section deals with our efforts to obtain and evaluate (via pre-established screening protocols) advanced cell materials for high-power HEV applications. Where appropriate, the established screening test protocols are streamlined or otherwise refined. Our goal in this work is to find lower-cost materials that simultaneously address the performance, life, safety, and cost goals of the FreedomCAR Partnership. The work described in this section is closely linked to our efforts to track and reduce material costs at the battery level, as reported in the previous section of this report, with a goal of reducing the battery-level materials costs to ≤$10/kW. The electrochemical performance characteristics of each material, as determined in these material screening studies, are used as input to the design of HEV batteries that would incorporate these materials and meet the FreedomCAR weight, volume, energy and power requirements, through the use of our HEV battery design and battery-level material cost models.

In this section, we provide a summary of our screening test results on advanced anode, cathode, separator, and electrode binder materials. In a subsequent section, entitled "Novel Materials," we describe complimentary work that involves the development of more optimal low-cost cathode materials and low-cost electrolyte systems. In those efforts, we work closely with industrial firms to study production-level processing and cost issues, including the pilot-scale production of some of ANL's advanced cathode materials. Results obtained from our materials screening studies and the materials development and scale-up studies are used to develop new high-power cell chemistries that offer major cost reduction benefits—relative to our Gen 2 cell chemistry—while simultaneously enhancing the life and inherent safety characteristics, as well.

Anode Materials

During the last year, ANL has evaluated numerous advanced graphite materials and worked with industrial material suppliers to optimize their materials for high-power HEV applications. The screening test protocols used in these evaluations are:

- Check morphology and particle size via SEM
- Develop electrode process for high rate
- Conduct initial performance characterization using 2032 coin cells
- Conduct HPPC tests in 32 cm^2 lab cells
- Conduct 2-week accelerated aging at 100% SOC & 50-55^oC in coin cells
- Check inherent safety via DSC @100% SOC

The results of these tests are then provided to the FreedomCAR industrial battery developers. Also, upon request, ANL will help secure samples of these materials for the FreedomCAR industrial battery developers.

Table 1 provides a summary of the anode materials that were evaluated over the last year. The majority of these materials are natural graphite materials that are projected to cost ≤ $10/kg when produced in quantities sufficient to supply an introductory HEV battery market. The material from Schunk is a synthetic graphite that is likely to be too expensive (>$25/kg) for this application. The LiTech C-C composite material is a unique carbon composite material that was developed under a DOE SBIR project and could be cost competitive if it can be used without a copper foil current collector.

ANL has been studying the carbon-coated natural graphite materials from Mitsui Mining for several years. The early materials were more of a flake-type natural graphite with a particle size that was too large for the thin coatings needed in high-power HEV cells. Through the feedback and recommendations made by

ANL, Mitsui Mining continued to refine their materials for use in our high-power applications and currently makes one of the best materials for this application. Figure 1 is an HRTEM photograph of a cross-sectioned particle of their material, showing the amorphorous soft-carbon coating on the surface of the particle. Using the information provided by ANL, Mitsui Mining developed an optimal thickness carbon coating and an optimal particle size for use in high-power applications. Also, they refined their particle shaping to produce a round-edge particle. An SEM photograph of their latest round-edge particle material is shown in Figure 2.

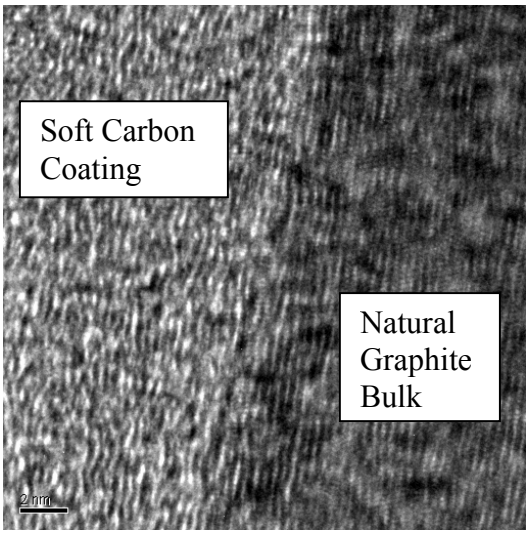

Fig. 1. HRTEM photo showing the amorphous soft carbon coating on the surface of GDA-N2-3 graphite.

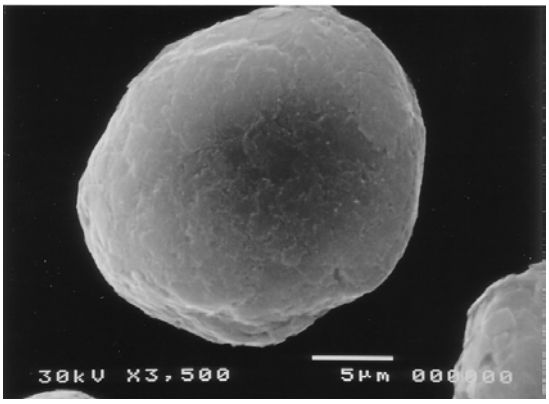

Fig. 2. SEM photo showing the round-edge morphology of the GDR-AA-3 natural graphite.

The GDR-AA-3 material exhibits excellent capacity and high rate capabilities. Figure 3 shows HPPC data on a cell that employs this material in the anode, our Gen 2 positive electrode, and LP40 electrolyte. This is the lowest ASI that we've seen in any of our screening tests. Figure 4 shows that cell ASI values with this chemistry are stable during very aggressive accelerated aging tests. Based these data and others, including results from DSC tests, this material appears to be an excellent low-cost graphite material for use in high-power cell chemistries. Another major advantage of this material is its ability to perform well in PC-based electrolytes without exfoliation, via co-intercalation of the PC.

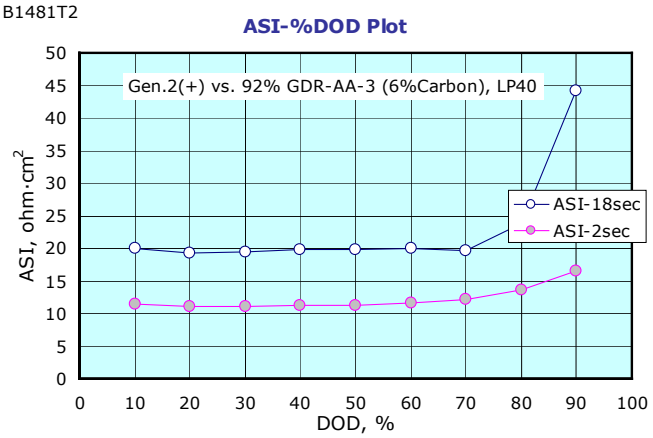

Fig. 3. Cell ASI values measured during HPPC-L test in a cell with GDR-AA-3 graphite anode.

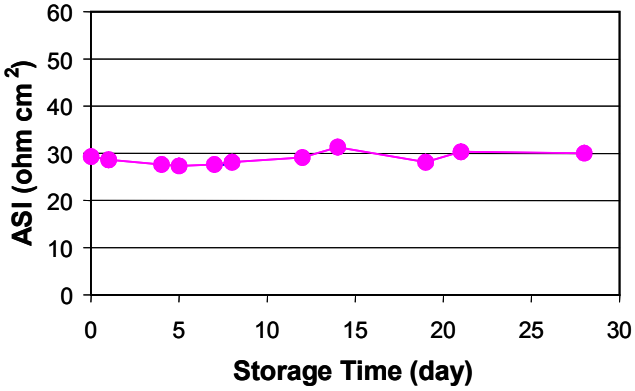

Fig. 4. Cell ASI as a function of time, during very aggressive accelerated aging (100% SOC and 50°C) of cell with GDR-AA-3 graphite anode.

Another promising low-cost anode material is the Diabeck DJG natural graphite. This material also possesses a coating of amorphous soft carbon at the particle level. This material exhibits good capacity performance and good high rate capabilities, as shown by the HPPC data in Figure 5. The 18-sec

discharge ASI values for cells using this material are slightly higher than those for cells that use the GDR material, but they are still acceptable. Also, preliminary accelerated aging tests indicate that it has a somewhat higher rate of impedance rise than GDR. However it exhibits very good inherent safety characteristics, as determined via DSC experiments. Figure 6 shows low exothermic heat generation up to 300°C. At $6/kg this is a promising low-cost anode material for high-power cells and batteries.

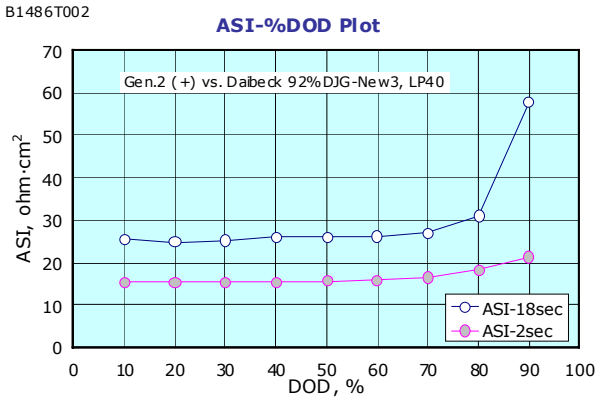

Fig. 5. Cell ASI values measured during HPPC-L tests in a cell with DJG graphite anode.

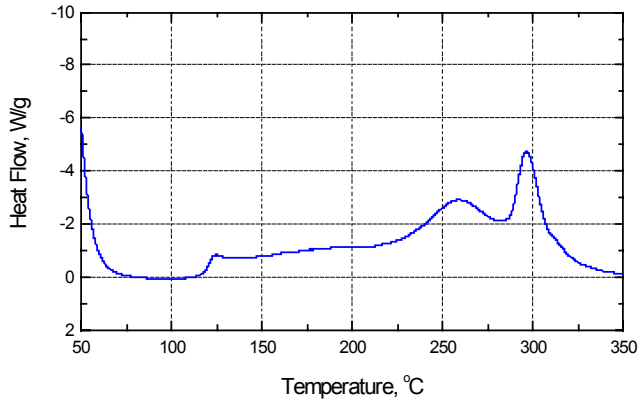

Fig. 6. DSC data on DJG natural graphite anode material, at 100% SOC, and LP40 electrolyte.

At $5/kg, another very low-cost natural graphite anode material is the SLC 20A round-edge natural graphite from Bejing Advanced Materials. It's performance under HPPC-L tests is not as good as the GDR or the DJG natural graphite materials, as shown in Figure 7. However, with some refinements in the material, it may be possible to improve its high-rate performance characteristics. It does exhibit good

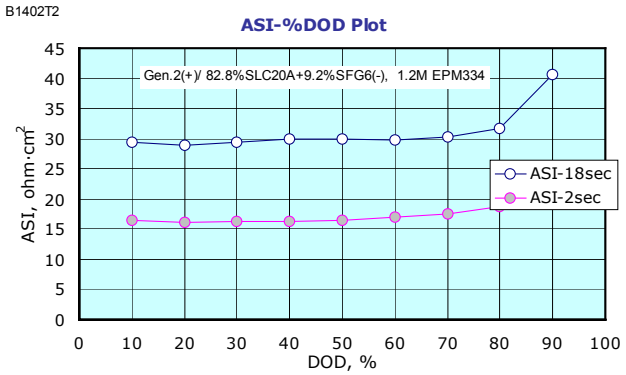

aging characteristics, as shown in Figure 8. It also performs well in DSC tests.

Fig. 7. Cell ASI values measured during HPPC-L tests in a cell with SLC 20A natural graphite anode.

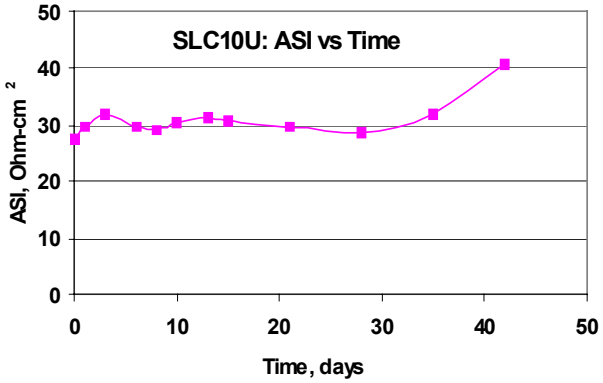

Fig. 8. Cell ASI as a function of time, during very aggressive accelerated aging (100% SOC and 50°C) of cell with SLC 20A natural graphite anode.

Superior Graphite Co. continues to develop round-edge natural graphite materials that have good high rate capabilities. There SLC 1015 material performs in a manner comparable to the Diabeck round-edge natural graphite, when tested in cells with the Gen 2 cathode and LP40 electrolyte. This material exhibits excellent safety characteristics in DSC tests, as shown in Figure 9.

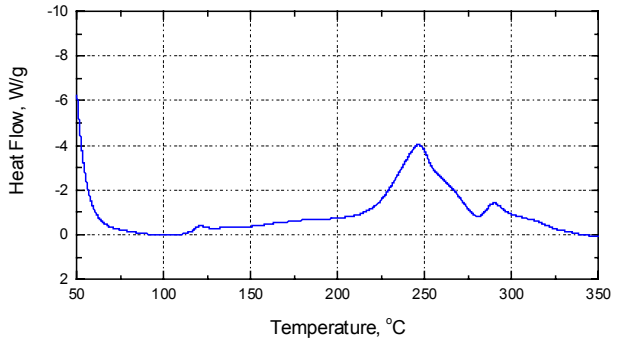

Fig. 9. DSC data on SLC 1015 natural graphite anode material, at 100% SOC, and EC:PC:DMC electrolyte.

The Timcal Timrex E-SLP 50 graphite is another low-cost natural graphite material at $6/kg. As shown in Figure 10, it exhibits good high-rate capabilities.

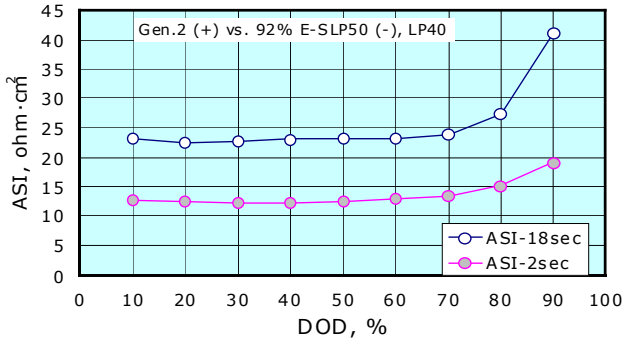

Fig. 10. Cell ASI values measured during HPPC-L tests in a cell with Timrex E-SLP 50 natural graphite anode.

The Schunk Graphite round-edge synthetic graphite has good high-rate capabilities and very good inherent safety (via DSC tests). However, its cost does not compare favorably to our ≤$10/kg cost goal.

The LiTech C-C composite technology is a carbon fiber matrix that has sufficient electronic conductivity along the fibers that a copper current collector is not needed for low-rate applications. It also eliminates the cost associated with the electrode binder. Figure 11 shows a SEM photograph of this material. Initial performance data indicate the impedance of the existing material is too high for high-rate applications and ANL is working with LiTech to evaluate improvements derived from a denser version of this material.

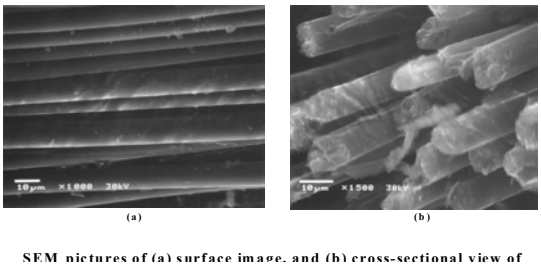

SEM pictures of (a) surface image, and (b) cross-sectional view of

Fig. 11. SEM photos of C-C composite fiber technology.

Cathode Materials

During the last year, ANL has evaluated numerous advanced low-cost cathode materials and worked with industrial material suppliers to optimize their materials for high-power HEV applications. The screening test protocols used in these evaluations are the same as those used in our anode evaluations:

- Check morphology and particle size via SEM
- Develop electrode process for high rate
- Conduct initial performance characterization using 2032 coin cells
- Conduct HPPC tests in 32 cm^2 lab cells
- Conduct 2-week accelerated aging at 100% SOC & 50-55°C in coin cells
- Check inherent safety via DSC @100% SOC

The results of these tests are then provided to the FreedomCAR industrial battery developers. Also, upon request, ANL will help secure samples of these materials for the FreedomCAR industrial battery developers.

Table 2 provides a summary of advanced low-cost cathode materials that were evaluated over the last year. Our efforts in this area focused on materials that contain low levels of cobalt, types of layered nickel materials that could be more easily and cheaply processed, and/or materials that contain high levels of manganese. In prior years, ANL synthesized lab-scale quantities of $LiNi_{0.95}Ti_{0.05}O_2$ materials that performed well in lab cells. In the production-scale cost analysis conducted for ANL by Fuji (described briefly in the previous section) they projected that this type of material would be lower in

cost than our Gen 2 cathode material. Three industrial material supply companies—FMC, Fuji, and OMG--produced pilot-scale quantities of this type of material for our evaluation. Figure 12 provides SEM photographs of the materials supplied to ANL by these three companies. Different processing technologies were used to produce these materials. The round-edge particle morphology of the materials produced by the OMG and Fuji processes are more optimal. Fuji also produced an Al-doped version of this material ($LiNi_{0.92}Ti_{0.05}Al_{0.03}O_2$) for our evaluation and this material possessed a similar round-edge particle morphology. These materials exhibit good high-rate capabilities, as shown by the HPPC-L (10C current pulses on discharge) data in Figure 13. Addition of a small amount of Al doping seems to increase the impedance of this cathode material, as shown in Figure 14. Both the doped and undoped forms of this material exhibit excellent impedance stability with aging.

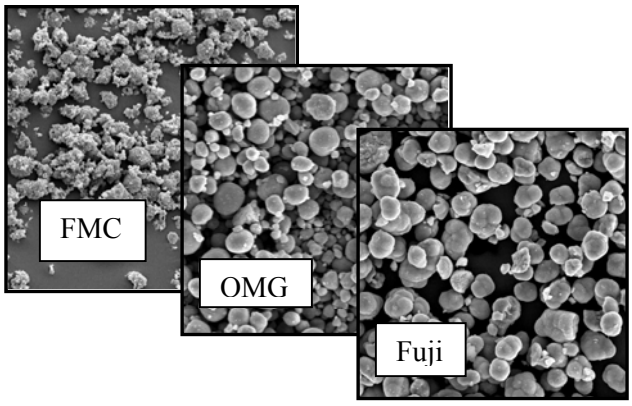

Figure 12. SEM photographs of $LiNi_{0.95}Ti_{0.05}O_2$ materials produced and supplied to ANL by three industrial material suppliers.

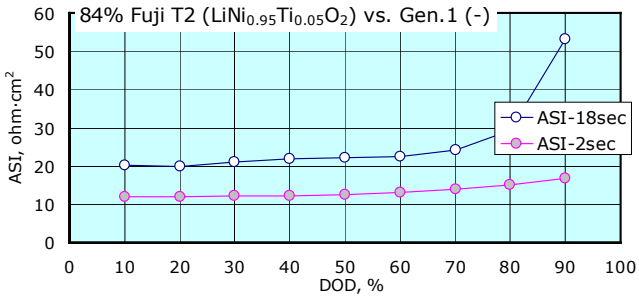

Figure 13. Cell ASI values measured during HPPC-L tests in a cell with Fuji's $LiNi_{0.95}Ti_{0.05}O_2$ cathode material.

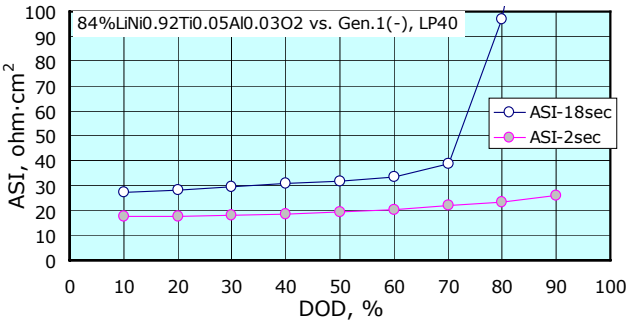

Figure 14. Cell ASI values measured during HPPC-L tests in a cell with Fuji's $LiNi_{0.92}Ti_{0.05}Al_{0.03}O_2$ cathode material.

Numerous industrial material suppliers have developed $LiNi_{0.5-x}Mn_{0.5-y}M_{x+y}O_2$ type cathode materials. This reduces the amount of tetravalent nickel for enhanced stability versus our Gen 1 and Gen 2 cathode materials. These materials exhibit excellent accelerated aging and inherent safety characteristics. However, the impedance of these materials is typically higher than desired and is sensitive to both dopants and processing conditions. More refinements are needed to achieve the high-rate performance needed for the HEV application.

The $LiNi_{1/3}Mn_{1/3}Co_{1/3}O_2$ layered cathode material appears to be quite promising. Despite the fact that it contains 1/3 nickel and 1/3 cobalt, industrial material suppliers project a production volume cost of $13-15/kg, based on the ease and speed of processing this type of material. Here again, this material offers enhanced stability, vs. our Gen 1 and Gen 2 cathode materials, due to its reduced level of tetravalent nickel. Figure 15 shows that structurally this material should be very stable, because its unit cell volume remains almost constant when charged to ~4.6 volts and it can deliver ~190 mAh/g capacity density. The limited expansion and contraction that occurs during normal charge and discharge operation, should render this material relatively stress free and little or no particle cracking should occur.

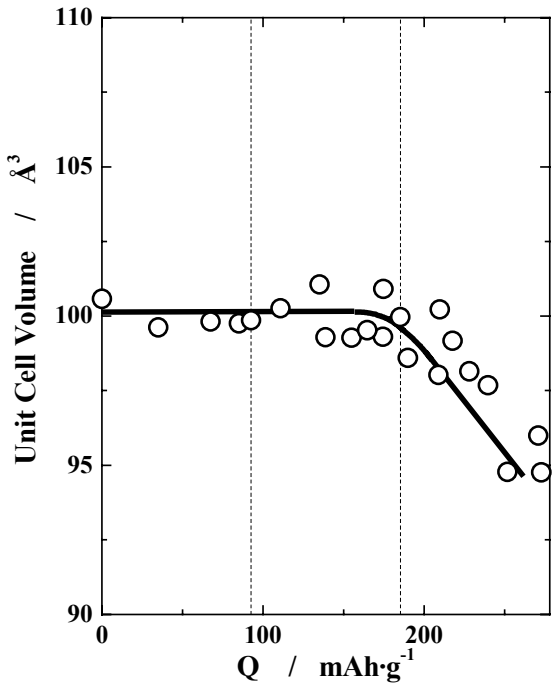

Fig. 15. Unit cell volume vs. charge capacity.

Data in Figure 16 show that that this cathode material possesses acceptable high-rate performance capabilities, via HPPC-L tests. Also, it operates at a slightly higher voltage, which offers a slight power advantage over our Gen 1 and Gen 2 cathode materials. Also, preliminary safety studies show this material to be more inherently safe than our Gen 1 and Gen 2 cathode materials.

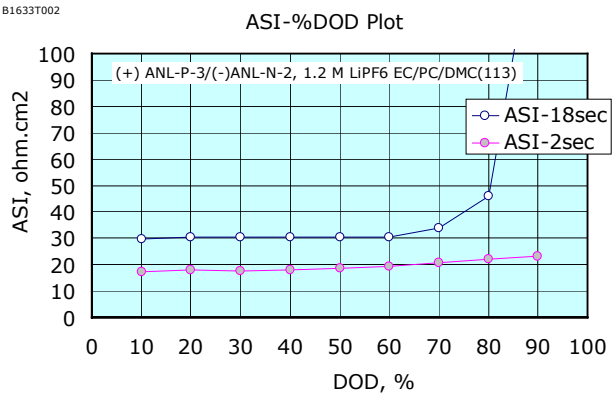

Fig. 16. Cell ASI values measured during HPPC-L tests in a cell with Seimi $LiNi_{1/3}Mn_{1/3}Co_{1/3}O_2$ cathode material.

In the long term, the $LiMn_2O_4$ Spinel cathode material appears to be the most promising candidate, if one can develop a stable cell chemistry around this type of material. Industrial material developers have used a variety of approaches for stabilizing this material from dissolution in conventional lithium-ion battery electrolytes. These approaches include the addition of excess lithium and/or dopants. ANL evaluated several so-called "stabilized" spinel materials available from industrial suppliers. Also, it should be noted that DOE is funding R&D efforts in this area as part of the BATT and ATD programs. The ATD program activities in this area are briefly discussed in the following section of this report. That work includes the development of a more compatible electrolyte system for use with $LiMn_2O_4$ Spinel cathode materials.

The three-dimensional structure of the $LiMn_2O_4$ Spinel material makes it an excellent candidate for high-rate applications, as compared to the two-dimensional layered materials. Figure 17 provides HPPC data obtained on a Tosoh-supplied spinel material at the 29C rate, during the 18-second discharge current pulses. The ASI values shown here are comparable to those measured at the 10C rate and lower. In comparison, our Gen 1 and Gen 2 cathode materials are not capable of sustaining current pulses at the 15C rate (during the 18-second discharge pulses) without undergoing appreciable polarization. Over the last few years, ANL has evaluated several versions of "stabilized" spinels from Tosoh and provided them with feedback on their materials. SEM photographs of a lithium-rich Al-doped spinel from Tosoh are provided in Figure 18.

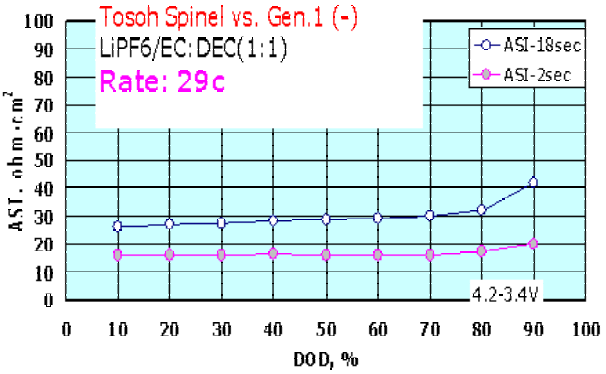

Fig. 17. Cell ASI values measured during HPPC tests, with discharge current pulses at the 29C rate, in a cell employing a Tosoh $LiMn_2O_4$ spinel cathode material.

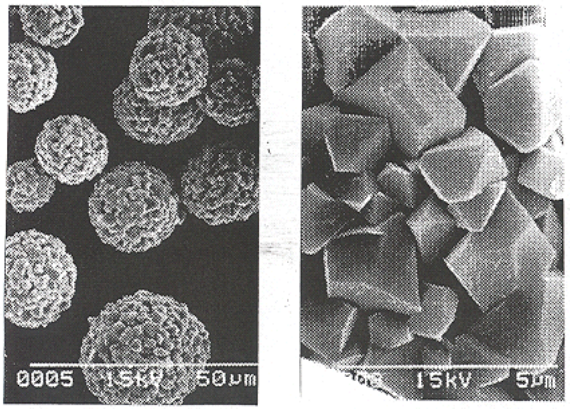

Fig. 18. SEM photographs of Al-doped $Li_{1.06}Mn_{1.94}O_4$ spinel cathode material, showing spherical secondary particles (left) and primary particles (right).

The $LiMn_2O_4$ spinel cathode materials also possess inherent safety advantages over nickel-based cathode materials. Figure 19 compares DSC data on our Gen 1, Gen 2, and two advanced cathode materials. The $LiNi_{1/3}Mn_{1/3}Co_{1/3}O_2$ cathode and the $LiMn_2O_4$ spinel cathode materials both provide significant improvements in the inherent safety of the cell chemistry, based on these preliminary DSC data.

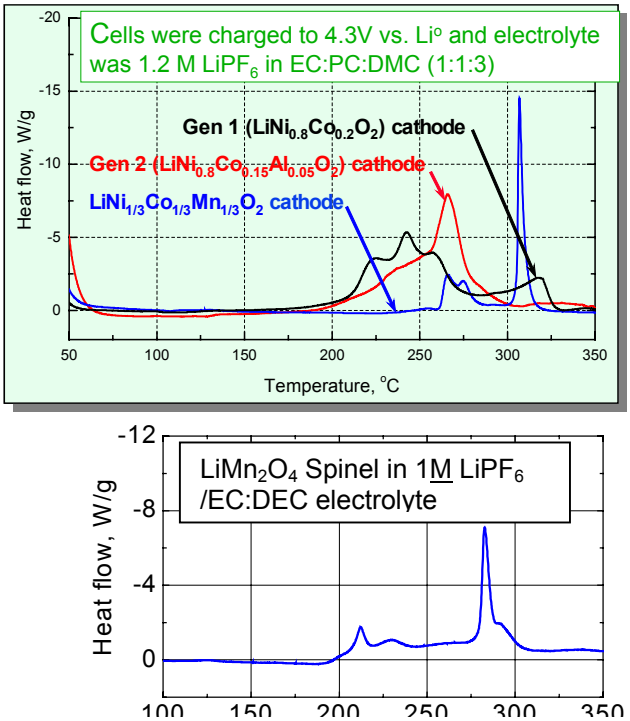

Fig. 19. DSC data on four different cathode materials. In all cases, $LiPF_6$ salt was used, however the $LiMn_2O_4$ spinel cathode was evaluated in a more reactive electrolyte system. Both of the advanced cathode materials exhibit superior inherent safety relative to the Gen 1 and Gen 2 cathode materials.

For the purpose of stabilizing the $LiMn_2O_4$ spinel cathode against dissolution in the electrolyte, we have been conducting studies with a new LiBOB salt-based electrolyte system and working to develop an optimal solvent system for this salt. This is discussed elsewhere in this report. However, it should be noted here that switching to the LiBOB-based electrolyte almost totally eliminates any heat generation between the delithiated $LiMn_2O_4$ spinel cathode and the electrolyte up to 350°C.

Electrolytes and Separators

The electrolyte is an active component of the battery chemistry and it plays a role in the performance, life, safety, and cost of the cell. The diagnostic studies, on our aged Gen 1 and Gen 2 cells, have shown that the $LiPF_6$ salt plays a role in the surface films that form and grow on the surfaces of the electrodes. Also, it is thermally unstable at elevated temperatures (decomposes at 180°C); it reacts with trace amounts of water or alcohol in the

cell to form HF, which is an undesirable side product; and it is rather expensive at ~$50/kg.

Therefore, ANL evaluated a few new salts, the most promising of which is lithium bis(oxalate) borate (denoted LiBOB) salt. LiBOB is projected to be less expensive than $LiPF_6$ salt at ~$33/kg, when manufactured on an industrial scale; it has a significantly higher decomposition temperature (320°C); and it is less sensitive to moisture. Our initial electrochemical evaluations of this salt were conducted using an electrolyte solvent system that was developed for use with LiBOB by its manufacturer (Chemetall, Frankfurt, Germany). The solvent system used in this electrolyte contains a high vapor pressure solvent and ANL is working with the Army Research Laboratory and Idaho National Engineering and Environmental Laboratory to develop a more optimal high-power salt/solvent system for this promising salt. Progress on this topic is discussed in the "Novel Materials" section of this report.

Over the last year the FreedomCAR Energy Storage Technical Team initiated contracts with several industrial firms to develop low-cost separators with a cost goal of $\leq$$1.00/m^2. We've solicited and obtained permission from the FreedomCAR Energy Storage Technical Team to secure samples of advanced low-cost separator materials from these companies. These evaluations will be initiated during the next year.

Late this year we obtained samples of new low-cost separator materials that are being developed by Degussa. These new separators employ non-woven polymeric supports that are coated with nano-particle ceramic materials to enhance their wetability by the organic carbonate based electrolytes. This new type of separator is depicted in Figure 20. The ceramic nano-particles are applied as a suspension to the polymeric support. Table 3 provides additional information on these materials. The cost of the non-woven support is less than $0.30/m^2, while the final separator is projected to cost between $1.00-1.50/m^2 when produced in volumes sufficient to supply the 100,000 battery per year introductory market for HEVs. Figure 21 provides ASI values measured on cells that employ the Degussa separator, as well as ASI values for a similar cell with a standard Celgard separator. The ASI values were obtained using the standard FreedomCAR protocols for HPPC tests. These preliminary data suggest that the Degussa separator could be a viable low-cost alternative to the standard separators.

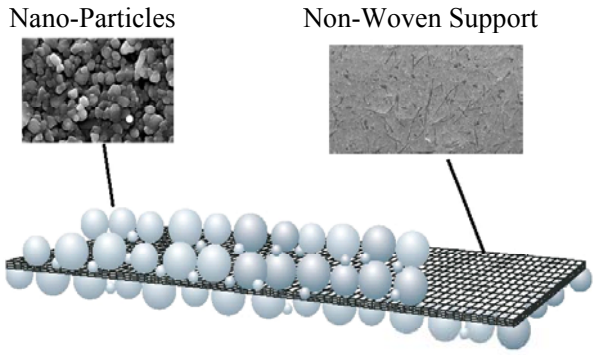

Fig. 20. Representation of the new Degussa separator technology.

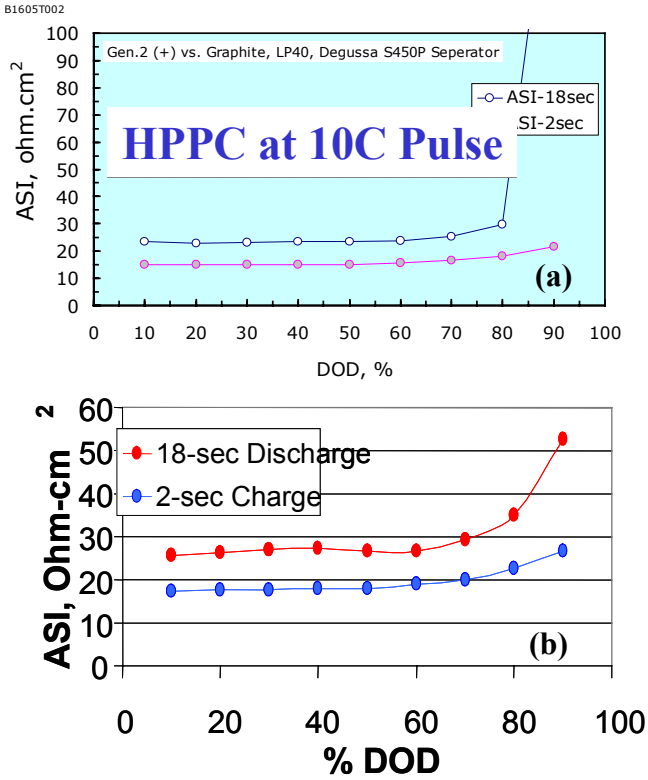

Fig. 21. HPPC data on similar cells, one employing a Degussa separator (a) and the other a Celgard separator (b). The results are comparable.

New Electrode Binders

In recent years there has been a move to soft butyl rubber (SBR) binders in the lithium-ion battery business. The Japanese battery companies are now using these SBR binders in their anodes. The use of these binders requires special electrode processing technology and ANL has obtained detailed processing information binders from the two principle suppliers (Nippon Zeon and JSR). These two companies will be shipping materials to ANL for evaluation in the near future.

Meanwhile, Kureha—a major supplier of PVDF binders—has been developing advanced PVDF binders to compete with the SBR binders. ANL has independently evaluated these materials for performance in high power applications. The Kureha KF binder "L series" are solutions of PVDF resins in NMP. The binding properties of the "L series" binders are superior to the old PVDF binders sold by Kureha, which were used in our Gen 1 and Gen 2 cell chemistries. The new product L#9300 is used as an ultra high adhesion bonding binder for anodes in lithium-ion secondary batteries. This material exhibits a very high peel strength (binding strength of the coating to the metal foil current collector) even at low concentrations of binder. This enhanced peel strength property is illustrated by the data in Figures 22 (for the negative electrode) and 23 (for the positive electrode). Additional benefits demonstrated by these new binders include improved cell cyclability and reduced heat generation.

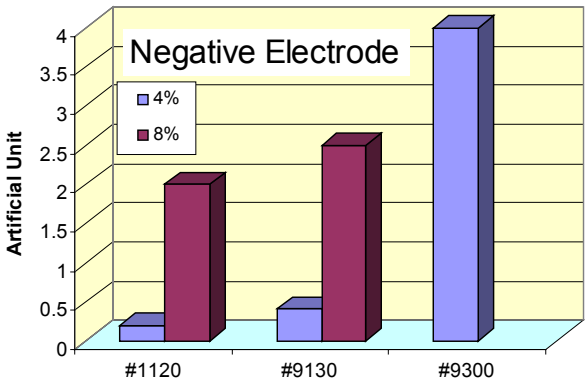

Fig. 22. Relative peel strength of negative electrode binders. The Kureha L#9300 binder is superior to other PVDF binders, even when used at the 4 wt% level (compared to the standard 8 wt% level).

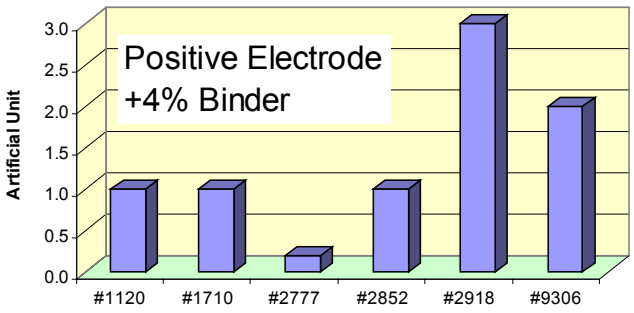

Fig. 23. Relative peel strength of positive electrode binders. The Kureha KF#2918 binder exhibits exceptional binding properties at the 4 wt% level.

Status, Recommendations, & Future Work

A large number of advanced materials from international material suppliers were evaluated during the last year. In general, these materials offer cost savings over the materials used in our Gen 2 cell chemistry. The most promising low-cost materials are:

- Round-edge natural graphites at \$5-10/kg (vs. \$15/kg for our Gen 2 flake-type synthetic graphite), especially those with soft carbon coatings that allow use of PC-based electrolytes. Also, these graphites enhance the inherent safety of the anode.

- The $LiNi_{1/3}Mn_{1/3}Co_{1/3}O_2$ layered cathode material at \$13-15/kg (vs. \$20-25/kg for our Gen 2 cathode material), which also appears to offer enhanced stability (leading to longer life and enhanced saftety) compared to our Gen 2 cathode.

- The partially-stabilized $LiMn_2O_4$ spinel cathode materials at \$7.40/kg, when used in combination with a more compatible salt-based electrolyte system, e.g. LiBOB. The 3-dimensional structure of this material facilitates higher-rate capabilities than the 2-dimensional layered materials and allows the use of smaller capacity cells, thereby further reducing material costs.

- The LiBOB salt at $33/kg (vs. $50/kg for the $LiPF_6$ salt) if we can develop a more optimal solvent system for use in high-power applications. It is less sensitive to moisture and thermally more stable than $LiPF_6$, which would tend to enhance the calendar life and the inherent safety of high-power lithium-ion cells.

Most of these materials have been considered for use in advanced cell chemistries and included in our battery design and battery-level material cost studies (reported elsewhere in this report).

ANL will maintain existing contacts and establish new contacts with international material suppliers and provide them feedback on our evaluation of their materials, as well as recommendations as to how their materials could be improved for use in high-power applications. We will continue to solicit samples of their most promising advanced materials for evaluation. With the aid of the FreedomCAR Energy Storage Technical Team, we will obtain samples of the low-cost separators that are being developed by their industrial contractors. We will continue to conduct comprehensive screening tests on these new low-cost cell materials and refine the screening tests, where possible, to expedite the testing and minimize costs. Results of these screening tests will be reported to the FreedomCAR Energy Storage Technical Team and to their industrial battery developers, via project review meetings, report deliverables, and DOE annual reports.

Additionally, ANL will utilize its battery design model to design batteries for 42-volt battery applications, as well as batteries for use in fuel cell electric vehicles. These two types of high-power batteries are now being pursued under the FreedomCAR Partnership. We will examine the appropriateness of our screening test protocols and the advanced materials for these applications, as well as for the power-assist HEV application.

Industrial Supplier (Country)	Types of Material	Product Grade	Unit Cost
Mitsui Mining Co. Ltd. (Japan)	Carbon-coated round-edge natural graphite	GDR	$10/kg
Diabeck (S. Korea)	Carbon-coated round-edge natural graphite	DJG	$6/kg
Beijing Advanced Materials (China)	Round-edge natural graphite	SLC 20A	$5/kg
Superior Graphite (USA)	Round-edge natural graphite	SLC 1015	$10/kg
Timcal Ltd (Switzerland)	Natural graphite	Timrex E-SLP 50	$6/kg
Schunk Graphite (Germany)	Synthetic graphite	FU 2651	>$25/kg
LiTech LLC (USA)	Carbon Fiber	C-C Composite	

Table 1. Advanced graphite materials evaluated as low-cost anodes for high-power HEV batteries.

Industrial Supplier	Type of Advanced Cathode Material			
	$LiNi_{0.95-x}Ti_{0.05}M_xO_2$	$LiNi_{1/3}Mn_{1/3}Co_{1/3}O_2$	$LiNi_{0.5-x}Mn_{0.5-y}M_{x+y}O_2$	$LiMn_2O_4$ Spinel
FMC	X			
Fuji	X		X	
JMC				X
Mitsubishi			X	X
Mitsui			X	X
OMG	X			
Seimi		X	X	X
Tanaka			X	
Toda				X
Tosoh				X

Table 2. Advanced materials evaluated as low-cost cathodes for high-power HEV batteries.

Type	D90 [nm]	Material	Support
S 700 P	700	Al_2O_3/SiO_2	Polymeric non-woven
S 600 P	600	Al_2O_3/SiO_2	Polymeric non-woven
S 450 P	450	Al_2O_3/SiO_2	Polymeric non-woven
Z 700 G	700	Al_2O_3/ZrO_2	Glass woven
Z 450 G	450	Al_2O_3/ZrO_2	Glass woven

Table 3. Types of new low-cost separator materials available from Degussa.

III.D.3. Gel Electrolyte Technologies

Khalil Amine, Bookeun Oh, Sang Young Yoon, Yoo-Eup Hyung, Chun-hua Chen, and Gary Henriksen
Argonne National Laboratory, Argonne, IL 60439
(630) 252-3838; fax (630) 252-4176; e-mail: amine@cmt.anl.gov

Objectives

- Assess viability of gel electrolyte lithium-ion systems for use in high-power HEV applications.
  - Evaluate high-power performance via HPPC tests.
  - Evaluate calendar life characteristics, via preliminary accelerated aging at 50°C.
  - Conduct post test analyses of gel electrolyte cells to understand performance decay mechanisms and delamination problems.
  - Conduct preliminary safety studies via DSC and/or ARC.

Approach

- Collaborate with industrial developers of gel electrolyte technologies to evaluate their electrolyte technologies, in combination with our Gen 2 electrodes, for high-power HEV applications:
  - Work with Ultralife Batteries Inc. to evaluate their PVDF-based gel electrolyte, via their Plastic Lithium Ion (PLI) battery technology.
  - Work with Daiso to evaluate their branched PEO-based gel electrolyte technology in pouch cells.
  - Work with Dai-ichi Kogyo Seiyaku (DKS) Co. to evaluate their macromonomer PEO-based gel electrolyte technology in pouch cells.
  - Work with Showa Denko and Quallion to evaluate the Showa Denko acrylate oligomer electrolyte technology in pouch cells.
- Use HPPC tests and elevated temperature aging to study power capabilities/limitations and energy/power losses during aging.
- Thoroughly examine aged/tested cells for adhesion, wetting, and gassing problems.
- Develop approaches to improve the high-power performance and life of cells that use these gel electrolyte technologies.

Accomplishments

- Fabricated and evaluated PVDF-based PLI and gel electrolyte cells for ASI (via HPPC tests), gas evolution, adhesion, and delamination issues.
- Supplied ANL electrode materials to industrial collaborators to fabricate cells with their gel electrolyte technologies: advanced PEO and macromonomer gel electrolytes.
- Evaluated the power and aging characteristics of cells that employ the gel electrolytes from Daiso and DKS.

- Evaluated thermal safety of Daiso pre-gelled (liquid) electrolyte cell chemistry.
- Evaluated VEC as an additive to the Daiso electrolyte and determined that it reduces cell capacity fade.
- Investigated the performance of two DKS cells and determined that such cells with the Gen 2 electrodes showed excellent rate capability, but initial ASI was somewhat higher than Gen 2 baseline cell chemistry.

Future Studies

- Continue working with Showa Denko and Quallion to evaluate the Showa Denko technology. Quallion has agreed to fabricate cells with the Showa Denko gel polymer electrolyte and ANL-supplied electrode materials. They can readily fabricate cells with the $LiCoO_2$ cathode material, but experienced problems with curing cells (only achieve ~60% cure) when they use our Gen 2 ($LiNi_{0.8}Co_{0.15}Al_{0.05}O_2$) cathode material.Further evaluate the DKS gel electrolyte technology. They are fabricating six additional cells for evaluation by ANL.
- Continue the evaluation of $LiBF_4$/EC/GBL as an advanced PEO gel electrolyte and develop additives to stabilize the cell ASI. $LiPF_6$ salt can not be used in these systems, which are cured at 100°C.
- Continue the development of cell materials for use with gel electrolytes (lithium salts, electrode materials, etc.).

Introduction

Gel polymer electrolytes are being developed as alternatives to the solid polymer electrolytes, because they offer similar advantages with fewer problems. The gel polymer electrolytes are not solid electrolytes. As indicated by the name, the phase of this electrolyte is a stable gel whose ionic conductivity is higher than the solid polymer, due to this gel state. The methods for making gel polymer electrolytes are simple. One method (used for making PVDF hybrid type gels) starts with solid polymers, which are dissolved in a solvent and then a film is formed by adding a small amount of plasticizer. Then the solvent is removed and the final step in making the gel phase is to place the film into liquid electrolyte. A second method (used for making cured type gels) uses a reactive monomer, liquid electrolyte, and a radical initiator. These are mixed together to make a precursor solution. The precursor solution is then heated or irradiated by UV, thereby curing it to form the gel.

The conductivities of these gel polymer electrolytes are close to those of typical liquid electrolytes, over a wide temperature range, due to the stable gel phase. One of the problems with the gelled electrolytes is their relatively poor mechanical strength. However, this can be overcome by properly designing the cell.

ANL is evaluating several types of advanced gel electrolyte technologies, via collaborative efforts with the industrial developers of these technologies. The gel electrolyte systems appear to offer several advantages over liquid electrolyte cells. The liquid electrolyte is immobilized by the gel thereby preventing the leakage of liquid electrolyte from the cell. Due to the absence of free liquid electrolyte, these technologies offer promise in terms of extending calendar life, enhancing inherent safety, and facilitating the use of low-cost flexible packaging for cell containment. At issue are potential power limitations, problems created by gas generation, and potential delamination at interfaces with these technologies. Also, the accelerated aging and safety characteristics of these technologies must be evaluated.

The following technologies are being evaluated by ANL:

- PVDF gel polymer: ANL makes 20-50 mAh cells & Ultralife fabricates 0.5 and 3 Ah cells.

- Branched PEO gel polymer: Daiso fabricates pouch cells with their gel electrolyte technology.

- Macromonomer gel polymer: Dai-ichi Kogyo Seiyaku (DKS) fabricates pouch cells with their gel electrolyte technology.

- Acrylate oligomer gel polymer: Showa Denko provides their technology to Quallion and Quallion fabricates sealed prismatic cells with the Showa Denko gel electrolyte technology.

ANL reached a 3-way agreement with Showa Denko and Quallion. Under this agreement, Quallion fabricates cells with our Gen 2 electrode materials and Showa Denko's gel-polymer electrolyte. Cells using all of these gel electrolyte technologies are being built using ANL-supplied Gen 2 electrode materials, whenever possible, to obtain comparative data with our Gen 2 baseline cells. Because we depend on the industrial developers to fabricate cells for us, progress on this task has been slower than planned.

PVDF Cells *(hybrid polymer electrolyte)*

The cell chemistries incorporated in PVDF-based gel polymer cells are listed in Table 1. ANL fabricated small PVDF gel polymer cells to evaluate their thermal behavior via ARC calorimetry. Ultralife fabricated larger capacity pouch cells. The specifications for these PVDF-based electrolyte cells are provided in Table 2. The nominal capacities of Ultralife cells are 0.5 and 3.0 Ah.

ANL conducted gas analyses on a few of the Ultralife 3Ah cells using a combination of an HP 6890 series GC, equipped with TCD and an HP 5973 Mass selective detector (MSD). Before gas collection, the cells were cycled 10 times at the 1C rate, followed by 10 days of accelerated aging at 50°C. The generated gases were collected directly using gas-tight syringes attached to the tested pouch cells in a glove-box. Gas analyses were performed on cells with electrolyte additives (2% VC + 2% VEC) and cells without additives. Data on these cells are compared in Figure 1. It is obvious that the additives suppressed gas generation, especially CO_2 generation. From Figure 2 we can see that the additives changed the composition of the generated gases. The cell without additives generated more ethane than ethylene, while the reverse is true for the cell without additives.

Figure 3 shows test results on Ultralife 500 mAh cells, using the HPPC protocol with 3.75C charge and 5C discharge current pulses. These cells meet the FreedomCar power requirement initially, irrespective of whether they employ the electrolyte additives. These cells exhibit similar non-ohmic ASI values (less than 10 ohm-cm^2) when compared to our Gen 2 18650 baseline cells (see Figure 4), as determined by electrochemical impedance spectroscopy (EIS).

Figure 5 shows how the ASI values and Ah capacities of these Ultralife 500 mAh cells change, during accelerated aging at 60% SOC and 50°C. The ASI values gradually increase, while the capacities gradually fade. The AC impedance of one of these cells was analyzed using EIS, as shown in Figure 6. The ohmic impedance remained unchanged during the aging test, while the non-ohmic impedance increased significantly. Post test analyses of Ultralife cells uncovered evidence of intra-electrode delamination and areas of stress, as shown in Figure 7. This figure shows areas of poor adhesion between laminated layers within the anode (possibly due to variations in coating thickness). Also, we observed areas of stress (gray areas on top of electrodes), which could be caused by locally high currents, possibly resulting from an inhomogeneous lamination process or non-uniformity in electrode laminate thicknesses. It is not clear how much these phenomena contribute to the non-ohmic impedance rise.

The effect of using VEC and VC electrolyte additives was investigated. Figure 8 shows the discharge capacity and the ASI values, as a function of accelerated aging time, for two Ultralife 500 mAh cells: One using standard LP40 (1.0M $LiPF_6$ /EC:DEC [1:1]) electrolyte and the other using LP40 electrolyte with 2% each of VEC and VC. While these cells were not designed for the high power application, the cells showed good power characteristics. The initial ASI values meet

the FreedomCar power requirements. With increased aging time at 60% SOC and 50°C, the ASI values increase gradually. No positive or negative effects of using the combined VEC/VC additive package were observed during this short-term accelerated aging test. As the aging time increased, however, the VEC/VC additive package tended to stabilize the cell capacity and cell ASI values—rendering a lower rate of capacity fade and lower rate of impedance rise for the cell that employed the VEC/VC additive package.

Figure 9 shows how the EIS of these cells changed when aged at 60% SOC and 50°C. The impedance of these cells continues to increase as a function of aging time. These data agree with the capacity fade data and ASI increase data presented in Figure 8. We can examine these EIS data more thoroughly by separating out the different components, as shown in Figure 10. In general, the high frequency intercept (region 1) is attributed to the ohmic resistance (including electrolyte/separator); region 2 is associated with Li^+ migration through surface films (kinetics 1), region 3 is attributed to charge transfer (kinetics 2) and region 4 is attributed to solid state diffusion. If we analyze regions 1, 2, and 3 of our experimental EIS data, we obtain the results plotted in Figure 11. Most of the impedance growth occurs in regions 2 (kinetics 1) and 3 (kinetics 2), which are associated with interfacial phenomena. Significant reductions in the impedance growth in these two regions occur when the VEC/VC additive package is used. This is indicative of more stable surface films (SEI layers), which should suppress impedance rise and capacity fade during long-term aging tests.

A charged ANL-built PVDF gel polymer cell was put into the ARC bomb to study the thermal degradation of its components at elevated temperature. The data are shown in Figure 12. There was not a big difference in the thermal behavior of this cell vs. a standard liquid-electrolyte Gen 2 cell, except there was a delay in the on-set temperature for the initial exothermic reaction.

DAISO Cells *(branched PEO electrolyte)*

Advanced PEO compounds produced by Daiso have branched PEO structure, as shown in Figure 13. The PEO compounds contain an allyl group that reacts with the bismaleimide type crosslinking agent to form the gel structure.

ANL fabricated 2032 button cells of the following type: pre-gelled (liquid) electrolyte (composition: 1.5M $LiBF_4$ in EC/GBL (1:2 by vol%) + 3.0% advanced PEO polymer). The cells contained VEC electrolyte additive at the following levels: 0%, 1%, 3%, and 5% by weight. The cells were evaluated as pre-gelled liquid-electrolyte cells, because Daiso was unable to ship their standard initiator to ANL.

Figure 14 shows 1C rate charge/ discharge data on a 2 mAh 2032 button cell, operating at 25°C, which employs the Daiso pre-gelled electrolyte and our Gen 2 electrodes. The capacity density of the cathode in this cell is similar to that of the Gen 2 cathode in our baseline cells (~150 mAh/g). The cell operated with no initial capacity decay and exhibited excellent Ah efficiency.

VEC, as an electrolyte additive, was studied in cells that employ the Diaso pre-gelled liquid electrolyte to assess its effects on performance and life, if any. In these cells not much of an effect was observed at room temperature. However, at elevated temperature (55°C) VEC appeared to enhance and somewhat stabilize the capacity of these cells, which operated with a lower rate of capacity fade than cells without the VEC additive (see Figure 15).

The Diaso pre-gelled electrolyte appears to enhance the thermal safety characteristics, relative to standard LP40 electrolyte. Figure 16 shows DSC data, where charged (delithiated) Gen 2 cathodes are in contact with LP40 (1.0M $LiPF_6$ /EC:DEC [1:1]) and Daiso pre-gelled electrolyte. The initial exotherm is shifted to a higher temperature when the Diaso pre-gelled electrolyte is used. We would anticipate further improvements in the safety characteristics after the electrolyte is gelled.

In HPPC tests, as shown in Figure 17, cells using the pre-gelled Daiso liquid electrolyte exhibit ASI values that meet the FreedomCAR requirements. Based on conductivity measurements, there is not much of a decrease in

conductivity that results from the curing to form the gel. Therefore, it is anticipated that full gelation of the electrolyte solution will not increase the cell ASI very much.

DKS Cells *(PEO macromonomer gel)*

The DKS macromonomer is comprised of trifunctional acrylate groups that are bound to random copolymers of ethylene oxide (EO) and propylene oxide (PO) (with a molecular weight of ca. 8,000 g/mol) (see Figure 18). A gel precursor solution was prepared by mixing 5 wt% of the macromer and 95 wt% of 2M $LiBF_4$ in EC/GBL = 3/7 (by Vol) with a radical initiator. The viscosity of the precursor solution is an important factor for cell fabrication. A precursor solution with high viscosity will not fully penetrate inside of the electrode pores resulting in low capacity. The DKS macromonomer precursor solution does not have any viscosity problems, as seen in Figure 19. It readily fills all the pores of our Gen 2 electrodes. Our Gen 2 baseline electrode laminates were soaked in the precursor solution and a porous PE separator (filled with precursor electrolyte) was interposed between two electrode laminates to fabricate a pre-cell. The pre-cell was heated up to ca. 80°C for curing. The effective area of positive electrode was 17.5 cm^2 and the estimated cell capacity was around 20.6 mAh. This work clearly shows that use of the DKS macromonomer precursor solution presents no serious problems in cell fabrication.

Cells built with our Gen 2 baseline electrodes and the DKS gelled electrolyte (tri-functional PEO macromonomer + $LiBF_4$/EC:GBL) are being evaluated for the HEV high power application. The C/5 capacity density of the cathodes in these cells were >150 mAh/g, similar to the Gen 2 baseline cells. Figure 20 shows that cells employing the DKS technology have good rate capability.

Despite the promising 2C-rate discharge performance (see Figure 21) of the DKS cells, the ASI of the cell was somewhat higher than that of the Gen 2 baseline cells (see Figure 22). When ANL monitored ASI values of the cell over an 8-week accelerated aging period (60% SOC and 50°C temperature), the ASI of the cell continued to increase during this aging test, see Figure 23. Aging data is expected to improve as the quality of the cells improve, which should occur as a result of DKS joining forces with Sharp.

Our preliminary evaluation of 2 pouch cells, built by DKS, was quite promising. The ASI values were a little high (~50 ohm-cm^2 on 18-sec discharge pulses), but the capacities were good. Additional Gen 2 electrode materials were sent to DKS for the purpose of fabricating more cells with their gel-polymer electrolyte system and these cells, fabricated by Sharp, should be of higher quality than the first two pouch cells.

Future Work

ANL will initiate curing experiments to fabricate Daiso gel polymer electrolyte as soon as we receive their prescribed initiator, a highly branched PEO and cross-linking agent. After setting-up the gel fabrication technology, ANL will conduct investigations to determine how various electrolyte additives and LiBOB salt effect the performance characteristics of this system.

ANL shipped sets of Gen 2 baseline electrodes and a quantity of LiBOB salt to DKS for them to build cells with Gen 2 baseline electrodes and 2 different salts. These cells will be supplied to ANL for more detailed evaluations.

Also, ANL has received cells built by Quallion that contain the Showa Denko gel electrolyte, in a partially-cured state. These 110 mAh prismatic cells will be used for an initial evaluation of the Showa Denko technology, since Quallion has had problems curing the electrolyte in cells that employ our Gen 2 cathode material. The partial cure level in these cells is near 60% and Quallion continues to work on achieving a 100% cure in future cells built with our Gen 2 cathode material.

	ANL	Ultralife
Cathode	$LiNi_{0.8}Co_{0.15}Al_{0.05}O_2$	$LiNi_{0.8}Co_{0.15}Al_{0.05}O_2$
Anode	MCMB/MAG10/GDR	MCMB
Electrolyte	Gen2 (1.2M $LiPF_6$ in EC:EMC(3:7)) W/0, 5% VEC or VC / 1.0M $LiPF_6$ in EC:DEC(1:1)	- ELT series
Polymer	PVdF-HFP copolymer (Kynar Flex 2801 grade)	PVdF-HFP copolymer (unknown grade)

* For PVdF gel polymer cells, GEN2 electrodes & electrolyte were used.

Table 1. Cell chemistries used in PVDF gel polymer electrolyte cells.

Cell	Dimensions (mm)			Capacity (mAh)	Target
	Thickness	Width	Length		
PLI-ANL*	0.6~0.7	20	20	20~40	- Safety **(ARC)**
UBC10106102	1.0	102	106	~ 500**	- **Gas evolution**
UBC34106102	3.4	102	106	~ 3000**	- **Adhesion**

* Dimensions are only for actual cell size without pouch.
**Nominal capacity
Table 2. Specification of PVDF gel polymer cells evaluated by ANL.

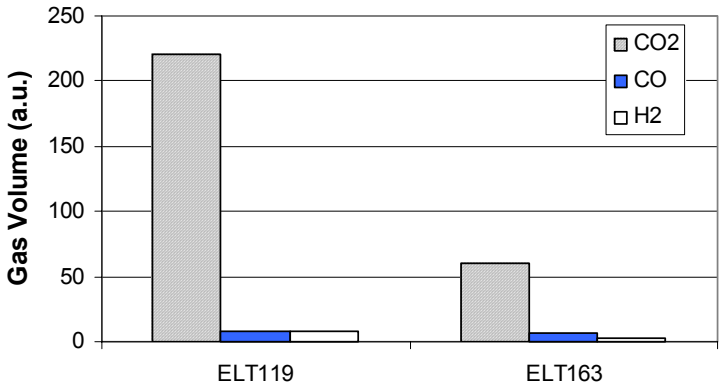

Figure 1. Gas analysis data obtained on 3Ah Ultralife cells that were cycled and aged at 50°C.

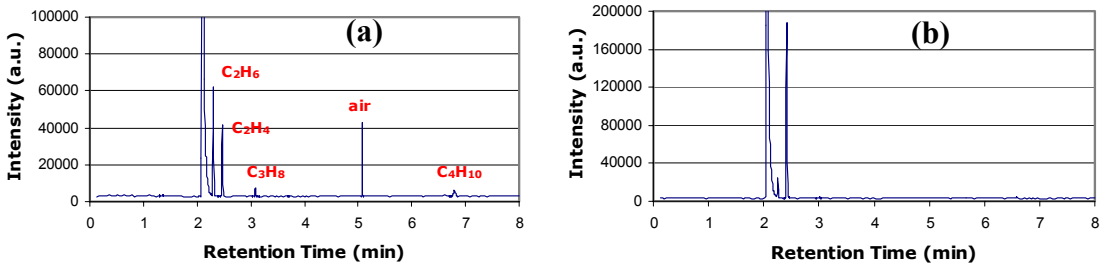

Figure 2. Gas chromatograms of the gases generated in 3 Ah Ultralife cells: (a) with standard electrolyte and (b) with electrolyte containing 2% VEC and 2% VC additives.

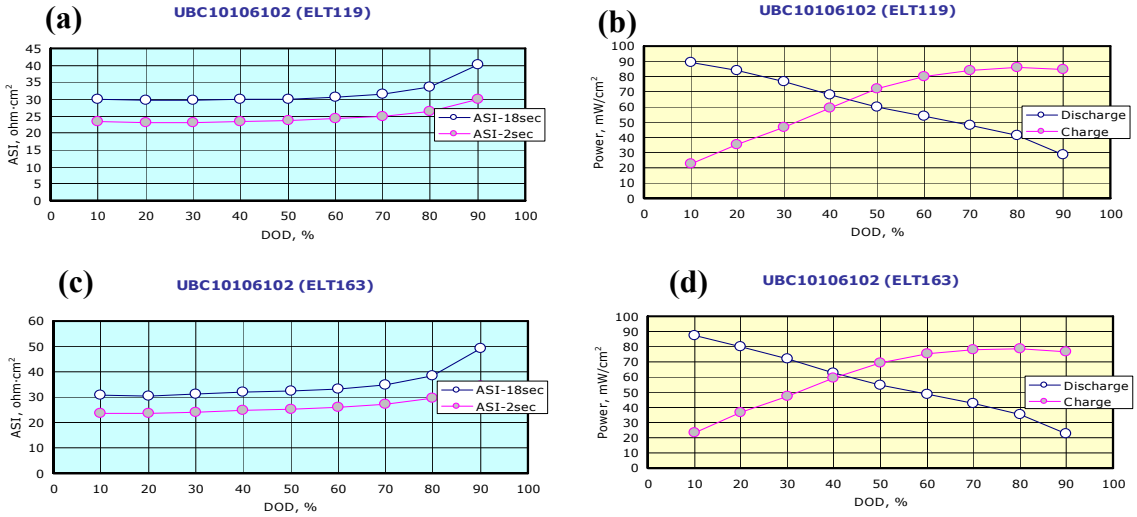

Figure 3. HPPC test results on 500 mAh Ultralife PLI cells: (a) & (b) ASI and power data on standard cell (ELT119) and (c) & (d) ASI and power data on cell with 2% VEC & 2% VC as additives (ELT163).

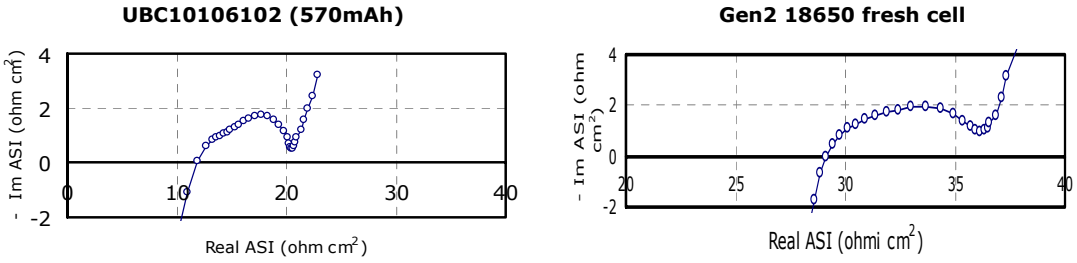

(a) (b)

Figure 4. Comparison EIS curves for: (a) Ultralife PLI pouch cell and (b) Gen 2 baseline 18650 cell.

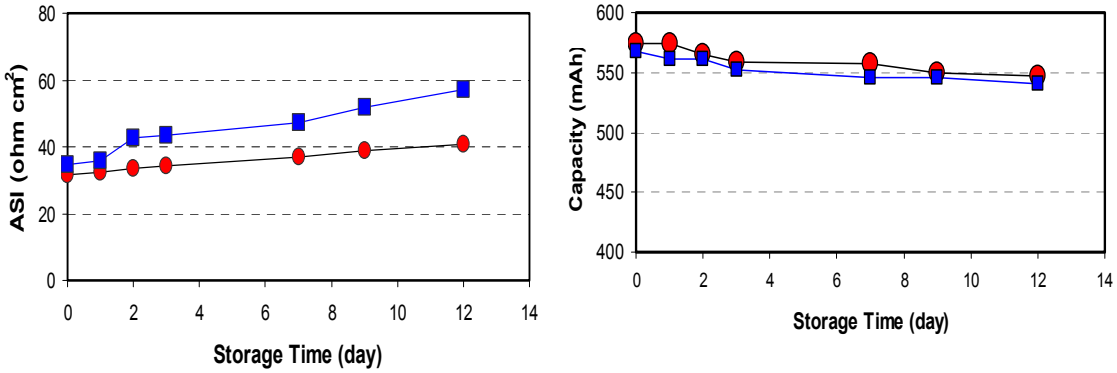

(a) (b)

Figure 5. Results of accelerated aging tests (60% SOC and 50°C) on Ultralife 500 mAh PLI cells: (a) ASI vs storage time and (b) C/5 capacity (3.0-4.1V) vs. storage time. The cell capacity was intermittently checked at RT.

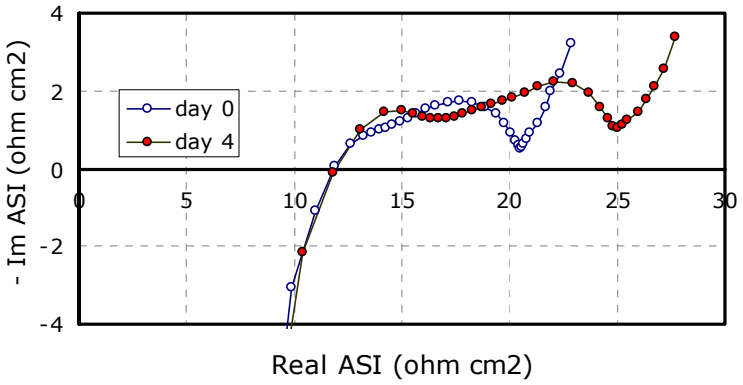

Figure 6. EIS curves on Ultralife 500 mAh PLI cell during 60% SOC & 50°C aging.

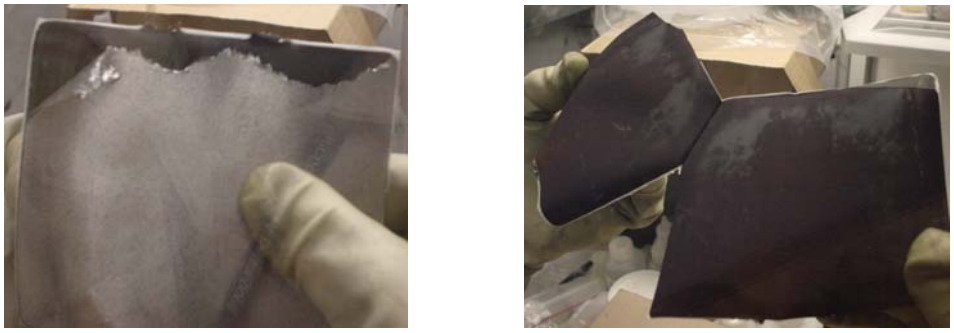

(a) (b)

Figure 7. Post test observations on Ultralife built cell: (a) delamination of cathode from Al current collector and (b) weak adhesion & areas of stress within anode laminate.

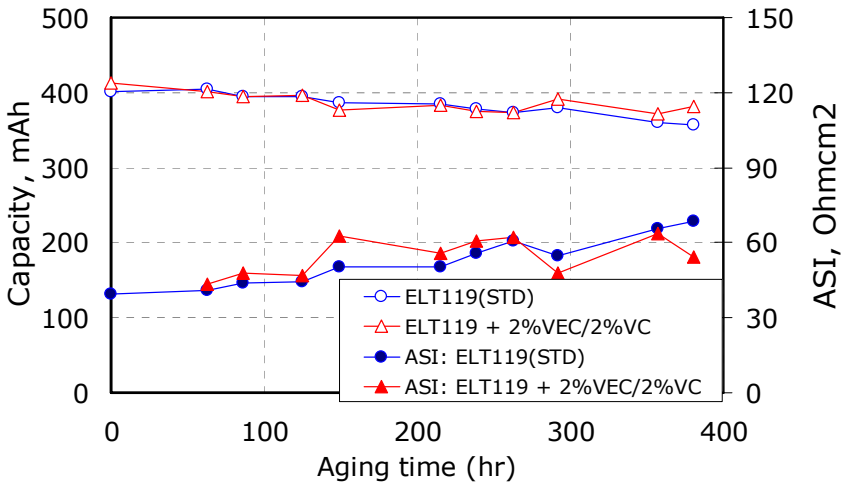

Figure 8. Discharge capacity density and impedance vs. time during aging at 60% SOC & 50°C.

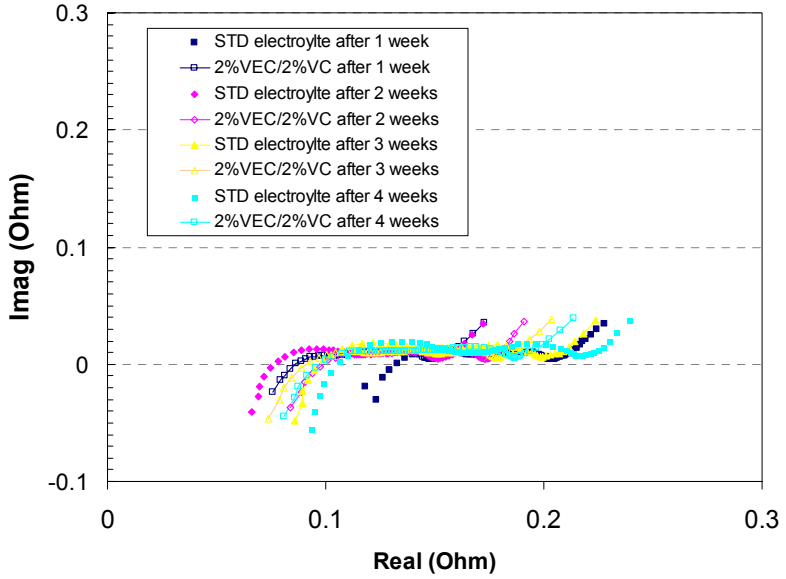

Figure 9. EIS curves on Ultralife 500 mAh cells aged at 60% SOC and 50°C.

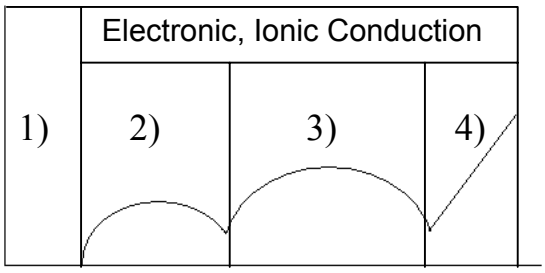

Figure 10. Schematic of EIS curve: 1) bulk ohmic resistance—current collectors, electrolyte, & separator; 2) surface film impedance—Li^+ migration through insulating layer; 3) charge transfer impedance--across the surface film/active mass interface; and 4) diffusion and more--solid state diffusion of Li within active materials.

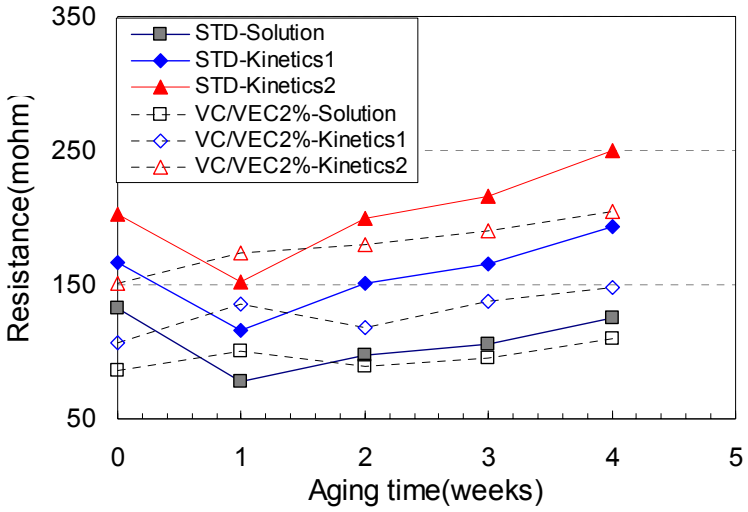

Figure 11. Component level impedance changes as a function of aging time, as derived from EIS data on Ultralife 500 mAh cells.

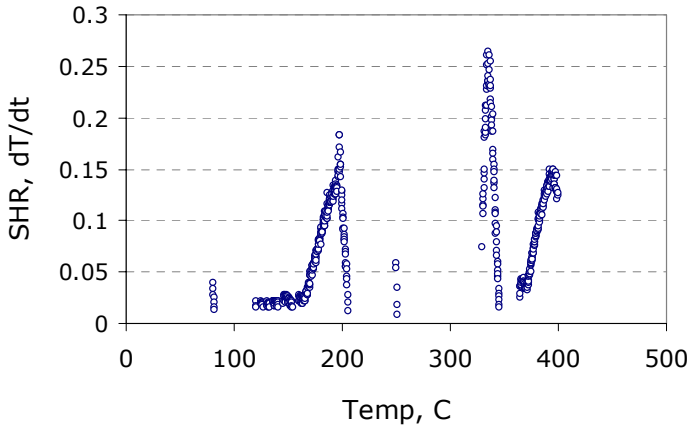

Figure 12. ARC test data on PVDF PLI button cell built at ANL.

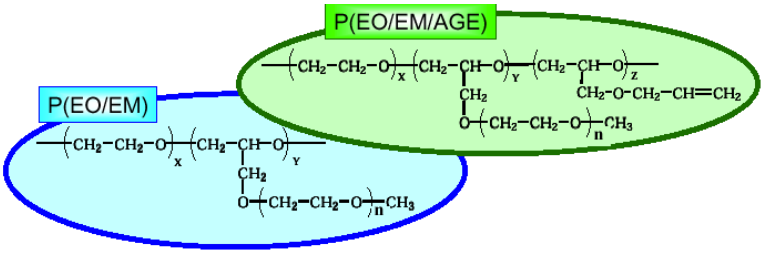

Figure 13. Chemical structures of Daiso branched PEO-based gel polymer electrolytes.

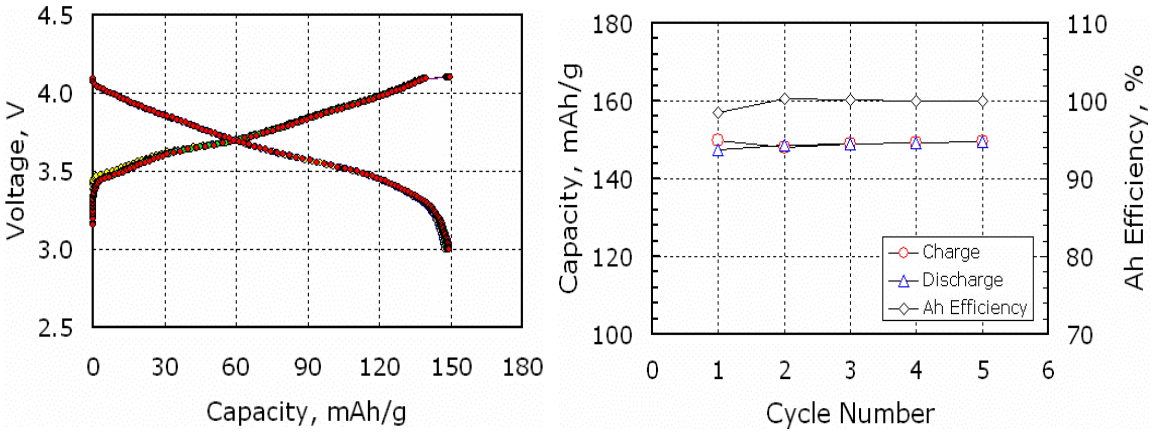

(a) (b)

Figure 14. Data from 5 charge/discharge cycles (at 1C rate) on a 2032 button cell containing 1.5M LiBF4 in EC/GBL (1:2) with less than 5% of Daiso advanced PEO, not cured: (a) charge/discharge voltage vs. capacity profiles and (b) capacity & efficiency vs. cycle number.

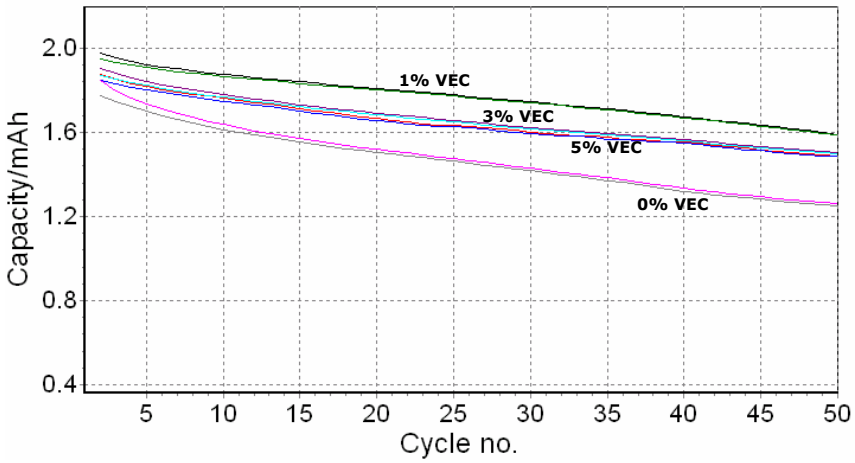

Figure 15. Effect of VEC as an additive in the Diaso electrolyte on 2032 button cells being cycle tested at 55°C.

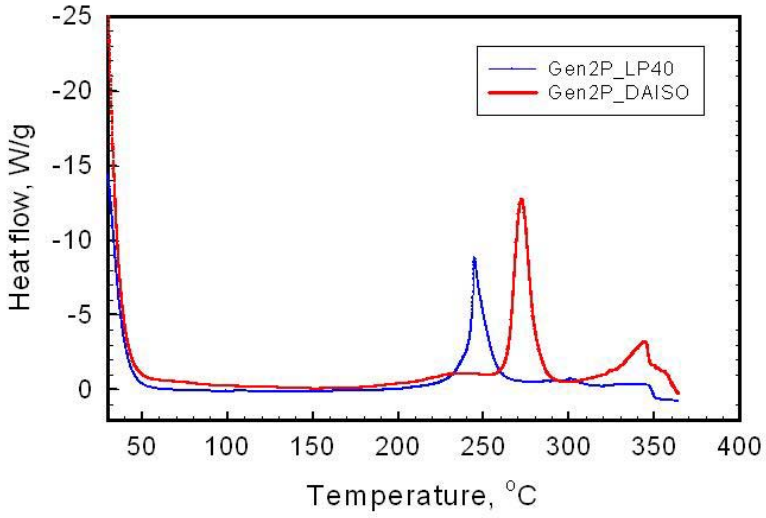

Figure 16. Comparison DSC data on charged Gen 2 cathode with LP40 electrolyte and Daiso pre-gelled electrolyte.

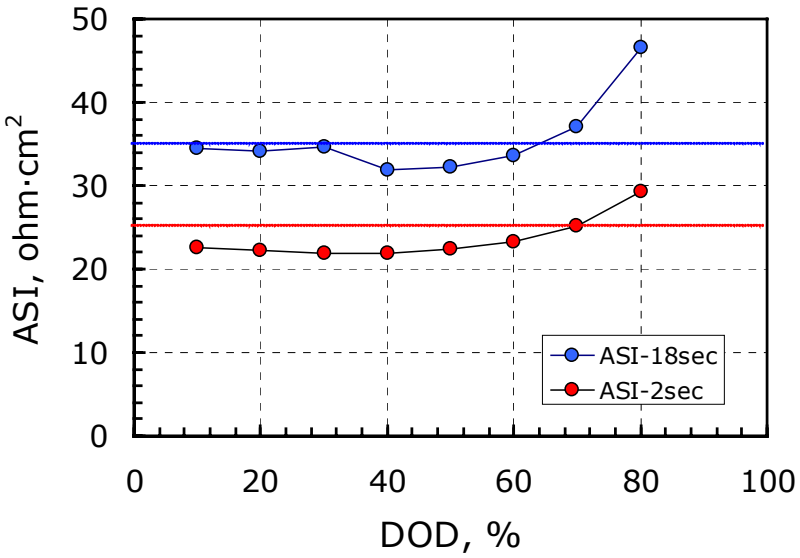

Figure 17. Initial ASI data on a cell with Daiso pre-gelled electrolyte and Gen 2 electrodes.

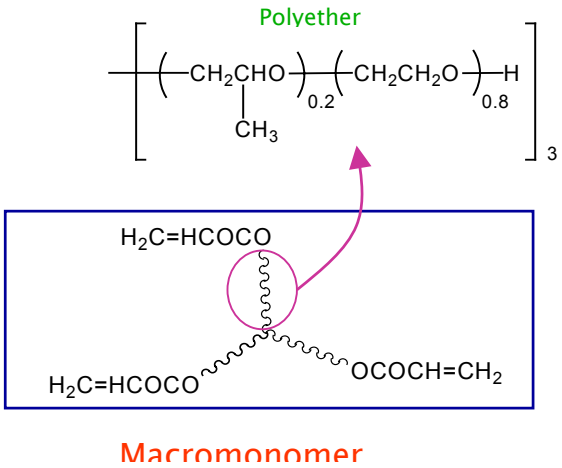

Figure 18. Chemical structure of DKS macromonomer.

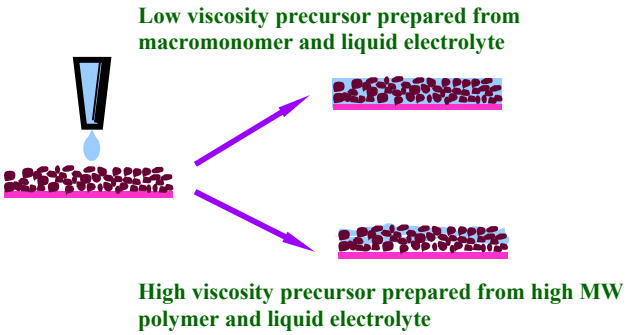

Figure 19. Shape of electrodes after impregnation of precursor solutions according to the viscosity.

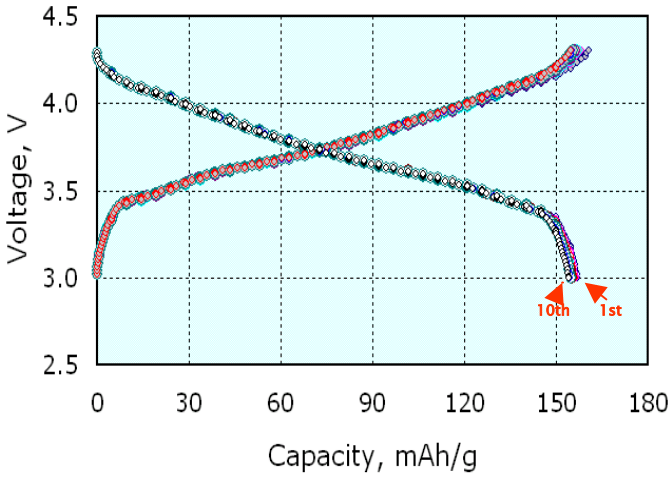

Figure 20. Charge/discharge voltage vs. capacity data from 10 cycles on a DKS gel polymer cell that incorporates our Gen 2 electrodes.

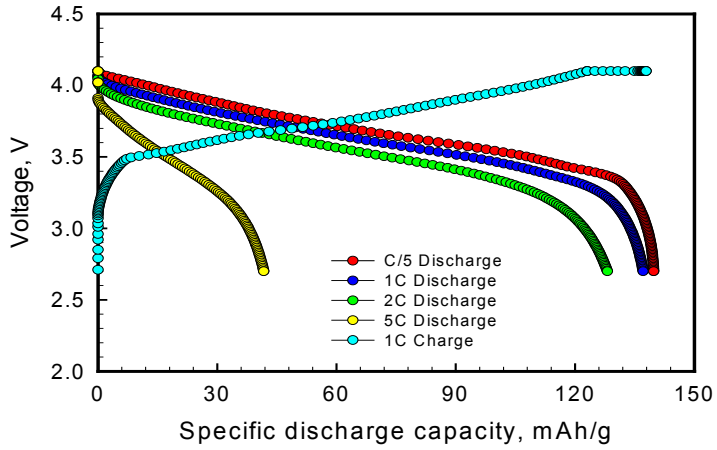

Figure 21. Rate capability of DKS gel polymer cell that incorporates our Gen 2 electrodes.

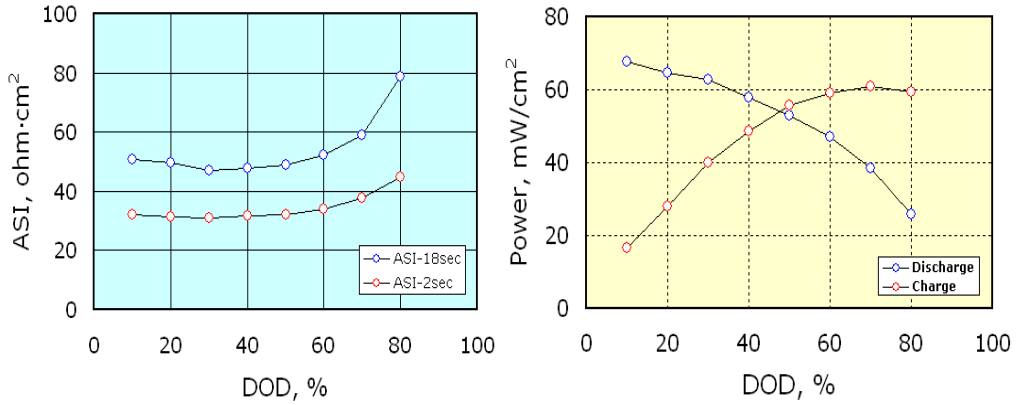

Figure 22. ASI and power/cm^2 vs. DOD data, from HPPC tests, on a DKS gel polymer cell that incorporates our Gen 2 electrodes.

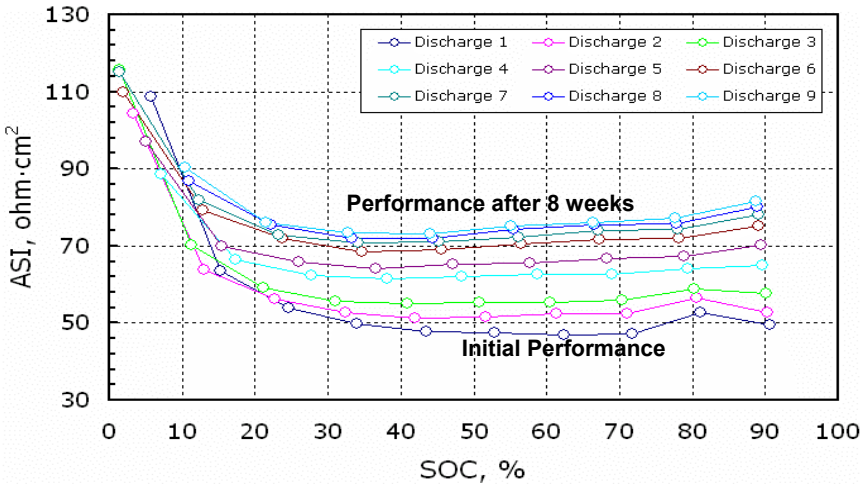

Figure 23. ASI changes in DKS gel polymer cell (with Gen 2 electrodes) during aging at 60% SOC and 50°C, as measured by HPPC tests.

III.D.4. Low-Cost Cell Packaging

Andrew Jansen, Khalil Amine, David Chaiko, Argentina Leyva, and Gary Henriksen
Argonne National Laboratory, Argonne, IL 60439
(630) 252-4261; fax (630) 972-4461; e-mail: jansen@cmt.anl.gov

Stephen W. Cornell
Plastic Technology Partners, Naperville, IL 60540
(630) 357-2894; fax (630) 357-4384; e-mail: scornell.ptp@juno.com

---

Objective

- Explore novel approaches for reducing the cost of cell packaging for high-power lithium-ion batteries.

Approach

- Develop a flexible cell containment system using laminates that are barriers to air, moisture, and electrolyte.
- Develop a new class of organoclay nanocomposite materials that can greatly improve the barrier properties of the sealant layer.
- Develop a new class of organoclay nanocomposite materials that can improve the adhesion of the sealant layer to the aluminum foil layer and also serve as a feedthrough sealant.
- Develop a new flexible pouch design that limits permeation of electrolyte and moisture from the seal edges by means of pattern coating of absorbent near the seal areas.

Accomplishments

- Evaluated four different laminate rolls that were previously contracted to an industrial vendor, Rollprint, for manufacture. These rolls became this program's 2nd Generation of laminates.
- Determined from analysis of 1st and 2^{ond} Generation laminates that adhesive compatibility with electrolyte is critical.
- Evaluated numerous solvent cast adhesives, 2-part adhesives, hot-melt adhesives, and tie-layer adhesives for their compatibility with electrolyte at elevated temperature.
- Collaborated with Sumitomo Electric Industries (SEI) to develop HEV-sized flexible battery packaging.
- Obtained state-of-the-art commercial laminates for lithium-ion batteries from SEI. Evaluated this laminate in pouch tests with water, solvent, and electrolyte at various temperatures. Preliminary results look promising.
- Purchased and installed a custom-made co-rotating twin screw extruder to use in our development of organoclay nanocomposite materials.
- Produced an initial organoclay nanocomposite material with the new extruder and made it into a laminate for pouch testing.
- Established baselines using polypropylene and low-density polyethylene film pouches to use for comparison to organoclay nanocomposite films.

Future Directions

- Continue collaboration with Sumitomo Electric Industries to develop and evaluate their HEV-sized flexible battery packaging under abuse conditions.
- Investigate methods to improve the adhesion between aluminum (copper/nickel) and polyolefins for foil lamination and feedthrough assembly.
- Develop organoclay nanocomposite films for evaluation as a barrier/sealant layer and possible use as an adhesive material.

Introduction

The FreedomCAR Program issued new targets for the battery that is needed in a power-assist hybrid electric vehicle (HEV). The most important of these is the cost target, which has been increased to $500 per battery pack (at the 100,000 units/year production rate). The calendar life target remains at 15 years. This implies that for the estimated 48 cells in a battery pack, the cost per cell has increased to a more favorable target of $10.50 per cell. An earlier analysis indicated that the production cost of a 10-Ah cell is approximately $31 per cell. Of this cost, an estimated $15 per cell is devoted just to cell assembly and packaging hardware. The industrial developers projected that they can reduce costs to approximately $9/cell with design refinements, combined with high volume production. Reducing the cost of the hardware and the assembly process would go a long way to meeting this goal. The objective of this project is to explore innovative methods for reducing cell packaging costs in order to meet the FreedomCAR cost target. Argonne National Laboratory (ANL), in collaboration with several industrial partners, is working on low cost flexible packaging as an alternative to the packaging currently being used for lithium ion batteries.

Low-Cost Flexible Packaging

The ANL packaging approach consists of developing a low-cost flexible cell container based on plastic laminate technology. The concept is to fabricate a pouch-type container, consisting of a metal foil, which forms the support base for applying polymeric coatings. The layers of the laminate work synergistically to create a cell packaging material that has chemical resistance, heat sealability, and good rupture strength. The required properties of this laminate are as follows:

- A moisture barrier, which prevents ambient moisture from penetrating into the cell and reacting with electrolyte.
- An electrolyte barrier layer, which prevents electrolyte solvents from leaking out of the cell.
- A material incorporated into the sealant layer that neutralizes any HF that might form, thus protecting the cell and pouch from HF attack.

A sealant layer, which provides the seal between the laminates and also seals the laminates to the current feedthroughs, via a simple and inexpensive hot pressing process. The plan is to develop seals that will yield at the same pressure as the rupture disks in the present metal cans, which are a critical pressure relief safety component of the cells. Therefore, the pouch containment could eliminate the need for this expensive safety vent.

The loss of electrolyte solvent from the flexible cell package is one of the primary concerns for the cell cycle life performance. This phenomenon could lead to cell starvation and performance degradation. The solvent potentially could exit the pouch by three means: (1) through the laminate face, (2) through the edges where the two laminates are sealed together, and (3) at the feedthroughs where they seal to the pouch. In addition, the permeation of the solvent through the face of the laminate could lead to the degradation of the adhesive layers that bond the barrier films together, resulting in film delamination. Another concern is the permeation of moisture into the packaging. Potential pathways for entry of the moisture are the

same as those mentioned above for solvents exiting the pouch. The moisture permeation could cause degradation of the polymer sealant layer, the formation of HF due to the decomposition of the lithium hexafluorophosphate ($LiPF_6$), and the reaction with the lithium from the negative electrode to form hydrogen. The overall result is a degradation of cell life and performance.

Based on results from earlier work in this program it was decided to use a laminate construction approach with an additional layer of aluminum foil to minimize the effects of pinholes. This scheme consists of four layers: a tough polymer exterior barrier, typically oriented polyester; two 9-25 μm thick aluminum foils; and a polyolefin sealant layer, such as polyethylene or polypropylene. Rollprint Packaging Products Inc., an industrial converter company, manufactured several muti-layer laminates during the course of this development. Adsorbents can be incorporated into the pouch design to limit the passage of moisture that enters into the cell. An appropriate adsorbent was determined in previous year's effort and several methods of implementing this adsorbent were discussed then.

Our approach for evaluating the various films and laminates is to form them into pouches, fill them with a multi-component solvent system (with or without the $LiPF_6$ salt), seal the pouches, and store them at elevated temperature in a high humidity environment. We monitor the change in weight of each pouch to assess any gain or loss in weight. Weight gains would correspond to water ingress, while weight loss would correspond to solvent egress.

It was observed in this work that nearly all of the electrolyte-filled pouches suffered from delamination of the sealant/barrier film(s) from the Al foil. Such delamination would increase the permeation area by a factor of 1000 for a 10 Ah cell. Efforts were then directed to identifying better adhesives. A method was developed to evaluate commercial adhesives by applying the adhesive to aluminum foil and then soaking in electrolyte at elevated temperatures. The test strips were then examined periodically to look for signs of delamination or degradation. Numerous commercial adhesives were tested for their electrolyte compatibility; these include hot melt adhesive, two-part adhesives, epoxies, silicones, solvent-cast adhesives, and tie layer adhesives. In general, the tie-layer materials performed the best in the electrolyte soak test. A summary of these materials is listed in Table 1. The Tymor materials offered the best compatibility to date. They are polyolefin based materials usually with maleic anhydride grafted onto their backbone. It is not surprising that many of the commercial adhesives failed because this battery packaging application is outside of their intended use, which usually requires resistance to water and air only.

The search for a better adhesive material and method of applying the adhesive is on-going. A significant portion of the program's effort is devoted to this task, due to its importance; the lamination of the sealant film to the aluminum foil is the linchpin to attaining a calendar life of 15 years. It will also form the basis for sealing the metal feedthroughs between the two laminate sheets that comprise the pouch. The problem of sealing the feedthroughs to the pouch is very similar to that of adhering the sealant layer to the aluminum foil. In essence, the feedthrough is just a metal that must be attached to a sealant material just like the aluminum foil is attached to the sealant layer; only the dimensions are different.

Some effort was devoted to developing the feedthrough during this year's program. Three areas of concern were identified that must be addressed for a successful feedthrough design: the voltage drop down the length of the feedthrough; the temperature rise of the feedthrough; and delamination, or separation, of the feedthrough from the laminate.

It is assumed that identifying an appropriate adhesion material and method will solve the delamination concern. A simple Excel spreadsheet program was written to explore the voltage drop and temperature rise in the feedthrough in the most severe condition, which is during the 18-sec pulse. For a battery pack that consists of 48 cells at 3.5 V each, a 25-kW pulse would imply that 149 Amps is flowing through each feedthrough. In the spreadsheet it was further assumed that one feedthrough was copper, the other was aluminum, each feedthrough is 5 cm long, the resistance of each lead would be equal, and the voltage drop due to the

feedthroughs would be 0.5 % of the cell voltage (18 mV). These parameters can be varied in the spreadsheet, as well as the type of metal.

The results of the model indicate that the aluminum feedthrough would need a cross-sectional area of at least 0.24 cm^2 and the copper would need at least 0.15 cm^2 cross-sectional area. The actual feedthrough would most likely be a rectangular bar with either rounded edges or an elliptic shape to prevent tearing of the laminate sheet. The bar must not be too thick as this would distort the face of the pouch and be difficult to seal; a thickness of 1 mm would be appropriate. Thus, the aluminum feedthrough would be approximately 1 mm x 24 mm and the copper would be approximately 1 mm x 15 mm.

Assuming that the temperature rise due to resistive heating (I^2R) is under adiabatic conditions is a fair assumption to make during the 18-sec pulse. This conservative assumption essentially means that the heat cannot be dissipated readily during the short duration of the current pulse. Under such conditions, the temperature rise is 8.0°C in the aluminum feedthrough and 9.3°C in the copper feedthrough. These temperature rises are not insignificant but are manageable. If the feedthrough is undersized, and the current pulse is excessive in magnitude or duration, it is possible that the feedthrough could heat up to the point where the sealant film melts, causing the pouch to rupture. Keep in mind that the feedthrough is also responsible for conducting the heat generated by the cell out to the thermal management system. This spreadsheet model shows that it is probably more important to design the feedthrough to maximize thermal conduction rather than just minimize the IR voltage loss.

Sumitomo Electric Industries (SEI) is one of the largest producers of flexible packaging for batteries in the world. ANL has been collaborating with SEI for the last two years in the area of low-cost flexible packaging for lithium-ion batteries. Meetings have taken place between ANL staff and SEI staff on several occasions, here in the U.S. as well as at their facility in Japan. As a result of these meetings, SEI has dedicated several staff members to achieving ATD's flexible packaging goal of 15 years. Their approach to meeting the severe conditions posed by the lithium-ion system is similar to the approach at ANL, namely, the sealant layer is a polyolefin-based material and they incorporate an adsorbent material in the sealant layer to adsorb any moisture that diffuses in from the pouch edges.

As part of Argonne's collaboration with SEI, they have sent ANL a roll of their latest laminate for our evaluation in December of 2001. Pouches were made from these laminates by cutting out 7.6 cm squares, heat-sealing on three sides, filling with the desired liquid, and heat-sealing the final side. The liquid being water, solvent blend (EC/EMC/DMC/DEC/PC), or electrolyte blend (1M $LiPF_6$ in EC/EMC/DMC/DEC/PC), as was done in previous pouch tests. The pouches were stored at 55 °C, 37 °C, and room temperature. Duplicate pouches were made for each temperature condition to check for reproducibility. These accelerated aging tests are on going, but preliminary results appear very promising. There has been no significant weight change observed for the pouches filled with water (Fig. 1a), even at 55 °C. The pouches filled with electrolyte (Fig. 1b) also had no significant weight change at room temperature and 37 °C; there was a slight weight loss at 55 °C.

The ability of the flexible pouch to survive thermal changes from –40 to 60 °C is a concern that must be addressed. SEI has agreed to make 30 HEV-sized pouches at their Japanese facility for ANL to thermally cycle. The pouches will be filled with 50 g of the electrolyte blend and have two metal feedthroughs sealed to the pouch. No electrodes will be inside the pouches. A general test plan was discussed and will be finalized when the pouches arrive. This will be discussed more in next year's annual report.

The calendar life goal of 15 years poses a significant challenge to the conventional flexible packaging approach. With this in mind, ANL proposed to investigate a novel organoclay nanocomposite barrier material that was already being developed within ANL under an unrelated program. This material is based on a unique method of combining natural clays with organic polymers to form organoclays. The organoclays are then compounded with traditional polymers to form barrier films. This year's effort was to determine if

these materials can offer significant reductions in solvent/electrolyte permeation rates.

A few preliminary organoclay nanocomposite materials were made in a small extruder offsite and then pressed into films with a Carver press between heated platens. These films were then made into pouches filled with water, solvent blend, or electrolyte blend and monitored for weight loss at room temperature. While these films were far from ideal due to defects such as occlusions, air bubbles, and non-uniform thickness, they did provide very promising initial test results. They demonstrated that the organoclays are completely compatible with our electrolyte, no swelling or disintegration was observed. More importantly, the permeation rates for water, solvent and electrolyte blends in these organoclay films appear to be much lower than the permeation rates with commercial low density polyethylene (LDPE). These data are presented in Fig. 2 (the solvent and electrolyte pouches for PE-165-Z leaked due to pinholes, and were discarded).

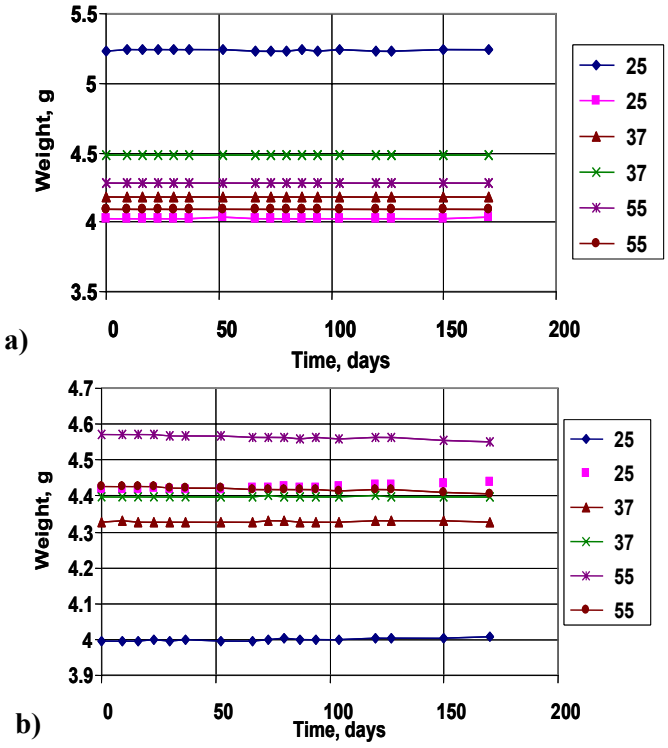

Figure 1. Weight losses for Sumitomo Electric Industries' laminates made into pouches by ANL at several storage temperatures with: a) water inside; and b) 1M $LiPF_6$ in EC/DEC/DMC/EMC/PC inside.

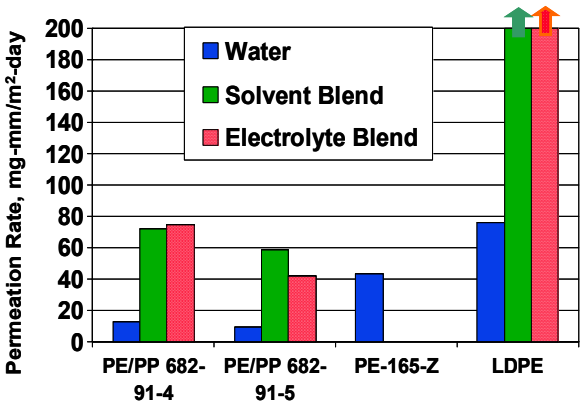

Figure 2. Summary of permeation rates for preliminary organoclay nanocomposite pouches filled with water, solvent blend (EC/DEC/DMC/EMC/PC), or electrolyte blend (1M $LiPF_6$ in EC/DEC/DMC/EMC/PC) at 25°C compared against low-density polyethylene (LDPE). Film pouches only (no aluminum foil substrate).

The thermal tolerance of the organoclay materials were also investigated using a Differential Scanning Calorimeter (DSC). This data indicates no decomposition occurs up to 400°C in inert atmosphere, which is well above normal polymer processing temperatures. To demonstrate this point, polyethylene nanocomposites were successfully extrusion coated onto aluminum at 320°C by an outside vendor. Most commercially available organoclays begin to decompose at 150°C, with catastrophic decomposition beginning at 200-210°C.

The nanocomposite films that were made offsite were done so using a twin-screw extruder having a barrel L/D of 8. While these films appeared crystal clear under light microscopy, X-ray results showed a small amount of non-exfoliated clay. Even though the permeation results shown in Fig. 2 are promising, it was felt that a better extruder was needed to produce a superior defect-free film. It was decided that the best course of action was to purchase an extruder and install it onsite. A new co-rotating, twin-screw extruder was made by NFM Welding Engineers (Massillon, OH) with an L/D of 52. The extruder is custom designed, per ANL specifications, for high shear, long residence time, which is ideal for nanocomposite processing. This is a lab-scale machine with nominal production capacity of 14 kg/hr that is capable of providing realistic scale-up data. The extruder barrel is fitted with several ports

for reactive processing and devolatization of polymer solutions – useful for custom synthesis of polymeric materials. It should produce complete clay dispersion, and hence, even better barrier improvements.

ANL received the new extruder in December of 2001, assembled it, connected it to the required utilities, and began shake-down runs in March of 2002. A schematic of the extruder with the accompanying equipment is provided in Fig. 3 and a photo of the complete unit is given in Fig. 4. Presently, the extruder is only capable of producing a round bead that is chilled and then fed into the pelletizer; it cannot produce films. The film head was planned to be purchased at a later date, once it was determined that the extruder was capable of producing organoclay nanocomposites. Small films could be made using hot platens in the Carver press, as was done before.

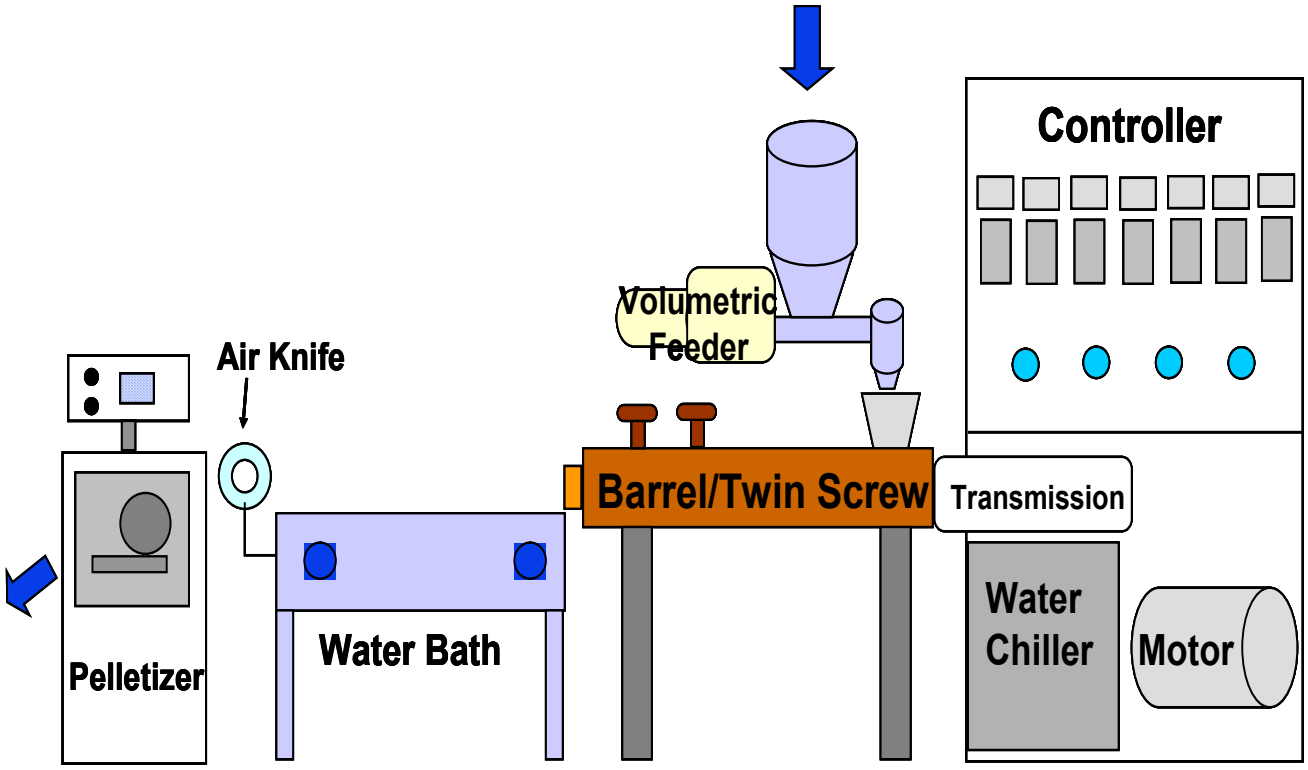

Figure 3. Schematic of ANL's extruder equipment recently installed for development of organoclay nanocomposites.

A few laminates were made in this manner from organoclay nanocomposite pellets produced in shakedown runs with the new extruder. Pouches were made from these laminates and filled with solvent or electrolyte blend and monitored for weight loss at 55°C. These preliminary results, shown in Fig. 5 for the pouch filled with the solvent blend, are encouraging. The pouch filled with electrolyte blend failed early on due to a pinhole near the seam. This defect again emphasized the difficulty in producing quality films with a Carver press.

Based on the encouraging results of the preliminary nanocomposite materials, it was decided that the additional expense of the film head was warranted. An order was placed for a 10-cm wide film head, take up spools, and a gear pump. The gear pump is necessary to minimize flow fluctuations, which are common for twin screw extruders that have high shear rates. It is hoped that this new equipment will arrive by February of 2003.

Figure 4. Photo of ANL's extruder equipment before shake down runs.

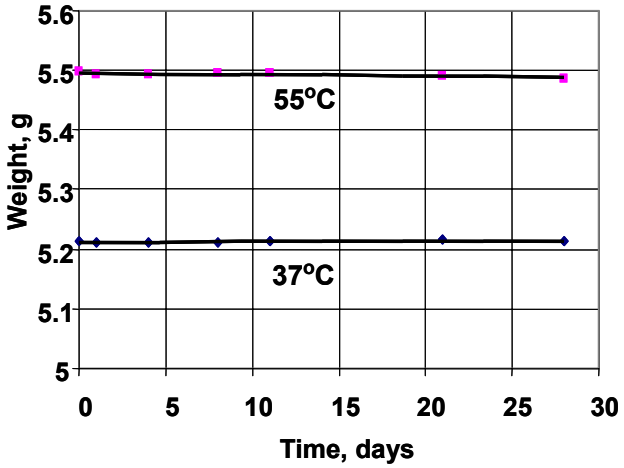

Figure 5. Weight losses for initial organoclay nanocomposite pouches made with ANL's new extruder, filled with solvent blend (EC/DEC/DMC/EMC/PC).

Future Work

We plan to continue our close working relationship with Sumitomo Electric Industries. We will conduct accelerated aging of their newest flexible packing technology, which is being supplied to ANL as pouches sized for 9-10 Ah high-power lithium-ion cells. The test plan will include thermal cycling, as well as elevated temperature aging. Results of these tests will be supplied to SEI for their use in refining their flexible packing technology.

We plan to work on improving the adhesion between our metal feedthroughs and the polyolefin packaging. The metal feedthroughs will be Al for the positive electrode and copper/nickel for the negative electrode. A similar problem exists in adhering the barrier layer film(s) to the Al foil, as part of the flexible laminate. Therefore, we will continue to search for and evaluate promising adhesives for this application, as well as to develop optimal methods for applying the adhesives.

In the area of organoclay nanocomposite technology, we will continue to develop and evaluate nanocomposite films for use as water and electrolyte barrier layers and we will study the use of nanocomposites as improved adhesives. When our film head is built and installed on the extruder, we will be capable of extruding small quantities of high quality thin films of many different organoclay nanocomposite compositions for evaluation. These films will be of much better quality than those that we are currently able to make on a heated-platen Carver press. This will dramatically accelerate our development and evaluation of this promising technology for use as barrier layer materials.

Adhesive	Manufacturer	Results
Tymor 1N05 (Modified Polyolefin)	Rohm & Haas	Held tight
Tymor 1221E (PE-based)	Rohm & Haas	Held tight
Tymor 1258B (PE-based)	Rohm & Haas	Peel with greater force
Tymor 2216 (PP-based)	Rohm & Haas	Peel with moderate force
Admer QF551A (anhydride modified copolymer PP-based)	Mitsui Chem.	Peel with moderate force
Primacor 5980I (ethylene acrylic acid)	DOW Chemical	Peel with moderate force
Primacor 3340 (ethylene acrylic acid)	DOW Chemical	Peel with slight force
Primacor 3440 (ethylene acrylic acid)	DOW Chemical	Peel with slight force
Eastobond Copolyester 19411	Eastman Chem.	Peel with slight force
EMAC SP2220 (ethylene-methyl acrylate copolymer)	Voridian (Eastman)	Completely delaminated

Table 1. Summary of "tie-layer" adhesive material compatibility with electrolyte blend (1M $LiPF_6$ in EC/DEC/DMC/EMC/PC) at 55°C for 24 hours. Material was hot-pressed onto aluminum foil.

IV. LONG TERM RESEARCH

IV.A. Introduction

The Long term Research Activity is supported by the DOE's FreedomCAR and Vehicle Technologies Program (DOE-FCVT) to help develop high-performance rechargeable batteries for use in electric vehicles (EVs) and hybrid-electric vehicles (HEVs). The work is carried out in the Batteries for Advanced Transportation Technologies (BATT) Program by the Lawrence Berkeley National Laboratory (LBNL) and several other organizations, and is organized into six separate research tasks.

Background and Program Context

The development of an advanced battery for automotive applications is a difficult undertaking. There is a strong need to identify and understand performance and lifetime limitations to help guide battery scale-up and development activities. High cell potentials and demanding cycling requirements lead to chemical and mechanical instabilities, which are important issues that must be addressed. The BATT Program addresses fundamental issues of chemistries and materials that face all lithium battery candidates for DOE EV and HEV applications. The Program emphasizes synthesis of components into battery cells with determination of failure modes, coupled with strong efforts in materials synthesis and evaluation, advanced diagnostics, and improved electrochemical models. The selected battery chemistries are monitored continuously with periodic substitution of more-promising components. This is done with advice from within the BATT Program, from outside experts, and from assessments of world-wide battery R&D. The BATT Program also educates battery and electrochemical scientists who move on to work for battery developers.

Task Descriptions

The six primary BATT Program task areas are: (1) Cell Development, (2) Anodes, (3) Electrolytes, (4) Cathodes, (5) Diagnostics, and (6) Modeling. Task 1 comprises cell fabrication, testing and characterization, Tasks 2-4 are aimed at identifying new materials, and Tasks 5-6 support all BATT Program work. Brief summary descriptions of each task follow.

The Cell Development task has identified three "baseline" rechargeable Li cell chemistries. The polymer-electrolyte cell chemistry includes a Li metal negative electrode (anode), $Li(CF_3SO_2)_2N$ + cross-linked poly(ethylene) oxide (PEO)-based polymer electrolyte, and V_6O_{13} or a tunnel-structure Li_xMnO_2 positive electrode (cathode). The gel-electrolyte cell chemistry includes a natural graphite anode, $LiBF_4$ + cross-linked gel electrolyte, and a $LiFePO_4$ or $Li_{1.02}Al_{0.25}Mn_{1.75}O_{3.92}S_{0.03}$ cathode. The baseline Li-ion chemistry is based on the DOE Advanced Technology Development (ATD) Program "Generation 2" chemistry: a graphite-based anode, a $LiPF_6$ + ethylene carbonate-ethyl methyl carbonate (EC-EMC) electrolyte, and a $LiAl_{0.05}Ni_{0.80}Co_{0.15}O_2$-based cathode. Cell test data are posted on the web page http://isswprod.lbl.gov/battdatasite/.

The Anodes task seeks to overcome the two major problems associated with the carbon-based anodes used in all commercial Li-ion batteries: poor safety characteristics and short lifetimes. It is for these reasons that either improved anode structures or non-carbonaceous anodes must be developed as possible alternatives. Low-cost metal alloys with acceptable capacity, rate, cyclability, and calendar life are under investigation.

Polymer Electrolyte research aims to understand performance characteristics by studies of the transport properties of the electrolyte as a function of polymer and salt structure, polymer structural changes as a function of temperature, and interactions at the electrode/electrolyte interface related to transport and chemical/mechanical stability. A multi-pronged approach involving chemical synthesis, advanced diagnostic tools, and coordinated modeling studies is being used.

The identification and development of novel Cathodes are critical because of the fundamental cost and environmental limitations of cobalt-based and vanadium-based materials used in present-day rechargeable Li batteries. The focus of this effort is to develop a high-rate and stable MnO_2 cathode. Although manganese is a low-cost constituent, MnO_2 cathodes tend to lose capacity at an unacceptable rate. Research is directed at understanding the reasons for the capacity fade and developing methods to stabilize this material, as well as the evaluation of novel forms of MnO_2 cathodes.

Advanced Diagnostics are essential to investigate life-limiting and performance-limiting processes in batteries. We use post-test analyses and enhanced spectroscopic and microscopic techniques to investigate morphology, structure, and compositional changes of electrode materials. Examples include providing better understanding of electrode surface processes, and a detailed investigation of the Li/polymer interface *via* advanced microscopies and spectroscopies.

Sophisticated Modeling is required to support BATT Program Tasks 1-5. This effort brings physical understanding to complex interactions through the development of comprehensive phenomenological models. Models are being advanced to elucidate the failure mechanisms of Li battery components and to understand the mechanisms for thermal runaway.

This report summarizes the research, financial and management activities of the BATT Program in FY 2002. A website for the BATT Program, which provides Internet links to recent quarterly and annual reports, is found at http://www.berc.lbl.gov/BATT/BATT.html.

IV.B. Cell Development

IV.B.1 Cell Fabrication and Testing

Kathryn A. Striebel
Lawrence Berkeley National Laboratory, 70R0108B, Berkeley CA 94720-8168
(510) 486-4385, fax: (510) 486-7303; email: kastriebel@lbl.gov

---

Objective

- Benchmark the performance of new materials for low-cost and high-power Li-ion cells.

Approach

- Prepare uniform electrodes from novel battery materials, assemble them into baseline cells with proven components, and test them with a standard protocol.

- Disassemble the cells, after testing, for analysis by the diagnostic tasks within the BATT Program.

Accomplishments

- Demonstrated 65 Wh/kg, 155 Wh/l (on a cell basis), and a cycle life of 120 cycles for low-cost baseline cells $LiFePO_4$/gel/natural graphite (NG) from Hydro-Québec (HQ) have
- Attributed poor cycle life of the $LiFePO_4$/NG to side-reactions, not structural degradation of the active materials
- Characterized Gen 2 high-power baseline cell performance and fade mechanisms under constant current cycling.
- Received novel components for the baseline cells from Mitsui, Superior Graphite, U. Waterloo, MIT, ANL, SUNY Binghamton and the LBNL materials development tasks.

Future Directions

- Compare performance of $LiFePO_4$ from five sources, improve cyclability and evaluate additives
- Prepare and study low-cost baseline gel cells which need no external compression

---

Low-Cost Baseline Cell

Li-ion pouch cells containing $LiFePO_4$ and NG with either liquid electrolyte (12 cm^2 LBNL pouch cells) or gel electrolyte (3.8 cm^2 HQ pouch cells) were characterized for cycle performance and capacity fade. The $LiFePO_4$, prepared by U. of Montreal, routinely showed a capacity of 159 mAh/g-active at C/25 and excellent cyclability against a Li-metal anode, with an irreversible capacity loss (ICL) usually <3%. LBNL-$LiFePO_4$ cathodes showed similar high-rate capacity to the HQ-$LiFePO_4$ cathodes when a carbon-coated Al current collector was used.

Figure 1 shows the C/2 cycling performance of $LiFePO_4$/liquid electrolyte/NG pouch cells with three different carbon anodes in $LiPF_6$/EC/DEC electrolyte. The capacity fade rate in all cells is unacceptably high. Post-test electrochemical analysis of anode and cathode samples, in Swagelok half-cells, showed no evidence of capacity fade. Since both anode and cathode cycle efficiently with minimal fade against Li, one electrode must be causing the other to consume the cycleable Li in the cell. We propose that a minor impurity is migrating from the $LiFePO_4$ cathode to the anode causing instability of the solid electrolyte interphase (SEI) layer. Preliminary transmission electron microscopy (TEM) analysis of anodes cycled against $LiFePO_4$ suggest that there is iron on the anode. Confirmation of this mechanism will be obtained through further diagnostics analysis.

Also shown in Fig. 1 is the performance of an HQ gel cell (see pg. 8). The LPK (HQ) cathode has a lower loading than the LFP (LBNL) cathode. A slightly lower capacity is observed with the gel cell, compared to the LBNL-prepared pouch with $LiPF_6$ electrolyte and Celgard, due to the lower conductivity. The similar rate of capacity fade suggests a similar fade mechanism for the gel cell. Calendar life studies of cells at high state-of-charge (SOC) showed a similar fade rate, consistent with a solvent reduction mechanism on the charged anode. The performance of the 3.8cm^2 HQ gel cell was used to prepare the gap chart shown in Table. 1.

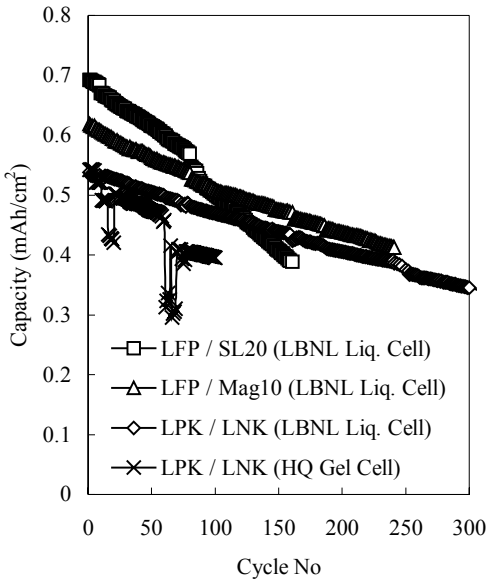

Figure 1. Discharge capacity during C/2 cycling of $LiFePO_4$/NG cells with three different graphites, 25°C.

$LiFePO_4$ samples in the form of powder or electrodes have been received from SUNY Binghamton, MIT, and the U. Waterloo. Full and half-cell studies of these $LiFePO_4$ samples vs. NG are currently in progress. Collaboration with the modeling effort (Newman) is proving very helpful in the comparison of electrode performance at different loadings.

High-Power Baseline Cell

Pouch cells and 100 mAh Quallion cells with the ATD Gen 2 chemistry were cycled at constant-current (C/2) and with the Power-Assist (PA) pulse profile. The capacity loss of the LBNL-pouch cell cycled at 100% depth-of-discharge (DOD) and room temperature for 1000 cycles was ca. 70% (0.07%/cycle). However, a cell cycled at 70% DOD showed no loss after 1000 cycles. Post-test diagnostics of the anodes showed no capacity loss. However, the nature of the SEI was dependent on cycling conditions. The cathode showed different capacity loss behavior due to a loss of conductivity, film formation on its surface and/or dislocation of structure. The 100 mAh Quallion cells cycled with the pulse and constant current profiles showed similar capacity loss rates. However, at an equivalent of 400 full cycles the area specific impedance (ASI) for the cell cycled at constant current increased by a factor of 2.5 while the PA cell impedance was essentially unchanged.

Anode Studies

The effect of anode compression on resistivity, performance and cycle life was studied in collaboration with Sastry (see pg. 55). NG anodes were prepared with SL-20 (Superior Graphite), and two amorphous carbon-coated NG's (Mitsui Mining). Matrix conductivity and current collector contact resistance were found to be strong functions of anode density. The amorphous-carbon coating reduced the electrolyte reduction peak on formation, compared to the SL-20, except for the highly pressed anodes. However, the amorphous carbon coating led to an increased overall ICL. The effect of pressing on the cycling stability of the anodes was less well-defined.

Gel Electrolyte Studies

Thermally crosslinkable gel samples from Daiso (Korea), Dai-ichi gel (Japan), and LBNL (Kerr) were evaluated. Cross-linking conditions for good conductivity and mechanical stability were studied as a function of curing time and temperature for polymer precursors mixed into $LiBF_4$/EC/γBL electrolyte. Gel electrolyte cells were assembled with five types of gel electrolyte with the Daiso gel showing the most promising performance. However, due to poor reproducibility, a decision was made to pursue the poly(vinylidene fluoride) (PVdF) type gel electrolyte cell.

		USABC Goals		HQ-gel cell
	Units	**Mid-Term**	**Long-Term**	**$LiFePO_4$/NG**
Power Density	W/l	250	600	618
Specific Power, Dischg (80%DOD/30 s)	W/kg	150	400	262 (18s)
Specific Power, Regen (20% DOD/10s)	W/kg	75	200	597
Energy Density	Wh/l	135	300	155
Specific Energy	Wh/kg	80	200	65
Life	years	5	10	NA
Cycle Life	cycle	600	1000	115 (100%DOD)
Power & Capacity Degradation	% rated	20	20	20
Ultimate Price (10,000 units @ 40 kWh	$/kWh	150	100	NA
Operating Environment	°C	-30 - 65	-40 - 85	25
Normal Recharge Time	hours	6	3 to 6	2
Fast Recharge Time, 40 to 80% SOC	minutes	15	15	NA
Continuous Dischg. in 1 hr	% rated energy	75	75	NA
Cell Weight (electrodes and electrolyte)	mg/cm^2			26
Cell Volume	cm^3/cm^2			0.011

Table 1. Gap Chart for Low-Cost Baseline Cell

Publications and Presentations

J. Shim, R. Kostecki, T.J. Richardson, X. Song and K.A. Striebel, "Electrochemical Analysis for Cycle Performance and Capacity Fading of a Lithium-Ion Battery Cycled at Elevated Temperature", *J. Power Sources* **112**, 222-230 (2002).

J. Shim and K.A. Striebel, "Effect of Electrode Thickness and Pressure on the Cyclability of Graphite Anodes in Li-ion Cells", *11th International Meeting on Lithium Batteries,* Monterey, CA, June 2002.

J. Shim, and K.A. Striebel, "Cycling Performance of Low-Cost Lithium Ion Batteries with Natural Graphite and $LiFePO_4$," *11th International Meeting on Lithium Batteries*, Monterey, CA, June 2002.

K. Striebel, A. Guerfi, J. Shim, M. Armand, M Gauthier and K. Zaghib, "$LiFePO_4$ Advanced Cathode Material for the BATT Program," *11th International Meeting on Lithium Batteries*, Monterey, CA, June 2002.

IV.B.2. Active Materials Characterization Using X-Ray Diffraction and Chemical Analysis

Thomas J. Richardson
Lawrence Berkeley National Laboratory, MS 62R0203, Berkeley, CA 94720-8253
(510) 486-8619, fax: (510) 486-8619, e-mail: tjrichardson@lbl.gov

Objectives

- Support cell development through structural characterization of active electrode components before, during, and after cycling.
- Investigate inexpensive, self-actuating overcharge protection mechanisms.
- Synthesize and evaluate alternative electrode materials.

Approach

- Address primary causes of capacity and power fading by correlating them with the composition and structure of electrode active materials using x-ray diffraction (XRD), vibrational spectroscopy, and voltammetry.
- Develop internal overcharge protection mechanism that becomes active when needed and allows continued, undegraded cycling of unaffected cells.
- Develop improved cathode materials *via* a rational approach to active material synthesis.

Accomplishments

- Evaluated cycled electrodes by XRD and Fourier transform infrared (FTIR) to assist in determining mechanisms for capacity and power degradation.
- Demonstrated self-actuating, internal overcharge protection in Li-TiS_2 cells using separators containing an electroactive polymer with voltage-sensitive electronic properties.
- Prepared and evaluated new manganese and iron phosphates with theoretical capacities similar to $LiFePO_4$ but with better electronic conductivity, intercalant ion mobility, and ease of preparation.

Future Directions

- Extend conducting polymer overcharge protection studies to Li-ion cells.
- Search for polymers with higher switching potentials for use in 3.5 V ($LiFePO_4$) and 4 V cells.
- Examine mixed oxide-phosphate phases for higher capacity while retaining good cycling stability.

Materials Characterization

Active materials for cells built at LBNL were characterized before use. Electrodes taken from cells cycled in Task 1.1 were examined for compositional and structural changes related to decreased performance. XRD and FTIR evaluation of the SOC and the uniformity of charge distribution in cycled cathodes has been useful in determining degradation

mechanisms in both ATD-type Gen2 and $LiFePO_4$ cells.

Overcharge Protection

Overcharging of Li batteries can shorten their lifetimes and create hazardous conditions including overheating, toxic releases, and even explosion. A low-cost, internal shunt mechanism is especially desirable for the large multicell stacks required for traction applications where failure of one cell can render the entire stack inoperative and where weight and volume are constrained. We are using a polymer with voltage-sensitive electronic properties to provide self-actuated, internal overcharge protection. The polymer is incorporated within the separator during cell assembly and is inactive during normal charging and discharging. If, at the end of charge, the safe voltage limit is exceeded, a reversible electrochemical reaction converts the polymer to a near-metallic state, temporarily providing an alternative path for the current, and preventing damage to the cell. On subsequent discharging, the polymer returns to its original state and the cell behaves normally. An example is shown in Fig. 2. The potential of an unprotected Li-TiS_2 cell cycled at a 2C rate goes rapidly to the 3.5 V limit at the end of charge (Fig. 2a). If the voltage were allowed to rise further, the cell would be damaged. In a protected cel (Fig. 2b), the polymer shunt becomes conducting at around 3 V, and a 20-fold overcharge can be applied without raising the voltage above 3.2 V.

The relationship between SOC, conductivity, and open-circuit voltage (OCV) of a conducting polymer is important in understanding its characteristics as a charge carrier, and these data are essential inputs for the model of our system being developed by Karen Thomas and John Newman. Measurements reported in the literature have generally not been quantitative due to the inherent difficulty of preparing a uniform sample. An electrode was specially designed to allow us to adjust the oxidation state of the polymer

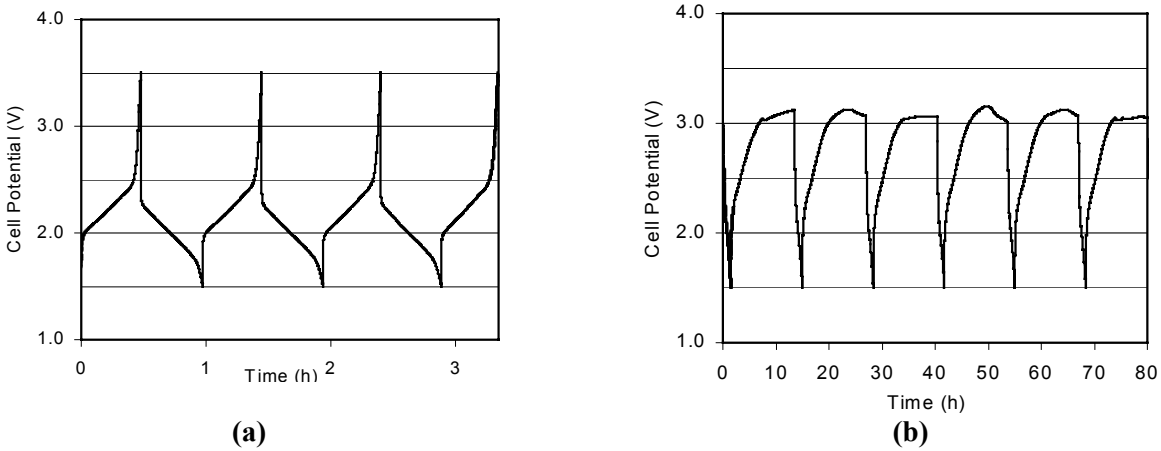

Figure 2. $LiTiS_2$ cells without (a) and with (b) internal polymer shunt.

electrochemically, while sequentially measuring its conductivity. A neutral polymer film was cast on a piece of stainless steel plate. A second stainless steel plate provided contact for the conductivity measurements. The polymer was brought to the desired SOC, the OCV was recorded after relaxation, and its electronic conductivity was determined from AC impedance measurements.

Cathode Development

Discovery of new cathode materials is essential to improving the energy and power performance of lithium batteries. The primary criteria for considering a new material are cost, toxicity, energy density, stability, and ease of preparation. Recent advances in the use of $LiFePO_4$ and related compounds have shown the importance of having a host lattice that is stable toward structural changes caused by exceeding voltage limits and interactions with other cell

components. Strongly bonded PO_4 sub-units in the metal phosphates contribute to their excellent stability and cyclability. The low electronic conductivity and two-phase nature of the intercalation reaction in $LiFePO_4$, however, result in poor utilization at high rates. We have prepared novel iron and manganese phosphates with the same metal-to-phosphate stoichiometry but with different crystal structures. These are easily synthesized in air with short reaction times. The metal-oxygen polyhedra share edges, rather than opposite corners as in $LiFePO_4$, giving them higher electronic conductivities. In addition, these structures accommodate mixed metal oxidation states, which should improve rate capability. Other materials under investigation are mixed phosphate-oxides such as $Fe^{III}{}_3O_3PO_4$, which contain some phosphate groups for stability, but have higher theoretical capacities closer to those of simple oxides. While a suitable high-capacity cathode material has not yet been found among the twenty compounds tested thus far, a better understanding of the structural factors that make a useful electrode material is being developed.

Publications and Presentations

M.C. Tucker, M.M. Doeff, T.J. Richardson, R. Fiñones, E.J. Cairns and J.A. Reimer, "Hyperfine Fields at the Li Site in $LiFePO_4$-Type Olivine Materials for Lithium Rechargeable Batteries: A ^{7}Li MAS NMR and SQUID Study," *J. Amer. Chem. Soc.*, **124**, 3832 (2002).

M.C. Tucker, M.M. Doeff, T.J. Richardson, R. Finones, J.A. Reimer and E.J. Cairns, "^{7}Li and ^{31}P Magic Angle Spinning Nuclear Magnetic Resonance of $LiFePO_4$-Type Materials," *Electrochem. Solid State Lett.*, **5**, A95 (2002).

T.J. Richardson, "New Phosphate-Stabilized Cathodes for Lithium Batteries," *11th International Meeting on Lithium Batteries*, Monterey, CA, June 2002.

IV.B.3. Research on Lithium-Ion Polymers Batteries Utilizing Low-Cost Materials

Karim Zaghib
Hydro-Québec, IREQ, 1800 Lionel Boulet, Varennes, QC, J3X 1S1
(450) 652 8019, fax: (450) 652 8424, email: karimz@ireq.ca

Objectives

- Fabricate Li-ion polymer cells (4 cm^2 area), graphite/gel polymer/$LiFePO_4$, using cell chemistries proposed by DOE.
- Investigate interfacial phenomena at the anode/electrolyte and cathode/electrolyte in Li-ion polymer cells.
- Determine the cycle life of Li-ion polymer cells at different temperatures (0.0 to 55°C) and self-discharge rates.
- Synthesize $LiFePO_4$ cathode material for Li-ion polymer cells.

Approach

- Synthesize and coat electrodes (anode and cathode) with low-cost materials for evaluation in Li-ion polymer cells containing gel polymer electrolyte.
- Investigate the effect of $LiFePO_4$ particle size, conductive carbon content in electrodes, salt concentration, mixed-salt concentration (from 1 to 2 M) on cell performance.

- Study the effect of pressure and interfacial phenomena on the performance of electrodes.

Accomplishments

- Produced electrodes (graphite and $LiFePO_4$) with optimized porosity that were submitted to LBNL.
- Assembled Li-ion cells with gel polymer and send (50% of the total cells) to LBNL for testing.
- Completed study on the effect of conductive carbon content on the performance of $LiFePO_4$ electrodes, and the influence of Li salt composition and concentration on cell performance.
- Determined that 10-psi cell pressure is necessary to obtain acceptable reversible capacity of anode and cathodes.

Future Directions

- Investigate the effect of $LiFePO_4$ particle size on performance in Li-ion gel polymer cells.
- Develop new gel polymer electrolytes that provide improved performance in cells.

The effect of pressure on the performance of the polymer gel electrolytes at the anode and cathodes interfaces was investigated by impedance spectroscopy and scanning electron microscopy (SEM). The data show that increasing the pressure to 10 psi is necessary to obtain good reversible capacity with both electrodes.

A problem with high irreversible capacity in the anode was observed. Consequently a major effort was undertaken to resolve this problem: (i) a new generation of natural graphite was examined and (ii) the effect of porosity of the anode and cathode was investigated. After optimization of the electrode porosity, the graphite exhibited better performance. In the first cycle, the irreversible capacity was reduced from 50% to less than 25%. The optimized electrodes of $LiFePO_4$ and graphite were evaluated in Li-ion gel cells. The reversible capacity increased by 15% (Fig. 3) compared to the first-generation cells. In the second set of ten cells (March 2002), a new polymer electrolyte based on poly(ethylene oxide) (PEO) that was coated and cross-linked at LTEE (Shawinigan) by electron-beam irradiation was evaluated.

We have studied the effect of solvent mixtures and type of Li salt on Li-ion polymer cell performance. The electrochemical performance of the HQ solvent, tetra-ethyl-sulfamide (TESA), mixed with ethylene carbonate(EC) (3/1) was comparable to EC/γ-butyrolactone (GBL) (3/1). With a mixed salt (1 M LiTFSI + 0.5 M $LiBF_4$ in EC/GBL), a higher capacity fade (>20%) was observed compared to the same molar concentration of the single salt (LiTFSI or $LiBF_4$).

Studies were completed on the effect of different amounts of conductive carbon (1 to 15%) on the performance of $LiFePO_4$ electrodes. The aim of these experiments is to identify the appropriate cathode composition to improve the high-rate performance. Mixtures of carbon black (3 or 6%) and graphite (6% or 6%) were used in electrodes containing a total carbon content of 9% and 12%. The data in Fig. 4 shows that an increase in the carbon content in $LiFePO_4$ improves the performance at high rates. A carbon content of 6% seems to be good compromise for energy and power, while still achieving a reversible capacity of 65% at 2C rate and 62% at 3C rate. Even with only 1% carbon, more that 50% of the reversible capacity was obtained at 3C rate.

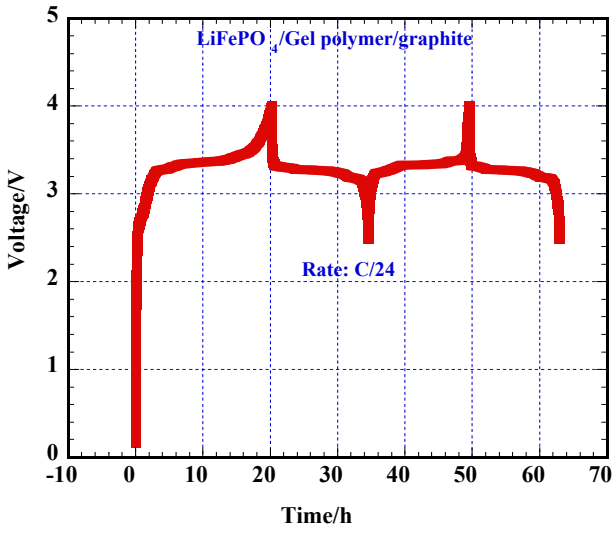

Figure 3. Charge-discharge profiles for graphite/gel polymer/$LiFePO_4$ at charge-discharge rate of C/24.

An investigation on *in situ* SEM of gel polymer cells at 0°C was initiated. We are able to cycle cells under vacuum in an electron microscope using an electrolyte based on GBL, which has a high boiling point. These studies are continuing.

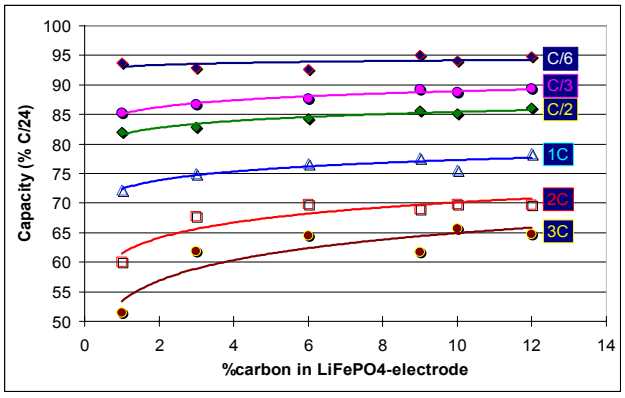

Figure 4. Carbon effect on the reversible capacity of $LiFePO_4$ in Li/gel polymer/$LiFePO_4$ cells.

Presentations

K. Zaghib, X. Song, A. Guerfi, R. Rioux and K. Kinoshita, "Purification of Natural Graphite for Anodes in Li-Ion Batteries: Chemical versus Thermal Processing," *11th International Meeting Lithium Batteries,* Monterey, CA, June 2002.

A. Guerfi, S. Sévigny and K. Zaghib, "Nano-particles $Li_4Ti_5O_{12}$ Spinel Structure Electrode for Electrochemical Generator," *11th International Meeting Lithium Batteries,* Monterey, CA, June 2002.

K. Striebel, A. Guerfi, J. Shim, M. Armand, M. Gauthier and K. Zaghib, "$LiFePO_4$ Advanced Cathode Material for the BATT Program," *11th International Meeting Lithium Batteries*, Monterey, CA, June 2002.

A. Guerfi, S. Sevigny, and K. Zaghib, "High Stable $Li_4Ti_50_{12}$ as Negative Electrode for Electrochemical Generator: Micro vs Nano," *201st Meeting of the Electrochemical Society*, Philadelphia, PA, May 2002.

K. Zaghib, G. Nadeau, A. Guerfi, and K. Kinoshita,"Effect of Particle Size on Lithium Intercalation Rates in Natural Graphite for Li-ion Batteries," *201st Meeting of the Electrochemical Society*, Philadelphia, PA, May 2002.

IV.C. Anodes

IV.C.1. Non-Carbonaceous Anode Materials

Michael M. Thackeray
Chemical Technology Division, Argonne National Laboratory, Argonne IL 60439
(630)-252-9183, fax: (630)-252-4176, email: thackeray@cmt.anl.gov

Objective

- Replace carbon with an alternative anode material that is inexpensive and that will improve the safety of Li-ion cells.

Approach

- Search for, characterize, and develop inexpensive intermetallic electrodes that provide an electrochemical potential a few hundred millivolts above that of metallic Li with capacities >400 mAh/g and 1000 mAh/ml.

- Focus on nickel-arsenide and zinc-blende-type structures, and study their structural and electrochemical behavior during discharge and charge in Li cells.

Accomplishments

- Performed studies to understand the root causes for the capacity loss of intermetallic electrodes in Li cells

- Achieved capacity target of 300 mAh/g for 2002 with Fe-doped Cu_6Sn_5 and MnSb electrodes. Performance was limited by an irreversible capacity loss of 20% or more on the initial cycle, and a slow but steady decrease in capacity on cycling.

Future Directions

- Improve the processing of intermetallic electrodes, particularly those containing copper and/or tin to reduce the irreversible capacity loss on the first cycle.

- Continue to explore intermetallic compounds in which there is a strong crystallographic relationship between parent and lithiated structures and to find improved systems.

- Initiate studies on substituted, electronically conducting $Li_4Ti_5O_{12}$ spinel electrodes with the view to coupling them with high-voltage (4.5-4.8 V) metal oxide electrodes to provide safe, high-rate 3.0 -3.5 V Li-ion cells.

During 2002, efforts were placed on attempts to improve the performance of intermetallic electrodes that operate by Li insertion/metal extrusion reactions and to find new or modified systems. Attention was focused predominantly on $Cu_{6-x}M_xSn_5$ (M=Fe, Ni, Zn), Cu_2Sb and MnSb. Studies were performed to investigate the underlying reasons for the large irreversible capacity loss which is associated with intermetallic electrodes in Li cells and to find ways to combat them . Parameters that were investigated included (i) oxide passivation coatings, (ii) particle size effects, (iii) electrode porosity, and (iv) the addition of additional metal, *e.g.,* Cu to a Cu_6Sn_5 electrode. None of these factors was found to make a major contribution to the capacity loss. It was determined that two of the dominant factors that

limited the performance of ANL's intermetallic electrodes were 1) the loss of extruded metal that is displaced from the intermetallic structure and 2) electronic isolation of the electrode particles that occurs because of relatively large volume changes and the consequent pulverization of intermetallic particles during their initial reaction with Li.

Although good reversibility was achieved when the voltage limits of the Li cells were strictly controlled, and although capacities slightly in excess of the targeted 300 mAh/g were achieved from both Fe-substituted Cu_6Sn_5 and MnSb electrodes, the studies showed that these electrodes always suffered from an unacceptably large irreversible capacity loss on the first charge/discharge cycle. For example, Fig. 5 shows that although steady cycling behavior above the targeted goal of 300 mAh/g could be achieved, the capacity loss on the first cycle of the Li/MnSb cells was >20%. These cells deliver most of their capacity between 1.0 and 0.5 V *vs.* Li during discharge. Cu_6Sn_5 and MnSb electrodes have a hexagonally close-packed NiAs-type structure and they both exhibit hysteresis effects during charge and discharge. This phenomenon can be attributed to the diffusion of the Sb and Sn atoms during phase transitions from the NiAs-type structure to an intermediate cubic-close packed LiMnSb or Li_2CuSn-type structure, respectively. The final discharge products consist of Li_3Sb and the extruded transition metal.

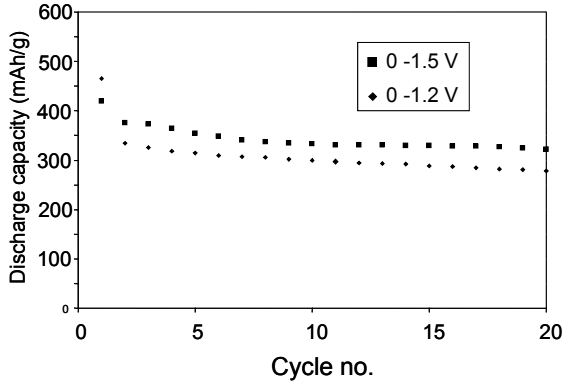

Figure 5. Capacity *vs.* cycle no. for a Li/MnSb cell.

Our findings are consistent with the reported behavior of other intermetallic electrodes, such as SnSb and Mg_2Si. Our attempts to reduce the initial capacity loss associated with intermetallic electrodes will continue to be a major thrust of the research effort in 2003. In addition, in 2003, we plan to initiate studies on substituted, electronically-conducting $Li_4Ti_5O_{12}$ spinel electrodes to investigate their electrochemical properties against high-voltage (4.5-4.8 V) metal oxide electrodes in an attempt to provide safe, high-rate 3.0-3.5 V Li-ion cells.

Publications and Presentations

L.M. L. Fransson, E. Nordström, L. Haggström, J.T. Vaughey and M.M. Thackeray, "Structural Transformations in Lithiated η'-Cu_6Sn_5 Probed by *In situ* Mössbauer Spectroscopy and X-ray Diffraction," *J. Electrochem. Soc*. **149**, A736 (2002).

H. Tostmann, A.J. Kropf, C.S. Johnson, J.T. Vaughey and M.M. Thackeray, "In-Situ X-ray Absorption Studies of Electrochemically Induced Phase Changes in Lithiated InSb," *Phys. Rev. B*. **66**, 014106 (2002).

M.M. Thackeray, J.T. Vaughey and L.M.L. Fransson, "Recent Developments in Anode Materials for Lithium Batteries," *JOM* (a publication of The Minerals, Metals and Materials Society), p. 20 (March, 2002).

M.M. Thackeray, J.T. Vaughey, C.S. Johnson, R. Benedek, L.M.L. Fransson and K. Edstrom, "Structural Considerations of Intermetallic Electrodes for Lithium Batteries," *11th International Meeting on Lithium Batteries, Monterey, CA,* June 2002.

J.T. Vaughey, H. Swinger, C.S. Johnson, M.M. Thackeray, L.M.L. Fransson and K. Edström, "Alternative Anode Materials for Lithium Batteries," *11th International Meeting on Lithium Batteries*, Monterey, CA, June 2002.

L.M.F. Fransson, K. Edstrom, J.T. Vaughey and M.M. Thackeray, "Phase Transformations in MnSb and Mn_2Sb, *11th International Meeting on Lithium Batteries*, Monterey, CA, June 2002.

L.M.L. Fransson, K. Edström, J.T. Vaughey and M.M. Thackeray, "Phase Transitions in Lithiated Intermetallic Anodes for Lithium Batteries – In Situ XRD Studies," *202nd Meeting of the Electrochemical Society, Salt Lake City*, UT, October 2002.

IV.C.2. Novel Anode Materials

M. Stanley Whittingham
Chemistry and Materials Research Center, State University of New York at Binghamton, Binghamton, NY 13902-6000
(607) 777-4623, fax: (607) 777-4623, e-mail: stanwhit@binghamton.edu

Objective

- Replace the presently used carbon anodes with safer materials that will be compatible with manganese oxide cathodes and the associated electrolyte. In particular we will investigate manganese-tolerant anode materials.

Approach

- Explore, synthesize, characterize and develop inexpensive materials that have a potential around 500 mV above that of pure Li (to minimize risk of Li plating and thus enhance safety) and have higher volumetric energy densities than carbon.

- Place emphasis on simple metal alloys/composites, and specifically on understanding and mitigating capacity fade. All materials will be evaluated electrochemically in a variety of cell configurations, and for thermal and kinetic stability.

Accomplishments

- Developed a program to understand the cycling of pure metal and alloy anodes that will lead to the mitigation of capacity fading and thus to the possible use of metals in place of carbonaceous materials.

- Determined that pure tin in the foil form can be charged and discharged for at least 10 cycles with no loss of capacity.

Future Directions

- Improve the electrochemical performance of the materials identified.

- Identify the cause of capacity fade in simple metal and metal alloy anodes.

- Investigate the impact of starting with materials in different morphological forms, such as Exmet *vs.* bulk foil.

The goal of this project is to identify low-cost, low-weight anode materials that are safer than the presently used carbonaceous materials and are compatible with next-generation cathode materials. Although carbonaceous materials are being successfully used in the Sony Li-ion cells, there are safety issues as the capacity increases. Aluminum is the ideal anode material, being low cost, readily available and forming a simple alloy with lithium, LiAl. However, it does not cycle well in carbonate electrolytes, in contrast to ether electrolytes where it was successfully coupled with TiS_2 (Exxon-1978).

As agreed in the Annual Plan we are now generating a plan to build a better understanding of the capacity loss in simple binary metal systems, particularly for carbonate-based electrolyte systems. For example $MnSn_2$ cycles well for a few cycles then decays rapidly. There is a complete reaction (turnover) of the Sn of around five before degradation sets in, indicating that the compound is inherently reversible. We will compare this system with the SnBi eutectic, wherein Sn and Bi are present as separate species and no compound formation occurs on Li removal.

This year's major emphasis was on understanding the behavior of pure Sn as an anode

material, as it can be used without the addition of any conductive diluent like carbon or a binder. This will then be a reference for all other Sn-containing anode compositions.

Commercial Sn foil was rolled and used as-is as the electrode in a carbonate based electrolyte cell with a pure Li counter-electrode. The cycling capacity is shown in Fig. 6, and as can be seen, the capacity is essentially maintained for more than ten cycles before a marked fall-off is observed. The maximum capacity observed is about 3.6 Li/Sn rather than the expected $Li_{4.4}Sn$.

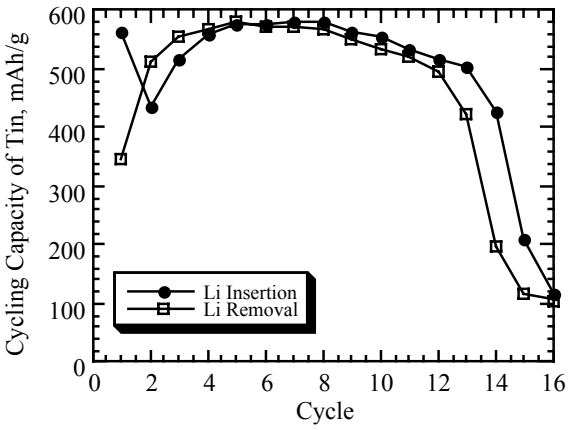

Figure 6. Cycling of Sn foil at 3 mA/cm^2.

In an attempt to determine what might be causing the capacity fall-off, an impedance study was carried out on almost completely discharged Sn electrodes as a function of the number of cycles completed. The preliminary results are shown in Fig. 7. It can be seen that the cell impedance increases at the same time as the cell capacity decreases. There is clearly a correlation here, and we are now determining the source of this impedance increase and why it should suddenly increase at about ten cycles.

The pure Sn foil cycles much better than electrodeposited Sn, and is comparable to Cu_6Sn_5 formed by heating Sn deposited on Cu (Tamura et al, *J. Power Source,s* **107,** 48-55 (2002) , and Sn_2Mn as shown in Fig. 8.

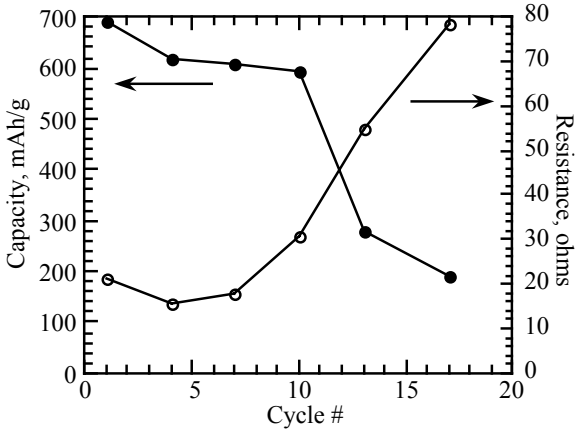

Figure 7. Capacity of Sn foil and cell resistance as function of cycling.

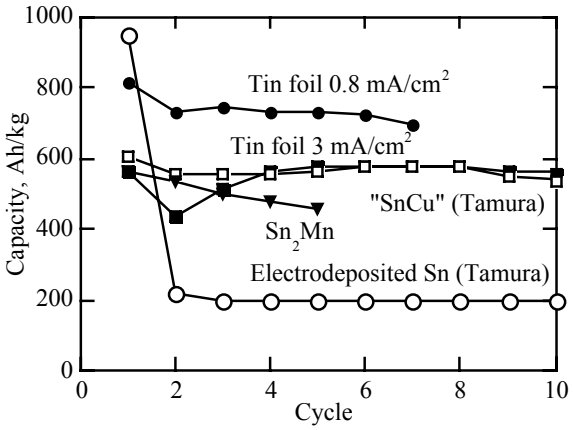

Figure 8. Cycling of tin materials in Li cells.

Presentation

S. Yang, P.Y. Zavalij and M.S. Whittingham, "Sn and SnBi Foil as Anode Materials for Secondary Lithium Battery," *MRS Meeting*, Boston, MA December 2002.

IV.C.3. Optimization of Anodes for Li-Ion Batteries

*M. David Curtis, Gholam-Abbas Nazri and Tad Malinski**
*University of Michigan, Department of Chemistry, Ann Arbor MI 48109-1055; *(Ohio University)*
(734) 763-2132, fax: (734) 763-2307; e-mail: mdcurtis@umich.edu

Objective

- Improve the overall safety, cycle life, shelf life, and overall energy density of the Li-ion battery through the development of a novel composite anode with no irreversible capacity loss during initial cycles, and with high-power rate capability.

Approach

- Develop composite anodes through prelithiation of oxides, nitrides, and phosphides (of metals capable of alloying with Li) to remove the irreversible capacity loss and provide high-performance anodes with thermal and chemical stability for application in large Li batteries.
- Engineer the composite anode to be compatible with the existing Li-ion chemistry.
- Use composite anode to provide a new opportunity to construct Li cells using lower-cost and available electrolytes.

Accomplishments

- Prepared a novel composite anode with almost zero irreversible capacity loss during initial charge-discharge cycles.
- Developed a mechanomilling process to eliminate the irreversible capacity loss of oxide, nitrides, and phosphide anodes.
- Investigated the energy density of the composite anode, and monitored the charge-discharge cycling performances of the composite anodes.

Future Directions

- Continue development and scale-up of process to make stable and safe anodes for large Li batteries.
- Test performance of the composite anode in the presence of low-cost propylene carbonate (PC) based electrolytes.
- Test the prelithiated composite anode against high-capacity and high-rate cathodes for EV and HEV applications.

The safety and stability of the anode/electrolyte interface are major concerns for further development of large Li batteries for EV and HEV applications. Alternative anodes such as oxides, nitrides, and phosphides with energy densities much higher than the current carbonaceous anodes have been proposed. These alternatives have large ICLs during initial charge-discharge cycles and are impractical for application in large battery modules and packs. This work has been focused on the development of a safe composite anode with no ICL during initial cycles and with much higher energy density and rate capability than the current carbonaceous and graphitic anodes. The preparation of the new composite anodes involves the mechanomilling process of oxides, nitrides, or phosphides with

Li-containing precursors according to the reaction pathways shown in Fig. 9.

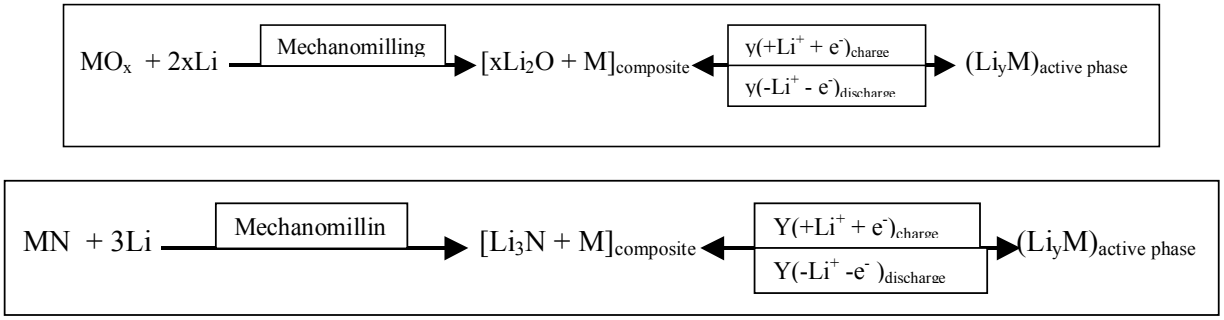

Figure 9. Mechanomilling Process.

The large ICL of oxides, nitrides, and phosphides are removed by mechanomilling of the alternative anodes with Li-containing precursors. During this process a nano-scaled metal phase is formed and protected by the ionic coating (Li_2O, Li_3N, or Li_3P). The metal cluster inner-core serves as an active anode, and the ionic coating serves as a Li^+-conducting membrane to protect the inner core and prevent electrolyte decomposition during Li alloying and dealloying processes (charge and discharge). We have studied several oxides and nitrides using the mechanomilling process. Anode plates were made and tested in conventional multi-blend carbonate-based electrolyte, (EC-DMC-PC, 50:30:20, containing 0.8M $LiPF_6$). Results of electrochemical charge-discharge cycles are shown in Fig. 10. The best result in terms of charge-discharge cycles were observed for oxides with higher oxygen content; $SnO_2 > Sb_2O_3 > Sn_3N_4 >$ SnO. The results indicate that the lithium oxide coating provides a more protective film than the lithium nitride films. In order to completely eliminate the first ICL of the anode, we have investigated the PbO as a model compound, where we added a small amount of electrolyte (10 ml to a 20 gram batch) to the ball-milled sample and milled again for a short period (1-2 hrs). The performance of the new composite was studied and compared with PbO milled with Li, without addition of electrolyte. Figure 11 shows less initial capacity for the new composite (black dots), however, the capacity of the new composite was improved by cycling and a higher capacity was obtained after many charge-discharge cycles.

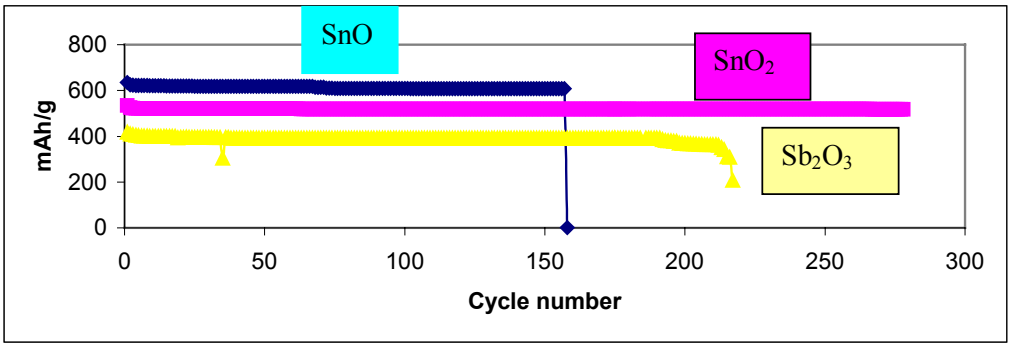

Figure 10. Cell capacity *vs.* cycle number.

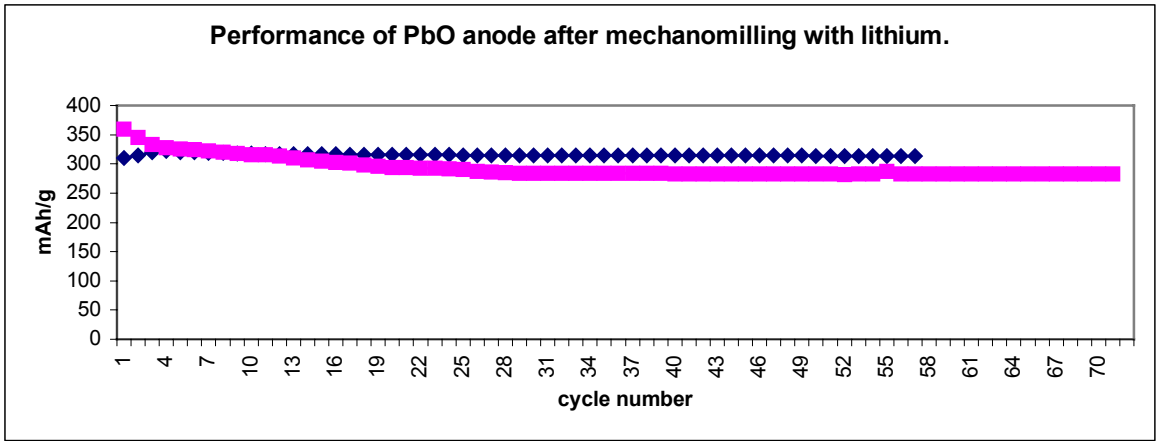

Figure 11. Cell capacity *vs.* cycle number.

IV.D. Electrolytes

IV.D.1. R&D for Advanced Lithium Batteries

Nitash Balsara and John B. Kerr
University of California, Lawrence Berkeley National Laboratory, MS 62R0203, Berkeley, CA 94720-8253
(510)-486-6279, fax (510)-486-4995; email: jbkerr@lbl.gov

Objectives

- Determine the feasibility of the Li metal electrode with organic electrolytes and provide operating conditions that prevent dendrite growth.
- Determine the limitations on Li-ion transport in polymer electrolytes and composite electrodes and develop materials capable of ambient temperature operation with Li metal.
- Determine the limits of stability of organic electrolytes at high-voltage cathode materials (4V) and develop materials and methods to increase stability.

Approach

- Combine synthesis, analysis, modeling, and testing in an approach to electrolyte design, thereby ensuring that not only are the sources of poor performance and failure pinpointed but the problems can be corrected through as-developed materials design and synthesis capabilities.

Accomplishments

- Made quantitative estimates of the properties of polymer electrolytes needed to inhibit dendrite growth sufficiently to meet USABC requirements.
- Showed that polymer electrolytes containing trimethylene oxide solvating units provide significant increases in conductivity and salt diffusion coefficients, which can be clearly related to depression of the glass transition temperature (T_g).

- Performed experiments with addition of nano-particulate filler materials to polymer electrolytes and showed that the widely reported improvements in ion transport properties are due to entrainment of water or other impurities.

- Used polarization experiments on Li half cells combined with impedance measurements to demonstrate that a component of the interfacial impedance is due to salt concentration profiles that lead to phase changes close to the electrode surfaces.

Future Directions

- Carry out detailed quantitative measurements of the transport and mechanical properties of polymer electrolytes to optimize transport *vs.* interfacial behaviors to minimize dendrite growth.

- Prepare and optimize polymers with new ion-solvating groups and appropriate architectures to achieve ambient-temperature operation with polymer electrolytes.

- Develop polymer electrolyte systems capable of operation with 4-volt cathodes and Li metal electrodes.

Links between Dendrite Growth and Mechanical and Transport Properties

Polymer electrolyte properties that affect the growth of dendrites on Li metal electrodes have been identified and measured. Minimum values have been estimated that are required to inhibit dendrite formation These values change as the cell geometry changes, but important properties at the temperature of operation include shear modulus (>6 MPa), conductivity (>5 x 10^{-4} S/cm), salt diffusion coefficient (>4 x 10^{-8}cm^2/s), transference number (t^0_+ >0.3), T_g of polymer (< -70^{o}C), T_g of polymer electrolyte (*e.g.,* 3 molar Li salt T_g< -60^{o}C), a single T_g in dynamic mechanical analysis to indicate uniformity of cross-linking, and morphology profile variations in Atomic Force Microscopy (AFM) after cross-linking <10 nm. Some impurities such as fumed silica (10%) and BHT (1000 ppm) appear to be tolerable.

Polymers with Improved Ion Transport Properties in the Bulk and at Interfaces

New polymer structures have been prepared with conductivity that is superior to what has been achieved to date with PEO-based polymers. In collaboration with modeling groups (G. Smith, O. Borodin, L. Curtis and J. Halley), who provided theoretical guidance, the polymer structures have evolved from linear PEO-like materials to comb-branch polymers with side chains that contain trimethylene oxide (TMO) solvating groups. Although the TMO groups appear to have little influence on the activation energy involved in Li-ion transport, they greatly reduce the dependence of T_g upon salt concentration. Preliminary experiments show a reduced interfacial impedance compared with PEO, indicating that the surface layers of polymer remain more mobile than PEO.

Composite Polymer Electrolytes

Careful preparation of composite polymer electrolytes with added fumed silica nano-particles (8 nm diameter) such that water is completely excluded shows that the presence of the particles reduces the conductivity and the salt diffusion coefficient. Rheology experiments show that the modulus increases with added filler. Literature reports of increased ion transport appear to be due to adventitious water trapped by the particles.

Property Changes at (Electrode) Surfaces

Impedance measurements of cycled Li half-cells show a time dependence for the interfacial impedance following polarization. These observations are consistent with relaxation of the concentration gradients at the electrodes. The dependence of T_g with salt concentration and the inhibition of segmental motion by the surfaces (as described with fillers) indicate that quite different transport properties and even ion transport mechanisms exist in the interfacial layers that extend out into the bulk.

These effects should have a considerable impact upon the operation of composite electrodes and may be mitigated by use of single-ion conductors containing low-T_g groups (*e.g.,* TMO).

Publication

J.B. Kerr, S.E. Sloop, G. Liu, Y.B. Han, J. Hou and S. Wang, "From Molecular Models to System Analysis for Lithium Battery Electrolytes," *J. Power Sources*, **110(2)**, 389-400 (2002).

IV.D.2. Composite Polymer Electrolytes for Use in Lithium and Lithium-Ion Batteries

Saad A. Khan, Peter S. Fedkiw and Gregory L. Baker*[+]
Department of Chemical Engineering, North Carolina State University, P.O. Box 7905, Raleigh NC 27695-7905;
[+]*Department of Chemistry, Michigan State University, East Lansing, MI 48824-1322*
**(919) 515-4519; Fax: (919) 515-3465; e-mail: khan@eos.ncsu.edu*

Objective

- Develop composite polymer electrolytes (CPEs) that are low cost, have high conductivities, impart electrode-electrolyte interfacial stability, and yield long cycle life.

Approach

- Use surface-functionalized fumed silica fillers in BATT baseline systems to determine the effects of filler type and concentration on interfacial stability and cell cycling.
- Utilize a combination of electrochemical characterization, rheological techniques, and chemical syntheses to correlate electrochemical characteristics with mechanical properties and materials chemistry (*e.g.,* silica-type or PEO-type).

Accomplishments

- Determined that the presence of fumed silica in CPEs increases rate capabilities and electrochemical efficiency of Li/V_6O_{13}.
-
- Investigated the effect of the addition of fumed silica into high-molecular-weight (MW) PEO on transport properties (conductivity) and rheological properties.
- Studied the interfacial stability of Li/Li and full-cell cycling of Li/V_6O_{13} using high-MW PEO.

Future Directions

- Determine how fumed silicas (hydrophobic R805 and hydrophilic A200) affect transport and rheological properties of mixed-MW (low + high MW) polymer electrolytes.
- Investigate the interfacial stability and full-cell cycle studies of mixed-MW polymer + fumed silica system.

Introduction

The objective of this research is to develop a new range of CPEs for use in rechargeable Li and Li- ion batteries. In particular, our goal is to develop highly conductive electrolytes that exhibit good mechanical properties, and at the same time show good compatibility with typical electrode materials. The

unique feature of our approach is the use of surface-functionalized fumed silica fillers to control the mechanical properties of the electrolytes and enhance electrode-electrolyte interfacial stability.

Rate capabilities of Li/V_6O_{13} using low-MW PEO

We have previously demonstrated that fumed silica stabilizes the Li/electrolyte interface, and effectively suppresses Li dendrite growth using low-MW PEOs. We have also demonstrated that adding fumed silica significantly improves the capacity fading during cycling using full cells of $Li/LiCoO_2$, $Li/LiMn_2O_4$, and Li/V_6O_{13} cells. In this fiscal year, we investigated the rate capabilities of Li/V_6O_{13} cells using fumed silica-based CPEs. Specific discharge capacity and electrochemical efficiency are improved at middle to high C-rates (C/10 to C/2). Figure 12 shows the average coulombic efficiency over the first 20 cycles as a function of C rate for the different electrolytes studied. For liquid electrolytes, a near unity coulombic efficiency appears at C/15, but with increasing C rate the coulombic efficiency drops rapidly to 71% at C/5. Compared with liquid electrolyte, the coulombic efficiency for the composite gel electrolytes is stable at about 99%, even at C/2 (1.19 mA/cm^2).

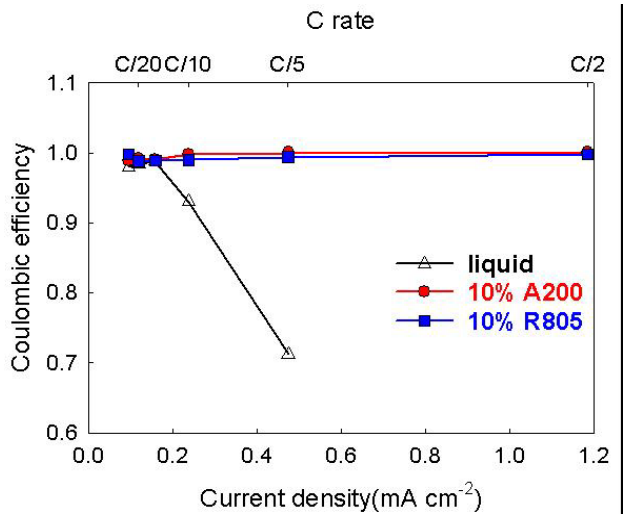

Figure 12. Average coulombic efficiency during first 20 cycles *vs.* current density for Li/V_6O_{13} cells using three different electrolytes: (1) LiTFSI + PEG-dM (250) (Li:O=1:20); (2) LiTFSI + PEG-dM (250) (Li:O=1:20) + 10% A200; (3) LiTFSI + PEG-dM (250) (Li:O=1:20) + 10% R805. Current density from 0.095 (C/25) to 1.185 (C/2) mA/cm^2; voltage range 1.8 to 3.0 V; room temperature; cathode material V_6O_{13} at a loading of 5.8 mg/cm^2; liquid electrolyte could not be cycled at C/2.

Effects of fumed silica on conductivity using high-MW PEO

We have investigated the effect of adding fumed silica into baseline high-MW polymer. Composite polymer electrolytes are obtained by dispersing fumed silica particulates into PEO (MW=200K or 600K) + LiTFSI. We have found that addition of 10% fumed silica causes high-MW PEO to exhibit solid-like behavior (*i.e.,* flat G′ at low frequency) at 80°C, above the melting point of PEO. This ability of fumed silica to produce a mechanically strong network structure might be exploited to extend the useful temperature range of PEO-based electrolytes. Adding nanoparticles of fumed silica improves the rheological properties of polymer electrolytes, whereas the addition of fillers can be either beneficial or detrimental to ion-transport behavior. In crystalline polymer electrolytes, adding nanofillers increases the conductivity as the crystallinity decreases. In amorphous polymer electrolytes, adding fillers decreases conductivity according to a volume-dilution effect. X-ray diffraction (XRD) and differential scanning calorimetry (DSC) results taken together indicate that fumed silica addition increases the conductivity through a decrease in crystallinity.

Interfacial stability and full-cell cycling using high-MW PEO

We have found that adding fumed silica improves the stability of the Li/composite polymer electrolyte interface: the voltage of a Li/CPE/Li cell oscillates at high frequency without fumed silica present in the electrolyte but the cell voltage is more stable with fumed silica present, which is similar to behavior observed in the low-MW PEO system. We have also demonstrated that fumed silica improves cycle performance of $Li/CPE/V_6O_{13}$ full cells.

Publications and Presentations

Y. Li, P.S. Fedkiw and S.A. Khan, "Lithium/V_6O_{13} Cells Using Silica Nanoparticle-Based Composite Electrolytes," *Electrochim. Acta,* **47**, 3853 (2002).

J. Zhou, P.S. Fedkiw and S.A. Khan, "Interfacial Stability between Lithium and Fumed-Silica

Based Composite Polymer Electrolytes," *J. Electrochem. Soc.*, **149**,1121 (2002).

H.J. Walls, M.W. Riley, R.J. Spontak, P.S. Fedkiw and S.A. Khan, "Nanocomposite Electrolytes from Fumed Silica and Clay," *International Polymer Electrolytes Conference*, Santa Fe, NM, August 2002.

H.J. Walls, P.S. Fedkiw and S.A. Khan, "Electrophoritic NMR Measurement of Lithium Transference Numbers in Composite Electrolytes," *International Polymer Electrolytes Conference,* Santa Fe, NM, August 2002.

P.S. Fedkiw, "Electrolytes Based on Fumed Oxides for Rechargeable Lithium Batteries," *invited talk*, University of Iowa, December 2002.

Y. Li, P.S. Fedkiw and S.A. Khan, "Electrochemical Performance of Nanocomposite Gel Electrolyte," *National Academy of Engineering Regional Meeting*, Raleigh, NC, May 2002.

Y Li, P.S. Fedkiw and S.A. Khan, "Self-Discharge of V_6O_{13}/Li Cells Using a Fumed Silica-Based Composite Electrolyte," *11th International Meeting on Lithium Batteries*, Monterey, CA, June 2002.

H.J. Walls, P.S. Fedkiw and S.A. Khan, "Yield Stress and Wall Slip Phenomena in Colloidal Silica Gels," *Society of Rheology Conference*, Minneapolis, MN, October 2002.

Y. Li, J.A. Yerian, P.S. Fedkiw and S.A. Khan, "Effect of Silica Nanoparticles on PEO-LiTFSI Polymer Electrolytes," *202nd Meeting of the Electrochemical Society*, Salt Lake City, UT, October 2002.

J.A. Yerian, P.S. Fedkiw and S.A. Khan, "Role of Monomer in the Reactions of Cross-linkable Fumed-Silica Based Electrolytes," *202nd Meeting of the Electrochemical Society*, Salt Lake City, UT, October 2002.

IV.D.3. New Battery Electrolytes based on Oligomeric Lithium bis((perfluoroalkyl)sulfonyl)imide Salts

Darryl D. DesMarteau[(1)] and Stephen E. Creager[(2)]
Department of Chemistry, Clemson University, Clemson, SC 29634-0973.
[1](864) 656-4705, fax: (864) 656-6613, email fluorin@clemson.edu
[2](864) 656-4995; email screage@clemson.edu

Objectives

- Develop methods for synthesizing oligomeric ionene d Li salts based on the bis((perfluoroalkyl)-sulfonyl)imide anions.
- Develop methods for preparing solid polymer electrolytes (SPEs) from the target salts.
- Acquire data on the ionic conductivity and Li transference of the target SPEs at variable temperature and composition.

Approach

- Synthesize salts using methodologies developed at Clemson over the last 15 years (D. DesMarteau, *J. Fluorine Chem.* 1995, 72, 203-208). SPEs will be prepared from crosslinked low-MW polyethylene glycol (PEG) and also non-crosslinked PEG for comparison. Conductivities will be measured using electrochemical impedance spectroscopy (EIS).

Accomplishments

- Synthesized small quantities (<10 g) for testing purposes of a new series of Li salts of general structure $F_3CSO_2N(Li)[SO_2N(CF_2)_xSO_2N(Li)]_nSO_2CF_3$, for the following values of x and n: n=1, x=2,4,6,8; n=3, x=4,6,8; n=5, x=4,6; n=17, x=4,6
- Prepared SPEs from the above-cited salts using non-crosslinked and also crosslinked PEO/PEG as host matrix
- Characterized the resulting SPEs using impedance spectroscopy to study ion transport, and DSC and wide-angle x-ray diffraction (WAXD) to study thermal and structural properties.

Future Directions

- Synthesize oligomeric salts with average n values near 4 , 8, 16, 30 and 100, for $R_f = (CF_2)_{4,6}$, and with other R_f linkers between imide groups, containing ether links and longer $–CF_2-$ segments. The effort will result in sufficient samples for electrochemical testing using EIS, and also using DSC and WAXD.
- Use nuclear magnetic resonance (NMR) and electrochemical (galvanostatic polarization) methods to evaluate anion and cation transport, and Li transference, in SPEs prepared using the target salts.
- Pursue exploratory studies of gel electrolytes prepared from the target salts.
- Synthesize several new allyl ether Li salts for use by other BATT program workers in preparing single-ion conductors for Li.

Introduction

Research under BATT support between Oct 2001 and Sept 2002 was focused on the preparation and characterization of a series of new oligomeric Li salts, and SPEs from those salts, in which the anion has an oligomeric structure illustrated in Scheme 1. It is expected that SPEs containing these salts will possess both very high conductivity due to the low lattice energy of salts containing imide anions, and also high Li transference due to the expected low mobility of the anions due to entanglement with the matrix.

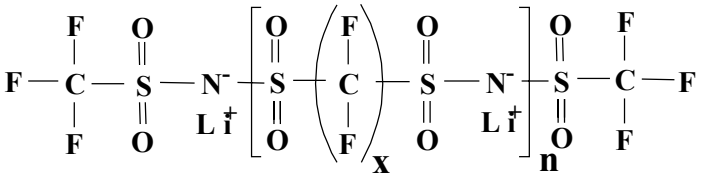

Scheme 1 . Ionene lithium salts with a perfluorohexyl chain linking imide anions.

Synthesis of new salts

A general method was developed for synthesizing oligomeric imide-based Li salts of fixed anion size and oligomer length. The method involves a series of stoichiometric sequential coupling reactions between difunctional reactants, always with one reactant in large excess. A sample reaction scheme is presented in Scheme 2 for synthesis of a dianion. This method was used to prepare a broad range of salts with the general structure in Scheme 1. Specifically, salts were prepared with n and x values as follows: n=1, x=2,4,6,8; n=3, x=4,6,8; n=5, x=4,6; n=17, x=4,6.

Preparation and characterization of SPEs containing the new salts in crosslinked PEG

SPEs were prepared by dissolving salts and PEO host in DMF and removing solvent by evaporation. The crosslinking agent was 4,4',4"-methylidyne-tris(4-phenylisocyanate), which was also added to the formulation to prepare SPEs with crosslinked PEG as host. Figure 13 presents

some representative variable-temperature conductivity data, presented in an Arrhenius format, for a SPE with an EO/Li ratio of 10:1. Conductivities of SPEs prepared using crosslinked PEG are consistently less than those for SPEs prepared using non-crosslinked, hi-MW PEO, which probably reflects a greater overall retardation of ion motion in the crosslinked SPEs. The ordering of the different salts with respect to their conductivity is different in crosslinked and non-crosslinked hosts, which again suggests that the anions interact quite strongly with the host. A consequence of this finding is that the optimal anion size/structure for achieving high Li transference and high conductivity may not be the same in crosslinked and non-crosslinked hosts.

Publications

O.E. Geiculescu, J. Yang, R. Bailey-Walsh, G. Shafer, S.E. Creager, W.T. Pennington and D.D. DesMarteau, "Solid Polymer Electrolytes from Dilithium Salts Based on New bis[(perfluoroalkyul)sulfonyl]imide Dianions. Preparation and Electrical Characterization," *Solid State Ionics* **148**, 173-183 (2002).

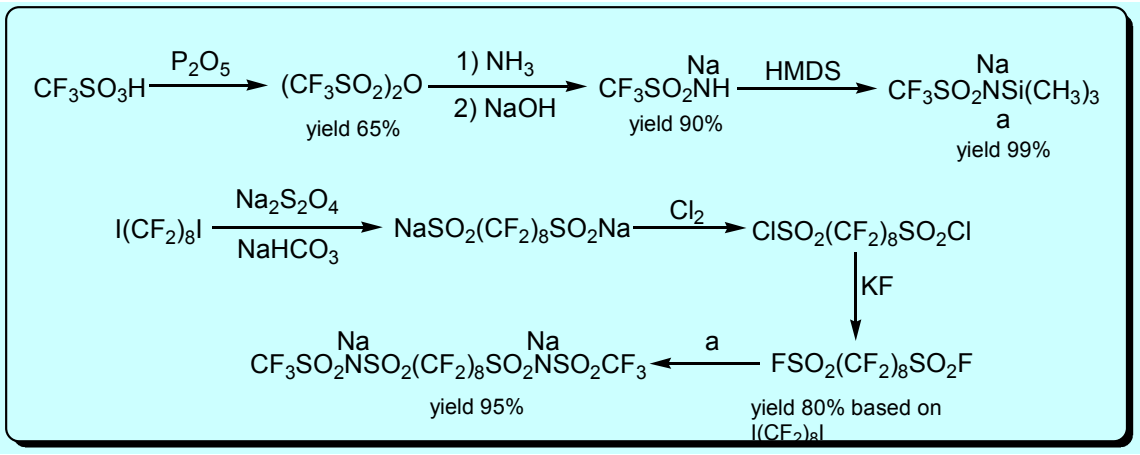

Scheme 2. Preparation scheme for a di-imide Li dimer salt.

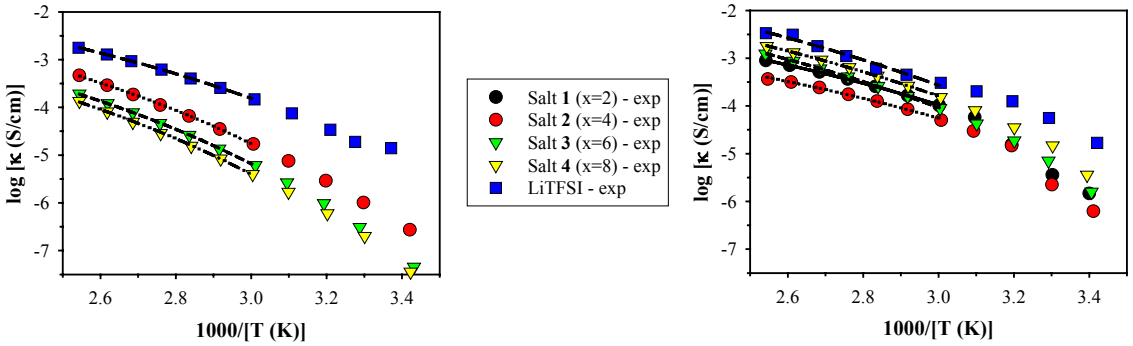

Figure 13. Arrhenius plots for SPEs prepared from dimeric di-imide Li salts using crosslinked (left) and non-crosslinked (right) PEG hosts. The EO/Li ratio for these SPEs was 10:1.

IV.D.4 A Molecular Dynamics Simulation Study of the Influence of Polymer Structure on Complexation Thermodynamics, Kinetics and Transport of Lithium Cations in Polyether-based Solid Polymer Electrolytes

O. Borodin and G.D. Smith
Department of Material Sciences and Engineering, University of Utah, 122 S. Central Campus Dr., Rm 304, Salt Lake City, UT 84112-0560
(801)585-3381, fax (801) 5814816, e-mail: gsmith2@gibbon.mse.utah.edu

Objectives

- Understand influence of polymer structure and polymer-ions interaction on ion aggregation and transport in polymer electrolytes.
- Provide guidance to rational design of novel polymer electrolytes.

Approach

- Employ *ab initio* quantum-chemistry calculations to obtain energetics of polyether complexes with Li-salts and use these data to develop classical force fields for polyether/$LiBF_4$.
- Use atomistic molecular dynamics (MD) simulations of polyether-based Li/polymer electrolytes to examine the influence of polyether structure, strength of the polyether-lithium and Li-anion interactions and barrier of conformational isomerization reaction on ion transport.

Accomplishments

- Developed quantum-chemistry based force fields for poly(ethylene oxide) (PEO), poly(methylene oxide) (PMO), poly(trimethylene oxide) (PTMO), poly(propylene oxide) (PPO), and a copolymer of poly(ethylene oxide-trimethylene oxide) (PEO-TMO) and their interactions with $LiBF_4$.
- Performed molecular dynamics simulations on PEO, PMO, PTMO, PPO, PEO-TMO melts. The initial simulations of these polyethers doped with $LiBF_4$ salts are currently being performed.
- Examined the influence of the strength of the polyether-Li and Li-anion interactions, and barrier of conformational isomerization reaction on ion aggregation and transport.

Future Directions

- Develop *ab initio* quantum chemistry based classical force fields and perform molecular dynamics simulations of polyether-based comb-branch copolymers, single-ion conductors and gel electrolytes in order to provide guidance to the experimental efforts aimed at development of novel single-ion conductors and gel electrolytes through synergetic experimental-MD simulations studies.

Influence of polymer-salt interactions on ion aggregation and transport

Optimization of transport properties of polymer electrolytes is a complicated task involving many variables such as polymer-cation and cation-anion interactions, polymer conformational dynamics. Experimental examination of the above parameters on ion aggregation and transport is expensive and cumbersome, hindering progress toward fundamental understanding of polymer electrolytes, whereas atomistic molecular dynamics simulations can be readily used to investigate influence of the polymer-salt interactions on ion aggregation, self-diffusion coefficients, and conductivity in high-temperature polymer electrolytes. PEO doped with $LiBF_4$ at (ether oxygen):Li ratio of 15:1 at 393 K has been selected as a reference point for the parametric investigation. A two-body force field with an approximate mean-field like treatment of polarization interactions has been used. Polarization interactions accounting for approximately 30% of the PEO-Li^+ complexation energy have been varied from

50 to 200% of the original force field covering the range of systems from polymer electrolytes with less than 1% of free Li^+ cations (*e.g.,* only 1% of cations not having any anions in its first coordination shell) to those with almost all (92 %) of Li^+ cations being free from anions in their first coordination shell as shown in Fig. 14. An increase in polarization interaction between polymer and Li^+ resulted in a monotonic increase in the fraction of free cations and a decrease in cation self-diffusion coefficient for the free ion fraction higher than 22 % as shown in Fig. 14. These two factors have an opposite effect on conductivity of polymer electrolytes: an increase in the fraction of free charge carriers (Li^+) increases conductivity, whereas a decrease in ion self-diffusion decreases conductivity. Our simulations demonstrate that over wide range of parameters (22-92 % of free ions) the polymer electrolyte conductivity changes less than 2 times as the benefits of an increase in the fraction of charge carriers on conductivity with increasing polymer-Li^+ interactions are lost due to diminished ion mobility. Indeed, an effect of a 4-times increase in the fraction of free ions from 24 to 92% on conductivity is offset by a roughly 2- times drop of the ion self-diffusion coefficient resulting in only a modest increase in conductivity, *e.g.*, slightly less than 2 times. An effect of the initial increase in the fraction of free ions (from less than 1 to 22%) on conductivity is more dramatic (e.g. an order of magnitude) than the one observed for the range of free ion fraction from 24 % to 92 % due to significantly higher fraction of free ions (22% *vs.*<1%) and comparable ion self-diffusion coefficients between two systems.

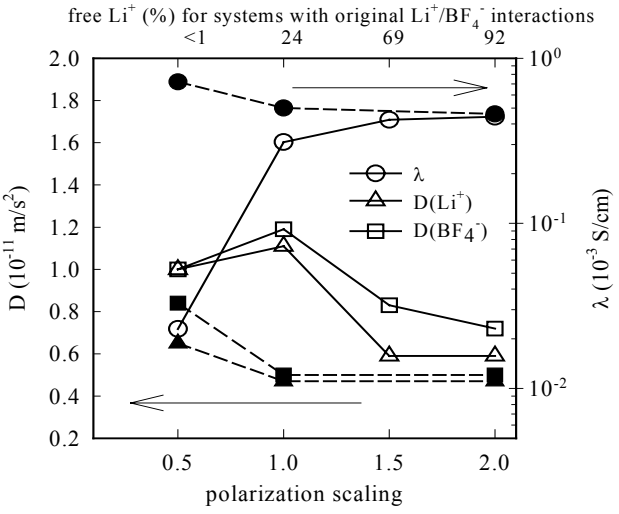

Figure 14. Conductivity (□) and ion self-diffusion coefficient (D) as a function polarization for $PEO/LiBF_4$ with original Li^+/BF_4^- interactions (open symbols) and Li^+/BF_4^- repulsion increased by a factor of three (closed symbols).

At the next stage we investigated the effect of polymer-Li^+ complexation energetics on ion transport for polymer electrolytes in which nearly all ions are dissociated and thus no ion pairs or aggregates exists. Ion dissociation was facilitated by increasing repulsion between cation and anion by a factor of three resulting in the $PEO/LiBF_4$ systems with no ion pairs or aggregates. MD simulations revealed that the fully dissociated $PEO/LiBF_4$ systems exhibited qualitatively different behavior of conductivity as a function of polymer-Li^+ interaction shown in Fig. 14 from the previously described systems with the partial ion aggregation. In fully dissociated systems a decrease of the polymer-Li^+ interaction was found to enhance conductivity, whereas in the system with partial aggregation the effect was the opposite suggesting that different strategies should be applied for enhancing conductivity in partially aggregated and fully dissociated polymer electrolytes.

A separate set of MD simulations of $PEO/LiBF_4$ employing potentials with various PEO conformational barriers revealed that ion transport is intimately connected to polymer conformational dynamics, allowing improvement of ion conduction by lowering conformational barriers.

MD simulations of polyethers doped with $LiBF_4$

Quantum chemistry based force fields have been developed for poly(ethylene oxide) (PEO), poly(methylene oxide) (PMO), poly(trimethylene oxide) (PTMO), poly(propylene oxide) (PPO), and a copolymer of poly(ethylene oxide-trimethylene oxide) (PEO-TMO) and their interactions with $LiBF_4$. Molecular dynamics simulations have been performed on PEO, PMO, PTMO, PPO, PEO-TMO melts with a similar number of backbone atoms (≈160). Good agreement with dielectric spectroscopy experiments and NMR data were observed where data were available. Local dynamics of the melts were measured through backbone atom mean-square displacements and dynamic structure factor and was found to follow the order PMO<PPO<PEO≈PEO-TMO≈TMO. Initial

simulations at 393 K of these polyethers doped with $LiBF_4$ salts are currently been performed indicating that their conductivity of polyethers will also follow the same order as the polymer dynamics, e.g. PMO<PPO<PEO≈PEO-TMO≈TMO in agreement with the experimental observations.

IV.D.5. Highly Conductive Rigid Polymers

Duward F. Shriver and Semyon Vaynman***
**Chemistry Department, Northwestern University, Evanston, IL 60208*
***Department of Materials Science and Engineering, Northwestern University, Evanston, IL 60208*
(847) 491-5655; fax: (847) 491-7713; e-mail: shriver@chem.northwestern.edu, svaynman@northwestern.edu

Objectives

- Synthesize a new class of rigid polymer electrolytes.
- Test rigid polymer electrolytes in rechargeable Li batteries.

Approach

- Synthesize new types of polymer electrolytes that contain a rigid polymer rather than the flexible low-T_g polymers used in conventional polymer electrolytes.
- Fabricate electrochemical cells with these electrolytes and evaluate their performance.
- Correlate the performance of electrolytes in the cells with their chemical structure and their reactivity toward components of the electrochemical cell.

Accomplishments

- Synthesized highly conductive rigid polymer electrolytes that contain functional groups such as carboxy and sulfone and tested them in cells. Polymer-salt complexes that contain carboxy groups have higher ionic conductivity than similar polymer-salt complex that contains sulfone (appr. 10^{-4} S/cm *vs.* $5x10^{-6}$ S/cm at room temperature). However, the polymer-salt complexes that contain carboxy groups are unstable toward Li; they form very resistive interface with Li. Much less-resistive layers are formed between Li metal and sulfone-containing rigid polymer electrolytes.
- Incorporated rigid polymer electrolytes into Li cells. The capacity of the cells with carboxy-containing rigid polymer electrolyte was not satisfactory. The capacity of the cell with sulfone-containing rigid polymer electrolytes was >100 mAh per gram of active cathode material at current density of 15 $\mu A/cm^2$. The capacity of the cell was reduced significantly with an increase in current density due to high resistance of that electrolyte.

Future Directions

- This project was completed on May 31, 2002.

Introduction

During the 2002 FY we continued the synthesis and investigation of the properties of polysulfones (a) - (c) (Fig. 15). The conductivity of the polysulfone (a)-lithium triflate complex is approximately $5x10^{-6}$ S/cm at room temperature. This complex is much more stable toward the Li anode

than the complex containing carboxy groups. Due to low ionic conductivity of electrolyte, the capacity of the cells containing the polysulfone (a) - lithium triflate polymer electrolyte was low.

The conductivity of the polysulfone (b)-lithium triflate (2:1 molecular ratio) complex isextremely low; it could not be measured at room temperature. At 60°C the conductivity was ~$3x10^{-9}$ S/cm and this may be due to the low density of cation-coordinating sites in this polysulfone.

The sulfone-containing polymer (c), which has a much higher density of cation-coordinating sites than polysulfone (a or b) was also synthesized. As expected, when doped with lithium triflate in 2:1 molecular ratio, polymer (c) displayed much higher ionic conductivity (~10^{-4} S/cm at room temperature) than polymers (a and b). (Fig. 16). This polymer-salt electrolyte was retested after 2 weeks storage in the glove box and the ionic conductivity was a few orders of magnitude lower. We suspected the decomposition or contamination caused the dramatic conductivity change. The synthesis of polysulfone (c) was repeated several times with fresh starting materials but the high conductivity was not reproduced.

During this project a number of rigid polymers were synthesized. The polymer that contained carboxy group when mixed with lithium triflate exhibited high ionic conductivity. However, the reactivity of this polymer toward Li metal prevents its use in Li batteries. Polymers that contain sulfone groups were found to be much more resistant toward Li metal, but their conductivity was lower than that of carboxy-containing polymer.

This work demonstrates that highly conductive polymer electrolytes (with an ionic conductivity of an order of 10^{-4} S/cm) can be synthesized. Further work is needed to develop new polymer electrolytes that combine good ionic conductivity with redox stability in the battery.

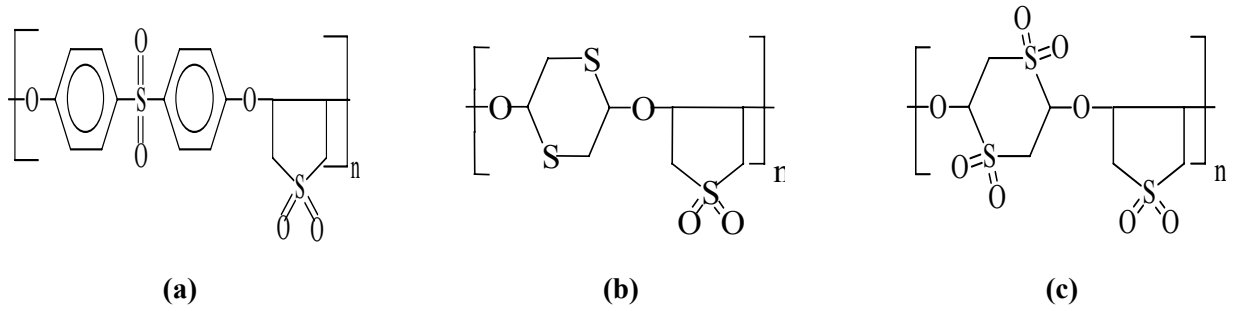

(a) **(b)** **(c)**

Figure 15. Structure of synthesized polysulfones.

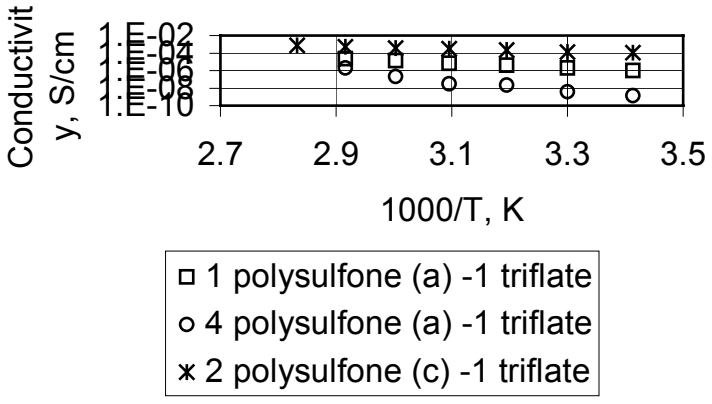

Figure 16. Conductivity of polysulfone (a) and (c) – lithium triflate salt complexes

IV.D.6. Electrolyte Additives

Kim Kinoshita and John B. Kerr
Lawrence Berkeley National Laboratory, MS 62R0203, Berkeley CA 94720-8253
(510)-486-6279, fax (510)-486-4995, email: jbkerr@lbl.gov

Objective

- Identify chemical additives that improve the safety of nonaqueous electrolytes for Li-ion batteries by stabilizing the SEI layer on carbon.

Approach

- Identify species that are incorporated in the SEI layer to improve its stability.
- Conduct electrochemical evaluation of additives to determine the reversible and irreversible capacity loss using the baseline liquid or gel electrolytes.

Accomplishment

- Pyridine stabilizes the thermal reactions of this electrolyte in the bulk of the solutions by intercepting the PF_5 formed from the salt.
- Addition of vinylene carbonate (VC) to the ATD Gen 2 electrolyte in an increase of interfacial impedance on Gen 2 carbon anodes and alters the SEI layer.
- Redox catalysis experiments with VC and similar additives such as methyl benzoate and dicyanobenzene, show that reduction of CO_2 is easier than reduction of EC which in turn is easier than reduction of EMC.

Future Directions

- Use additives such as VC, methylbenzoate and dicyanobenzene to investigate the mechanisms of electrochemical reduction of CO_2, EC and EMC. In particular the effect of ion-pairing due to the presence of Li ions needs to be elucidated.
- Investigate the effect of additives on the build up of impedance in the anode and cathode.
- Investigate the effect of additives on reversible and irreversible capacity loss plus power fade in Li ion cells.

The effect of pyridine as an additive to Gen 2 electrolyte

Thermal treatment of $LiPF_6$-containing electrolytes at > 40°C gives chemical reactions that remove EC, increase transesterification products, and yield polyether carbonate polymers and CO_2 gas. Solutions that do not contain $LiPF_6$ do not react in this manner. Addition of pyridine to the solution suppresses the thermal reactions. It is thought that thus occurs by formation of an adduct between the pyridine, a strong Lewis base, and PF_5, a strong Lewis acid. This adduct does not react with the EC to initiate polymerization. Cyclic voltammetry (CV) and impedance spectroscopy shows that the pyridine reduces on the carbon anode to form a film that interferes with Li intercalation

The effect of addition of additives such as VC into LP40 electrolyte, 1M $LiPF_6$-EC-DEC(1:1 w/w)

The addition of additives such as VC have been found to greatly improve calendar and cycle life in

Li-ion batteries according to SAFT. It is generally thought that the reduction of the VC improves the behavior of the anode by forming a film on the electrode that reduces side reactions. We have found evidence in CV and impedance spectroscopy to support this hypothesis. However, we have pursued an alternative scenario regarding the action of such additives. It is known that CO_2 is formed in Li-ion cells and this is reducible at the anode. The products of reduction of CO_2 in PC/R_4NClO_4 on carbon and copper are CO, carbonates and oxalate whereas on Cu in the presence of water the formation of methane, ethane, and ethylene has been reported. Reduction of CO_2 in the presence of tetra-alkylammonium cations by means of a redox catalyst yields solely oxalate. A redox catalyst is an additive such as VC, methyl benzoate or dicyanobenzene that is able to pass electrons to the compound of interest in solution. Thus the redox catalyst is designated O and its reduced form R:

$$O + e^- \leftrightarrow R$$

$$R + CO_2 \leftrightarrow O + CO_2^{\cdot-}$$

$$2\ CO_2^{\cdot-} \rightarrow {}^-O_2C\text{-}CO_2^- \text{ (oxalate)}$$

The additive is recycled to the electrode and facilitates the reduction of the CO_2. This also occurs with EC and EMC but these compounds are reduced more slowly that CO_2. The oxalate is sufficiently soluble to reach the cathode where it can be re-oxidized to CO_2 resulting in a reversible self-discharge shuttle mechanism. The presence of additives such as VC can increase the reversible self-discharge mechanism at the expense of the irreversible self-discharge mechanism, which results when CO_2 is reduced directly at the anode to CO and carbonate. Experiments are planned with the Cell Development task to measure reversible self-discharge and the effect, if any, of the addition of additives such as VC on this variable. Since reversible self-discharge is not thought to be involved in power fading and impedance rise, this mechanism represents a possible mode of action of VC in Li-ion cells.

IV.D.7. Development of Nonflammable Electrolytes

J. Prakash
Illinois Institute of Technology, Department of Chemical and Environmental Engineering,
10 W 33rd Street, Chicago, IL 60616
(312) 567-3639, fax: (312) 567-8874; e-mail: prakash@iit.edu

Objective

- Develop non-flammable electrolytes (NFEs) with high flash point (>100°C), ionic conductivity (10^{-3} S/cm), and wider voltage window (0-5 V *vs*. Li) in an effort to provide better thermal stability and fire safety.

Approach

- Modify existing electrolytes by using novel flame-retardant (FR) additives that are compatible with active electrode materials and the environment.

- Use chemical, electrochemical, and thermal techniques to investigate the stability and performance of electrolytes modified with FR additives.

Accomplishments

- Completed an extensive study on the thermal and electrochemical characterization of the FR additive, hexa-methoxy-tri-aza-phosphazene $N_3P_3[OCH_3]_6$ (HMTAP $N_3P_3[OCH_3]_6$, in Li-ion cells.
- Completed the scale-up synthesis of the flame retardant HMTAP.
- Supplied the HMTAP material to ANL, Electrovaya Company (Canada), and Mitsubishi Chemical Company (Japan).
- Demonstrated the feasibility of using this material as a FR additive in PNGV Li-ion cells.

Future Directions

- This project is complete.

Introduction

The main focus of this project is to develop electrolytes that meet the criteria for NFEs for Li-ion batteries. Our research in FY 2002 was focused on completing the scale-up synthesis of the FR material hexa-methoxy-tri-aza-phosphazene ($N_3P_3[OCH_3]_6$) and establishing the mechanism of its FR action.

We completed the scale-up synthesis (25 g batch) of the FR hexa-ethoxy-tri-aza-phosphazene (HETAP) and characterized this additive for its structure and purity. The synthesis was carried out by dissolving hexa-chloro-cyclo-triphosphazatriene in pyridine followed by the addition of ethanol. The temperature was maintained at 0-5°C during the addition and the reaction mixture was stored overnight. Diethyl ether was then added in this mixture with stirring, and the pyridinium chloride was removed by filtration. Subsequent distillations produced hexa-ethoxy-cyclotri-phosphazatriene (yield =52%). The FTIR spectra confirmed the molecular structure of the HETAP synthesized. The FTIR spectra of the synthesized HETP compound exhibited two strong absorptions at 2980 and 2934 cm^{-1} (asymmetric stretching of the $-CH_2$ and $-CH_3$ groups), absorption at 2877 and 2819 cm^{-1} (symmetric stretching of the $-CH_2$ and $-CH_3$ groups), and absorption at 1388 and 1364 cm^{-1} (symmetric and asymmetric bending frequency of the ethyl groups). The stretching of P-N and P=N group was also observed at 1213, and 750cm^{-1}. Strong absorption bands at 1262, 1097 cm^{-1} indicated the presence of symmetric and asymmetric stretching of P-O-C group.

The material was then supplied to various organizations including ANL, Electrovaya Co., and Mitsubishi Chemical Co. for its characterization in Li-ion cells. Electrovaya informed us that the HMTP FR additive showed excellent fire safety (70% success rate) in their high capacity Li-ion cells under nail penetration tests.

The thermal properties of the HMTAP in Li-ion cells were investigated in collaboration with ANL using DSC and accelerating rate calorimeter (ARC) methods. It was found that the addition of 5-10 wt% FR additive in the electrolyte shifts the onset of the exothermic peaks to higher temperatures (Fig. 17).

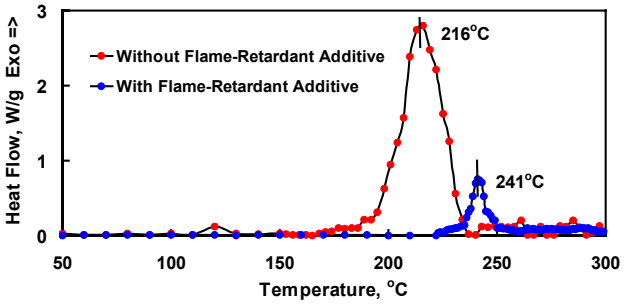

Figure 17. Effect of HMTP additive on fully charged $LiNi_{0.8}Co_{0.2}O_2$ cathode.

The shift of the exothermic peak with 5-10 wt% FR additive in comparison with those for the electrolyte without the FR additive was attributed to the passivation layer formed on the surface of the electrode. In addition, the investigations of the pressure development within the ARC bomb also showed that 5-10 wt% FR additives significantly reduce the pressure buildup in the ARC bomb

compared with those for the electrolyte without the FR under similar conditions.

We have completed the spectral characterization of the carbon electrode subjected to the potential of 10 mV (cathodic) and 4.2 V (anodic) *vs.* Li/Li^+ for 3 hr in 1M $LiPF_6$ in EC-DMC (50:50 wt%) containing 10 wt% of HMTP. After each experiment, the electrode surface was washed and studied using FTIR (PARAGON 1000, Perkin Elmer), EDS, ^1H NMR, and ^{31}P NMR ((300 MHz FT-NMR spectrometer, Varian Gemini). ^1H NMR studies confirmed the presence of the $-OCH_3$ group of the HMTP on the electrode surface. In addition, a single peak in the ^{31}P NMR measurement (Fig. 18) suggested that the HMTP is the source of the phosphorous signal. We also observed that the peak position shifts to the lower region compared to the pure HMTP suggesting that Li is coordinated to P in the adsorbed film on the carbon electrode surface. These results indicate the presence of $Li\text{-}P(OCH_3)_2$ species on the electrode surface, which is probably responsible for the thermal safety and flame retardancy. With this new structural information, one can further reduce the self-heat rate of the Li-ion cells by synthesizing new FR additives containing $-P(OCH_3)_2$ groups.

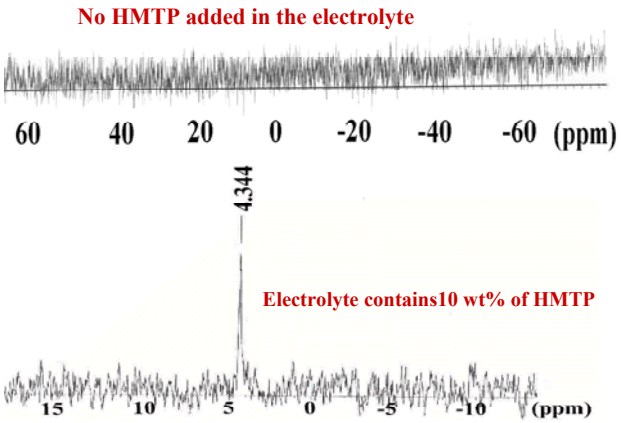

Figure 18 ^{31}P NMR spectrum of a carbon electrode subjected to 10 mV *vs*. Li for 3 hrs.

Publication

J. Prakash, C. Lee, and K. Amine, "A Novel Flame-Retardant Additive for Li-ion Batteries," *U.S. Patent No. 6455200* (2002).

IV.E. Cathodes

IV.E.1 Novel Cathode Materials

Michael M. Thackeray
Argonne National Laboratory, Chemical Technology Division, Argonne IL 60439
(630)-252-9183, fax: (630)-252-4176, email: thacheray@cmt.anl.gov

---

Objective

- Develop low-cost manganese oxide cathodes to replace cobalt/nickel oxide electrodes in Li-ion cells and vanadium oxide electrodes in Li-polymer cells.

Approach

- Develop and characterize manganese oxides for Li-ion and Li-polymer cells.
- Focus on composite layered $xLi_2M'O_3\bullet(1\text{-}x)LiMO_2$ electrodes (M′=Mn, Ti, Zr, Ru; M = Mn, Ni, Co) for Li-ion cells, and stabilized alpha-MnO_2 for Li-polymer cells.

- Reinstate research to stabilize $LiMn_2O_4$ spinel electrodes.

Accomplishments

- Prepared and evaluated several $xLi_2M'O_3 \bullet (1-x)LiMO_2$ electrode compositions in Li cells; the performance target of 160 mAh/g for 100 cycles at 50°C was achieved.
- Restarted effort to stabilize $LiMn_2O_4$ spinel electrodes.
- Determined significance of the tetrahedral A-site of the spinel in stabilizing electrochemical performance at 50°C.

Future Directions

- Seek improved performance from $xLi_2M'O_3 \bullet (1-x)LiMO_2$ composite electrodes. A performance target of 190 mAh/g for 100 cycles at 50°C in $Li/xLi_2M'O_3 \bullet (1-x)LiMO_2$ cells has been set.
- Attempt to minimize the irreversibility capacity loss of $xLi_2M'O_3 \bullet (1-x)LiMO_2$ electrodes.
- Continue efforts to stabilize $LiMn_2O_4$ spinel electrodes at 50°C.
- Evaluate metal-oxide electrodes in Li/polymer cells in collaboration with J. Kerr at LBNL.

Introduction

During 2002, the prime focus of the research effort was to continue to exploit the concept of using a layered $Li_2M'O_3$ (rock salt) component (M′=Mn, Ti, Zr, Ru) to stabilize a layered electrode $LiMO_2$ structure (M = Mn, Ni, Co) during the electrochemical cycling of $Li/LiMO_2$ cells. It was discovered during this contract period that when M = Ni and Mn, for example, in $LiMn_{0.5}Ni_{0.5}O_2$, or in a composite $0.31LiTi_2O_3 \bullet 0.69LiMn_{0.5}Ni_{0.5}O_2$ system, electrochemical capacity could be obtained not only by Li extraction from the parent electrode above 3 V *vs*. Li, but also by Li insertion below 2 V without destroying the layered framework of the host electrode. During the electrochemical process above 3 V, the Li ions occupy octahedral sites in a $Li_{1-x}MO_2$-type structure, whereas below 2 V a Li_2MO_2-type structure is formed in which the Li ions occupy tetrahedral sites. When discharged between 4.6 and 1 V, these electrodes can yield extremely high capacities that can exceed 250 mAh/g. The electrochemical reaction path and change in electrode composition during Li insertion into and extraction from $xLi_2M'O_3 \bullet (1-x)LiMO_2$ composite electrodes is shown in a compositional MO_2-Li_2MO_2-$Li_2M'O_3$ phase diagram in Fig. 19.

Changes in the oxidation states of these $xLi_2M'O_3 \bullet (1-x)LiMO_2$ composite electrodes were tracked by *in situ* x-ray absorption studies at the Advanced Photon Source at ANL. These studies showed that charge transfer occurred predominantly in a two-electron process both during Li extraction ($Ni^{2+} \rightarrow Ni^{4+}$) and during Li insertion $Mn^{4+} \rightarrow Mn^{2+}$). The absence of Jahn-Teller ions, Mn^{3+} and Ni^{3+}, during charge and discharge is believed to contribute to the remarkable reversibility of the overall reaction.

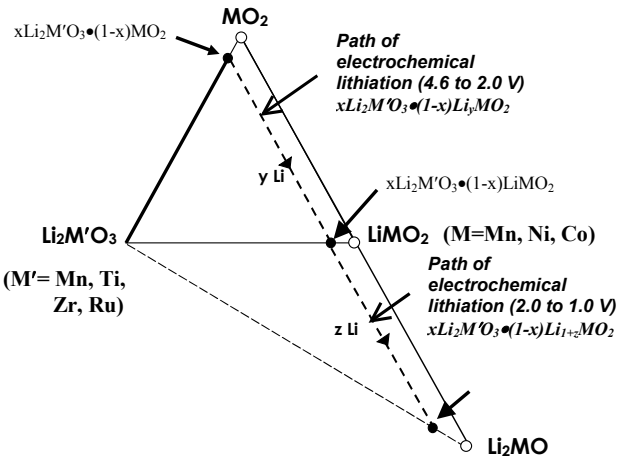

Figure 19. A compositional MO_2-Li_2MO_2-$Li_2M'O_3$ phase diagram.

The discovery of Li_2MO_2 electrode compositions that are stable to electrochemical cycling raises the possibility of using these compounds to combat the irreversible capacity loss effects that occur at graphite or intermetallic negative electrodes.

During 2002, a task to stabilize $LiMn_2O_4$ electrodes at 50°C was reinstated into the project. Electrochemical evaluations and structural analyses by neutron diffraction of substituted $LiMn_{2-x}M_xO_4$ electrodes (M = Li^+, Mg^{2+}, Zn^{2+} and Al^{3+}) have demonstrated that the occupation of the tetrahedral sites of the spinel by the substituted ions may play a significant role in stabilizing the spinel electrode.

No further progress was made on improving the electrochemistry of stabilized alpha-MnO_2 electrodes in Li/polymer cells. However, further work on cathode materials for Li/polymer cells is planned for 2003 in collaboration with J. Kerr at LBNL.

Publications and Presentations

J-S. Kim, C.S. Johnson and M.M. Thackeray, "Layered $xLiMO_2 \bullet (1-x)Li_2MO_3$ Electrodes for Lithium Batteries: A Study of $0.95LiMn_{0.5}Ni_{0.5}O_2 \bullet 0.05Li_2TiO_3$," *Electrochem. Comm.*, **4**, 205 (2002).

C.S. Johnson, J-S. Kim, A.J. Kropf, A.J. Kahaian, J.T. Vaughey and M.M. Thackeray, "The Role of Li_2MO_2 Structures (M= Metal Ion) in the Electrochemistry of $xLiMn_{0.5}Ni_{0.5}O_2 \bullet (1-x)Li_2TiO_3$ Electrodes for Lithium Batteries," *Electrochem. Comm.*, **4**, 492 (2002).

C.S. Johnson, J.-S. Kim, J.T. Vaughey, A.J. Kropf and M.M. Thackeray, "Structural and Electrochemical Evaluation of $(1-x)Li_2TiO_3 \bullet xLiMn_{0.5}Ni_{0.5}O_2$ as an Electrode Material for Lithium Batteries," *11th International Meeting on Lithium Batteries, Monterey, CA,* June 2002.

G.J. Moore, C.S. Johnson and M.M. Thackeray, "The Electrochemical Behavior of Composite $xLiMO_2 \bullet (1-x)Li_2RuO_3$ Electrodes in Lithium Cells (M=Co, Ni, Zr, Li)," *11th International Meeting on Lithium Batteries, Monterey, CA,* June 2002.

Y. Paik, C.S. Johnson, J.-S. Kim, M.M. Thackeray, C.P. Grey, "Lithium and Deuterium NMR Studies of Acid-Leached Layered Lithium Manganese Oxides," *11th International Meeting on Lithium Batteries, Monterey, CA,* June 2002.

J.-S. Kim, J.T. Vaughey, C.S. Johnson and M.M. Thackeray, "Elevated Temperature Performance of $LiMn_{2-x}Mn_xO_4$ Electrodes (M=Li, Mg, Al, Zn) as a Function of Tetrahedral Site Occupancy," *202nd Meeting of the Electrochemical Society*, Salt Lake City, UT, October 2002.

J.-S. Kim, J.T. Vaughey, C.S. Johnson, A.J. Kropf and M.M. Thackeray, "Electrochemical Evaluation of $xLi_2TiO_3 \bullet (1-x)LiMn_{0.5}Ni_{0.5}O_2$ ($0 \le x \le 0.31$) Electrodes for Lithium-Ion Batteries," *202nd Meeting of the Electrochemical Society*, Salt Lake City, UT, October 2002.

IV.E.2. New Cathode Materials Based on Layered Structures

M. Stanley Whittingham
State University of New York at Binghamton, Chemistry and Materials Research Center, Binghamton, NY 13902-6000
(607) 777-4623, fax: (607) 777-4623, e-mail: stanwhit@binghamton.edu

Objective

- Find lower-cost and higher-capacity cathodes, exceeding 200 Ah/kg, that are based on benign materials.

Approach

- Place emphasis on manganese dioxides, both pure and modified with other transition metals, using predominantly low-temperature synthesis approaches.
- Synthesize these materials and characterize them structurally for thermal and chemical stability.
- Evaluate above electrochemically in a variety of cell configurations; then compare with lithium iron phosphates.

Accomplishments

- Determined that layered manganese dioxides can be stabilized, that their electronic conductivity and cell cycling can be significantly enhanced by the addition of other transition metals, and that nickel-based compounds such as $LiNi_{0.4}Mn_{0.4}Co_{0.2}O_2$ exhibit very good properties.
- Completed a study of the $LiFePO_4$ cathode as a base-case system. We have shown that the conductive coating method is not critical, and that the as-synthesized $LiFePO_4$ material has a resistivity of $10^5 – 10^6$ ohm-cm.
- Showed that in the charged state, the $FePO_4$ (FeO_6 octahedra) is kinetically stable relative to conversion to the thermodynamically stable quartz form (FeO_4 tetrahedra). However, over-discharge must be avoided as rechargeability is impeded by the formation of Li_3PO_4. The rate capability is reasonable, 1 mA/cm^2 at 20°C, even at high loadings approaching 100 mg/cm^2. This will be the base case against which all our future cathode studies will be compared.
- Showed that vanadium oxides can also be stabilized by the addition of Mn ions, and can achieve capacities over 220 Ah/kg.

Future Directions

- Identify changes in $LiMnO_2$ structure as a function of current density during cell cycling.
- Determine the structure and composition of the nickel-stabilized $LiNi_{1-y}Mn_yO_2$.
- Determine the role of cobalt in these layered compounds $LiNi_{1-y-z}Mn_yCo_zO_2$, and determine how to increase their rate capability.
- Complete, for Li-polymer cells, the evaluation of the Mn-stabilized □-vanadium oxides and compare them to the iron phosphates. Emphasis in all cases will be placed on understanding the reasons for capacity fade.

Introduction

The goal of this project is to identify transition metal oxides with superior properties to $LiCoO_2$, including higher capacity, lower cost, and being benign to the environment. Our emphasis remains on low-cost materials with capacities approaching 200Ah/kg, in particular layered manganese oxides. In addition, $LiFePO_4$ was studied as a low cost intermediate capacity system (that might meet the power capabilities for HEV) and □-vanadium oxides as a very high capacity system.

(a) Stabilized Manganese Oxide Cathodes – low cost, high capacity, safe systems

Layered $LiMnO_2$ has the potential of cycling 1 Li per Mn ion but is unstable relative to the spinel $LiMn_2O_4$ on cycling. Two approaches were used to stabilize the layer structure of manganese dioxide: (1) the incorporation of pinning ions to disrupt the oxygen cubic close packing thus minimizing the diffusion of Mn which is required for spinel formation, and (2) the partial substitution of some

of the Mn ions by later transition metals such as Fe, Co or Ni. In the former we found that vanadium oxide pillars prevented the formation of spinel-like phases; however, the rate capability requires improvement, and we are using Co to achieve this.

In the electronic approach, we make $LiMnO_2$ behave more like $LiCoO_2$ by substituting an element to the right of Co in the periodic table, such as Ni. Earlier we showed that this doping by Ni, Fe or Co enhances the electronic conductivity and cyclability of the manganese oxide. However, 10% substitution did not prevent spinel formation. Higher levels, ≥50%, as in $LiMn_{0.4}Ni_{0.4}Co_{0.2}O_2$, were found to maintain the layered structure. This compound cycled well with capacities approaching 200 Ah/kg at low rates. The rate capability was improved by an aqueous carbon gel coating. The Ni rather than the Mn is the electrochemically active ion, the Mn remaining in the +4 Oxidation state. The cycling behavior is shown for one sample (Fig. 20).

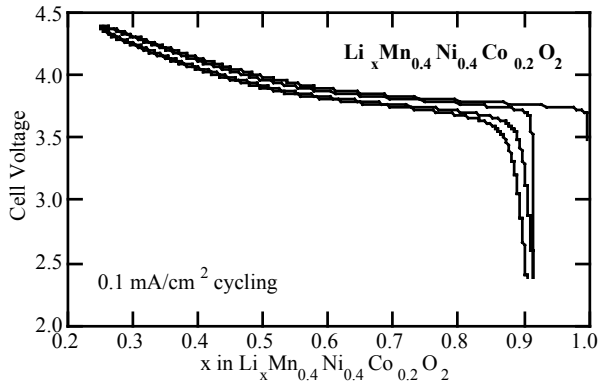

Figure 20. Electrochemical cycling of $Li_yMn_{0.9}Ni_{0.4}Co_{0.2}O_2$ at room temperature.

A range of compositions has been studied, and the first discharge capacity was proportional to the Ni content suggesting that the redox active specie is Ni, which cycles between Ni^{2+} and Ni^{4+}. The charging regime for the Co is mostly above the 4.3 to 4.4 volt cut-off used here. The Co appears to enhance the cyclability maybe through enhanced electronic conductivity, and we are working with G. Ceder at MIT to better understand the role of Co. To better understand the redox processes occurring, XPS and magnetic studies have been initiated. The susceptibility data is consistent with either Ni(III) + Mn(III) or Ni(II) + Mn(IV). The available literature data (from the Nesper group on $LiMn_{0.5}Ni_{0.5}O_2$) is inconsistent with the present ideas on the redox couple; initial interpretation of our XPS data (L. Matienzo of IBM) is underway. We see changes in the oxygen spectrum between different samples, but not between the Ni, Mn or Co spectra.

We have prepared carbon-coated samples of the stabilized layer phase, $Li_{1+x}Ni_{1-y-z-x}Co_zMn_yO_2$. These samples show good rate capability even at room temperature; 1st cycle capacity is 150, 140, and 95 mAh/g at 0.5, 0.83 and 3 mA/cm^2, respectively.

(b) Iron Phosphate Cathodes – low-cost, base-case 150 Ah/kg system

We are nearing completion of our study on the $LiFePO_4$ base-case cathode, which we will use for comparison against other cathodes such as the layered manganese nickel compounds discussed above. Hydrothermal synthesis was not found to be a viable preparative procedure due to lattice iron disorder. We found that the $FePO_4$ fully charged material was kinetically stable, although not thermodynamically stable. However, on over-discharge Li_3PO_4 is formed which is not readily reversible. 100% capacity is readily attained at
0.1 mA/cm^2, dropping to 80% at 1 mA/cm^2 with loadings of 20 to 80 mg/cm^2. The method of carbon coating was not found to be important, and carbon levels of 6 to 12 wt% were found to be effective. The capacity at 50°C increased to 100% at 1 mA/cm^2. The capacity/rate relationship is shown in Fig. 21. Capacity retention on cycling is very good.

Studies are continuing on other iron phosphate phases, both crystalline and amorphous. The Giniite phase is undergoing characterization at Binghamton and at Stony Brook (Clare Grey), and offers the opportunity for extensive exchange of the Fe for other metals such as Mn. However, $LiFe_{1-y}Mn_yPO_4$ was not particularly attractive, cycling only ≈ 0.5 Li at steady state.

(c) Stabilized Vanadium Oxide Cathodes – high-capacity system

We have continued the evaluation of layered vanadium oxides stabilized by Mn and Zn. These have the double-sheet δ structure, and exhibit initial capacities exceeding 300 Ah/kg double those of lithium iron phosphate. We have optimized the intercalated cations, and are evaluating the dramatic effect morphology and electrolyte cation has on the initial capacity and cycling.

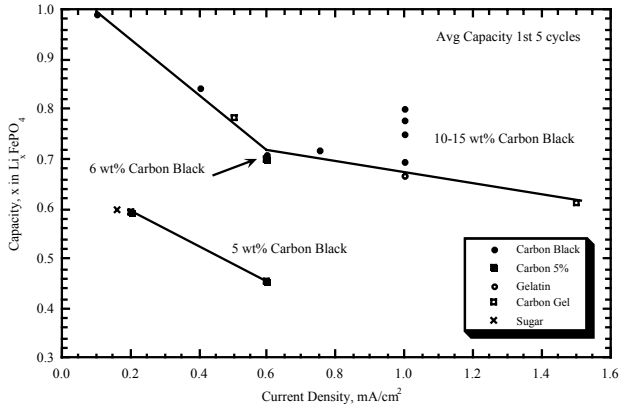

Figure 21. Capacity-rate relationship for $LiFePO_4$ cathodes with various carbon coatings. The capacities are the mean of the first 5 cycles.

Conclusions

$LiFePO_4$ provides a low-cost highly reversible cathode but has a lower volumetric capacity than $LiCoO_2$. It is a good base-case system. The stabilized manganese oxides (aka manganese-stabilized nickel oxides) show promise as the next-generation cathode. The vanadium oxides offer the greatest capacity, but at a lower voltage.

Publications

S. Yang, P.Y. Zavalij and M.S. Whittingham, "Hydrothermal Synthesis of Lithium Iron Phosphate Cathodes," *Electrochem. Commun.*, **3**, 505-508 (2001).

S. Yang, Y. Song, P.Y. Zavalij and M.S. Whittingham, "Reactivity, Stability and Electrochemical Behavior of Lithium Iron Phosphates," *Electrochem. Commun.*, **4**, 234-239 (2002).

Y. Song, S. Yang, P.Y. Zavalij and M.S. Whittingham "Temperature-dependent Properties of $FePO_4$ Cathode Materials," *Mater. Res. Bull.*, **37**, 1249-1257 (2002).

P.Y. Zavalij, F. Zhang and M.S. Whittingham, "The Zinc-Vanadium-Oxygen-Water System: Hydrothermal Synthesis and Characterization," *Solid State Sciences*, **4**, 591-597 (2002).

S. Yang, Y. Song, P.Y. Zavalij and M.S. Whittingham, "Nanocomposite Electrodes for Advanced Lithium Batteries: The $LiFePO_4$ Cathode," *Mater. Res. Soc. Proc.,* **V7.9**,703 (2002) .

IV.E.3. Synthesis and Characterization of Cathode Materials

Marca M. Doeff
Lawrence Berkeley National Laboratory, 62R0203, Berkeley CA 94720-8253
(510) 486-5821, fax: (510) 486-4881, e-mail: mmdoeff@lbl.gov

Objective

- Develop low-cost, benign cathodes (*e.g.*, manganese oxides, metal phosphates) having electrochemical characteristics (cycle life, energy, and power densities) consistent with the goals of the USABC and/or FreedomCar.

Approach

- Synthesize candidate materials with optimum purity, particle size, and morphology by various methods.
- Determine physical and structural properties relevant to battery operation.
- Evaluate electrochemical performance in relevant cell configurations.

Accomplishments

- Provided baseline cathode material ($Li_{1.02}Al_{0.25}Mn_{1.75}O_{3.98}S_{0.02}$) to BATT for testing (11/01), completed electrochemical characterization, and made a "no go" recommendation based on the results.
- Demonstrated effect of particle size and nature of residual carbon on electrochemical properties of $LiFePO_4$.
- Synthesized and characterized a series of substituted layered manganese oxides, which discharge up to 200 mAh/g in a Li/liquid electrolyte cell configuration.

Future Directions

- Investigate high-capacity layered substituted manganese oxides with intergrowth structures and compounds with tunnel structures.
- Finish evaluation of sol-gel method to produce $LiFePO_4$ with small particles and make "go-no go" decision.

Introduction

The spinel $LiAl_{0.25}Mn_{1.75}O_{3.98}S_{0.02}$ has been reported to cycle well when discharged on the 3 V plateau *vs*. Li. We synthesized this compound and $Li_{1.02}Al_{0.25}Mn_{1.75}O_4$ by solid-state and sol-gel methods using Li_2S (optionally) as the sulfur source. We also received a sample from the Korean group who originally reported on this compound, made by sol-gel. XRD, EDS, and ^7Li MAS-NMR (Cairns' group) indicate that sulfur is not present in the bulk of any of the samples. All materials showed low capacity (~ 90 mAh/g) and poor rate capability at 4 V *vs.* Li compared to undoped Merck SP30 spinel. All lost capacity rapidly when cycled below 3 V *vs*. Li, although the donated sample showed a marked resistance to tetragonal phase conversion (cells gave almost no extra capacity, but polarized instead). Because of this, the fade rate was slower and overall capacities lower than for other samples. The difference in behavior is attributed to the unusual particle morphology; a consequence of firing in the presence of sulfur-containing compounds. This is difficult to reproduce due to the reactivity of Li_2S with water and air. Because of poor electrochemical properties and irreproducibility of the synthesis process, we recommended dropping this material from the BATT program.

$LiFePO_4$ suffers from poor utilization in electrochemical cells because of low electronic conductivity and ionic diffusivity. Reduction of the particle size of $LiFePO_4$ by planetary milling greatly improves utilization. Carbon coating $LiFePO_4$ also improves rate capability markedly. We have synthesized $LiFePO_4$ by a sol-gel method, which allows use of iron-nitrate precursors and results in high-purity products with well-controlled particle sizes. The amount, structure, and distribution of residual carbon in sol-gel $LiFePO_4$, as determined by Raman microprobe spectroscopy (R. Kostecki) differ considerably depending on processing details. As a result, products vary greatly in their electrochemical properties. Uncoated materials made from iron acetate or oxalate perform better than sol-gel compounds due to the larger amount of residual carbon in the former. Superior performance, however, is

expected for coated sol-gel samples, because coating thicknesses and distribution are more easily controlled.

Tunnel-Li_xMnO_2 with the $Na_{0.44}MnO_2$ structure cycles stably and has excellent rate capability, but limited capacity. O2 layered compounds made from sodium manganese oxides with the P2 structure potentially have higher energy densities but may be less stable than tunnel compounds. CV, galvanostatic cycling, and XRD experiments show no evidence of phase conversion for at least 30 cycles. Spinel formation, which occurs fairly rapidly during cycling of O3 layered manganese oxides is not observed. O2 compounds do not have a cubic close-packed oxygen array, in contrast to O3 and spinel compounds. Because more bond breaking and rearrangement is required to form spinel from the O2 structure during cell cycling, they are inherently more stable.

Capacities vary from ~80-180 mAh/g for the O2 layered compounds depending upon substituents. Best results are obtained for 11% Ni, Co, or Al-substituted manganese oxides. Some of the variation is due to kinetic effects, but Li in an O3 environment (observed by NMR and XRD) was observed in all of the high-capacity electrodes, suggesting a correlation. The sodium-containing precursors of these compounds are actually intergrowths of P2 and P3 (Fig. 22), which convert to stacking faulted O2/O3 compounds upon ion exchange. The ratios of these components can be controlled by varying Na content of the precursors.

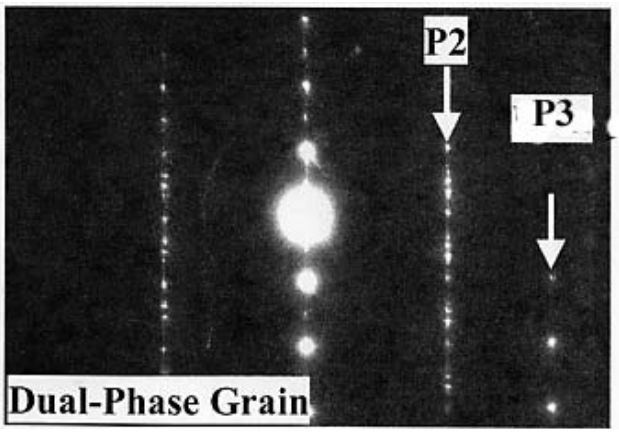

Figure 22. Electron diffraction pattern of $Na_{0.7}Al_{0.11}Mn_{0.89}O_2$, showing that it is a P2/P3 intergrowth. Photograph courtesy of Dr. X. Feng of the Materials Sciences Division, LBNL.

A 100% O3 $Li_xNi_{0.2}Mn_{0.8}O_2$ compound discharges 200 mAh/g in a Li cell (Fig. 23) proving that O3 is the higher capacity/rate component. It is very interesting that the stacking-faulted O2/O3 compounds do not undergo the expected transition to spinel. We speculate that O3 layers are "pinned" by the surrounding O2 layers, impeding phase conversion. It is, however, important to demonstrate stability under conditions that batteries are likely to encounter in vehicular applications (high rates, prolonged cycling, overcharge, etc.), so this requires more extensive investigation. Ideally, the perfect compromise between the high rate/high capacity of O3 and the stability of O2 compounds can be obtained by manipulating the relative amounts and distributions of these components in the intergrowths. Some work in FY2003 will be devoted to this task. We will continue to investigate tunnel compounds with the $Na_{0.44}MnO_2$ and psilomelane structures. (Preliminary results indicate higher initial capacities but more sensitivity to over-discharge for the latter compared to the former.)

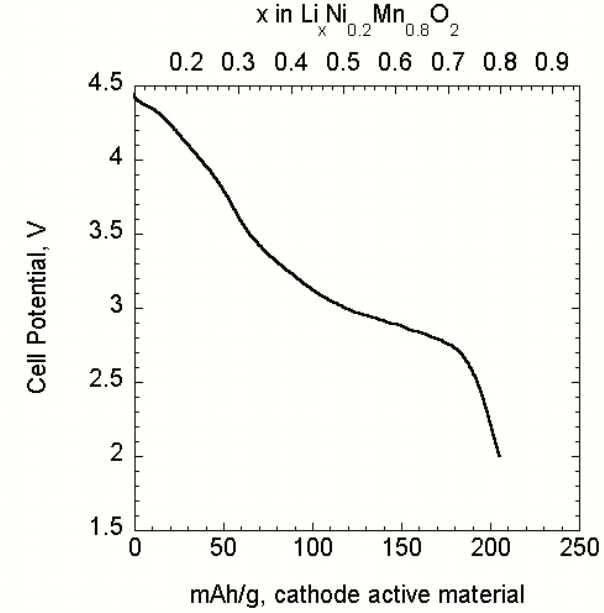

Figure 23. Discharge profile of a Li/1M $LiPF_6$, EC-DMC/100% O3-$Li_xNi_{0.2}Mn_{0.8}O_2$ cell at 0.055 mA/cm^2. The cell was initially charged to 4.5 V.

Publications and Presentations

M.M. Doeff, T.J. Richardson, K.-T. Hwang and A. Anapolsky, "Improved Discharge Characteristics of Tunnel-Containing Manganese Oxide Electrodes for Rechargeable Lithium Battery Applications," *ITE Battery Lett.*, **2(3),** B-63 (2001).

M.C. Tucker, M.M. Doeff, T.J. Richardson, R. Fiñones, J.A. Reimer and E.J. Cairns, "^{7}Li and ^{31}P MAS NMR of $LiFePO_4$-Type Materials", *Electrochem. and Solid State Letters*, **5**, A95 (2002).

M.C. Tucker, M.M. Doeff, T.J. Richardson, R. Fiñones, E.J. Cairns and J.A. Reimer, "Hyperfine Fields at the Li Site in $LiFePO_4$-Type Olivine Materials for Lithium Rechargeable Batteries: A ^{7}Li MAS NMR and SQUID Study," *J. Am. Chem. Soc.*, **124**, 3833 (2002).

M.M Doeff, R. Fiñones and Y. Hu, "Electrochemical Performance of Sol-Gel Synthesized $LiFePO_4$ in Lithium Batteries" *202nd Electrochem. Soc. Meeting*, Salt Lake City, UT, October 2002.

T.A. Eriksson and M.M. Doeff, "A Study of Layered $Li_xM_yMn_{1-y}O_{2+z}$ (M=Fe, Co, Ni, Zn, Al) Cathode Materials," *11th International Meeting on Lithium Batteries*, Monterey, CA, June 2002.

M.M. Doeff, J. Hollingsworth and J.-P. Shim, "Factors Influencing the Electrochemical Behavior of Sulfur-doped Aluminum-substituted Lithium Manganese Oxide Spinels in Lithium Cells," *201st Electrochem. Soc. Meeting*, Philadelphia, PA, May 2002.

M.M. Doeff, T.J. Richardson, M. Gonzales and K.-T. Hwang, "Effect of Ion Substitution on the Electrochemical Characteristics of Tunnel-containing Manganese Oxide Electrodes," *200th Meeting of the Electrochemical Society,* San Francisco, CA, September 2001.

IV.E.4. Novel Cathode Materials

John B. Goodenough
University of Texas at Austin, 1 University Station, C2200, Austin, TX 78712
(512)-471-1646, fax: (512)-471-7681, email: jgoodenough@mail.utexas.edu

Objective

- Evaluate alternative layered oxides as cathode materials for a Li-ion battery that operates between Ni(II) and Ni(IV).

Approach

- Prepare $LiNi_{0.5}Mn_{0.5}O_2$ nanoparticles and coat them with carbon.
- Construct button cells for investigation of charge and discharge characteristics of the cathode material with and without carbon coating.
- Examine, using SEM, the morphology of the particles and the carbon coat.

Accomplishments

- Prepared $LiNi_{0.5}Mn_{0.5}O_2$ nanoparticles and coated agglomerates of particles with carbon.
- Conducted tests with button cells, which demonstrated that carbon coating improves capacity and stability under repeated cycling.

Future Directions

- Investigate ball milling to achieve coating of individual particles.
- Investigate influence of other cations than Mn(IV) on the performance of operation on Ni(III)/Ni(II) and NI(IV)/Ni(III) redox couples.
- Compare performances of spinel *vs.* layered oxides.

Introduction

$LiMn_{0.5}Ni_{0.5}O_2$ has a face-centered-cubic oxygen array with Li^+ occupying alternate (111) planes of octahedral sites and $Mn_{0.5}(IV)Ni(II)_{0.5}$ occupying the other planes of edge-shared octahedral sites. The Li^+ ions can be reversibly extracted electrochemically (or chemically); extraction of the first 0.5 Li/formula unit oxidizes the Ni(II) to Ni(III); further extraction of Li would oxidize Ni(IV) to Ni(III) as occurs in $Li_{1-x}Co_{0.3}Ni_{0.7}O_2$. However, the 90° M-O-M interactions and the tortuous Ni-O-Ni percolation result in a poor electronic conductivity, which limits the power capability of the material as a cathode in a rechargeable Li^+-ion battery. We have therefore investigated the use of a Li^+-permeable carbon coating on the electrode particles to supply electrons to the interior of the cathode particles.

$LiMn_{0.5}Ni_{0.5}O_2$ (LMNO) was prepared by direct reaction between LiOH, Ni metal, and Mn_2O_3; the ground reactants were heated overnight at 800°C and then reground, compacted into 2.5-cm-diameter pellets and heated to 900°C for 20 h in air.

The carbon source for coating the oxide particles was a carbon xerogel formed from a resorcinal-formaldehyde (R-F) polymer. The $LiMn_{0.5}Ni_{0.5}O_2$ particles were carbon coated by compacting into a pellet a mixture of the oxide and R-F in an 85:15 weight ratio. Li was extracted from the pellet with excess I_2 in an acetonitrile solution. The products were characterized structurally by powder XRD and then combined with acetylene black and teflon in a 70:25:5 weight ratio and rolled into sheets from which cathodes were cut.

Button-type electrochemical test cells used a Li anode and 1 M $LiPF_6$ in 1:1 ethylene carbonate:diethyl carbonate as the electrolyte. Comparison was made between the performances of cells with coated (LMNO-C) and with uncoated (LMNO) oxide particles. The carbon content of the coated particles was 2.5% (w/w) determined by thermogravimetric analysis. SEM showed that both the coated and uncoated oxides contain 10-100 nm particles bound into 10-150 μm agglomerates. A carbon map obtained with an energy-dispersive x-ray spectrometer showed the carbon coating was evenly distributed across the agglomerate surfaces.

Charging was limited to 4.3 V *vs*. Li, and the discharge curves ranging from 4.1 to 3.5 V *vs*. Li gave the discharge capacities as a function of cycle number shown in Fig. 24 for various current densities. Fig. 25 summarizes the average discharge capacities of LMNO and LMNO-C over the first 50 cycles at various current densities. These data show that carbon coating enhances the capacity and reduces the capacity fade. However, better performance can be expected if the carbon coats the individual particles, not just the surface of the agglomerates.

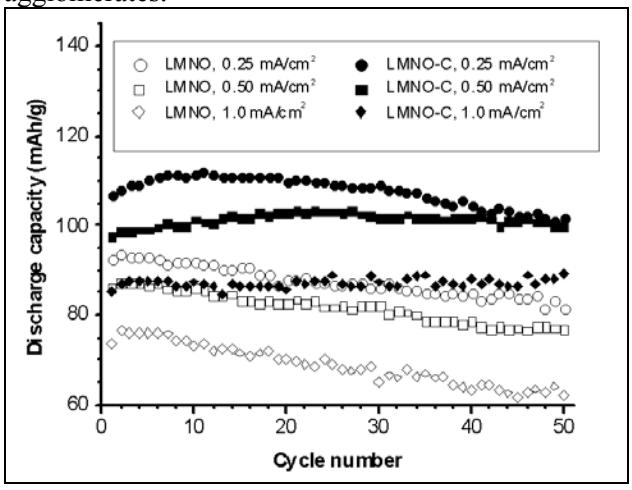

Figure 24.

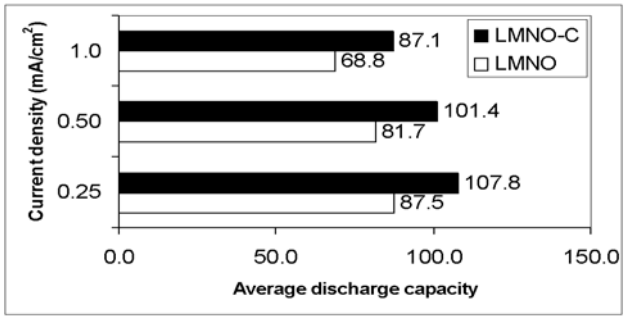

Figure 25.

Publication

B.L. Cushing and J.B. Goodenough, "Influence of Carbon Coating on the Performance of a $LiMn_{0.5}Ni_{0.5}O_2$ Caathode," *Solid State Sciences* **4**, 1487-1493 (2002).

IV.F. Diagnostics

IV.F.1. Electrode Surface Layers

Frank R. McLarnon and Robert Kostecki
Lawrence Berkeley National Laboratory, 70R0108B, Berkeley CA 94720-8168
(510) 486-4636, fax: (510) 486-426, e-mail: frmclarnon@lbl.gov

Objective

- Establish direct correlations between electrode surface changes, interfacial phenomena, and cell capacity decline.

Approach

- Use ellipsometry, Raman spectroscopy, and advanced microscopic techniques to characterize electrodes taken from baseline BATT Program cells, as well as thin-film electrodes in model cells.
- Measure changes in electrode surface morphology and structure, electrode surface chemistry, and SEI thickness and composition that accompany cell cycle-life tests.

Accomplishments

- Defined relationships between electrode history, electrode surface properties, and temperature for baseline $LiAl_{0.05}Ni_{0.8}Co_{0.15}O_2$ cathodes.
- Characterized structural disordering of graphite anodes during cycling at elevated temperatures and correlated the mechanism of SEI reformation upon cycling with graphite structural degradation.

Future Directions

- Correlate changes of cathode surface morphology and chemistry to the mechanism of $LiFePO_4$ cathode degradation in BATT Program cells.
- Determine the impact of anode carbon disordering on long-term Li-ion cell performance.
- Provide full diagnostic results for model thin-film $LiMn_2O_4$ cathodes.

Introduction

We used Raman microscopy and AFM to monitor and understand the effect of structural changes that occur in graphitic materials upon extensive cycling at elevated temperatures. By combining these two methods of surface analysis we could evaluate the surface and near-surface changes resulting from exposure of BATT Program anodes to stresses that arise from numerous Li intercalation-deintercalation cycles and elevated temperatures. BATT Program task 1.1 (K. Striebel) provided cycled cells with synthetic graphite anodes (Hitachi Chemical MAG-10), $LiNi_{0.8}Co_{0.15}Al_{0.05}O_2$ cathodes, and either $LiPF_6$-EC-DEC electrolyte for cells Q0120V and PG04, or LP40 electrolyte for cell PG13. The cells were charged and discharged ~400 times at the C/2 rate and 100% DOD between 3.0 and 4.1 V at ambient temperature (Q0120V, PG04) and at 60°C (PG13). All cells exhibited significant capacity loss: 13%, 33%, and 65%, respectively, for cells Q0120V, PG04, and PG13.

The integrated intensity ratio of carbon D/G bands, which is inversely proportional to the size of microparticles and increases with carbon disorder, was used to evaluate carbon structure. The G-band, which is located at 1580 cm^{-1}, arises from the first-order scattering associated with the in-plane E2g mode, whereas the D-band is associated with the break of symmetry occurring at the edges of graphite sheets. Figure 26 shows Raman images of the integrated intensity ratio of D/G carbon Raman bands, represented by different shades of gray, collected from a 40 x 60 mm area with 0.7 μm resolution. The lighter is the shade of gray on the image, the more graphitic is the electrode structure. The Raman images reveal that the graphite undergoes gradual structural degradation upon

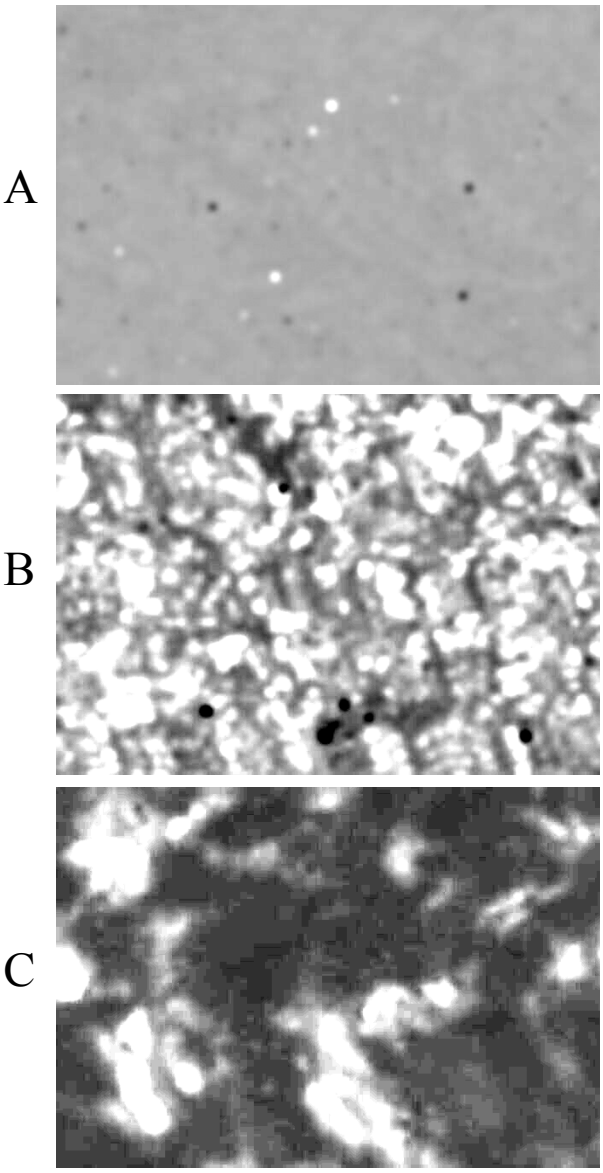

Figure 26. Raman maps of D/G band ratio of graphite BATT Program anodes. A) fresh anode, B) anode from a cell cycled at room temperature, C) anode from a cell cycled at 60°C. The lighter is the shade of gray on the image, the more graphitic is the electrode structure.

cycling. Severe structural disorder was observed in the anode from the cell cycled at 60°C. Interestingly, the structural degradation of graphite did not occur uniformly over the anode surfaces. Even for the anode, which shows substantial damage on its surface (cell PG13), one can still identify regions which consist of undisturbed graphite. Distortions in the graphite structure can create a barrier for Li ion diffusion during the intercalation-deintercalation process, contributing to electrode impedance rise and

cell capacity loss. Also, structural degradation of the graphite led to increased anode surface reactivity *vs*. the electrolyte, and the formation of SEI layers. A thick layer of inorganic products from side reactions, signaled by Raman bands at 1000-1100 cm^{-1} that are characteristic for lithium carbonates and phosphates, was observed on the disordered part of the carbon anode. The presence of these products suggests that structural changes in the anode surface greatly affected the composition of the SEI layer and caused a permanent shift in Li inventory in the tested cells, contributing to the observed capacity loss.

We continued *in situ* spectroscopic ellipsometry studies of thin-film $LiMn_2O_4$ spinel electrodes. Our objective was to determine how the electrode composition profile and structure change as the electrode is cycled in EC-DMC (1:1 by vol.) + 1 M $LiPF_6$ electrolyte. We were able to accurately simulate the ellipsometric data in the initial stages of Li^+ intercalation into with a simple model, the one-dimensional growth of a linear Li-ion concentration gradient in the thin-film $LiMn_2O_4$ electrode. From our analysis we derived a Li^+-ion diffusion coefficient of $6.3 \bullet 10^{-12}$ cm^2/s, a value which agrees well with published data, see *J. Electrochem. Soc*., **145**, 3024 (1998). The change in slope of the Ψ-t curve indicates that a phase transition took place. We were able to accurately simulate the ellipsometric data in subsequent stages of Li^+ intercalation with a complex double-gradient model, in which the electrode was assumed to contain two manganese oxide phases. From our analysis, we derived an apparent average Li^+-ion diffusion coefficient of $5.1 \bullet 10^{-12}$ cm^2/s in this region. The positive Ψ-t curve slope implied that an additional phase transition took place as the cathode was charged further.

We also used *in situ* spectroscopic ellipsometry to investigate the formation and growth of SEI layers on thin-film $LiMn_2O_4$ cathodes. We confirmed that a SEI layer formed as soon as the cathode came into contact with the electrolyte (1.0 M $LiPF_6$ in EC/DMC), as signaled by a sharp change of ellipsometric values when electrolyte was injected into the electrochemical cell. To account for the observed change, it was necessary to include in our model a SEI layer between the cathode and electrolyte. Our physical model, in which a SEI layer is included, fit the ellipsometric data very well. By analyzing the ellipsometric data and calculating the resulting SEI optical constants, we found that SEI layer developed slowly during the first few cycles. We concluded that the SEI layer composition had reached at a stable state after the third charge/discharge cycle

We carried out a series of Raman microscopy and current-sensing atomic force microscopy (CSAFM) diagnostic tests on $LiNi_{0.8}Co_{0.15}Al_{0.05}O_2$ cathodes from ATD and BATT Program cells, and $LiFePO_4$ cathodes from BATT Program baseline cells. We confirmed that Al has a stabilizing effect on the structure of mixed Ni and Co oxides and prevents their decomposition upon cycling or storage at elevated temperatures. Our diagnostic studies of composite cathodes revealed a gradual loss of carbon additive from the cathodes, especially at elevated temperatures. Interestingly, the two carbon components disappear from the cathode surface at different rates, depending on their particle size and structure; *i.e*., the surface concentration of acetylene black decreases at a higher rate than does graphite. Among possible causes of this phenomenon are carbon migration or peeling, oxide particle dissolution-deposition, and anion intercalation into carbon. CSAFM measurements revealed that the cathode surface electronic conductance decreases dramatically with increasing cell test temperature, which is in concert with the observed carbon loss. Moreover, we determined that the cathode surface consists of partially (and sometimes almost fully) charged $Li_{1-x}Ni_{0.8}Co_{0.15}Al_{0.05}O_2$ particles, despite deep discharges at the end of cell testing. Degradation of electronic contact between grains of active material may be responsible for this effect. We found no clear evidence of nano-crystalline deposits or non-conductive SEI's on the $LiNi_{0.8}Co_{0.15}Al_{0.05}O_2$ cathode surfaces; however, we observed poly-phosphorous compounds that may contribute to SEI layer formation on $LiNi_{0.8}Co_{0.15}Al_{0.05}O_2$ and $LiFePO_4$ cathodes.

IV.F.2. Battery Materials: Structure and Characterization

James McBreen
Brookhaven National Laboratory, MSD-Bldg. 555, P.O. Box 5000, Upton, NY 11973-5000
(631) 344-4513, fax. (631) 344-5815, email jmcbreen@bnl.gov

Objective

- Establish direct correlations between electrode material changes, interfacial phenomena, and cell capacity decline.

Approach

- Apply a combination of *in situ* and *ex situ* synchrotron techniques to characterize electrode materials and electrodes taken from baseline BATT Program cells.
- Develop and apply X-ray absorption spectroscopy (XAS) techniques that are sensitive to both surface and bulk processes in electrodes.

Accomplishments

- Completed studies of $LiMn_2O_4$ spinel.
- Completed development of techniques for XAS studies of phosphorous decomposition products in cycled cells and applied it to ATD Program.
- Completed most of the *in situ* XAS and XRD work on $LiFePO_4$ and $LiNi_xMn_{1-x}O_2$.

Future Directions

- Carry out soft x-ray XAS studies of new cathode materials.
- Characterize Mn- and Fe-based cathode materials with improved stability.
- Pursue studies of non-carbon anodes.

Introdution

Our objectives are to develop and apply advanced diagnostic techniques, with sensitivity to bulk and surface processes, to monitor degradation processes in Li-ion batteries. These techniques are also being used to elucidate properties of starting materials that determine performance and stability of $LiMn_2O_4$ and other low-cost cathode materials with higher capacity ($LiFePO_4$ and $LiNi_xMn_{1-x}O_2$). We use a combination of *in situ* and *ex situ* XAS and XRD to study bulk processes in electrodes. We also use *ex situ* soft x-ray XAS in both the electron yield and fluorescence mode to distinguish between surface and bulk processes on electrodes. In the soft x-ray regime from 500-1000 eV, the escape depth for the Auger electrons is about 50 Å and the sampling depth for the fluorescent signals is about 3000 Å. Thus the former probes close to the surface whereas the latter probes the bulk.

XRD Studies of $LiMn_2O_4$

In FY 2002, we completed an extensive study of $LiMn_2O_4$. *In situ* XRD on $LiMn_2O_4$ that in the 4.1 V region indicates that there are two first-order phase transitions with three cubic phases. The studies of $LiMn_2O_4$ indicate that the cycle life and stability of $LiMn_2O_4$ can be greatly improved by use of excess Li stoichiometry, elimination of oxygen deficiency and by using stable electrolytes that do not generate acidic species in the cell. Excess Li stoichiometry increases the range of lattice constants for all three phases and

yields pseudo-single-phase behavior. Increasing oxygen deficiency promotes the conversion of the cubic spinel to a tetragonal phase at low temperature. The transition temperature, the transition kinetics, and the amount of the spinel converted to the tetragonal phase increases with increasing oxygen deficiency.

XRD and XAS Studies of $LiFePO_4$ and $LiNi_{0.5}Mn_{0.5}O_2$

Both *in situ* XRD and XAS reveal the presence of a first-order phase transition during charge ($LiFePO_4 \rightarrow FePO_4$). Principal component analysis of the Fe near edge XAS clearly show that a maximum of two components (indicating the presence of only two distinct phases) can account for the XAS data at all states of charge. *In situ* XRD of $LiNi_{0.5}Mn_{0.5}O_2$ indicates that it has the $R\bar{3}m$ structure. During charge the H1 phase is converted to the H2 phase, accompanied by an elongation of the c-axis and a contraction of the a-axis. Unlike other materials with the $R\bar{3}m$ structure ($LiNiO_2$ and $LiNi_{0.8}Co_{0.2}O_2$) there is no conversion to the H3 phase, even at 4.6 V. However, $LiNi_{0.3}Mn_{0.7}O_2$ did show formation of the H3 phase, indicating that stable operation requires the $LiNi_{0.5}Mn_{0.5}O_2$ composition.

XRD Studies of Carbon Coated Si Anodes

In situ XRD indicate that, during charge, intercalation first takes place in the graphite coating and then in the Si. The graphite coating promotes uniform lithiation of the Si to produce an amorphous material. Without the coating, there is only localized incomplete lithiation of the Si. The coating either acts as a buffer that promotes uniform lithiation or it protects the Si surface from the electrolyte. A combination of both mechanisms is also possible.

Publications

X. Sun, H.S. Lee, X.-Q. Yang and J. McBreen, "Improved Elevated Temperature Cycling of $LiMn_2O_4$ Spinel Through the Use of a Composite LiF Based Electrolyte," *Electrochem. Solid-State Lett.,* **4**, A184 (2001).

M. Balasubramanian, J. McBreen, I.J. Davidson, P.S. Whitfield and I. Kargina, "*In Situ* X-ray Absorption Study of a Layered Manganese-Chromium Oxide Based Cathode Material," *J. Electrochem. Soc.,* **149**, A176 (2002)

X. Sun, X.-Q. Yang, M. Balasubramanian, J. McBreen, Y. Xia and T. Sakai, "*In Situ* Investigation of Phase Transitions of $Li_{1+y}Mn_2O_4$ Spinel During Li-ion Extraction and Insertion," *J. Electrochem. Soc*. **149**, A842 (2002).

J. McBreen and M. Balasubramanian, "Rechargeable Lithium-Ion Battery Cathodes," *JOM* **54**(3), 25 (2002).

W.-S. Yoon, Y. Paik, X.-Q. Yang, M. Balasubramanian, J. McBreen, and C.P. Grey, "Investigation of the Local Structure of the $LiNi_{0.5}Mn_{0.5}O_2$ Cathode Material during Electrochemical Cycling by X-ray Absorption and NMR Spectroscopy," *Electrochem. Solid-State Lett*. **5**, A263 (2002).

X.-Q. Yang, J. McBreen, W.-S. Yoon, and C. Grey, "Crystal Structure Changes of $LiMn_{0.5}Ni_{0.5}O_2$ Cathode Materials During Charge and Discharge Studied by Synchrotron Based *In Situ* XRD," *Electrochem Commun.* **4**, 649 (2002).

X.-Q. Yang, J. McBreen, W.-S. Yoon , M. Yoshio, H. Wang, K. Fukuda and T. Umeno, "Structural Studies of New Carbon Coated Silicon Anode Materials Using Synchrotron Based *In Situ* XRD," *Electrochem. Commun.* **4***,* 893 (2002).

M. Balasubramanian, J. McBreen, K. Pandya and K. Amine**,** "Local Structure of Dilute Gallium Ions in $LiNi_{0.908}Co_{0.085}Ga_{0.003}O_2$ Cathode Material: *InSitu* X-Ray Absorption Study," *J. Electrochem. Soc.* **149**, A1246 (2002).

IV.F.3. Interfacial and Reactivity Studies

Philip N. Ross, Jr.
Lawrence Berkeley National Laboratory, MS 2R0100, Berkeley CA 94720-8196
(510) 486-6226, fax: (510) 486-5530, e-mail: pnross@lbl.gov

Objective

- Establish direct correlations between electrode surface changes, interfacial phenomena, and cell failure.

Approach

- Use FTIR spectroscopy and X-ray photoelectron spectroscopy (XPS) to study model electrode/electrolyte combinations, *e.g.*, using glassy carbon electrodes and BATT Program electrolytes, to provide the basis to interpret more-complex spectra recorded for ATD Program cell materials.

Accomplishments

- Completed experimental measurements of the electrochemical potentials of all carbonate solvents of interest in Li-ion batteries.
- Completed experimental measurements of the electrochemical reduction and oxidation potentials of selected electrolyte additives of interest in Li batteries.

Future Directions

- Establish thermal stability of the SEI layer on graphite anodes in ATD Program Gen 2 electrolyte.
- Identify some routes to improved stability *via* electrolyte additives and/or graphite pre-treatment.

Introduction

The oxidation potentials of a commonly used Li-ion battery electrolyte, EC:DMC (1:1) – 1 M $LiPF_6$ (LP 30 Selectipur from Merck), was measured using a combination of CV with a rotating disk electrode (RDE) and *in situ* infrared reflection absorption spectroscopy (IRAS). The use of the RDE enabled us to distinguish small currents from the oxidation of impurities from the onset of oxidation of the electrolyte. The oxidation potential at a Pt or glassy carbon electrode is at or just above 5.2 V, depending on the criterion used. The IRAS spectra clearly show the appearance of CO_2 in solution from solvent oxidation above 5 V using a glassy carbon electrode. The oxidation potential of an important Li-ion battery additive, VC, was determined from IRAS experiments to be near 4 V. The experimental values of the oxidation potentials determined here are consistent with the predicted values from Density Functional Theory (DFT) for one-electron oxidation (ionization) of the carbonate molecule to the radical cation (molecular ion). Neither the salt nor the electrode material affected the oxidation potential determination in these experiments.

An IR spectroelectrochemical cell with a flat CaF_2 window was used for the *in situ* IRAS experiments. A glassy carbon disk served as the working electrode and Li metal as both counter and reference electrodes. The cell was assembled in the dry box and transferred to the Nicolet Model 670 FTIR spectrometer. FTIR spectra were obtained as a function of potential with the electrode pushed against the CaF_2 window. For each potential step, the working electrode was retracted from the window and the reaction was allowed to progress for 5 min. before returning the electrode to the window. A strain gauge was used to monitor the force applied on the window to assist in returning the electrode to the

same position at each potential and to prevent excessive pressure that could cause window to crack. Spectra were measured with a resolution of 4 cm^{-1} by accumulating 20–30 scans using a high-sensitivity LN cooled MCT detector.

Figure 27 shows the disk and ring current profile when the potential was scanned from 3.5 to 5.5 V using a Pt disk and a Pt ring in a RDE experiment. Oxidation of the EC:DMC(1:1) –1 M $LiPF_6$ electrolyte was observed to start only at potentials above 5.1 V on the Pt disk. The disk currents at potentials above 5 V were independent of rotation rate, indicative of oxidation of a species present in relatively high concentrations, such as the solvent or the solute. There was no evidence of passivation of the disk electrode from the oxidation process.

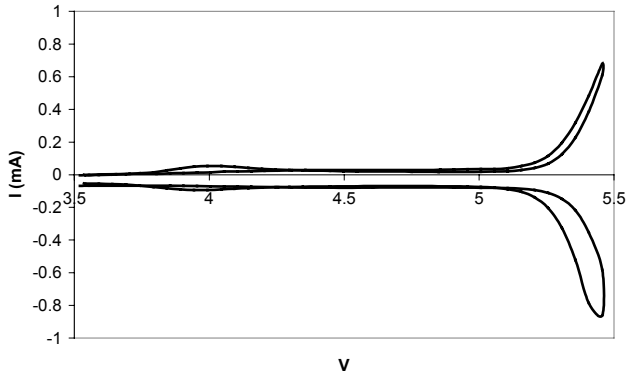

Figure 27. Cyclic voltammetry on a Pt RDE in EC:DMC – 1 M $LiPF_6$ sweeping between 3.5 and 5.4 V (*vs*. Li/Li^+) at 5 mV/s and 1600 rpm.

The disk currents at potentials below 5 V were less than 50 μA, and were *dependent on rotation rate*, *i.e.*, proportional to $\omega^{1/2}$. Since the diffusion-limiting current for oxidation of either the solvent or the salt would be orders of magnitude higher than this value, the small currents below 5 V are attributed to oxidation of the impurities in the electrolyte. We note that the current at 4.5 V in our voltammetry experiment (40 μA) is more than an order of magnitude lower than that reported by Aurbach and coworkers[1] for a similar but not identical electrolyte (1:1 EC:DEC – 1 M $LiClO_4$ on Pt or 1:1 EC:DEC – 1 M $LiAsF_6$ on Au). Using our criterion for the onset of electrolyte oxidation, the oxidation potential derived from the data of Aurbach and co-workers would be around 4–4.1 V for the EC-based solvents used in that study. This is about 1 V lower than in ours, and cannot be attributed to the *criterion* used for determining the onset of oxidation. Our conclusion is that the low oxidation potential reported by Aurbach and co-workers is due to impurities in their electrolyte, most probably water.

In situ IRAS was used to provide more detail about the electrolyte oxidation process using a glassy carbon electrode. IR spectra at potentials from open circuit (ca. 3.8 V) up to 5.6 V are shown in Fig. 28.

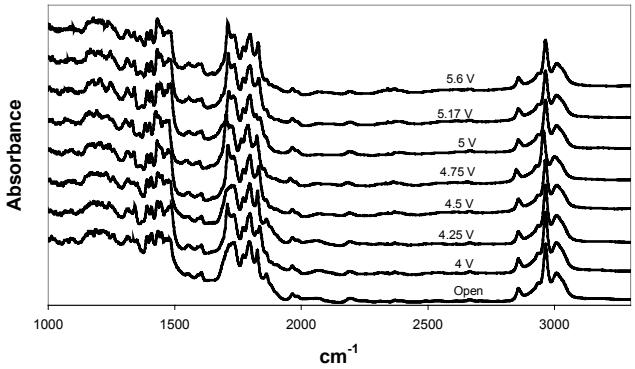

Figure 28. IRAS spectra from a glassy carbon electrode in EC:DMC – 1 M $LiPF_6$ as a function of potential.

All the spectra are dominated by electrolyte features, as expected, and it is necessary to use subtractive normalization (SNFTIR) to isolate the interfacial species. The spectrum at 4 V was taken as the reference spectrum and at each higher potential subtractively normalized spectra were obtained as $\Delta R/R$,

$$\Delta R/R = (R_E - R_{ref})/R_{ref}$$

The result for EC:DMC electrolyte is shown in Fig. 29. It was clear from the SNFTIR spectra in the 2300–2400 cm^{-1} spectral region shown in Fig. 29 that a CO_2 peak begins to appear at about 5 V and above. This result is in good agreement with the CV data, indicating that the electrolyte was oxidized to CO_2 at potentials above 5 V. The intensity of the CO_2 signal obtained at 5.6 V was comparable to that from the electrolyte after it was saturated with CO_2 in a glove bag filled with CO_2, indicating that the electrolyte was saturated with the CO_2 produced by solvent oxidation at that potential. Our SNFTIR results were very similar to those reported by Joho and Novak[2] for the same electrolyte (LP 30) with a Ni working electrode. Joho and Novak[2] also reported that the oxidation potential of alkyl carbonate electrolytes

was lowered by the addition of water to nominally dry electrolyte.

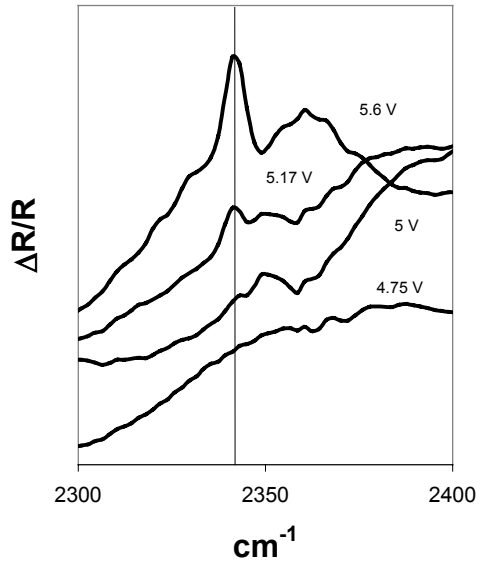

Figure 29. SNFTIR spectra from a glassy carbon electrode in EC:DMC – 1 M $LiPF_6$ as a function of potential derived from the IRAS spectra shown in Fig. 28.

As shown by the reaction Scheme 3 used in our density functional theory (DFT) calculations[3], CO_2 is an expected product in the oxidation mechanisms of both EC and DMC, and both solvents were predicted to have nearly identical (within 0.1 V) oxidation potentials, 5.6 V *vs.* Li/Li^+. The experimental oxidation potential of 5.2 V found here for the EC:DMC (1:1) electrolyte, assuming that the co-solvents have a single oxidation potential, are in reasonable agreement with the calculated potentials, and agree well with the results of Joho and Novak[2], but not that of Aurbach and co-workers[1].

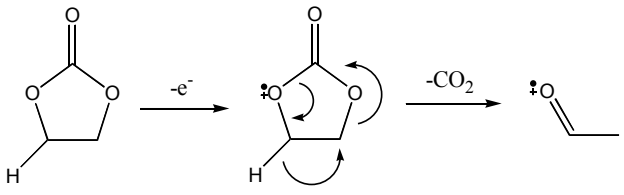

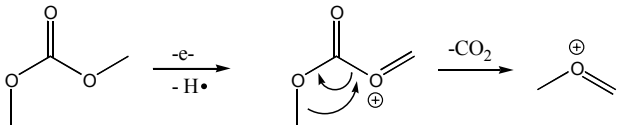

Scheme 3

Because of the relatively impure sample of VC available, we did not use CV to measure the oxidation potential. We were, however, able to observe a distinct oxidation potential using *in situ* IRAS that was not effected by the impurities present. Figure 30 shows a series of SNFTIR spectra for VC – 0.1 M $LiPF_6$ at potentials from 3.25 V up to 4.6 V.

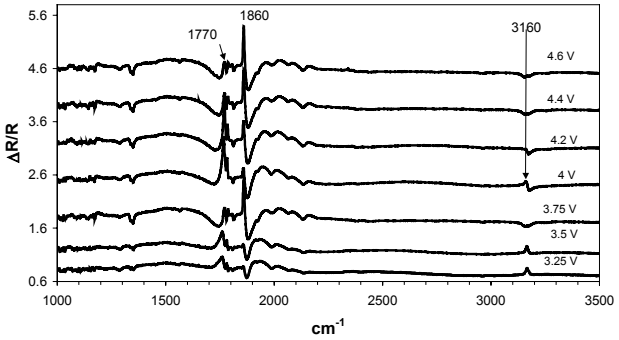

Figure 30. SNFTIR spectra for a glassy carbon electrode in VC – 0.1 M $LiPF_6$ as a function of potential (IRAS spectrum at 2.75 V used as reference).

The reference spectrum was that at open circuit (in this case about 2.7 V). In SNFTIR spectra, positive-going intensity is an increase in concentration of a species and negative going intensity is a decrease in concentration. The electrochemical Stark shift, the effect of the electric field in the inner Helmholtz layer on the vibrational frequency of molecules in the inner layer, is a complication that makes interpretation of any vibrational feature near those of the solvent molecules very difficult. In general, the Stark shift produces bipolar bands in SNFTIR spectra, the most well known being the bipolar bands for the C=O stretching of CO adsorbed on Pt surfaces, and the ΔR/R spectra in Fig. 30 have similar bipolar bands in the C=O stretching region (near 1800 cm^{-1}) and in the vinyl C-H stretching region (at 3160 cm^{-1}) which in our opinion are characteristic of Stark tuning shifts of VC molecules in the inner Helmholtz layer. However, a sharp peak at about 1860 cm^{-1} starts to appear at potentials above 4 V with a concurrent decrease in the

intensity the vinyl C-H stretching at 3160 cm^{-1}. These spectral changes are indicative of VC oxidation above 4 V, perhaps initiating at about 4.2 V. There are many C=O containing compounds that have vibrational bands in the region near 1800 cm^{-1}, so that one has to be cautious about assigning the features to a specific compound. We note that the symmetric C=O stretching from a cyclic acid anhydride could produce such an IR feature. The asymmetric stretch for cyclic anhydrides is usually at 1800–1775 cm^{-1} whereas the symmetric stretch is at 1870–1845 cm^{-1}. The asymmetric stretch usually provides a peak with stronger intensity than the symmetric one. The oxidation of VC produces a relatively strong new band at 1860 cm^{-1}, and possibly a weaker new band at 1770 cm^{-1} uniquely characteristic of a cyclic acid anhydride. There is a reasonable reaction path to produce a cyclic acid anhydride from electrochemical oxidation of VC, as shown in Scheme 4. According to our quantum chemical calculation[3], the VC molecular ion would be expected to decompose into CO and a vinyl radical cation, as shown in Scheme 4a. However, the VC used in our experiment has a purity of only 97%, with water being one of the impurities. One-election oxidation of VC to the molecular cation is followed by reaction with water, loss of a $H^{\cdot}$ radical, yielding hydroxy vinylene carbonate. This is followed by keto-enol tautomerization to give the cyclic carbonate of glycollic acid, $C_3H_2O_4$, as shown in Scheme 4b. Because the reaction with water occurs after ionization of the VC molecule to the molecular ion, the oxidation potential is not affected by the presence of water, *i.e.*, the water only affects the subsequent reactions of the cation with the electrolyte. The observed VC oxidation potential near 4 V is in very good agreement with the value of 4.06 V given by the DFT calculations.

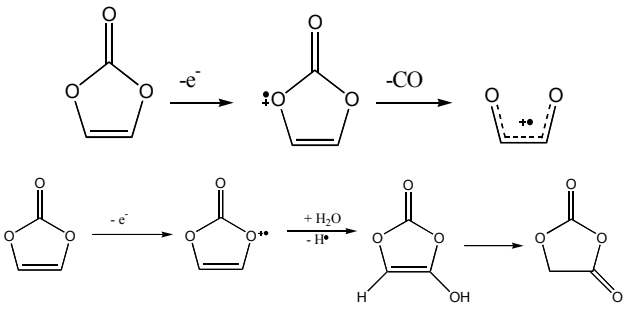

Scheme 4

References

[1] M. Moshkovic, M. Cojocaru, H.E. Gottlieb, and D. Aurbach, *J. Electroanal. Chem.* **2001**, *497*, 84.

[2] F. Joho and P. Novak, *Electrochim. Acta* **2000**, *45*, 3589

[3] X.R. Zhang, J.K. Pugh and P.N. Ross, *J.Electrochem. Soc.*, **148**, E183 (2001).

IV.F.4. Corrosion of Aluminum in Lithium Cell Electrolytes

James W. Evans and Thomas Devine (Lawrence Berkeley National Laboratory)
University of California, 316 Hearst Mining Building, MC 1760, Berkeley CA 94720
(510) 642-3807, fax: (510) 642-9164; e-mail: evans@socrates.berkeley.edu

Objectives

- Determine the role of $LiBF_4$ and $Li(CF_3SO_2)_2N$ (LiTFSI), in EC and DMC electrolytes, in the corrosion of aluminum, as well as the corrosion rate and corrosion mechanism of Al in these electrolytes.

- Characterize and quantify corrosion of Al when used in present or candidate Li cell electrolytes by using the electrochemical quartz crystal microbalance (EQCM) and some microscopy techniques. This is in order to predict the 15-year performance of Al collectors with extreme-value statistical analyses.

Approach

- Use *in situ* EQCM combined with electrochemical techniques to understand the corrosion mechanism of Al in $LiBF_4$ and $Li(CF_3SO_2)_2N$ / EC + DMC electrolyte.
- Characterize the surface morphology, the corrosion product, and passivation layer by microscopy and other surface analysis techniques, *e.g.,* SEM, infrared spectroscopy.

Accomplishments

- Determined the role of $LiBF_4$ and LiTFSI in EC and DMC electrolyte in the corrosion of Al.
- Analyzed the corrosion product and mass change (corrosion rate) of Al in $LiBF_4$ and LiTFSI/EC+DMC.
- Reached conclusions concerning the corrosion mechanism of Al in $LiBF_4$ and LiTFSI /EC+DMC.

Future Directions

- Study the effect of other new battery electrolytes, cathode composites, and environmental factors on the corrosion of Al.
- Characterize and quantify corrosion of Al when used in present or candidate Li cell electrolytes from commercial and lab-made batteries.
- Develop a model to describe the role of corrosion in the capacity loss of Li-ion battery.

Introduction

This program focuses on characterizing and quantifying corrosion of Al current collector in battery electrolyte. LiTFSI, $LiPF_6$ and $LiBF_4$ are widely used as the electrolyte in Li-ion batteries. LiTFSI is one of the most reactive salts causing corrosion of Al. Hence, use of this salt in Li batteries has been limited, despite of its superior properties over other salts in terms of less moisture sensitivity and relatively high thermal stability. In fact it is difficult to find one single electrolyte that fulfills all the requirements for an electrolyte, and mixed electrolytes combining the best characteristics of single electrolytes are therefore interesting.

We have used EQCM to monitor, *in situ,* the mass change occurring on the electrode surface during CV. The equivalent weight (mass change per mole of electron, mpe) obtained from the EQCM may help to give some information of corrosion reaction on the surfaces. In case of uniform corrosion, both current and mass change by EQCM helps to identify the corrosion and passivation products and to understand the corrosion mechanism.

In the present work, corrosion of Al in $LiBF_4$, LiTFSI and in these two mixed salts in EC/DMC solvent was studied by EQCM. Information on surface chemistry was obtained from FTIR spectroscopy. Figure 31 clearly shows that the presence of $LiBF_4$ in LiTFSI electrolyte significantly suppressed the corrosion current, and corrosion was not observed when 0.5 M $LiBF_4$ was added. The complicated mass change of increase-decrease-increase in LiTFSI solution indicates deposition (or adsorption) of precipitates occurring at the first anodic scan, but some dissolution (desorption) of the precipitates at the beginning of cathodic scan followed by accumulation of precipitates. Mass accumulation is pronounced when $LiBF_4$ is present. Although mpe change during cycling does not match with mpe values of any expected deposited species, the calculated mpe of -227 on anodic scan when adding of 0.5 M $LiBF_4$ reflects the high molecular weight precipitates

deposited on the surface of Al to form a protective layer.

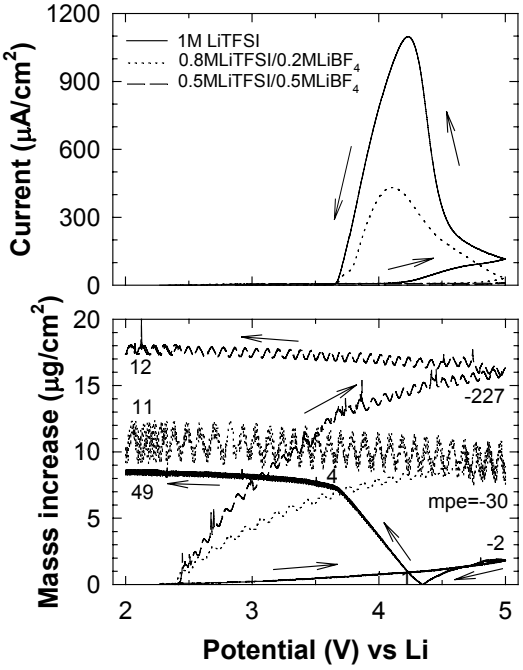

Figure 31. Comparative plots of CVs and the corresponding mass increase for the Al at the first cycle in 1 M LiTFSI/EC+DMC, 0.8M LiTFSI + 0.2 M $LiBF_4$/EC+DMC and 0.5 M LiTFSI + 0.5 M $LiBF_4$/EC+DMC; sweep rate = 5 mV/s .

Examination of the surface chemistry of Al has been carried out by FTIR spectroscopy. In Fig. 32(a) and (b), peaks at 1371, 1157 and 1209 cm^{-1} assigned to $\nu_a(SO_2)$, $\nu_s(SO_2)$ and $\nu_a(CF_3)$, respectively, must be of $TFSI^-$, indicating that corrosion products include this functional group. The broad peak around 3370 cm^{-1} reveals the presence of OH^-. Figure 32(c) shows peaks at 2925, 2854, 1727, 1000-1200 cm^{-1} of $\nu_s(CH)$, $\nu_a(CH)$and $\nu(C=O)$ respectively, together with other peaks from organic species. In particular, peaks of 1675 and 1354 cm^{-1} assigned to $\nu(CO_2)$, a coordination type C-O bond, are from lithium oxalate ($Li_2(CO_2)$). Apparently, the passivation layer consists of much organic species. The peak at 1065 cm^{-1} is attributed to some B-F bonding, and the very sharp peak at 3676 cm^{-1} corresponds to $\nu(OH)$ indicating the presence of free LiOH. Based on both the FTIR spectral findings and EQCM results, as well as consideration of the steric hindrance raised by large size of $N(SO_2CF_3)_2^-$ anion and the presence of OH^-, we suppose that the corrosion products present on Al after the experiment with LiTFSI/EC+DMC would be $Al[N(SO_2CF_3)_2]_{2-x}(OH)_x$ and some organic species. On the other hand, these passivation products are expected to contain organic species such as $ROCO_2Li$ and lithium oxalate.

Use of a mixed electrolyte of LiTFSI and $LiBF_4$ might be an effective way to increase the corrosion resistance of Al current collector and to improve the performance of Li-ion batteries. Severe pitting corrosion of aluminum in LiTFSI/EC+DMC electrolyte has been certainly suppressed in the presence of ≥ 20% $LiBF_4$ in the electrolyte. EQCM-CV response and SEM images showed that $LiBF_4$ plays an efficient role in building up a stable passive surface layer, protecting Al from the pitting corrosion. Surface chemistry studied by employing FTIR spectroscopy suggests that $Al[N(SO_2CF_3)_2]_{3-x}(OH)_x$ is the major corrosion products. However, the passive layer also includes organic precipitates which are solvent decomposition products such as $ROCO_2Li$, lithium oxalate and also insoluble inorganic salts such as $Al(BF_4)_3$. It is anticipated that mixing of these two salts helps to increase the corrosion resistance of Al current collector and to improve thermal stability and moisture sensitivity of the electrolyte in Li-ion batteries.

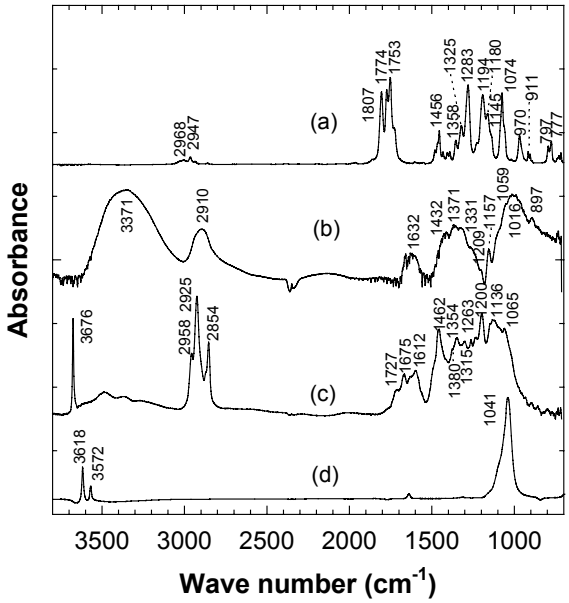

Figure 32. FTIR spectra of (a) 1 M LiTFSI/EC+DMC electrolyte solution, and of Al after CV-EQCM (b) in 1 M LiTFSI/EC+DMC, (c) in 0.8 M LiTFSI + 0.2M $LiBF_4$/EC+DMC and of (d) $LiBF_4$ salt alone.

IV.F.5. Synthesis and Characterization of Electrodes

Elton J. Cairns
Lawrence Berkeley National Laboratory, 70R0108B, Berkeley CA 94720-8168
(510) 486-5028, fax (510) 486-730, e-mail ejcairns@lbl.gov

Objective

- Make direct observation of Li in BATT Program cathode materials, characterize the local atomic and electronic environment, and determine changes in this environment with cycling.

Approach

- Use ^{7}Li MAS-NMR to characterize BATT Program electrodes before and after cycling.
- Determine the NMR isotropic chemical shift, linewidth, lineshape, and relaxation times for each Li species. Extend this to other important nuclei.
- Use NMR data on model failure mechanisms to interpret the spectra.

Accomplishments

- Obtained ^{7}Li MAS NMR spectra for several $LiMPO_4$ (M=Fe, Ni, Mn, Co) and $Li[Mn_xFe_{1-x}]\ PO_4$ olivine compounds and established the hyperfine shift mechanism. Showed that no structural changes occur with cycling.
- Obtained ^{7}Li MAS NMR spectra for layered $Li_y[M_{0.11}Mn_{0.89}]O_2$ (M=Al, Ni, Co, Zn, Cu, Fe) and determined various local environments in each composition. Identified the phases present in the most stable compositions, and clarified the structure of these materials.
- Obtained ^{7}Li MAS NMR spectra for Gen 2 electrodes after electrochemical cycling and at various states of charge. Identified Li loss from the NiO_x sites as a significant mechanism of capacity loss.

Future Directions

- Continue NMR work using 65 MHz magnet and spinning speeds of 20-25 kHz to improve resolution of spectra, giving more detailed information.
- Determine relaxation time for layered $Li_y[M_{0.11}Mn_{0.89}]O_2$ compounds to give additional information on the Li sites.
- Obtain ^{7}Li spectra for electrochemically cycled layered $Li_y[M_{0.11}Mn_{0.89}]O_2$ compounds for use in identifying capacity loss and stability information.
- Obtain the NMR spectra of layered compounds at various temperatures to aid in interpretation of spectra.
- Obtain 2-dimensional exchange spectra of layered compounds to determine the proximity of the Li cations in different local environments to aid in structure determination.
- Obtain ^{7}Li and ^{31}P NMR spectra of $LiFePO_4$ and $Li[Fe,Mn]PO_4$ at different states of charge and after repeated cycles to provide information on structural stability.
- Examine Gen 2 and Gen 3 electrodes to identify capacity loss mechanisms, as appropriate.

Olivine $LiMPO_4$ (M=Fe, Mn, Ni, Co)

Various olivine compounds, provided by M. Doeff, were studied using ^{7}Li MAS NMR. These studies revealed information about the nature of the hyperfine interaction. A single ^{7}Li isotropic resonance with a large spinning sideband envelope was seen for all the $LiMPO_4$ compounds, suggesting the presence of a single local environment for the Li cation (Fig. 33). Depending on the transition metal (TM) ion, various isotropic resonances are observed. Resonances at 68, -8, -49, and -86 ppm were observed for Mn, Fe, Ni, and Co- olivine, respectively. We found that each unpaired electron in the A' orbital contributes -28 ppm to the total Li NMR shift, whereas each unpaired electron in the A'' orbital contributes +80 ppm to the total shift. This work was extended to $Li[Mn_xFe_{1-x}]PO_4$ with various values of x. NMR spectra of these compositions suggest that Mn and Fe are homogeneously mixed. The Li NMR shift is a linear combination of those expected for pure Mn and pure Fe materials. These results provide a sound basis for the interpretation of spectra for cycled materials, and the interpretation of changes brought about by cycling.

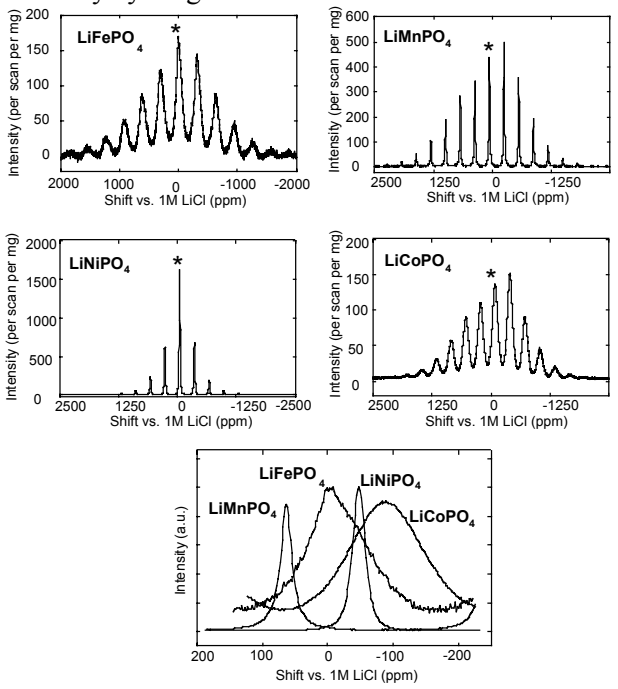

Figure 33. ^{7}Li MAS NMR spectra of olivine $LiMPO_4$ acquired with a 100 MHz magnet and 10 kHz spinning speed. The isotropic resonances are denoted with an asterisk.

Gen 2 Electrodes

NMR spectra of Gen 2 electrodes were obtained after electrochemical cycling using various protocols (Fig. 34). Two dominant resonances were observed for the fresh electrodes, a broad resonance at approximately 580 ppm and a sharp resonance at 0 ppm. The broad resonance at a higher shift is assigned to the Li cations containing Ni in their coordination environment ($LiNiO_2$ type). The sharp resonance at 0 ppm is assigned to Li with Co in the coordination sphere ($LiCoO_2$ type). The electrodes that showed capacity loss after electrochemical cycling exhibit a loss in the Li NMR signal for the resonance at 580 ppm. No noticeable change was observed for the resonance at 0 ppm for all the electrodes. Thus, it appears that the capacity loss is caused by changes in the Ni and/or its coordination sphere, possibly a preferential loss of Li from the vicinity of the Ni. NMR spectra of Gen 2 electrodes were also obtained at different states of charge. In the early stages of charging, the broad resonance at 580 ppm decreased in intensity and a new resonance at 313 ppm appeared, gradually shifting to lower frequencies as the charging proceeded. However, the resonance at 0 ppm appears to remain unchanged. This suggests that the oxidation of Ni^{3+} to Ni^{4+} occurs first, whereas the Co^{3+} is not oxidized until 4.4 V.

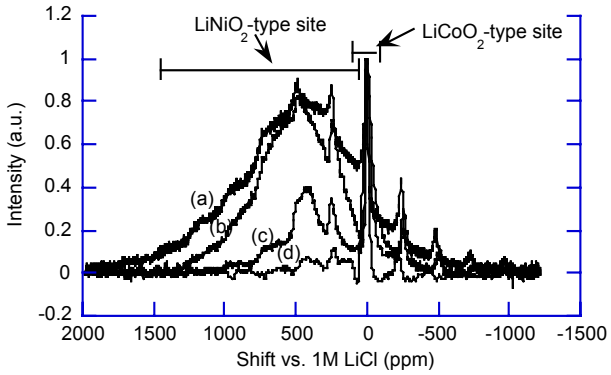

Figure 34. ^{7}Li MAS NMR spectra of Gen 2 electrodes ($LiAl_{0.05}Co_{0.15}Ni_{0.8}O_2$). Successive damage results in the loss in Li NMR signal from the $LiNiO_2$–type site. (a) Fresh electrode, (b) cycled once #I116, (c) stored, lost 24% power #A212, (d) cycled 140 times, lost substantial capacity #PG13.

Layered $Li_y[M_{0.11}Mn_{0.89}]O_2$ (M=Ni, Al, Cu, Fe, Zn, Co)

Lithium manganese oxides, which adopt a layered structure similar to that of $LiCoO_2$, have been studied as a promising cathode material for Li rechargeable cells. Various structural models have been proposed for the layered compounds (*i.e.*, O2, O3, P2, P3, T2) according to the stacking of oxygen and the site occupancy of the cations. Bruce *et al.* first synthesized the layered $LiMnO_2$ phase that is isostructural with $LiCoO_2$. This material is classified as O3-type and shows poor cycling characteristics resulting from the transformation to a spinel structure over repeated charging and discharging cycles. Recently, new layered compounds that adopt a structure related to the O2 structure were prepared by Dahn *et al*. In contrast to O3 $LiMnO_2$, it was reported that O2 $LiMnO_2$ does not convert to a spinel structure during cycling. However, the structure of these materials is not well defined due to the similarity between the structures and their poor crystalinity. Thus, our research has been focused on NMR spectroscopy to study the local Li environments as well as the long range effects in an attempt to better understand the relationship between the structure and the electrochemical properties.

^{7}Li MAS NMR spectra of various O2-type compounds, $Li_y[M_{0.11}Mn_{0.89}]O_2$ with M=Cu, Zn, Ni, Co, Fe, were acquired at 65 MHz magnetic field and at spinning speeds of 22 kHz (Fig. 35). M. Doeff provided these compounds. The low field and high spinning speed of MAS reduces the magnitude of the dipolar interaction between the Li nuclei and the unpaired electron on Mn, yielding spectra with higher resolution. Various combinations of resonances at ~700, 300, ~100 and -5 ppm were observed, depending on the metal substituent. All the compounds show a broad resonance at 650~720 ppm and a sharp resonance at -5 ppm. Additional resonances are observed at 100~124 ppm for Ni-, Co-, Fe- and Al-doped materials and at 300 ppm for Cu-doped material. Previously, it was shown that the predominant factor affecting the Li NMR shift in lithium manganese and lithium nickel oxides is the Fermi-contact interaction (Ref. *Phys. Rev. B*, 1997, 55, 12018). The Li NMR shift is determined by the sum of the individual contributions of the paramagnets in the cation coordination sphere. The size and the direction of the shift depend on the type of the bonds and the orbital overlap. Taking the same postulate, the local coordination environment of the Li cations in the various sites is examined for

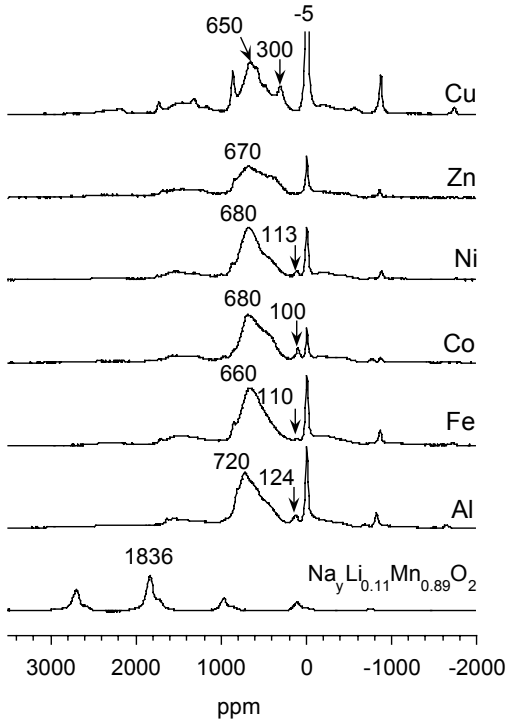

Figure 35. ^{7}Li MAS NMR spectra of O2 layered $Li_y[M_{0.11}Mn_{0.89}]O_2$ acquired with a 65 MHz magnet and 22 kHz spinning speed. The isotropic resonances are denoted in the figure.

our system. For Li in the tetrahedral site of a T2 structure with 10 Mn in the first coordination sphere, a shift of 270~430 ppm is predicted. A total contribution of 940~1160 ppm is predicted for Li in the octahedral site of an O2 structure containing 13 Mn in the coordination sphere. Therefore, the resonance at 300 ppm is assigned to the Li cations in the T2 environment and 650~720 ppm to Li in the O2 environment. The resonance at 100~124 ppm is attributed to Li in the O3 type environment, based on the previous study (Ref. *JACS*, 1998, 120, 12601). It appears that the compounds adopt predominantly an O2 structure with minor O3 or T2 type environments. Whether O3 and T2 type environments result from separate phase or stacking faults is not clear and further study is necessary. To check the presence of Li cations in the transition metal layer, $Na_y[Li_{0.11}Mn_{0.89}]O_2$ was prepared and a Li NMR shift of 1840 ppm is obtained. None of the O2 type $Li_y[M_{0.11}Mn_{0.89}]O_2$ studied shows a resonance at that high a frequency, suggesting that Li is not intercalated into the transition metal layer.

It appears that the O2-type compounds, which contain the O3 environment, exhibit higher specific capacity and the O2-type compound with T2 environment shows better capacity retention. Thus, optimizing the ratio of O2, O3, and T2-type environments would provide electrodes with higher capacity and better capacity retention.

Publications

M.C. Tucker, M.M. Doeff, T.J. Richardson, R. Finones, E.J. Cairns, and J.A. Reimer, *J. Am. Chem. Soc*. **2002**, 124, 3832

M.C. Tucker, M.M. Doeff, T.J. Richardson, R. Finones, J.A. Reimer, and E.J. Cairns, *Electrochem. and Solid State Lett*. **2002**, 5, 95.

IV.F.6. NMR and Modeling Studies

Gerbrand Ceder and Clare P. Grey

Massachusetts Institute of Technology, Department of Materials Science and Engineering, 13-5056, Cambridge, MA; (617) 253-1581, fax: (617) 258-6534; email: gceder@mit.edu

State University of New York at Stony Brook, Department of Chemistry, 669 Chemistry Building, Stony Brook, NY 11794-3400; (631) 632-9548; fax: (631) 632-5731; email: cgre@sbchem.sunysb.edu

Objective

- Evaluate alternative layered oxides as cathode materials for a Li-ion battery that operates between Ni(II) and Ni(IV).

Approach

- Use solid-state NMR and XAS to characterize local structure and oxidation states of the nearby cations (in the 1st and 2nd cation coordination spheres) as a function of state of charge and number of charge cycles.

- Use First Principles calculations (DFT) to identify redox-active metals, relative stability of different structures, the effect of structure on cell voltages and to identify promising cathode materials for BATT applications.

- Use calculations and NMR to characterize the stability of these materials and the effect of doping on conductivity by identifying low-activation-energy pathways for cation migration.

Accomplishments

- Used Li NMR results to determine the local environments in the materials $Li[Li_{(1-2x)/3}Mn_{(2-x)/3}Ni_x]O_2$, where x = 0.5, 0.33 and 0.1, and to determine which site are deintercalated as a function of SOC.

- Estimated cell voltages for different local environments and determined energies of different cation ordering schemes.

Future Directions

- Perform detailed investigations of cathode materials following extended cycling.

- Investigate the effect of cation doping on the structure and electrochemical behavior of these materials.

Introduction

Since the start of this project (June 1, 2002) we have made considerable progress in understanding the local structure of $Li[Li_{(1-2x)/3}Mn_{(2-x)/3}Ni_x]O_2$ and its effect on electrochemical properties. Lithium NMR results for the compositions x = 0.5, 0.33 and 0.1 show the presence of Li in both the Li and TM layers of these layered materials all systems (Table 2). The NMR results for $Li[Ni_{0.5}Mn_{0.5}]O_2$ are consistent with Ni^{2+} substitution into the Li layers as found in $LiNiO_2$. For compositions with $x \leq 1/3$, the fraction of Li in the Li layers is close to that predicted based on the stoichiometry of the materials.

Nickel Content (x)	Theoretical Li content in TM Layers* (% of total Li)	% Li in TM layer** (error)
1/2	0	7(1.5)
1/3	1/9 (8)	10 (2)
1/10	8/30 (20)	19 (2)
0	1/3 (25	22 (3)

**i.e.,* (1/3 – 2x/3)
***% based on total Li content

Table 2.

The Li local environments in the TM layers resemble the Li environments in the Mn layers of Li_2MnO_3 and can be represented by the local environment $Li(OMn)_{6-n}(ONi)_n$, where $n \leq 1$. These NMR are confirmed with Mn and Ni extended x-ray absorption fine structure (EXAFS) studies performed in collaboration with Dr. J. McBreen's group at BNL, which show that the Mn-ion local environments contain a larger number of Li ions than the Ni-ion local environments.

First Principles calculations have been performed on $(1–x)\ Li[Ni_{0.5}Mn_{0.5}]O_2 \bullet x\ Li[Li_{1/3}Mn_{2/3}]O_2$ and show that the environments for Li in the TM layers surrounded by more Mn ions are more stable than those surrounded by more Ni ions, and that Li doping in the TM layers reduces the tendency for Ni incorporation in the Li layers. A more detailed analysis of the Ni-Mn-Li arrangements in these materials is underway. Both the First Principles calculations and XAS experiments show that the redox process involves Ni, with the Mn ions remaining as Mn^{4+} during the 1st charge cycle at 4 V. The multiple electron change on Ni offers the possibility to engineer materials with high capacity.

A more detailed picture of the change in charge distribution with Li content is provided by generating charge density difference plots. Figure 36 shows the difference in charge density on the 100 plane of the spinel structure between the totally lithiated ($LiNi_{0.5}Mn_{0.5}O_2$) and the totally delithiated ($Ni_{0.5}Mn_{0.5}O_2$) states. Figure 36 demonstrates that charge is gained in sigma-type bonds of the Ni as the Li content increases. Conversely the charge on Mn remains roughly constant. The area where the t_{2g} orbitals point between the oxygens show little sign of change. This is consistent with all the redox activity being concentrated in the Ni e_g orbitals.

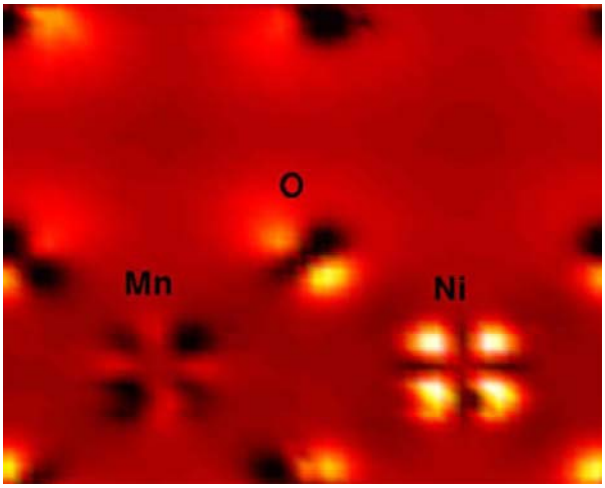

Figure 36. Change in spin density when Li is removed from $Li(Ni_{0.5}Mn_{0.5})O_2$. Bright(dark) regions indicate regions of high(low) change.

Additional evidence about the valence of Mn and Ni is provided by First Principles calculations of metal-oxygen bond lengths. As with spin, the Mn-O bond length is found to vary little with Li composition, confirming that little or no change to its valence state occurs. In contrast, the Ni-O bond length changes dramatically with Li composition. A Jahn-Teller distortion is observed at half lithiation which is consistent with Ni^{+3}.

First Principles calculations have also shed light on the precise sequence of Ni oxidation as Li is removed from the compound. Our calculations indicate that oxidation occurs locally whereby at high Li concentration, removal of each Li is

accompanied by a change in valence of one Ni from +2 to +3. Only after all Ni ions have been oxidized to +3 will oxidation to +4 occur with further Li removal. Interestingly, First Principles results predict that Li sites in the Li layer with an immediate environment rich in Ni are more stable than those with a Mn-rich environment. Hence, the Li ions removed first are those closest to the Mn ions, even though Mn does not participate in the redox process.

The NMR results for the compositions x = 0.5, 0.33 and 0.1 clearly demonstrate that the Li is removed from both the Li layers and the TM layers on cycling. Calculations were performed in order to understand this phenomenon in more detail and indicated that Li is removed from the Li and TM layers at similar potentials. The latter process is facilitated by Li vacancies in the TM layers. Li NMR showed that the Li ions return to the TM layers on discharging and that the process is reversible (Fig. 37).

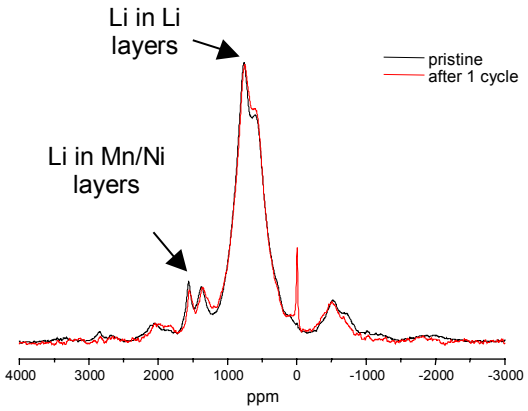

Figure 37. ^{6}Li MAS NMR $Li[Li_{1/9}Mn_{5/9}Ni_{1/3}]O_2$ shows that Li in both the Li layers and TM layers is removed but then returns following the first charge cycle.

The average voltage calculated by *ab initio* methods for the extraction of Li from the Li plane was found to vary from 2.84 to 2.98 V, whereas the voltage for Li from the TM plane ranged from 3.23 to 3.27 V. These numbers display the usual underestimation of the potential by the computational approach, but can be used to make relative comparisons. It was also found that Li should readily leave the TM plane provided a neighboring tetrahedron is surrounded by three Li vacancies.

Presentations

W.–S. Yoon, Y. Paik, C.P. Grey, X.-Q. Yang and J. McBreen, "^{6}Li MAS NMR and *In Situ* XRD Studies of Lithium Nickel Manganese Oxides," *11th International Meeting on Lithium Batteries*, Monterey, CA, June 2002.

G. Ceder, D. Carlier, J.Reed and A. an der Ven, "Thermodynamics and Kinetics of Layered $Li(Li,Ni,Mn)O_2$," *11th International Meeting on Lithium Batteries*, Monterey CA, June 2002.

G. Ceder, D. Carlier, J.Reed E. Arroyo and A. an der Ven, "First Principles Approaches to Investigate and Predict the Properties of Li Intercalation Oxides," Short Course on Materials for Energy: Batteries and Fuel Cells, Madrid, Spain, November 4-6, 2002.

IV.G. Modeling

IV.G.1. Improved Electrochemical Models

John Newman (Lawrence Berkeley National Laboratory)
University of California, Department of Chemical Engineering, 201 Gilman Hall, MC 1462, Berkeley CA 94720
(510) 642-4063, fax: (510) 642-4778, e-mail: newman@newman.cchem.berkeley.edu

---

Objectives

- Develop experimental and computational methods for measuring and predicting transport, kinetic, and thermodynamic properties.
- Model the behavior of electrochemical systems to optimize performance, identify limiting factors, and mitigate failure mechanisms.

Approach

- Refine galvanostatic polarization technique to measure transport properties.
- Develop molecular dynamics simulation of diffusion in multicomponent solutions.
- Develop thermal model that accounts for concentration effects in insertion electrodes.
- Develop model of dendrite formation on Li metal.
- Develop model of growth of the SEI layer.
- Model the $LiFePO_4$ electrode to identify limiting factors.
- Simulate the use of conductive polymers for overcharge protection.

Accomplishments

- Analyzed the effect of side reactions on measurements of transference numbers and activity coefficients by the galvanostatic polarization method.
- Demonstrated how ion association with increasing salt concentration causes increased viscosity and decreased conductivity in electrolytes containing $LiPF_6$ in carbonate solvents.
- Derived equations for determining the heat of mixing in electrochemical systems.
- Examined effect of mechanical stresses on dendrite initiation.
- Developed model of electron and ion transport through the SEI layer.
- Developed model of the $LiFePO_4$ electrode and compared to experiments.

Future Directions

- Refine model of effect of mechanical stresses on dendrite initiation.
- Compare SEI model with data to refine kinetic and transport parameters.

- Examine the roles of diffusion, kinetics, and conductivity in the performance of $LiFePO_4$.
- Analyze use of two polymer layers of different stabilities and transport properties.
- Simulate use of conductive polymers for overcharge protection.
- Develop improved method for measuring transference numbers.

Introduction

We modeled the effect of a side reaction at the Li electrode on measurements of transport properties in polymer electrolytes. Measurements of diffusion coefficients and conductivity are not significantly affected, but measurements of transference numbers and activity coefficients using the galvanostatic-polarization and concentration-cell experiments can be substantially affected by side reactions. The presence of side reactions can be detected by performing transition-time experiments. The occurrence of side reactions can be mitigated by using a difference reference electrode such as $Li_4Ti_5O_{12}$ during the concentration-cell experiments. Future work will examine new experimental techniques to remove the effect of side reactions from measurements of transference numbers.

The MD model has been successfully used to understand how interatomic interactions affect transport of $LiPF_6$ in carbonate-based electrolytes. Association between the anion and cation causes rigid networks that reduce the conductivity as the salt concentration increases.

Equations have been derived to predict the magnitude of the heat of mixing in electrochemical systems (equal to the amount of heat released while a cell relaxes after the current is turned off). The heat of mixing is small in systems with good transport properties.

Lithium metal has the highest energy density of any electrode. However, it will never be safe to use commercially unless one can prevent the risk of dendrites shorting the cell. We have shown that any dendrite initiated will be a problem, and that separators of sufficiently high elastic modulus could suppress dendrite initiation. Future work will combine the model of mechanical stress into the electrochemical model for dendrite initiation.

The model of the SEI layer indicates that only part of the initial irreversible capacity of graphite electrodes goes into forming a solid interphase layer of the thickness observed experimentally; the rest of the irreversible capacity must form soluble products. Future work will compare the model to data from the literature in order to refine parameters such as the transference number for electrons and rate constants.

The full-cell-sandwich model, dualfoil.f, has been modified to include the two-phase reaction, which occurs in $LiFePO_4$, and results have been compared to experiments performed in Striebel's lab. The model shows that accessible capacity in these cells is limited by mass transport within the iron phosphate, and *not* by electronic conductivity. Future work will focus on improving the match between the model and high-rate experiments.

Publications and Presentations

K.E. Thomas, R.M. Darling and J. Newman, "Mathematical Modeling of Lithium Batteries," W. A. van Schalkwijk and B. Scrosati, eds., in: *Advances in Lithium-Ion Batteries*, New York: Kluwer Academic/Plenum Publishers, p. 345 (2002).

W.C. Wong and J. Newman, "Monte Carlo Simulation of the Open-Circuit Potential and the Entropy of Reaction in Lithium Manganese Oxide" *J. Electrochem. Soc.*,**149,** A493-A498 (2002).

D.R. Wheeler and J. Newman, "A Less Expensive Ewald Lattice Sum," *Chem. Phys. Lett.*, **366**, 537-543 (2002).

J. Newman, K.E. Thomas, H. Hafezi and D.R. Wheeler, "Modeling of Lithium-Ion Batteries," *11th International Meeting on Lithium Batteries*, Monterey, CA, June 2002.

K.E. Thomas and J. Newman, "Heats of Mixing and Entropy in Porous Insertion Electrodes," *11th International Meeting on Lithium Batteries*, Monterey, CA, June 2002.

IV.G.2 Failure Mechanisms in Li-Ion Systems: Design of Materials for High Conductivity and Resistance to Delamination

Ann Marie Sastry
The University of Michigan, Department of Mechanical Engineering and Applied Mechanics, Ann Arbor, MI 48109-2125
(313) 764-3061;, fax: (313) 747-3170, e-mail: amsastry@engin.umich.edu

---

Objectives

- Develop experimental and computation methods for measuring, and predicting electrical conductivity of Li-ion electrodes.
- Identify and optimize network morphologies resistant to electrochemical degradation.

Approach

- Extend of the Schumann-Gardner multilayer theory to measure electrical resistivity and contact resistance in electrodes.
- Develop image analyses to quantify electrode particle morphologies.
- Develop 2D and 3D conduction simulations based on particle morphologies.

Accomplishments

- Provided an experimental technique to determine electrode resistivity and contact resistance between active materials and current collectors.
- Validated of conduction models and simulations for BATT electrodes (collaboration with Striebel) for variety of particle types and manufacturing processes.

Future Directions

- Develop 3D pixilated conduction models.
- Integrate electrochemical, mechanical, and conduction model to benchmark theoretical results of damage analysis.
- Study contact of particles and current collectors.

Introduction

We are identifying and optimizing network morphologies capable of resisting electrochemical degradation. It is well known that carbonaceous Li-ion anodes are subject to electrolytic decomposition, and exfoliation of graphitic particles. However, phase diffusion limits fast discharge of lithium iron phosphate, which has recently attracted attention as Li-ion cathode. Both failure modes are closely related to the morphology of the electrodes. Thus, we are intensively modeling and measuring conductive properties of both electrodes and potential additives for use in Li-ion systems.

The conduction modeling builds on our previous numerical work, incorporating real material morphology and careful selection of boundary conditions to reduce the numerical difficulties posed by singularities in the field solution, due to phase contrast, sharp corners, etc. This approach can assist to identify the key parameters that optimize network morphology, and it also can predict the materials effective conductivity. In order to verify the accuracy of this approach, we developed an accurate experimental method — the four-point-probe technique (Fig. 38), which allowed independent characterization of contact resistance and layer resistivity.

Validation of the models was made in several types of materials received from LBNL and HQ (Table 3). Tested anodes were comprised of wide variety of particle shapes, including those comprised of fibers, particles and flakes. The modeling results showed significantly better prediction than effective medium theories. Also, we noted an overall trend of slightly increasing resistivity with density, pointing to particle breakup in compression of electrodes. Thus, though increasing conductive additive may initially improve conductivity, excessive compression may in fact increase both contact resistance and top-layer resistivity. We will explore this further with additional image analysis.

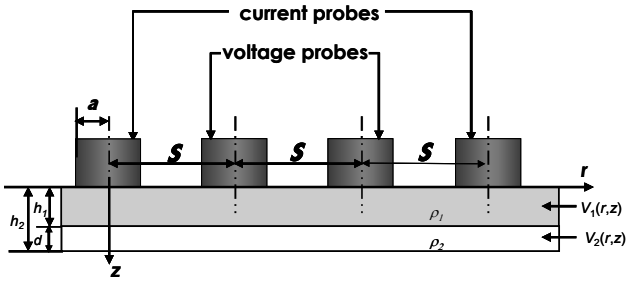

Figure 38. Schematic of test apparatus (four-point-probe) used in the measurement of resistivity.

The variation in conductivity of the various graphitized carbon materials was clearly shown to be related to the morphology of the active materials. Ultimately, the trade-offs among factors in electrochemical performance can be resolved with improved simulations of materials performance. An obvious subject of future work is combined electrochemical, conduction and mechanical modeling of these materials.

The importance of 3D *vs.* 2D modeling was also explored in this project year. We have developed analytical percolation solutions which have direct relevance to the conduction question, and compared 2D and 3D solutions, both analytically and numerically (Fig. 39). This will be the subject of intensive investigation in the coming year. Further work on interaction between particles and the current collector is also warranted.

electrode no.	electrode condition	electrode thickness (μm)	resistivity of active material (μΩcm)	stdev resistivity of active material (μΩcm)	contact resistance (μΩcm²)	stdev contact resistance (μΩ cm²)	uncertainty (%)
028-09-4	unpressed	100	7.99E+05	2.39E+05	3.24E+05	8.60E+04	15.55%
028-09-5	pressed	90	7.50E+05	2.28E+05	3.87E+05	9.38E+04	15.65%
028-09-6	pressed	85	7.71E+05	1.11E+05	4.93E+05	4.45E+04	15.73%
028-12-5	unpressed	91	7.91E+04	1.49E+05	1.86E+04	4.48E+04	15.77%
028-12-6	pressed	83	1.49E+05	9.21E+04	1.69E+04	1.04E+04	15.75%
028-12-7	pressed	80	8.73E+04	4.86E+04	1.45E+04	4.20E+03	16.56%
028-12-1	unpressed	94	1.60E+04	2.40E+03	1.85E+02	9.60E+01	15.07%
028-12-3	pressed	83	1.18E+04	2.11E+04	1.05E+03	1.51E+03	16.23%
028-12-4	pressed	81	1.44E+04	2.35E+04	1.22E+03	1.51E+03	16.30%
028-67-1	unpressed	179	1.51E+06	1.87E+05	3.59E+06	7.36E+05	15.93%
028-67-2	100 (kg/cm²)	129	3.81E+05	4.32E+04	1.54E+06	1.11E+05	16.00%
028-67-3	200 (kg/cm²)	115	1.88E+05	3.41E+04	1.50E+06	9.54E+04	16.03%
028-67-4	300 (kg/cm²)	109	1.91E+05	1.78E+04	1.10E+06	1.95E+05	16.02%
028-68-1	unpressed	150	2.64E+05	3.17E+04	1.18E+04	1.48E+03	15.21%
028-68-2	100 (kg/cm²)	125	1.62E+05	3.30E+04	1.44E+04	7.72E+03	15.33%
028-68-3	200 (kg/cm²)	103	6.39E+04	1.91E+04	2.22E+04	2.16E+02	15.43%
028-68-4	300 (kg/cm²)	105	6.73E+04	3.20E+04	3.29E+04	7.91E+03	15.62%
028-69-1	unpressed	141	3.15E+04	9.88E+03	2.07E+03	5.93E+02	16.47%
028-69-2	100 (kg/cm²)	121	1.74E+04	1.96E+03	4.47E+03	4.89E+02	15.12%
028-69-3	200 (kg/cm²)	117	4.75E+04	4.25E+04	6.32E+03	3.73E+03	15.38%
028-69-4	300 (kg/cm²)	112	1.12E+05	1.28E+05	7.57E+03	4.88E+03	19.43%

Table 3. Selected experimental results for anode resistivity and contact resistance.

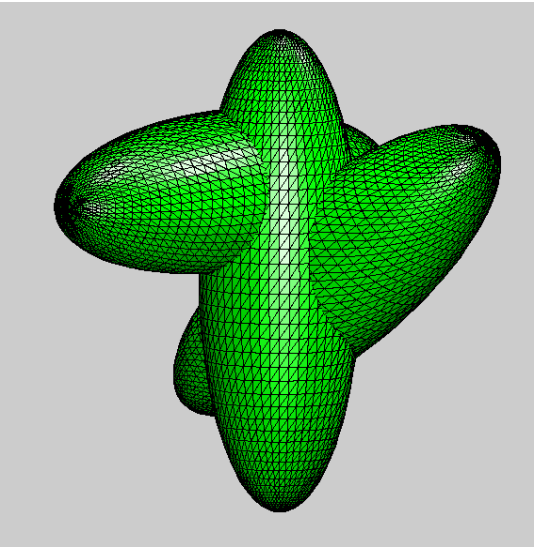

Figure 39. 3D mesh generation for complex particle geometries.

Publications

C.-W. Wang, Y.-B. Yi and A.M. Sastry, "Multiphase Conductive Networks: Simulations and Closed-Form Solutions for Selection of Conductive Anode Additives," *202nd Meeting of the Electrochemical Society*, Salt Lake City, UT, October 2002.

C.-W. Wang, A.M. Sastry, K.A. Striebel and J. Shim, "Exact Solution for Contact and Top-Layer Resistivity in Two-Layer Electrodes: Applications for Li-ion Anodes," *202nd Meeting of the Electrochemical Society*, Salt Lake City, UT, October 2002.

K. Striebel, J. Shim, C.-W. Wang and A.M. Sastry, "Anode Performance and Matrix Conductivity in Lithium Battery Electrolytes," *202nd Meeting of the Electrochemical Society*, Salt Lake City, UT, October 2002.

ACKNOWLEDGMENTS

This work was supported by the Assistant Secretary for Energy Efficiency and Renewable Energy, Office of FreedomCAR and Vehicle Technologies of the U.S. Department of Energy under Contract No. DE-AC03-76SF00098. The support from DOE and the contributions by the participants in the BATT Program are acknowledged. The assistance of Ms. Susan Lauer for coordinating the publication of this report is gratefully acknowledged.

V. APPENDIX

V.A. List Of Acronyms

AFM	Atomic force microscopy
ANL	Argonne National Laboratory
AOP	Annual Operating Plan
ASI	Area specific impedance
ATD	Advanced Technology Development
BATT	Batteries for Advanced Transportation Technologies
BHT	Butylated Hydroxytoluene
BNL	Brookhaven National Laboratory
CPE	Composite polymer electrolyte
CSAFM	Current-sensing atomic force microscopy
CV	Cyclic voltammetry
DEC	Diethyl carbonate
DFT	Density functional theory
DMC	Dimethylcarbonate
DMF	Dimethyl formamide
DOD	depth-of-discharge
DOE	Department of Energy
DSC	Differential scanning calorimetry
EC	Ethylene carbonate
EDS	Electron dispersive spectroscopy
EDX	Energy dispersive x-ray analysis
EIS	Electrochemical impedance spectroscopy
EMC	Ethyl methyl carbonate
EQCM	Electrochemical quartz crystal microbalance
EV	Electric vehicle
EXAFS	Extended X-ray absorption fine structure
FR	Flame retardant
FTIR	Fourier transform infrared
GBL	γ-butyrolactone
HETAP	Hexa-ethoxy-tri-aza-phosphazene
HEV	Hybrid electric vehicle
HMTAP	hexa-methoxy-tri-aza-phosphazene
HQ	Hydro-Québec
ICL	Irreversible capacity loss
IIT	Illinois Institute of Technology
IRAS	Infrared absorption spectroscopy
LBNL	Lawrence Berkeley National Laboratory

LiTFSI	Lithium bis(trifluoromethane-sulfonyl)imide
LN	Liquid nitrogen
MAS	Magic Angle Spinning
MCT	Mercury Cadmium Telluride
MD	Molecular Dynamics
MIT	Massachusetts Institute of Technology
mpe	Mole of electron
MW	Molecular weight
NFE	Nonflammable electrolyte
NG	Natural graphite
NMR	Nuclear magnetic resonance
OAAT	Office of Advanced Automotive Technologies
OCV	Open circuit voltage
PA	Power-Assist
PC	Propylene carbonate
PEG	Polyethylene glycol
PEO	Poly(ethylene oxide)
PMO	Poly(methylene oxide)
PNGV	Partnership for a New Generation of Vehicles
PPO	Poly(propylene oxide)
PTMO	Poly(trimethylene oxide)
PVDF	Poly(vinylidene fluoride)
RDE	Rotating disk electrode
R-F	Resorcinal formaldehyde
SEI	Solid electrolyte interphase
SEM	Scanning electron microscopy
SNFTIR	Subtractive normalization Fourier transform infrared
SOC	State of charge
SPE	Solid polymer electrolyte
SUNY	State University of New York
TEM	Transmission electron microscopy
TESA	Tetra-ethyl-sulfamide
TM	Transition metal
TMO	Trimethylene oxide
UHV	ultra high vacuum
USABC	United States Advanced Battery Consortium
VC	vinylene carbonate
WAXD	Wide-angle x-ray diffraction
XAS	X-ray absorption spectroscopy
XPS	X-ray photoelectron spectroscopy
XRD	X-ray diffraction

V.B. Annual Reports

1. Exploratory Technology Research Program for Electrochemical Energy Storage – Annual Report for 2000, LBNL-47960 (June 2001).
2. Exploratory Technology Research Program for Electrochemical Energy Storage – Annual Report for 1999, LBNL-45767 (May 2000).
3. Exploratory Technology Research Program for Electrochemical Energy Storage – Annual Report for 1998, LBNL-42694 (June 1999).
4. Exploratory Technology Research Program for Electrochemical Energy Storage – Annual Report for 1997, LBNL-41950 (June 1998).
5. Exploratory Technology Research Program for Electrochemical Energy Storage – Annual Report for 1996, LBNL-40267 (June 1997).
6. Exploratory Technology Research Program for Electrochemical Energy Storage – Annual Report for 1995, LBNL-338842 (June 1996).
7. Exploratory Technology Research Program for Electrochemical Energy Storage – Annual Report for 1994, LBL-37665 (September 1995).
8. Exploratory Technology Research Program for Electrochemical Energy Storage – Annual Report for 1993, LBL-35567 (September 1994).
9. Exploratory Technology Research Program for Electrochemical Energy Storage – Annual Report for 1992, LBL-34081 (October 1993).
10. Exploratory Technology Research Program for Electrochemical Energy Storage – Annual Report for 1991, LBL-32212 (June 1992).
11. Technology Base Research Project for Electrochemical Energy Storage – Annual Report for 1990, LBL-30846 (June 1991).
12. Technology Base Research Project for Electrochemical Energy Storage – Annual Report for 1989, LBL-29155 (May 1990).
13. Technology Base Research Project for Electrochemical Energy Storage – Annual Report for 1988, LBL-27037 (May 1989).
14. Technology Base Research Project for Electrochemical Energy Storage – Annual Report for 1987, LBL-25507 (July 1988).
15. Technology Base Research Project for Electrochemical Energy Storage – Annual Report for 1986, LBL-23495 (July 1987).
16. Technology Base Research Project for Electrochemical Energy Storage – Annual Report for 1985, LBL-21342 (July 1986).
17. Technology Base Research Project for Electrochemical Energy Storage – Annual Report for 1984, LBL-19545 (May 1985).
18. Annual Report for 1983 – Technology Base Research Project for Electrochemical Energy Storage, LBL-17742 (May 1984).
19. Technology Base Research Project for Electrochemical Energy Storage – Annual Report for 1982, LBL-15992 (May 1983).
20. Technology Base Research Project for Electrochemical Energy Storage – Report for 1981, LBL-14305 (June 1982).
21. Applied Battery and Electrochemical Research Program Report for 1981, LBL-14304 (June 1982).

22. Applied Battery and Electrochemical Research Program Report for Fiscal Year 1980, LBL-12514 (April 1981).